



# ENGINEERING IN THEORY AND PRACTICE

Editörler

Assoc. Prof. Dr. Abdulrezzak BAKIŞ

Assoc. Prof. Dr. Şakir PARLAKYILDIZ

Dr. Burçin YILMAZ



# **ENGINEERING IN THEORY AND PRACTICE**

**Editors:**

**Assoc. Prof. Dr. Abdulrezzak BAKIŞ**

**Assoc. Prof. Dr. Şakir PARLAKYILDIZ**

**Dr. Burçin YILMAZ**



***ENGINEERING IN THEORY AND PRACTICE***

***Editors: Assoc. Prof. Dr. Abdulrezzak BAKIŞ,***

***Assoc. Prof. Dr. Şakir PARLAKYILDIZ, Dr. Burçin YILMAZ***

**Editor in chief:** Berkan Balpetek

**Cover and Page Design:** Duvar Design

**Printing :** December -2024

**Publisher Certificate No:** 49837

**ISBN:** 978-625-5530-91-2

© Duvar Yayınları

853 Sokak No:13 P.10 Kemeraltı-Konak/İzmir

Tel: 0 232 484 88 68

[www.duvar yayinlari.com](http://www.duvar yayinlari.com)

[duvarkitabevi@gmail.com](mailto:duvarkitabevi@gmail.com)

***\*The publisher and editors are not obligated to accept responsibility for the views, opinions, and potential ethical violations stated by the authors. The responsibility for the content in the book lies solely with the author(s).***

## TABLE OF CONTENTS

<b>Chapter 1.....</b>	<b>5</b>
<b>Advanced Perspectives on Thermal Management Solutions for Batteries and Supercapacitors</b>	
<i>Şafak Melih ŞENOCAK, Yasin VAROL</i>	
<b>Chapter 2.....</b>	<b>32</b>
<b>Energy Production from Solid Waste: Mugla Province Example</b>	
<i>Ali Kemal ÇAKIR</i>	
<b>Chapter 3.....</b>	<b>41</b>
<b>Assessing Climate Policies For Achieving Sdg 13 Towards Net Zero Carbon</b>	
<i>Elif AYHAN, Aytac Perihan AKAN, Aysenur UGURLU4</i>	
<b>Chapter 4.....</b>	<b>79</b>
<b>Sustainable Energy Management Through Machine Learning Models for Natural Gas Consumption Prediction</b>	
<i>Didem GULERYUZ, Fatmanur BİLGEN</i>	
<b>Chapter 5.....</b>	<b>104</b>
<b>The Role of Chaotic Maps in Metaheuristic Optimization Algorithms: A Study on AVOA</b>	
<i>Osman ALTAY, Elif VAROL ALTAY</i>	
<b>Chapter 6.....</b>	<b>123</b>
<b>Numerical Investigation of The Effect Of Different Volume Concentrations Of Binary Hybrid Nanofluids On Entropy Generation In A Circular Heat Exchanger Tube</b>	
<i>Fatma OFLAZ</i>	

**Chapter 7.....146**

**Investigating the Effect of Dimpled Tubes on  
Thermal Performance and Flow Resistance**

*Fatma OFLAZ*

**Chapter 8.....163**

**Advancing Clean Energy: The Integration of Renewable Energy  
Sources, Smart Grids, and the Role of Electric Vehicles**

*Şafak Melih ŞENOCAK, Yasin VAROL2*

**Chapter 9.....188**

**Detection Damages in the Presence of Electric and  
Magnetic Fields Using Computer-Aided Tap Test**

*Imran ORAL*

**Chapter 10.....210**

**Magnesium Matrix Composites (MMCS):  
Materials, Processing, And Applications**

*Mikail Aslan*

**Chapter 11.....220**

**Mechanical Alloying:  
Principles, Techniques, And Applications**

*Mikail ASLAN*

**Chapter 12.....232**

**Energy Consumption Analysis and Prediction of Household Appliances  
by Machine Learning Approach**

*Serhat Berat EFE*

**Chapter 13 .....243**

**A Review on Liquefaction Studies in Geotechnical Engineering**

*Narin AYENGİN, Fatih YILMAZ*

## **Chapter 1**

### **Advanced Perspectives on Thermal Management Solutions for Batteries and Supercapacitors**

**Şafak Melih ŞENOCAK<sup>1</sup>**

**Yasin VAROL<sup>2</sup>**

---

1 Şafak Melih ŞENOCAK, Lecturer, Osmaniye Korkut Ata University, Osmaniye Vocational School  
e-mail: mlhsnck@gmail.com, ORCID ID: <https://orcid.org/0000-0003-0602-2836>

2 Prof. Dr. Yasin VAROL, Firat University, Technology Faculty, Elazig  
e-mail: yvarol@gmail.com, ORCID ID: <https://orcid.org/0000-0003-2989-7125>

# **Advanced Perspectives on Thermal Management Solutions for Batteries and Supercapacitors**

## **Summary**

This study provides a comprehensive research of thermal management systems (BTM) for electrochemical energy storage, focusing on batteries and supercapacitors. It discusses various cooling strategies, including air, liquid, PCM, and hybrid-based systems, emphasizing their advantages, limitations, and applications. Phase change materials (PCMs) are highlighted for their energy-saving and eco-friendly attributes, though their low thermal conductivity requires enhancement through nanomaterials such as metal foams and carbon nanotubes. Liquid cooling offers high heat transfer efficiency but presents challenges like leakage risks and added weight, while air cooling is cost-effective but limited by uneven temperature distribution. Hybrid systems that combine these methods show promise in achieving superior thermal performance. The study also explores innovative approaches, such as microchannel technologies, modular designs, and intelligent systems utilizing AI and machine learning, to optimize BTM efficiency. The findings underline the critical role of thermal management in enhancing the safety, performance, and lifespan of energy storage systems, with future research needed to expand applications and improve cost-effectiveness and sustainability.

**Keywords:** thermal management systems, supercapacitor, phase change materials, battery, cooling

## 1. Introduction

Over the past century, environmental degradation and the energy problem have arisen as significant worldwide challenges, with the transportation sector recognized as a primary contributor. (Tie & Tan, 2013). The release of gases into the atmosphere due to fossil fuel consumption, coupled with health concerns associated with climate change, has driven researchers to explore more sustainable and environmentally friendly energy alternatives (Olabi, 2012; Olabi & Abdelkareem, 2022). This development has driven the automotive and engineering industries to focus on clean energy systems that utilize renewable energy sources (Sayed et al., 2021; WADA, 2009). Particularly for the transportation sector, electric vehicles hold the greatest potential for development due to their environmental friendliness, high efficiency, and sustainability advantages (Lyu et al., 2019; Oca, Guillet, Tessard, & Iraola, 2019; Xie, Ge, Zang, & Wang, 2017). With the rapid growth of emerging electric vehicles (EVs), the demand for high-energy-density power batteries is increasing at an accelerated pace (Fan et al., 2019), (Joris Jaguemont, Omar, Abdel-Monem, Van den Bossche, & Van Mierlo, 2018). Batteries are regarded as one of the most promising methods for storing and transmitting electrical energy (Abo-Khalil et al., 2022; Malinauskaite, Anguilano, & Rivera, 2021). To meet this growing demand, renewable energy sources such as solar, wind, hydro, and tidal energy represent significant solutions for achieving this goal (Chu & Majumdar, 2012; Ellabban, Abu-Rub, & Blaabjerg, 2014). However, due to geographical limitations and the inherent variability of the energy they provide, these sources negatively impact storage cells and necessitate greater reliance on the electrical grid for connectivity (Adalati et al., 2022; Li, Ho, Xie, & Stern, 2022). Lithium-ion batteries (LIBs) and supercapacitors (SCs) represent the predominant energy storage devices in current applications. (Pomerantseva, Bonaccorso, Feng, Cui, & Gogotsi, 2019). Compared to other types of energy storage, lithium-ion batteries are preferred in new energy vehicles due to their low self-discharge rates, long service life, and high power and energy densities (Jouhara et al., 2019; L. Wei et al., 2020). On the contrary, supercapacitors store energy at the electrode interface, providing greater energy density than conventional capacitors. Moreover, they surpass lithium-ion batteries in terms of power density, energy efficiency, durability over cycles, and safety features (Akkinpally et al., 2022; Peng et al., 2022). Furthermore, supercapacitors exhibit significant potential for widespread industrial utilization in diverse sectors, such as military transportation and power grid systems (Akkinpally et al., 2023). Nevertheless, deviations from the optimal temperature range can negatively influence the performance and longevity of both batteries and supercapacitors. These temperature fluctuations

may compromise their storage capacity, charging and discharging efficiency, operational reliability, and overall durability (Kang & Rizzoni, 2014; Rafik, Gualous, Gallay, Crausaz, & Berthon, 2007; Sun, Zhang, Wang, Xu, & Ma, 2015). In addition, temperature differences between modules within a pack can disrupt electrical balance, thereby compromising the overall performance of the entire pack (Hameer & van Niekerk, 2015). For instance, the solid electrolyte interphase (SEI) layer on the anode expands more rapidly at high temperatures, becomes more porous during fast charging, and loses stability. Thermal runaway, a major safety concern, progresses through a chain reaction in which the decomposition of battery components occurs in succession. This process can escalate to produce smoke, fire, or even explosions, posing significant hazards to both drivers and passengers. Additionally, uneven temperature distribution within a single cell causes disparities in electrochemical reaction rates, which in turn reduce battery lifespan and limit the efficient utilization of stored energy. (Cai, Xu, Liao, Su, & Weng, 2019). A 5°C change in temperature can reduce the capacity of a battery pack by 1.5-2% and its power capacity by up to 10%. Similarly, in SC applications, precise adjustment of internal temperature under various operating conditions is essential to understand and accurately model the heat generation rate within the capacitor for effective system integration. Moreover, improper temperature distribution among capacitors can lead to thermal runaway, which, as heat accumulates, may result in emissions or even explosions, posing significant safety risks to vehicles and passengers (X. Feng et al., 2018), (Lai et al., 2022; Xinglei Zhang, Wang, He, Hua, & Heng, 2017). Affordable and efficient thermal management systems are essential to ensure that the temperatures of capacitor cells and modules remain within the optimal operating range. The design of these systems requires careful consideration of the structure and spatial geometry of battery cells. Particularly in automotive applications, batteries are categorized into three levels: cell, module, and pack (Wu et al., 2019). To construct a high-capacity, large-scale battery pack, several lithium-ion cells are interconnected in series, parallel, or a hybrid form. Figure 1 illustrates the impact of temperature on battery lifespan.

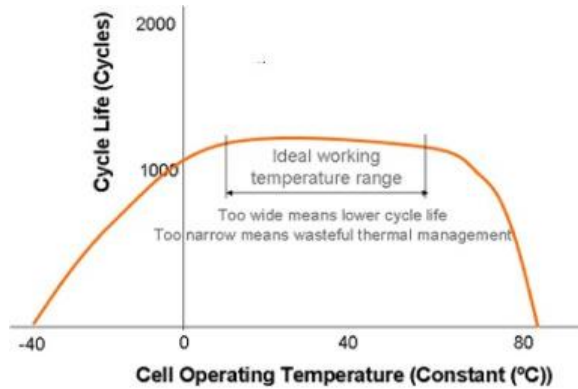


**Figure 1.** The effect of temperature on battery lifespan (Lawson, 2005)

While high temperatures have detrimental effects on batteries, low temperatures also negatively impact their performance. Low temperatures impede battery performance in frigid environments by augmenting the viscosity of the electrolyte, hence diminishing ionic conductivity and elevating the internal resistance of the battery pack. (Ma et al., 2018; Olabi et al., 2022; Ouyang et al., 2019). Additionally, a moderate temperature increase can offer certain advantages for SCs; however, their electrolyte is primarily formulated from mixtures of organic solvents, which begin to evaporate at an ambient temperature of 20°C. At higher temperatures, this evaporation tends to induce gas evolution (Atribowo, Sarjiya, Hadi, & Wijaya, 2022; Choudhari, Dhoble, & Sathe, 2020). At ambient temperatures exceeding 25°C, the lifespan of SCs diminishes by 50% for each 10°C rise (Schiffer, Linzen, & Sauer, 2006). Additionally, under relatively high ambient conditions or during high discharge rates, the internal temperature of SC modules similarly exhibits uneven distribution over extended periods. This uneven temperature distribution, particularly in areas with higher temperature gradients, leads to irregular performance among modules and individual units. The degradation rate of capacitors at high temperatures is significantly faster than at lower temperatures. Over time, physical discrepancies among capacitors become more pronounced, ultimately compromising consistency across the units, even if early failures occur. Therefore, measures to control temperature rise levels, along with limitations on charging and discharging power, must be implemented to ensure proper heat dissipation. Otherwise, excessive heating could degrade capacitor performance or even lead to thermal runaway. Despite this, SCs perform relatively well in low-temperature conditions, and no additional heating system is required unless the temperature drops below -40°C (Rashidi et al., 2022).

The heating of battery cells is an intrinsic process during charging and discharging cycles. However, abnormal temperature escalation can occur due to thermal runaway, a critical condition where heat rapidly spreads from a compromised cell to adjacent cells, potentially leading to ignition. When the cell temperature approaches 80°C, the solid electrolyte interphase (SEI) layer on the negatively charged anode begins to degrade. As the temperature rises to 100°C-120°C, exothermic reactions in the electrolyte result in the release of various gases within the cell. Between 120°C and 130°C, the separator starts to deteriorate, allowing direct contact between the anode and cathode, which generates additional heat and causes an internal short circuit. At 130°C-150°C, the cathode begins to decompose, releasing oxygen. This oxygen release, in combination with other chemical reactions, facilitates combustion. If heat dissipation remains insufficient, temperatures between 150°C and 180°C can lead to thermal instability, triggering a state of thermal runaway (TR). This phase is characterized by the emission of flammable gases and the onset of self-sustained fire, with the entire process potentially unfolding in under 10 seconds. (Zavalis, Behm, & Lindbergh, 2012) and the amount of heat generated is approximately 10<sup>7</sup> W/m<sup>3</sup> (Xu, Lan, Qiao, & Ma, 2017). Therefore, depending on the battery's structure, operating environment, and type, the desired operating temperature range is between 15°C and 50°C, with a maximum temperature difference ( $\Delta T_{\max}$ ) of less than 5°C between modules to maintain uniform temperature distribution. Additionally, under normal operating conditions, the safety limit is considered to be 60°C (Qin et al., 2019).

## **2. The Impact of Operating Temperature on Batteries**

Lithium-ion batteries, as previously mentioned in this study, operate within a narrow temperature range. When exposed to temperatures outside this range, their safety, performance, and lifespan are adversely affected. Battery performance deteriorates significantly under unfavorable conditions caused by improper storage or operating temperatures. Thermal runaway issues also become inevitable under certain extreme conditions. This section examines the detrimental effects of improper temperatures on batteries to better understand the importance of Battery Thermal Management (BTM). Performance degradation caused by high temperatures, as well as low temperatures and temperature imbalances, can result in unexpected thermal characteristics (H. Liu, Wei, He, & Zhao, 2017). The degradation mechanisms of lithium-ion cells are illustrated in Figure 2.

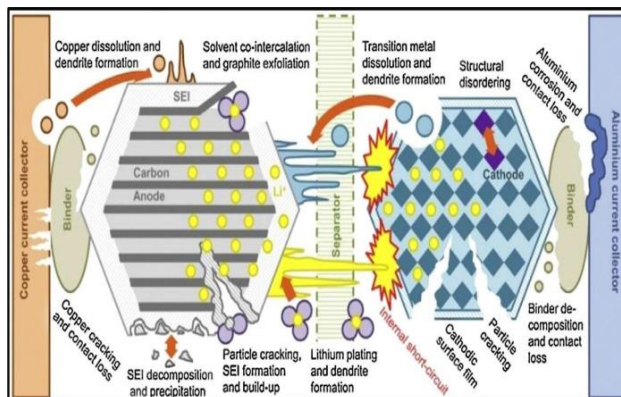


**Figure 2.** The consequences of high-temperature degradation in lithium-ion batteries (Birkel, Roberts, McTurk, Bruce, & Howey, 2017)

As discussed earlier, solid electrolyte interphases (SEIs) undergo intensified reactions at elevated temperatures, leading to alterations in SEI composition and the release of gases. These reactions deplete active lithium ions, causing irreversible losses in capacity. (Rodrigues et al., 2017). On the cathode side, elevated temperatures exacerbate metal dissolution and oxygen release, further contributing to capacity reduction and irreversible performance deterioration. Beyond diminishing battery longevity and impairing capacity, prolonged operation under high-temperature conditions significantly jeopardizes the safety of the entire power system. Batteries operating at low temperatures experience a significant decline in performance, making them unsuitable for use in cold-climate regions or high-altitude drones (J. Jaguemont, Boulon, & Dube, 2016). It is widely agreed that low temperatures have detrimental effects on battery performance, influencing parameters such as lifespan, round-trip efficiency, charge acceptance, and power and energy capacity (Burow et al., 2016; J. Jaguemont, Boulon, Venet, Dube, & Sari, 2015). When the temperature fall below  $-10^{\circ}\text{C}$ , lithium-ion batteries experience a noticeable decline in both power and energy output. At extreme conditions, such as  $-40^{\circ}\text{C}$ , these values plummet to merely 5% and 1.25% of their optimal performance at  $20^{\circ}\text{C}$ . Beyond ensuring functionality across varying temperatures, maintaining a consistent temperature distribution within the battery is crucial for stable operation. Uneven temperatures across cells, modules, or packs can disrupt electrochemical processes, causing irregular charging and discharging behaviors. This thermal inconsistency arises due to the distinct thermal properties and structural designs of the cell's internal components, leading to uneven heat generation and transfer. As a result, temperature gradients develop within the battery, further impacting its overall efficiency and reliability. (Wu, Wu, & Wang, 2018). Modules typically

consist of several cells; however, inevitable differences in internal resistance, capacity, and voltage exist among the cells (L. Lu, Han, Li, Hua, & Ouyang, 2013). The discrepancies will result in varying discharge or charge behaviors of the cells, causing an uneven temperature distribution within the module. Feng and associates suggested a methodology to examine the effects of temperature disparity on the phase transitions of cells inside a battery pack. Their studies indicated that a temperature variation of 5°C might diminish the capacity of the battery pack by 1.5-2% (X. Feng et al., 2018). Internal malfunctions or short circuits within individual cells, combined with uneven heat distribution between the edges and central regions of modules, can result in the formation of localized hot spots within battery or supercapacitor packs. These thermal irregularities have the potential to trigger thermal runaway (TR), leading to severe failures with catastrophic consequences. Therefore, implementing an effective Battery Thermal Management (BTM) system is crucial. Such systems ensure the safe operation of energy storage packs and play a vital role in preserving optimal charge and discharge performance under operational conditions.

### **3. Battery Thermal Management (BTM)**

Extensive studies on Battery Thermal Management (BTM) have focused on developing and implementing innovative technologies to regulate the thermal conditions of battery cells. By maintaining their temperature within an optimal range, these systems significantly enhance battery efficiency and functionality (Jouhara et al., 2019). Recently, research has increasingly focused on the cooling of electronic equipment and batteries, with studies conducted on air cooling, liquid cooling, nanofluids, and even vapor chamber technologies (Varol, Oztop, et al., 2025). BTM is critically important as temperature fluctuations directly affect the lifespan, power delivery, and overall reliability of battery cells. This research highlights commonly employed cooling strategies, including air cooling, liquid cooling, and phase change materials (PCMs), which are integral to modern battery thermal management systems (BTMs) (L. Feng et al., 2018). Among these technologies, liquid and air cooling systems are the most widely adopted due to their simplicity and cost-effectiveness (H. Liu et al., 2017; Sabbah, Kizilel, Selman, & Al-Hallaj, 2008). Despite their practicality, air cooling systems suffer from inherent limitations such as low thermal conductivity and specific heat capacity, which result in suboptimal cooling performance. This limits their ability to effectively lower the maximum temperature and ensure uniform thermal distribution across the battery pack. Similarly, in supercapacitor systems, thermal management is crucial to maintain operational temperatures. Thermal management strategies are generally classified as either active or passive cooling

systems based on their reliance on external energy sources. Active cooling systems, commonly applied in air and liquid cooling, utilize external energy to drive pumps and fans, enabling fluid movement. This reliance creates a balance between the cooling performance achieved and the overall system efficiency (Wang, Jiang, Li, & Yan, 2016). In contrast, passive cooling systems rely on the inherent thermal properties of materials and device configurations to regulate temperature. These systems enable heat dissipation through mechanisms such as phase change materials (PCMs), which facilitate effective thermal management without external energy input. (Xinghui Zhang, Li, Luo, Fan, & Du, 2022). Thermal management systems equipped with more advanced equipment rely on external energy sources, consuming additional energy to achieve more intensive heat dissipation. On the other hand, thermal management systems without additional energy consumption allow specific goals to be met, such as balanced temperature distribution and responsive flexibility. Among various cooling methods, liquid cooling stands out as a highly efficient approach due to the superior thermal conductivity and specific heat capacity of liquids. Its effectiveness in dissipating heat ensures better thermal regulation compared to other strategies. Furthermore, liquid cooling systems are characterized by their compact design, enabling integration into space-constrained environments. These advantages make liquid cooling a widely preferred and versatile solution in thermal management applications. Table 1 provides a comparison of different BTM structures.

**Table 1.** Comparison of Air, Liquid, and PCM Cooling Systems for BTM (M. Lu, Zhang, Ji, Xu, & Zhang, 2020; Shahjalal et al., 2021)

Method	Advantage	Disadvantage
Liquid cooling	<ul style="list-style-type: none"> <li>Common cooling media such as ethylene glycol, water, acetone, and oil are effective in providing uniform temperature distribution and achieving superior cooling performance.</li> <li>Liquid cooling systems excel in absorbing heat due to their higher heat transfer rates, greater mass flow rates, and superior specific heat capacities, ensuring efficient thermal management.</li> </ul>	<ul style="list-style-type: none"> <li>Complex design</li> <li>It incurs higher installation costs compared to air cooling               <ul style="list-style-type: none"> <li>Requires more components than air cooling, occupying more space and adding weight</li> </ul> </li> <li>Risk of leakage</li> <li>Short system lifespan</li> </ul>
Air cooling	<ul style="list-style-type: none"> <li>Cost-effectiveness</li> </ul>	<ul style="list-style-type: none"> <li>Efficiency is lower compared to other cooling systems because air</li> </ul>

	<ul style="list-style-type: none"> <li>• Occupies less space due to fewer components</li> <li>• Low maintenance and installation costs</li> </ul>	<p>has a lower heat transfer coefficient and specific heat capacity compared to many other mediums</p> <ul style="list-style-type: none"> <li>• High electricity consumption is required for the fan</li> <li>• The battery pack is exposed to external pollutants and airborne dust, leading to performance degradation</li> <li>• Primarily dependent on ambient air temperature</li> <li>• Uneven temperature distribution</li> </ul>
PCM	<ul style="list-style-type: none"> <li>• Occupies less space compared to liquid and air cooling</li> <li>• Lightweight due to the minimal need for components</li> <li>• Does not consume any power</li> <li>• More environmentally friendly, efficient, and has green attributes</li> <li>• Low initial investment and maintenance costs</li> </ul>	<ul style="list-style-type: none"> <li>• Despite its advantages, phase change materials (PCMs) exhibit low thermal conductivity, which can limit their heat transfer efficiency.</li> <li>• Once the material undergoes a complete phase change, its ability to regulate temperature diminishes, posing challenges for continuous operation.</li> <li>• There is a risk of leakage</li> <li>• The possibility of overcooling exists</li> </ul>

Table 1 reveals that each system exhibits its own set of advantages and disadvantages relative to the others. Generally, air cooling can be employed in environments where temperatures are not excessively high. PCM stands out due to its lightweight nature and environmental friendliness. Furthermore, designing the cooling configuration of a battery module requires comprehensive consideration of factors such as the type of cooling fluid, size, geometry, thermal properties, and electrochemical characteristics of the cells. Common cooling mediums include air, liquid, and phase change materials (PCMs), with their thermophysical properties presented in Table 2.

Battery Thermal Management (BTM) systems employing different cooling media vary significantly in terms of usability, adaptability, heat transfer performance, maintenance requirements, lifespan, and cost-effectiveness, including both initial and annual expenses. Prismatic, pouch, and cylindrical cells are the most commonly used battery types in electric vehicles, each with distinct packaging densities and cooling configurations. For instance, the unique geometry of cylindrical cells results in lower packaging compactness compared to prismatic or pouch cells. Cell size also plays a critical role in internal temperature distribution; as cell size increases, the surface area-to-volume ratio

decreases, leading to greater heat retention and a more pronounced temperature gradient. However, appropriately scaling cell size can enhance energy density and lower production costs, providing a balance between thermal management and economic efficiency (Xia, Cao, & Bi, 2017).

**Table 2.** Thermophysical properties of different coolants (G.H. Kim, 2006; Sabbah et al., 2008; van Gils, Danilov, Notten, Speetjens, & Nijmeijer, 2014)

Property	Air	Mineral Oil	Water/Glycol	PCM - Composite	Novac 7000
Density (kg×m <sup>-3</sup> )	1.225	924.1	1069	866	1400
Specific Heat Capacity (J×kg <sup>-1</sup> ×K <sup>-1</sup> )	1006	1900	3323	1980	1300
Thermal Conductivity (W×m <sup>-1</sup> ×K <sup>-1</sup> )	0.0242	0.13	0.3892	16.6	0.075
Kinematic Viscosity (m <sup>2</sup> ×s <sup>-1</sup> )	1.46×10 <sup>-5</sup>	5.6×10 <sup>-5</sup>	2.58×10 <sup>-6</sup>	-	3.2×10 <sup>-7</sup>

### 3.1. Air-Based Battery Thermal Management System

Air-based cooling is among the most prevalent thermal management technologies, utilized in a wide range of applications, including residential systems, vehicles, and computer cooling. In air-based Battery Thermal Management Systems (BTMS), there are two primary methods: forced and natural convection. Forced air convection relies on energy-driven mechanisms to circulate air around the battery pack, ensuring efficient heat transfer. In contrast, natural convection utilizes the natural movement of air without additional energy input, relying on temperature gradients to facilitate airflow around the battery pack. (Al-Zareer, Dincer, & Rosen, 2018). Active cooling systems differ from passive ones by sourcing pre-conditioned air from air conditioning or heating units, rather than drawing air directly from the cabin or atmosphere. Active systems provide significantly higher heating or cooling capacities, delivering up to 1 kW of power, compared to the approximately 100 watts typical of passive systems. A visual representation of these two systems is shown in Figure 3.

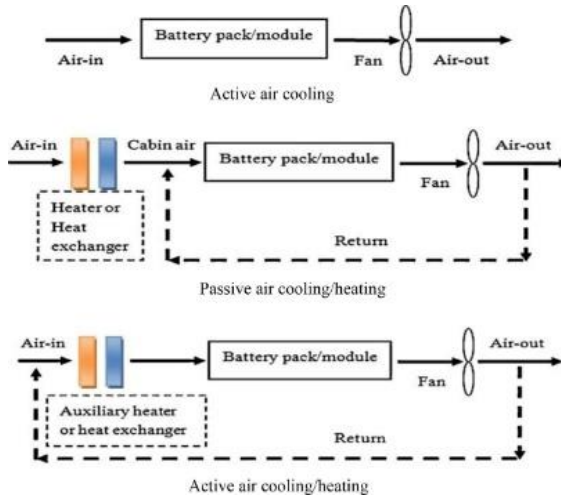


**Figure 3.** Battery thermal management in air-based cooling systems (Rao & Wang, 2011)

Both active and passive systems require key components, such as external power sources, fans, and heaters (for active systems), to enable effective cooling. Air, often driven by multiple fans, is directed across the surfaces of cells, providing direct cooling. Cooling configurations in these systems are typically arranged in series, parallel, or mixed series-parallel setups. Similarly, air-based BTMS is extensively used for supercapacitors (SCs). In these systems, air from the external environment or vehicle is guided through flow channels, where it comes into direct contact with the surface of the SC module. Among these methods, forced air convection is the most accessible, utilizing fans to circulate air effectively (Ianniciello, Biwolé, & Achard, 2018). Wind generated by vehicle motion aids in dissipating heat from batteries or capacitors within the cabin via exhaust fans. Increasing the airflow volume effectively lowers peak temperatures. Forced air convection enhances the convective heat transfer coefficient, maintaining optimal operating temperatures for batteries or capacitors. This method is particularly favored for cooling capacitors, offering greater reliability and significantly improved heat dissipation compared to natural convection approaches. (Xia et al., 2017). Although these systems are highly sensitive to the design of air channels and often face challenges in achieving a uniform flow field, they commonly result in uneven temperature distribution among capacitors. To mitigate these inconsistencies, researchers worldwide have explored various alternative approaches to improve temperature uniformity, emphasizing aspects such as the spacing between capacitors, air flow direction, and fan positioning (Soltani et al., 2019; Voicu, Rizk, Louahlia, Bode, & Gualous, 2019; Xinglei Zhang et al., 2017).

### **3.2. Liquid-Based Battery Thermal Management System**

The liquid cooling system is a type of conventional active cooling system that typically uses mediums such as mineral oil or water as the working fluid (Zhi et al., 2022). The liquid cooling system operates by relying on the movement of fluid around the surrounding cells to transfer heat. Due to the relatively high thermal diffusivity of heat from the liquid, it is more efficient than air cooling. Depending on the type of liquid used, various configurations can be designed. When using direct-contact liquids, modules are typically immersed in mineral oil. For indirect-contact liquids, several arrangements are possible: individual tubes surrounding each module, battery modules encased in jackets, modules integrated with plates and cooling/heating fins, or modules placed on heating/cooling plates. Indirect-contact cooling solutions are often favored as they provide greater isolation between the battery module and the surrounding environment, thereby enhancing safety and reliability. Liquid cooling systems, a widely used approach, are classified as active or passive depending on the type of heat sink employed. In passive liquid cooling systems, the heat sink typically consists of a radiator that facilitates heat dissipation but lacks the capability to provide heating. A closed-loop system circulates the heat transfer fluid using a pump, enabling the fluid to absorb heat from the battery pack and release it through the radiator. The effectiveness of passive liquid cooling is heavily influenced by the temperature gradient between the battery and the ambient air. Radiators equipped with fans can enhance cooling performance; however, when the temperature difference is minimal or the ambient air temperature exceeds the battery temperature, passive systems may fail to provide adequate cooling. In comparison, direct oil cooling—despite operating at a lower flow rate to optimize the balance between pressure drop and thermal efficiency—demonstrates superior thermal performance over direct air cooling methods.

The battery temperature in liquid cooling systems can be managed with 2-3 times less energy compared to air cooling systems. However, the disadvantages of liquid cooling systems include added weight, increased complexity, leakage risks, and additional costs (C. Zhao et al., 2020), (Lv et al., 2019). Maintaining the circulation of liquid at the required flow rate consumes additional power, increasing the vehicle's energy usage. Liquid-based direct cooling is rarely used in the BTMs of mass-produced EVs, largely due to safety concerns and limited awareness of its potential benefits.

### **3.3. Phase Change Material (PCM)-Based Cooling**

PCM cooling is a passive cooling technique that preserves parasitic power, thereby enhancing the range of electric vehicles. PCM is compact, economical,

has a high energy storage density, and has substantial energy-saving benefits. It plays a crucial role in applications such as peak power shifting, waste heat recovery, solar energy storage, building energy efficiency, cold chain logistics, and other energy-related uses. Furthermore, PCM absorbs and releases substantial heat during its phase change, facilitating temperature regulation of the surrounding environment. In contrast to conventional temperature control methods like active air cooling and circulating liquid cooling, PCM-based temperature control technology provides enhanced temperature management, is environmentally sustainable, highly efficient, and possesses eco-friendly characteristics (Huang, Cheng, & Zhao, 2019; Verma, Shashidhara, & Rakshit, 2019). The melting process remains near the phase change temperature for a prolonged period, as shown in Figure 4.

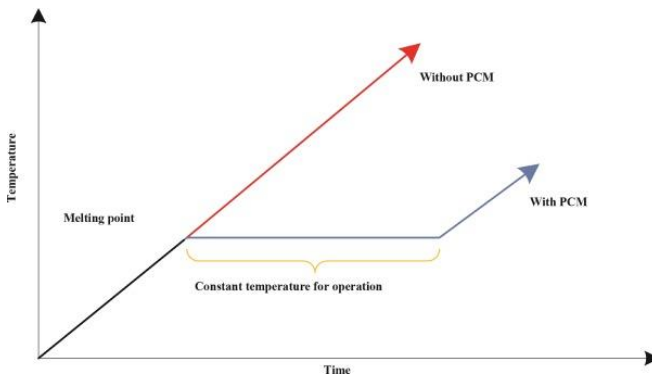


**Figure 4.** Feature of PCM based system

The latent heat property of PCM effectively regulates the operating temperature of cells within the desired range. This thermal reserve is driven by the energy absorbed or released during the phase change process. As PCM transitions between phases, it absorbs or releases substantial heat when the temperature reaches a specific threshold, enabling efficient thermal management. (Zhi et al., 2022). Paraffin wax is one of the most commonly used PCMs in thermal management systems due to its cost-effectiveness, chemical stability, and durability. However, the inherently low thermal conductivity of PCMs leads to heat saturation, limiting their effectiveness. BTMS relying solely on pure PCMs are insufficient for prolonged operation in high-power batteries, failing to adequately regulate temperatures. To address this challenge, researchers have developed advanced composite energy storage materials by incorporating high thermal conductivity components such as metal foams, expanded graphite, carbon nanotubes, and porous materials, significantly improving PCM

performance. (J. Chen et al., 2019). In contrast to conventional thermal management techniques like air and liquid cooling, the investigation into the utilization of phase change materials in battery thermal management systems commenced comparatively later. Nonetheless, PCM-based battery thermal management systems demonstrate extensive application potential and provide exceptionally promising performance.

#### **4. Numerical and Experimental Studies on BTM in the Literature**

Xia et al. (B. W. Liu, Wang, & Yuan, 2014), Cooling channels were designed for capacitor packs incorporating both parallel and series connections. These packs comprise six modules, each containing 15 capacitor cells, for a total of 90 cells connected in series. The heat dissipation system features a central air inlet and outlets on both sides, providing adequate airflow through each capacitor and efficiently removing generated heat. Results showed that this configuration maintained a maximum temperature variation of 5°C within the capacitor packs, ensuring thermal equilibrium and stable operating temperatures. Hybrid cooling methods, which are commonly used in electric vehicles with several dozen units, help avoid the placement of excessive devices in a single row. Additionally, the significantly shorter paths for coolant movement can mitigate issues related to temperature non-uniformity.

Mahamud et al. (Mahamud & Park, 2011), introduced an alternative air cooling approach for an aligned battery bank configuration and conducted two-dimensional computational fluid dynamics (CFD) simulations. Numerical results indicated that alternating flow conditions significantly improved thermal management compared to unidirectional flow. Specifically, alternating flow reduced the cell temperature difference in the battery system by approximately 4°C, representing a 72% reduction, and decreased the maximum cell temperature by 1.5°C for a motion period of  $\tau = 120$  seconds. This improvement was attributed to the periodic reversal of flow direction, which redistributes and disrupts thermal boundary layers on the cells, enhancing heat dissipation. Chen (K. Chen, Song, Wei, & Wang, 2018), substantially enhanced the cooling effectiveness of a U-flow parallel air-cooled Battery Thermal Management System by adjusting the dimensions of airflow inlets and outputs. Upon discharging the optimized battery pack at a 5C pace, the temperature differential across battery cells diminished by 70%, and power usage decreased by 32%. The efficacy of this strategy was observed to be significantly enhanced with alterations in battery spacing.

In the study conducted by Kong et al. (Kong et al., 2020), an integrated model of a composite PCM and liquid cooling-based thermal management system was developed. The simulation results demonstrated that the system exhibited

excellent thermal performance at an ambient temperature of 30 °C. As illustrated in Figure 5, the maximum surface temperature and the maximum temperature difference of the battery pack were maintained at 41.1 °C and 4 °C, respectively, at the end of the 3C discharge. These findings underscore the significant role of composite PCM in regulating the temperature of battery cells effectively. Furthermore, the study proposed a liquid cooling strategy that optimizes the flow rate and inlet temperature of the coolant by monitoring the PCM and ambient temperatures. This strategy not only enhanced the thermal performance of the battery pack during cycling under varying ambient conditions but also significantly reduced the power consumption of the liquid cooling process.

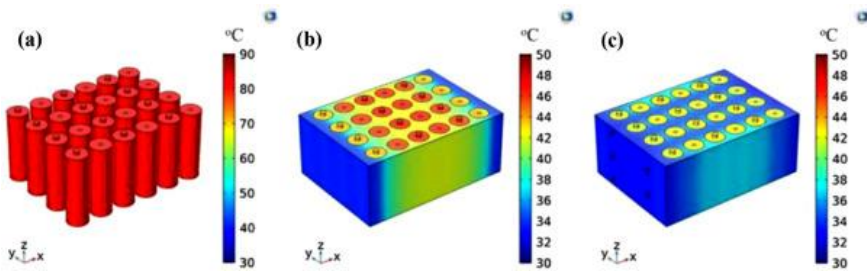


**Figure 5.** Contours of battery temperatures for three different thermal management systems (Kong et al., 2020)

Zhao (J. Zhao, Rao, & Li, 2015), presented a cylindrical battery cooling technique utilizing a microchannel liquid cooling cylinder (LCC). With a minimum of four microchannels and an inlet mass flow rate regulated at 1103 kg/s, the maximum temperature of the battery module remained below 40°C. With the rise in the number of microchannels in the LCC, the maximum temperature progressively diminished; however, it is advised not to exceed eight channels.

As evident from the literature, various methods have been employed to study battery thermal management systems. Additionally, numerical and experimental studies utilizing systems such as nanofluids, heat pipes, and vapor chambers have also been conducted (Jilte, Kumar, & Ahmadi, 2019; Liang, Gan, & Li, 2018; Mashayekhi, Houshfar, & Ashjaee, 2020; Varol, Coşanay, et al., 2025; A. Wei, Qu, Qiu, Wang, & Cao, 2019).

## 5. Conclusions

This review discusses various cooling strategies for the development of BTM, including liquid, air, PCM, and hybrid-based cooling approaches, highlighting the latest studies in each sector to provide recommendations for optimal thermal

management systems. The thermal management of electrochemical energy storage systems is critically important for optimizing the safety, performance, and lifespan of batteries and supercapacitors. The study addresses phase change materials (PCMs), liquid cooling, and air cooling systems, each aiming to enhance the efficiency of thermal management systems through their distinct advantages and disadvantages. Notably, PCM-based systems offer energy-saving and environmentally friendly features due to their latent heat capacity. However, limitations such as low thermal conductivity and phase change saturation underline the importance of incorporating performance-enhancing nanomaterials.

Liquid cooling systems, with their high heat transfer efficiency and compact structure, are advantageous in high-power applications, though issues like leakage risk and added weight present practical limitations. Air cooling, on the other hand, offers low cost, simple installation, and reliability but is constrained by its low heat transfer coefficient and uneven temperature distribution. This suggests a need for optimizing fan speeds, developing flow-guidance designs, and pursuing innovative approaches to enhance airflow uniformity. Recent studies in the literature indicate that forced convection systems are more effective than natural convection systems and that hybrid solutions can further enhance performance.

Supercapacitors (SCs) surpass batteries in terms of power density and high charge/discharge rates, which have attracted considerable attention. However, their usage remains impacted by performance and safety concerns. Furthermore, SCs have specific operational temperature requirements, necessitating a better understanding and regulation of the thermal effects surrounding them.

A review of the literature reveals a growing interest in innovative materials and methods in thermal management systems. Particularly, integrating PCM-based systems with metal foams, expanded graphite, and carbon nanotubes shows potential for addressing the issue of low thermal conductivity. Additionally, the development of hybrid systems that combine different cooling methods offers advantages in both cost and performance. Future research should focus on testing these hybrid systems across a broader range of energy densities and power levels. Moreover, numerical and experimental modeling studies provide valuable tools for optimizing the performance of these systems.

Future research can focus on the following areas:

- 1) **Hybrid Cooling Systems:** By combining air, liquid, and PCM cooling methods, more uniform temperature distribution and higher heat transfer capacity can be achieved. Optimizing hybrid systems for low power consumption would be particularly advantageous for electric vehicles.

2) Intelligent Thermal Management Systems: Leveraging artificial intelligence and machine learning algorithms could enable the design of thermal management systems capable of adapting to dynamic operating conditions. Such systems could enhance energy efficiency by relying on real-time temperature data from the battery.

3) Microchannel Liquid Cooling Technologies: These technologies are especially effective in ensuring uniform temperature distribution in high-energy-density battery modules. Studies on prismatic cells have shown that the number and arrangement of microchannels directly impact the thermal balance of the module. The scalability of this technology for smaller applications and its integration with nanofluids could offer innovative solutions for high-performance battery systems.

4) Modular Designs for Energy Storage Systems: Innovative designs at the cell, module, and pack levels should be developed to improve temperature homogeneity. In particular, designs must be optimized to prevent thermal imbalances between cells.

One of the innovative findings of this study is that no single cooling method can meet all requirements, underscoring the potential of hybrid approaches. Furthermore, future research should not only aim to enhance system performance but also consider cost-effectiveness and environmental sustainability. Such a comprehensive approach would enable the safer, more efficient, and environmentally friendly utilization of energy storage systems.

## REFERENCES

- Abo-Khalil, A. G., Abdelkareem, M. A., Sayed, E. T., Maghrabie, H. M., Radwan, A., Rezk, H., & Olabi, A. G. (2022). Electric vehicle impact on energy industry, policy, technical barriers, and power systems. *International Journal of Thermofluids*, 13, 100134. Retrieved from <https://doi.org/10.1016/j.ijft.2022.100134>
- Adalati, R., Sharma, M., Sharma, S., Kumar, A., Malik, G., Boukherroub, R., & Chandra, R. (2022). Metal nitrides as efficient electrode material for supercapacitors: A review. *Journal of Energy Storage*, 56, 105912. Retrieved from <https://doi.org/10.1016/j.est.2022.105912>
- Akkinepally, B., Neelakanta Reddy, I., Lee, C., Jo Ko, T., Srinivasa Rao, P., & Shim, J. (2023). Promising electrode material of Fe<sub>3</sub>O<sub>4</sub> nanoparticles decorated on V<sub>2</sub>O<sub>5</sub> nanobelts for high-performance symmetric supercapacitors. *Ceramics International*, 49(4), 6280–6288. Retrieved from <https://doi.org/10.1016/j.ceramint.2022.10.161>
- Akkinepally, B., Reddy, I. N., Manjunath, V., Reddy, M. V., Mishra, Y. K., Ko, T. J., ... Shim, J. (2022). Temperature effect and kinetics, LiZr<sub>2</sub>(PO<sub>4</sub>)<sub>3</sub> and Li<sub>1.2</sub>Al<sub>0.2</sub>Zr<sub>1.8</sub>(PO<sub>4</sub>)<sub>3</sub> and electrochemical properties for rechargeable ion batteries. *International Journal of Energy Research*, 46(10), 14116–14132. Retrieved from <https://doi.org/10.1002/er.8129>
- Al-Zareer, M., Dincer, I., & Rosen, M. A. (2018). A review of novel thermal management systems for batteries. *International Journal of Energy Research*, 42(10), 3182–3205. Retrieved from <https://doi.org/10.1002/er.4095>
- Apribowo, C. H. B., Sarjiya, S., Hadi, S. P., & Wijaya, F. D. (2022). Optimal Planning of Battery Energy Storage Systems by Considering Battery Degradation due to Ambient Temperature: A Review, Challenges, and New Perspective. *Batteries*, 8(12), 290. Retrieved from <https://doi.org/10.3390/batteries8120290>
- Birkel, C. R., Roberts, M. R., McTurk, E., Bruce, P. G., & Howey, D. A. (2017). Degradation diagnostics for lithium ion cells. *Journal of Power Sources*, 341, 373–386. Retrieved from <https://doi.org/10.1016/j.jpowsour.2016.12.011>
- Burow, D., Sergeeva, K., Calles, S., Schorb, K., Börger, A., Roth, C., & Heitjans, P. (2016). Inhomogeneous degradation of graphite anodes in automotive lithium ion batteries under low-temperature pulse cycling conditions. *Journal of Power Sources*, 307, 806–814. Retrieved from <https://doi.org/10.1016/j.jpowsour.2016.01.033>
- Cai, H., Xu, C., Liao, Y., Su, L., & Weng, Z. (2019). Mass Maldistribution

- Research of Different Internal Flowing Channels in the Cooling Plate Applied to Electric Vehicle Batteries. *Applied Sciences*, 9(4), 636. Retrieved from <https://doi.org/10.3390/app9040636>
- Chen, J., Kang, S., E, J., Huang, Z., Wei, K., Zhang, B., ... Liao, G. (2019). Effects of different phase change material thermal management strategies on the cooling performance of the power lithium ion batteries: A review. *Journal of Power Sources*, 442, 227228. Retrieved from <https://doi.org/10.1016/j.jpowsour.2019.227228>
- Chen, K., Song, M., Wei, W., & Wang, S. (2018). Structure optimization of parallel air-cooled battery thermal management system with U-type flow for cooling efficiency improvement. *Energy*, 145, 603–613. Retrieved from <https://doi.org/10.1016/j.energy.2017.12.110>
- Choudhari, V. G., Dhoble, D. A. S., & Sathe, T. M. (2020). A review on effect of heat generation and various thermal management systems for lithium ion battery used for electric vehicle. *Journal of Energy Storage*, 32, 101729. Retrieved from <https://doi.org/10.1016/j.est.2020.101729>
- Chu, S., & Majumdar, A. (2012). Opportunities and challenges for a sustainable energy future. *Nature*, 488(7411), 294–303. Retrieved from <https://doi.org/10.1038/nature11475>
- Ellabban, O., Abu-Rub, H., & Blaabjerg, F. (2014). Renewable energy resources: Current status, future prospects and their enabling technology. *Renewable and Sustainable Energy Reviews*, 39, 748–764. Retrieved from <https://doi.org/10.1016/j.rser.2014.07.113>
- Fan, Y., Bao, Y., Ling, C., Chu, Y., Tan, X., & Yang, S. (2019). Experimental study on the thermal management performance of air cooling for high energy density cylindrical lithium-ion batteries. *Applied Thermal Engineering*, 155, 96–109. Retrieved from <https://doi.org/10.1016/j.applthermaleng.2019.03.157>
- Feng, L., Zhou, S., Li, Y., Wang, Y., Zhao, Q., Luo, C., ... Yan, K. (2018). Experimental investigation of thermal and strain management for lithium-ion battery pack in heat pipe cooling. *Journal of Energy Storage*, 16, 84–92. Retrieved from <https://doi.org/10.1016/j.est.2018.01.001>
- Feng, X., Xu, C., He, X., Wang, L., Zhang, G., & Ouyang, M. (2018). Mechanisms for the evolution of cell variations within a LiNixCoyMnzO2/graphite lithium-ion battery pack caused by temperature non-uniformity. *Journal of Cleaner Production*, 205, 447–462. Retrieved from <https://doi.org/10.1016/j.jclepro.2018.09.003>
- G.H. Kim, A. P. (2006). Battery thermal management system design modeling: 22nd international battery, hybrid and fuel cell electric vehicle conference

and exhibition.

- Hameer, S., & van Niekerk, J. L. (2015). A review of large-scale electrical energy storage. *International Journal of Energy Research*, 39(9), 1179–1195. Retrieved from <https://doi.org/10.1002/er.3294>
- Huang, Y.-H., Cheng, W.-L., & Zhao, R. (2019). Thermal management of Li-ion battery pack with the application of flexible form-stable composite phase change materials. *Energy Conversion and Management*, 182, 9–20. Retrieved from <https://doi.org/10.1016/j.enconman.2018.12.064>
- Ianniciello, L., Biwolé, P. H., & Achard, P. (2018). Electric vehicles batteries thermal management systems employing phase change materials. *Journal of Power Sources*, 378, 383–403. Retrieved from <https://doi.org/10.1016/j.jpowsour.2017.12.071>
- Jaguemont, J., Boulon, L., & Dube, Y. (2016). Characterization and Modeling of a Hybrid-Electric-Vehicle Lithium-Ion Battery Pack at Low Temperatures. *IEEE Transactions on Vehicular Technology*, 65(1), 1–14. Retrieved from <https://doi.org/10.1109/TVT.2015.2391053>
- Jaguemont, J., Boulon, L., Venet, P., Dube, Y., & Sari, A. (2015). Low temperature aging tests for lithium-ion batteries. In *2015 IEEE 24th International Symposium on Industrial Electronics (ISIE)* (pp. 1284–1289). IEEE. Retrieved from <https://doi.org/10.1109/ISIE.2015.7281657>
- Jaguemont, Joris, Karimi, D., & Van Mierlo, J. (2019). Investigation of a Passive Thermal Management System for Lithium-Ion Capacitors. *IEEE Transactions on Vehicular Technology*, 68(11), 10518–10524. Retrieved from <https://doi.org/10.1109/TVT.2019.2939632>
- Jilte, R. D., Kumar, R., & Ahmadi, M. H. (2019). Cooling performance of nanofluid submerged vs. nanofluid circulated battery thermal management systems. *Journal of Cleaner Production*, 240, 118131. Retrieved from <https://doi.org/10.1016/j.jclepro.2019.118131>
- Jouhara, H., Khordehgah, N., Serey, N., Almahmoud, S., Lester, S. P., Machen, D., & Wrobel, L. (2019). Applications and thermal management of rechargeable batteries for industrial applications. *Energy*, 170, 849–861. Retrieved from <https://doi.org/10.1016/j.energy.2018.12.218>
- Kang, J., & Rizzoni, G. (2014). Study of relationship between temperature and thermal energy, operating conditions as well as environmental factors in large-scale lithium-ion batteries. *International Journal of Energy Research*, 38(15), 1994–2002. Retrieved from <https://doi.org/10.1002/er.3212>
- Kong, D., Peng, R., Ping, P., Du, J., Chen, G., & Wen, J. (2020). A novel battery thermal management system coupling with PCM and optimized

- controllable liquid cooling for different ambient temperatures. *Energy Conversion and Management*, 204, 112280. Retrieved from <https://doi.org/10.1016/j.enconman.2019.112280>
- Lai, X., Yao, J., Jin, C., Feng, X., Wang, H., Xu, C., & Zheng, Y. (2022). A Review of Lithium-Ion Battery Failure Hazards: Test Standards, Accident Analysis, and Safety Suggestions. *Batteries*, 8(11), 248. Retrieved from <https://doi.org/10.3390/batteries8110248>
- Lawson, B. (2005). Lithium battery failures. *Electropedia*.
- Li, J., Ho, M. S., Xie, C., & Stern, N. (2022). China's flexibility challenge in achieving carbon neutrality by 2060. *Renewable and Sustainable Energy Reviews*, 158, 112112. Retrieved from <https://doi.org/10.1016/j.rser.2022.112112>
- Liang, J., Gan, Y., & Li, Y. (2018). Investigation on the thermal performance of a battery thermal management system using heat pipe under different ambient temperatures. *Energy Conversion and Management*, 155, 1–9. Retrieved from <https://doi.org/10.1016/j.enconman.2017.10.063>
- Liu, B. W., Wang, J. J., & Yuan, H. Y. (2014). Analysis on a Gas Turbine Sealing Disk Structure and Material Strength. *Applied Mechanics and Materials*, 492, 60–70. Retrieved from <https://doi.org/10.4028/www.scientific.net/AMM.492.60>
- Liu, H., Wei, Z., He, W., & Zhao, J. (2017). Thermal issues about Li-ion batteries and recent progress in battery thermal management systems: A review. *Energy Conversion and Management*, 150, 304–330. Retrieved from <https://doi.org/10.1016/j.enconman.2017.08.016>
- Lu, L., Han, X., Li, J., Hua, J., & Ouyang, M. (2013). A review on the key issues for lithium-ion battery management in electric vehicles. *Journal of Power Sources*, 226, 272–288. Retrieved from <https://doi.org/10.1016/j.jpowsour.2012.10.060>
- Lu, M., Zhang, X., Ji, J., Xu, X., & Zhang, Y. (2020). Research progress on power battery cooling technology for electric vehicles. *Journal of Energy Storage*, 27, 101155. Retrieved from <https://doi.org/10.1016/j.est.2019.101155>
- Lv, Y., Zhou, D., Yang, X., Liu, X., Li, X., & Zhang, G. (2019). Experimental investigation on a novel liquid-cooling strategy by coupling with graphene-modified silica gel for the thermal management of cylindrical battery. *Applied Thermal Engineering*, 159, 113885. Retrieved from <https://doi.org/10.1016/j.applthermaleng.2019.113885>
- Lyu, Y., Siddique, A. R. M., Majid, S. H., Biglarbegian, M., Gadsden, S. A., & Mahmud, S. (2019). Electric vehicle battery thermal management system

- with thermoelectric cooling. *Energy Reports*, 5, 822–827. Retrieved from <https://doi.org/10.1016/j.egy.2019.06.016>
- Ma, S., Jiang, M., Tao, P., Song, C., Wu, J., Wang, J., ... Shang, W. (2018). Temperature effect and thermal impact in lithium-ion batteries: A review. *Progress in Natural Science: Materials International*, 28(6), 653–666. Retrieved from <https://doi.org/10.1016/j.pnsc.2018.11.002>
- Mahamud, R., & Park, C. (2011). Reciprocating air flow for Li-ion battery thermal management to improve temperature uniformity. *Journal of Power Sources*, 196(13), 5685–5696. Retrieved from <https://doi.org/10.1016/j.jpowsour.2011.02.076>
- Malinauskaite, J., Anguilano, L., & Rivera, X. S. (2021). Circular waste management of electric vehicle batteries: Legal and technical perspectives from the EU and the UK post Brexit. *International Journal of Thermofluids*, 10, 100078. Retrieved from <https://doi.org/10.1016/j.ijft.2021.100078>
- Mashayekhi, M., Houshfar, E., & Ashjaee, M. (2020). Development of hybrid cooling method with PCM and Al<sub>2</sub>O<sub>3</sub> nanofluid in aluminium minichannels using heat source model of Li-ion batteries. *Applied Thermal Engineering*, 178, 115543. Retrieved from <https://doi.org/10.1016/j.applthermaleng.2020.115543>
- Oca, L., Guillet, N., Tessard, R., & Iraola, U. (2019). Lithium-ion capacitor safety assessment under electrical abuse tests based on ultrasound characterization and cell opening. *Journal of Energy Storage*, 23, 29–36. Retrieved from <https://doi.org/10.1016/j.est.2019.02.033>
- Olabi, A. G. (2012). Developments in sustainable energy and environmental protection. *Energy*, 39(1), 2–5. Retrieved from <https://doi.org/10.1016/J.ENERGY.2011.12.037>
- Olabi, A. G., & Abdelkareem, M. A. (2022). Renewable energy and climate change. *Renewable and Sustainable Energy Reviews*, 158, 112111. Retrieved from <https://doi.org/10.1016/J.RSER.2022.112111>
- Olabi, A. G., Maghrabie, H. M., Adhari, O. H. K., Sayed, E. T., Yousef, B. A. A., Salameh, T., ... Abdelkareem, M. A. (2022). Battery thermal management systems: Recent progress and challenges. *International Journal of Thermofluids*, 15, 100171. Retrieved from <https://doi.org/10.1016/J.IJFT.2022.100171>
- Ouyang, D., He, Y., Weng, J., Liu, J., Chen, M., & Wang, J. (2019). Influence of low temperature conditions on lithium-ion batteries and the application of an insulation material. *RSC Advances*, 9(16), 9053–9066. Retrieved from <https://doi.org/10.1039/C9RA00490D>

- Peng, H., Wang, H., Wang, Y., Wang, X., Chen, S., & Yan, B. (2022). Achieving a highly safe supercapacitor via the combination of a temperature-responsive hydrogel-electrolyte and electrochromic electrodes. *Journal of Materials Chemistry A*, 10(38), 20302–20311. Retrieved from <https://doi.org/10.1039/D2TA04560E>
- Pomerantseva, E., Bonaccorso, F., Feng, X., Cui, Y., & Gogotsi, Y. (2019). Energy storage: The future enabled by nanomaterials. *Science*, 366(6468). Retrieved from <https://doi.org/10.1126/science.aan8285>
- Qin, P., Liao, M., Zhang, D., Liu, Y., Sun, J., & Wang, Q. (2019). Experimental and numerical study on a novel hybrid battery thermal management system integrated forced-air convection and phase change material. *Energy Conversion and Management*, 195, 1371–1381. Retrieved from <https://doi.org/10.1016/j.enconman.2019.05.084>
- Rafik, F., Gualous, H., Gallay, R., Crausaz, A., & Berthon, A. (2007). Frequency, thermal and voltage supercapacitor characterization and modeling. *Journal of Power Sources*, 165(2), 928–934. Retrieved from <https://doi.org/10.1016/j.jpowsour.2006.12.021>
- Rao, Z., & Wang, S. (2011). A review of power battery thermal energy management. *Renewable and Sustainable Energy Reviews*, 15(9), 4554–4571. Retrieved from <https://doi.org/10.1016/j.rser.2011.07.096>
- Rashidi, S., Karimi, N., Sunden, B., Kim, K. C., Olabi, A. G., & Mahian, O. (2022). Progress and challenges on the thermal management of electrochemical energy conversion and storage technologies: Fuel cells, electrolyzers, and supercapacitors. *Progress in Energy and Combustion Science*, 88, 100966. Retrieved from <https://doi.org/10.1016/j.pecs.2021.100966>
- Rodrigues, M.-T. F., Babu, G., Gullapalli, H., Kalaga, K., Sayed, F. N., Kato, K., ... Ajayan, P. M. (2017). A materials perspective on Li-ion batteries at extreme temperatures. *Nature Energy*, 2(8), 17108. Retrieved from <https://doi.org/10.1038/nenergy.2017.108>
- Sabbah, R., Kizilel, R., Selman, J. R., & Al-Hallaj, S. (2008). Active (air-cooled) vs. passive (phase change material) thermal management of high power lithium-ion packs: Limitation of temperature rise and uniformity of temperature distribution. *Journal of Power Sources*, 182(2), 630–638. Retrieved from <https://doi.org/10.1016/j.jpowsour.2008.03.082>
- Sayed, E. T., Wilberforce, T., Elsaid, K., Rabaia, M. K. H., Abdelkareem, M. A., Chae, K.-J., & Olabi, A. G. (2021). A critical review on environmental impacts of renewable energy systems and mitigation strategies: Wind, hydro, biomass and geothermal. *Science of The Total Environment*, 766,

144505. Retrieved from <https://doi.org/10.1016/j.scitotenv.2020.144505>
- Schiffer, J., Linzen, D., & Sauer, D. U. (2006). Heat generation in double layer capacitors. *Journal of Power Sources*, 160(1), 765–772. Retrieved from <https://doi.org/10.1016/j.jpowsour.2005.12.070>
- Shahjalal, M., Shams, T., Islam, M. E., Alam, W., Modak, M., Hossain, S. Bin, ... Iqbal, A. (2021). A review of thermal management for Li-ion batteries: Prospects, challenges, and issues. *Journal of Energy Storage*, 39, 102518. Retrieved from <https://doi.org/10.1016/j.est.2021.102518>
- Soltani, M., Berckmans, G., Jaguemont, J., Ronsmans, J., Kakihara, S., Hegazy, O., ... Omar, N. (2019). Three dimensional thermal model development and validation for lithium-ion capacitor module including air-cooling system. *Applied Thermal Engineering*, 153, 264–274. Retrieved from <https://doi.org/10.1016/j.applthermaleng.2019.03.023>
- Sun, X., Zhang, X., Wang, K., Xu, N., & Ma, Y. (2015). Temperature effect on electrochemical performances of Li-ion hybrid capacitors. *Journal of Solid State Electrochemistry*, 19(8), 2501–2506. Retrieved from <https://doi.org/10.1007/s10008-015-2876-x>
- Tie, S. F., & Tan, C. W. (2013). A review of energy sources and energy management system in electric vehicles. *Renewable and Sustainable Energy Reviews*, 20, 82–102. Retrieved from <https://doi.org/10.1016/j.rser.2012.11.077>
- van Gils, R. W., Danilov, D., Notten, P. H. L., Speetjens, M. F. M., & Nijmeijer, H. (2014). Battery thermal management by boiling heat-transfer. *Energy Conversion and Management*, 79, 9–17. Retrieved from <https://doi.org/10.1016/j.enconman.2013.12.006>
- Varol, Y., Coşanay, H., Tamdoğan, E., Parlak, M., Şenocak, Ş. M., & Oztop, H. F. (2025). Vapor chamber thermal performance: Partially heated with different heating areas at the center and supported by numerical analysis for the experimental setup. *Applied Thermal Engineering*, 260, 124978. Retrieved from <https://doi.org/10.1016/j.applthermaleng.2024.124978>
- Varol, Y., Oztop, H. F., Tamdoğan, E., Parlak, M., Şenocak, Ş. M., & Coşanay, H. (2025). Thermal Performance Investigation of Vapor Chamber Under Partial Heating and Different Heat Flux Conditions: Effects of Inclination Angle. *ASME Journal of Heat and Mass Transfer*, 147(1). Retrieved from <https://doi.org/10.1115/1.4066664>
- Verma, A., Shashidhara, S., & Rakshit, D. (2019). A comparative study on battery thermal management using phase change material (PCM). *Thermal Science and Engineering Progress*, 11, 74–83. Retrieved from <https://doi.org/10.1016/j.tsep.2019.03.003>

- Voicu, I., Rizk, R., Louahlia, H., Bode, F., & Gualous, H. (2019). Experimental and numerical study of supercapacitors module with air-cooling. *Applied Thermal Engineering*, 159, 113903. Retrieved from <https://doi.org/10.1016/j.applthermaleng.2019.113903>
- WADA, M. (2009). Research and development of electric vehicles for clean transportation. *Journal of Environmental Sciences*, 21(6), 745–749. Retrieved from [https://doi.org/10.1016/S1001-0742\(08\)62335-9](https://doi.org/10.1016/S1001-0742(08)62335-9)
- Wang, Q., Jiang, B., Li, B., & Yan, Y. (2016). A critical review of thermal management models and solutions of lithium-ion batteries for the development of pure electric vehicles. *Renewable and Sustainable Energy Reviews*, 64, 106–128. Retrieved from <https://doi.org/10.1016/j.rser.2016.05.033>
- Wei, A., Qu, J., Qiu, H., Wang, C., & Cao, G. (2019). Heat transfer characteristics of plug-in oscillating heat pipe with binary-fluid mixtures for electric vehicle battery thermal management. *International Journal of Heat and Mass Transfer*, 135, 746–760. Retrieved from <https://doi.org/10.1016/j.ijheatmasstransfer.2019.02.021>
- Wei, L., Lu, Z., Cao, F., Zhang, L., Yang, X., Yu, X., & Jin, L. (2020). A comprehensive study on thermal conductivity of the lithium-ion battery. *International Journal of Energy Research*, 44(12), 9466–9478. Retrieved from <https://doi.org/10.1002/er.5016>
- Wu, W., Wang, S., Wu, W., Chen, K., Hong, S., & Lai, Y. (2019). A critical review of battery thermal performance and liquid based battery thermal management. *Energy Conversion and Management*, 182, 262–281. Retrieved from <https://doi.org/10.1016/j.enconman.2018.12.051>
- Wu, W., Wu, W., & Wang, S. (2018). Thermal management optimization of a prismatic battery with shape-stabilized phase change material. *International Journal of Heat and Mass Transfer*, 121, 967–977. Retrieved from <https://doi.org/10.1016/j.ijheatmasstransfer.2018.01.062>
- Xia, G., Cao, L., & Bi, G. (2017). A review on battery thermal management in electric vehicle application. *Journal of Power Sources*, 367, 90–105. Retrieved from <https://doi.org/10.1016/j.jpowsour.2017.09.046>
- Xie, J., Ge, Z., Zang, M., & Wang, S. (2017). Structural optimization of lithium-ion battery pack with forced air cooling system. *Applied Thermal Engineering*, 126, 583–593. Retrieved from <https://doi.org/10.1016/j.applthermaleng.2017.07.143>
- Xu, J., Lan, C., Qiao, Y., & Ma, Y. (2017). Prevent thermal runaway of lithium-ion batteries with minichannel cooling. *Applied Thermal Engineering*, 110, 883–890. Retrieved from

<https://doi.org/10.1016/j.applthermaleng.2016.08.151>

- Zavalis, T. G., Behm, M., & Lindbergh, G. (2012). Investigation of Short-Circuit Scenarios in a Lithium-Ion Battery Cell. *Journal of The Electrochemical Society*, 159(6), A848–A859. Retrieved from <https://doi.org/10.1149/2.096206jes>
- Zhang, Xinghui, Li, Z., Luo, L., Fan, Y., & Du, Z. (2022). A review on thermal management of lithium-ion batteries for electric vehicles. *Energy*, 238, 121652. Retrieved from <https://doi.org/10.1016/j.energy.2021.121652>
- Zhang, Xinglei, Wang, W., He, H., Hua, L., & Heng, J. (2017). Optimization of the air-cooled supercapacitor module compartment for an electric bus. *Applied Thermal Engineering*, 112, 1297–1304. Retrieved from <https://doi.org/10.1016/j.applthermaleng.2016.09.003>
- Zhao, C., Zhang, B., Zheng, Y., Huang, S., Yan, T., & Liu, X. (2020). Hybrid Battery Thermal Management System in Electrical Vehicles: A Review. *Energies*, 13(23), 6257. Retrieved from <https://doi.org/10.3390/en13236257>
- Zhao, J., Rao, Z., & Li, Y. (2015). Thermal performance of mini-channel liquid cooled cylinder based battery thermal management for cylindrical lithium-ion power battery. *Energy Conversion and Management*, 103, 157–165. Retrieved from <https://doi.org/10.1016/j.enconman.2015.06.056>
- Zhi, M., Fan, R., Yang, X., Zheng, L., Yue, S., Liu, Q., & He, Y. (2022). Recent research progress on phase change materials for thermal management of lithium-ion batteries. *Journal of Energy Storage*, 45, 103694. Retrieved from <https://doi.org/10.1016/j.est.2021.103694>
- Zhu, L., Boehm, R. F., Wang, Y., Halford, C., & Sun, Y. (2011). Water immersion cooling of PV cells in a high concentration system. *Solar Energy Materials and Solar Cells*, 95(2), 538–545. Retrieved from <https://doi.org/10.1016/j.solmat.2010.08.037>

## **Chapter 2**

### **Energy Production from Solid Waste: Mugla Province Example**

**Ali Kemal AKIR<sup>1</sup>**

---

<sup>1</sup> Assoc. Dr. ; Adnan Menderes University Department of Machinery and Metal Technologies, Germencik Yamantürk Vocational School, ali.kemal.cakir@adu.edu.tr ORCID No: 0000-0002-2185-8108

## **Introduction**

As the global population continues to grow, so does the challenge of managing solid waste. Traditional waste disposal methods, such as landfilling and incineration, are increasingly seen as unsustainable due to their environmental impacts and limited capacity. However, an innovative solution is emerging: converting solid waste into energy. This process not only helps manage waste but also provides a renewable energy source, contributing to the global shift towards sustainable energy systems.

The World Bank estimates that by 2050, global waste generation will reach 3.4 billion tons annually. As urbanization increases, so does the volume of waste produced per capita.

The global average for waste generation is approximately 0.74 kg/capita/day, with variations from country to country ranging from 0.11 to 4.54 kg/capita/day. Municipal solid waste generation is expected to exceed 2.2 billion tonnes by 2025, with more than a third of this waste going uncollected (1). According to the World Bank, 4.3 billion urban dwellers are expected to produce 1.42 kg of waste per person per day by 2025 (2-3).

Traditional waste management practices are becoming inadequate, leading to overflowing landfills, increased greenhouse gas emissions, and pollution. In this context, energy production from solid waste offers a dual benefit: reducing waste and generating electricity or heat.

## **Methods of Energy Production from Solid Waste**

Several technologies exist for converting solid waste into energy, each with its unique processes, advantages, and challenges:

### **1. Anaerobic Digestion**

Anaerobic digestion involves the breakdown of organic materials by microorganisms in the absence of oxygen. This process produces biogas, primarily composed of methane, which can be used to generate electricity or heat. This method is particularly effective for food waste, agricultural residues, and certain types of industrial waste.

### **2. Incineration**

Incineration involves burning solid waste at high temperatures to reduce its volume and generate energy. The heat produced can be used to produce steam, which drives turbines to generate electricity. While this method significantly reduces waste volume, it raises concerns about air pollution and the need for stringent emissions controls.

### 3. Gasification and Pyrolysis

Gasification and pyrolysis are thermal processes that decompose organic material at high temperatures in a low-oxygen environment. Gasification converts waste into syngas (a mixture of hydrogen and carbon monoxide), which can be further processed into electricity or fuels. Pyrolysis, on the other hand, produces bio-oil and char, which can be used as fuel or for other applications.

### 4. Fermentation

Fermentation is another method to convert organic waste into energy. This process, typically involving the anaerobic breakdown of carbohydrates, results in the production of bioethanol, which can be used as a renewable fuel source (4-5).

## **Benefits of Energy Production from Solid Waste**

### 1. Waste Reduction

By converting waste into energy, these technologies help reduce the volume of waste sent to landfills, thus prolonging their lifespan and minimizing environmental impacts.

### 2. Renewable Energy Generation

Energy produced from solid waste is considered renewable, as it utilizes materials that would otherwise contribute to pollution. This can significantly reduce reliance on fossil fuels, helping to mitigate climate change.

### 3. Economic Opportunities

Developing waste-to-energy facilities can create jobs in construction, operation, and maintenance, contributing to local economies. Additionally, it can stimulate investment in new technologies and infrastructure.

### 4. Energy Security

Utilizing locally generated energy from waste can enhance energy security by reducing dependence on imported fuels. This is particularly relevant for countries with limited natural resources.

## **Challenges and Considerations**

Despite its potential, energy production from solid waste faces several challenges:

### 1. Public Perception

Public opposition to waste-to-energy facilities often stems from concerns about pollution, odor, and health risks. Effective communication and community engagement are crucial to address these issues.

### 2. Regulatory Frameworks

Robust regulations are necessary to ensure that waste-to-energy technologies operate safely and sustainably. Policymakers must balance environmental protection with the need for energy production.

### 3. Economic Viability

The initial investment in waste-to-energy technology can be substantial. Financial incentives, subsidies, and public-private partnerships may be needed to support the development of these projects.

### **Muğla Province Solid Waste Data**

Muğla is a province of Turkey. The province centered on Muğla has a population of 1,066,736 people according to the results of 2023 [6]. It is a settlement in the Aegean Region, a small part of which falls within the Mediterranean Region, famous for its holiday regions such as Ortaca, Dalaman, Köyceğiz, Fethiye, Marmaris, Milas, Datça and Bodrum. There are 13 districts in the province.

**Table 1.** The Amount of Municipal Waste Collected by Provincial/District Municipalities and Managed by Local Administrations (Metropolitan municipality/ municipality/unions) and collection, transport and disposal methods (7).

Metropolitan / City/ District Council or	Produced Waste The amount of (tons/day)	Collected Waste The amount of (tons/day)		Available Council Waste Management The facility				
		Summer	Winter	Organised But the warehouse	Front Process (Mechanical Separation/ Bio drying / Compost/	Burn m	Order you Breakdown	Warehouse The gas from Energy Production
BASEMENT	560.5*	651*	470*	None	None	None	There is	None
MILAS	253	260	247	There is	There is	None	None	There is
YATAGAN KAVAKLI STREAM HINGE	192	189	196	There is	There is	None	None	There is
MARMARI	240	278	202	There is	There is	None	None	There is
DATCA	55	71	39	There is		None	None	None
ORTICA DALAMAN	157	162	152	There is	None	None	None	There is
FETHIYE SEYDIKE	358	401	316	There is	There is	None	None	There is
Province Wide	1815.50	2012	1622					

**Table 2.** Solid Waste Composition in Mugla (7).

Waste Component- 2021	Summer %	Winter %	Average %
Kitchen Waste	43.68	46.54	45.11
Paper	5.08	6.21	5.64
Cardboard	7.05	5.45	6.25
Voluminous Cardboard	2.13	2.66	2.39
Plastic	14.63	10.50	12.57
Pine	8.36	8.56	8.46
Metal	2.79	2.37	2.58
Voluminous Metal	0.41	0.27	0.34
Waste Electrical-Electronics Equipment	0.95	0.69	0.82
Dangerous Waste	0.00	0.00	0.00
Park And Green Waste	6.27	9.68	7.98
Other Unburnt Waste	0.80	1.03	0.92
Other Flammable Waste	6.76	4.99	5.88
Other Burnable Voluminous Waste	0.62	0.53	0.57
Other Unburnt Voluminous Waste	0.00	0.02	0.01
Other (Above Groups Not including)	0.47	0.50	0.48
Total	100.0%	100.0%	100.0%

Domestic solid wastes generated throughout the province of Muğla are collected by district municipalities and brought to waste disposal facilities. The disposal of solid wastes generated throughout the province of Muğla is provided by the Muğla Metropolitan Municipality with 6 Regular Storage Facilities located in the districts of Ortaca, Fethiye, Marmaris, Datça, Menteşe and Milas and 1 Transfer Station located in the district of Yatağan.

In 2021;

Solid Waste Regular Storage Facility of Ortaca, 50,704.83 tons/year

Solid Waste Regular Storage Facility of Fethiye, 122,584.50 tons/year,

Solid Waste Regular Storage Facility of Marmaris, 78,103.85 tons/year,

Solid Waste Regular Storage Facility of Datça, 23,257.59 tons/year,  
 In Menteşe Solid Waste Regular Storage Facility, 74,754.55 tons/yea,  
 65,754.84 tons/year of waste was disposed of in Milas Solid Waste Regular  
 Storage Facility (7).

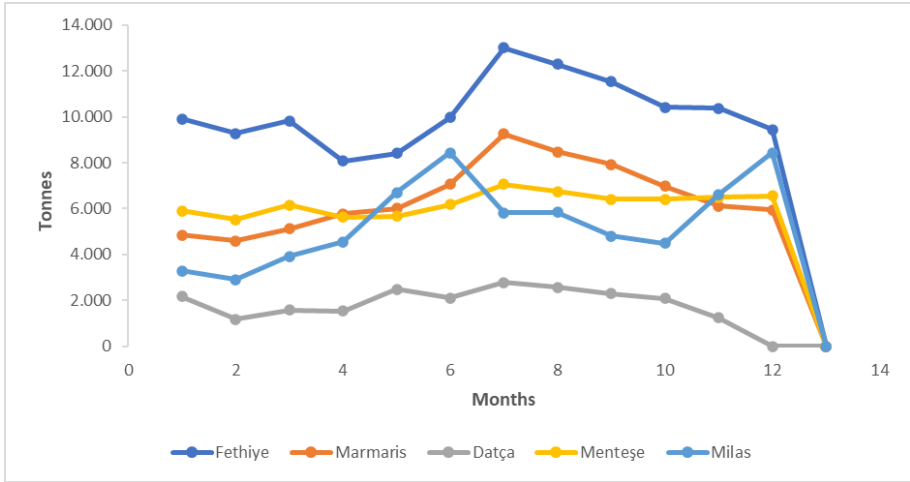


**Figure 1.** Solid waste amounts by month in in solid waste disposal facilities in 2021 (7).

In total, 415,160.16 tons/year of domestic waste was disposed of throughout Mugla Province.

### **Solid Waste Energy Production in Mugla Province**

Methane gas generated as a result of the disposal process is collected in Ortaca, Fethiye, Marmaris, Menteşe and Milas Solid Waste Regular Storage Facilities and converted into electrical energy in Biomass Energy Plants. Total energy production of Biomass Power Plants in 2021 is 40,366,350 kW.

The energy produced by five solid waste facilities provides a serious energy potential in the region. The energy produced by these facilities can provide energy input to housing, agriculture (greenhouse activities) and industrial facilities. Roughly, the energy needs of approximately 850,000 homes can be met. Considering the energy needs of the region, it is seen as a very important energy source.

**Table 3. Biomass The facility Energy Production (7).**

2021 Year Biomass The facility Energy Production (kW)					
Months	Menteş Solid Waste Storage Facility Electric Production	Marmaris Solid Waste Storage Facility Electric Production	Fethiye Solid Waste Storage Facility Electric Production	Ortaca Solid Waste Storage Facility Electric Production	Milas Solid Waste Storage Facility Electric Production
March	7,585,0 77	7,989,8 22	11,550,6 04	7,388,0 60	5,852,7 87

### Conclusion

Solid waste-to-energy production offers a promising path for sustainable energy solutions. It is also an important solution to cope with environmental problems and meet energy needs. By transforming waste into a valuable resource, we can overcome the dual challenges of waste management and energy production. Technological developments contribute to this. As technologies advance and public awareness increases, the transition to a circular economy that uses waste as a resource will become increasingly feasible. Embracing this change will not only benefit the environment, but also promote economic growth and energy security for future generations. In this context, it is important to convert waste into energy sources for a sustainable world in green energy. In the province of Mugla, projects in the recovery and conversion of waste into energy should continue to increase.

## References

- 1- Mor, Suman, and Khaiwal Ravindra. "Municipal solid waste landfills in lower-and middle-income countries: Environmental impacts, challenges and sustainable management practices." *Process Safety and Environmental Protection* 174 (2023): 510-530.
- 2- Rahman, Mohammad Mashiur, and Alok K. Bohara. "Assessing the preference and spatial dependence of a solid waste management system in Nepal: A choice experiment approach." *Journal of Environmental Management* 327 (2023): 116805.
- 3- Petro Karungamy, Energy recovery from solid waste valorisation: Environmental and economic potential for developing countries, *Scientific African*, Volume 26, e02402, ISSN 2468-2276, 2024.  
<https://doi.org/10.1016/j.sciaf.2024.e02402>.
- 4- IRENA, "Waste-to-Energy: A Renewable Energy Perspective." International Renewable Energy Agency (IRENA), 2020.
- 5- "The Role of Waste-to-Energy in the Circular Economy." European Commission, 2021, [https://environment.ec.europa.eu/strategy/circular-economy-action-plan\\_en](https://environment.ec.europa.eu/strategy/circular-economy-action-plan_en), (Last Date: 22.10.2024).
- 6- TÜİK, Adrese Dayalı Nüfus Kayıt Sistemi, <https://web.archive.org/web/20231221221023/https://biruni.tuik.gov.tr/medas/?kn=95&locale=tr>, (Last accessed: 6 Feb 2024).
- 7- Mugla Province Solid Waste Data, Mugla Metropolitan Municipality Archive, 2023.

## **Chapter 3**

### **Assessing Climate Policies For Achieving Sdg 13 Towards Net Zero Carbon**

**Elif AYHAN<sup>1</sup>**  
**Aytac Perihan AKAN<sup>2,3</sup>**  
**Aysenur UGURLU<sup>4</sup>**

---

<sup>1</sup> MSc, Hacettepe University, Department of Environmental Engineering, Beytepe, Ankara, Türkiye, ORCID: 0009-0002-1082-7805

<sup>2</sup> Asst. Prof. Dr., Hacettepe University, Department of Environmental Engineering, Beytepe, Ankara, Türkiye, ORCID:0000-0003-4626-4741

<sup>3</sup> Corresponding Author

<sup>4</sup> Prof. Dr., Hacettepe University, Department of Environmental Engineering, Beytepe, Ankara, Türkiye, ORCID:0000-0002-2322-7190

## **Abstract**

In the 2015 Paris Agreement, many countries committed to limit global average temperature increases to quite below 2°C under pre-industrial levels and set net-zero emissions targets. To achieve climate neutrality under sustainable development goals, all countries need to work together for the standardization of greenhouse gas mitigation policies on a global scale through multinational cooperations such as emission trading. Encouraging modes such as public transportation that will result in a lower carbon footprint instead of private vehicle use, creating incentive mechanisms such as tax deductions for the use of electric vehicles instead of fossil fuel vehicles, ensuring the widespread utilization of renewable energy sources rather than coal and natural gas sources in energy generation, providing the necessary services for the development and dissemination of carbon capture and utilization processes can be evaluated in the context of the measures to be implemented by the governments of the countries and the mandatory climate policies that the countries must implement reaching net zero carbon emission targets by 2050. In this paper, the countries with the highest CO<sub>2</sub> emissions in recent years and tended to increase in terms of CO<sub>2</sub> emissions compared to previous years were examined in terms of their commitments regarding the climate policies existing or planned to combat global climate change. The emission reduction policies of the countries summarized here are expected to offer alternative solutions, especially for countries with similar emission sources and trends, and to inform policymakers and decision-makers.

**Keywords:** Climate Policies, Climate Change, Sustainable Development Goal, Multinational Cooperation, SDG 13

## 1. Introduction

Climate change, one of the major issues that the world faces due to its negative consequences in the twenty-first century, is defined as a change in climate in which variable climatic values like temperature and precipitation patterns in a specific location change significantly in comparison to previous values (Ridhosari & Rahman, 2020; Ellouz & Barkouti, 2022). Intergovernmental Panel on Climate Change (IPCC) established by the United Nations Environmental Protection Agency (UNEP) in collaboration with the World Meteorological Agency expressed in its first assessment report in 1990 that the Earth's temperature had increased by 0.3-0.6°C over the past hundred years (IPCC, 1990). When we address today's current status, according to the synthesis report published by IPCC in 2023, it is stated that global surface temperatures in the first twenty years of the 21st century reached 0.99 °C, which is higher than the period between 1850 and 1900 (IPCC, 2023).

Climate change shows itself with indicators such as increasing surface temperatures, heavy weather events, stratospheric ozone depletion, melting of the glaciers, and an increase in sea levels. The most important reason for these consequences is primarily based on anthropogenic activities which particularly give rise to increasing in the concentration of greenhouse gases, such as CO<sub>2</sub> (carbon dioxide), CH<sub>4</sub> (methane), NO<sub>x</sub> (nitrogen oxides), and chlorofluorocarbons (CFCs) accumulating in the atmosphere (IPCC, 2013; Adedeji et al., 2014; Altug & Ozkan, 2015).

It is a well-known fact that human-induced activities including electricity generation, heating needs, rapid urbanization, and fossil fuel usage trigger significantly the release of greenhouse gas (GHG) emissions into the atmosphere (IPCC, 2023). Among these, the last one is the most important key contributor to CO<sub>2</sub> emissions. In each of the stages of fossil fuel extraction and utilization as energy, a variety of adverse impacts on public health, extinction of species, food security, agricultural productivity, terrestrial and marine ecosystems are inevitably present. These negative impacts make it difficult to reach the Sustainable Development Goals which cover sustainability from the equality of gender to the prevention of environmental pollution (Balat 2007; IPCC, 2023).

Sustainable development is an ambiguous term which can be interpreted in many ways (Ross 2009). The concept of sustainability, which first emerged in the 18<sup>th</sup> century, came together with the term "development" at the end of the 1980s (Scoones, 2016) and formed the most widely used aspect in the Brundtland report issued by the World Commission on Environment and Development (WCED) in 1987 which is "meeting the needs of the present without compromising the ability

of future generations to meet their own needs"(WCED, note 3 above, page 8; Robert et.al., 2005).

At the United Nations Conference on Environment and Development (UNCED) held in Rio de Janeiro in 1992, the United Nations Sustainable Development Commission (CSD) was established to assure the effective monitoring of the UNCED, and many principles have been adopted for countries to exhibit an environmentally friendly approach (RDED, 1992; Parris & Kates., 2003). Following this, the Open Working Group formed by the UN General Assembly endorsed The Agenda 2030: UN Sustainable Development Goals (SDGs) in New York, which covers environmental, economic, and social aspects and expresses the way to achieve world peace and prosperity. These SDGs comprise 17 goals and 169 targets, in particular climate action, affordable and clean energy, and clean water sanitation which are of crucial importance in combatting global climate change (Owusu- Sarkodie, 2016; Olabi et.al., 2022; Nerini et.al., 2019).

Since the Paris Agreement and the European Union Green Deal, many countries have presented various commitments every year to actively play a role in the fight against global climate change to reach sustainability and carbon neutrality. One of the objectives of the current review paper is to examine and evaluate the strategies of the countries to be taken by the governments' decision-makers to provide net zero carbon emission targets. On the one hand, undoubtedly, when the three aspects of the concept of sustainability, namely environment, economy, and society, are evaluated together, it is obvious that multinational companies play a critical role in the fight against climate change. In this regard, this paper aims to stress the significance of multinational cooperation on global climate change, the present study covers the decision-making mechanisms based on the interactions between the governments to adapt and mitigate the climate change effects. To summarize, this section will try to answer the questions of to what extent multinational companies contribute to the achievement of SDGs, especially within the scope of climate action policies, and also what is the relationship between the policies of countries for net zero emissions and their achievements.

## **2. Climate Action and Sustainable Development Goals**

Climate change affects fundamental natural and human living requirements and thus the pillars of social and economic development. Although Sustainable Development Goals and Climate Change seem like two different concepts, they have many common points and are in a dual relationship. Priorities of community for sustainable development affect both greenhouse gas emissions triggering

global climate change and climate vulnerability. To make climate policies more effective, they should progress together with the strategies prepared in line with the SDGs. Hence, measures to be taken for the prevention of climate change can help countries' socioeconomic development by affecting their ability to achieve SDGs. In addition, the pursuit of SDGs will positively accelerate the opportunities and success of climate policies. However, it should not be forgotten that these mutual effects can be positive as well as negative consequences if the processes are not managed correctly (IPCC 2007; Nerini et.al., 2019). It is mentioned in the Nationally Determined Contributions (NDCs) of the countries committed under the Paris Agreement that coordinated approaches for climate change mitigation policies are required by ensuring integrated planning and intersectoral alignment of climate change and development policies (Cohen et.al., 2021). So, by 2030, it is necessary to achieve the best balance for the world by trying to bring together and synchronize all stakeholders around common goals. In the following section, SDGs associated with global climate change mitigation and adaptation actions will be discussed in detail.

### ***2.1. Targets and indicators of SDG 13***

Targets in the SDGs describe the goals and indicators that stand for them by measuring whether the world is on track to achieve them. Referring to climate action under SDGs, SDG 13 aims to mobilize to mitigate the adverse impacts of climate change (Gomez-Echeverri, 2018). Under SDG 13, the Paris Agreement emphasizes that the global average temperature increase should be kept below 2 °C or even fixed at 1.5 °C (Schleussner et.al., 2016). In this context, to mitigate the negative effects of climate change and achieve the Sustainable Development Goals by 2050, the European Union adopted the Green Deal in 2019 and set a net mitigation target of a minimum of 40% in greenhouse gas emissions (Filipović et.al., 2022). Correspondingly, The United Nations has set five targets and eight indicators for SDG 13 (Fig. 1) (Filho et.al., 2020; UN, 2016).

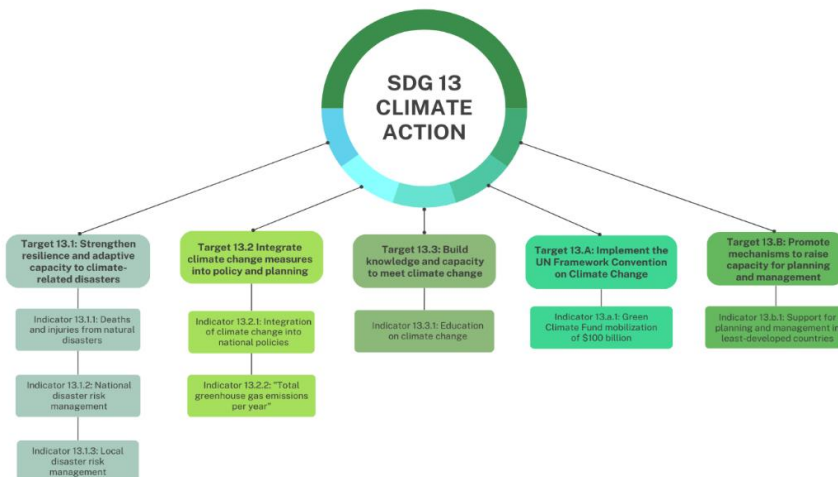


**Fig. 1.** Schematic representation of targets and indicators for SDG13 (climate action), (adapted from [https://sdgs.un.org/goals/goal13#targets\\_and\\_indicators](https://sdgs.un.org/goals/goal13#targets_and_indicators))

### ***2.1.1. Strengthen resilience and adaptive capacity to climate-related disasters***

Deaths and injuries from natural disasters contain the number of deaths, casualties, and persons directly impacted by disasters per 100,000 population. Although the frequency of natural disasters is not high, they are disasters with very high negative consequences. The number of deaths may vary from year to year. Considering the average death rate of the last ten years, approximately 45,000 people (~0.1% of global deaths) die each year on account of natural disasters (Ritchie et.al., 2022). With the rising negative influences of climate change, an increase was observed in flood disasters, which constitute approximately 40% of natural disasters. It has been determined that the Asia and the Pacific (APAC) region is much more affected by natural disasters when compared to other places in the world. Although flood intensity is high in the APAC region, flooding is a serious problem facing the entire world. Flood formation is associated with heavy rains and severe storms, and these occurrences are considered negative consequences of the climate crisis. Increasing population, urbanization to the stream bed, intense migration, industrialization, environmental degradation, and human activities are other causes of flood disasters. Flood causes loss of livestock, reduced industrial production, and extensive destruction or deterioration of goods, services, health, and crops (Kimuli et.al., 2021; Kozlowski, 1984). In addition, poverty makes people more vulnerable to natural disasters and increases the devastating impact, and exacerbates poverty in disasters vice versa. This serious impact on the economy

and sustainable development may lead to more serious problems in underdeveloped countries. SDG 13 seeks to reduce exposure to climate change and related natural disasters, to develop the ability of society to withstand and recuperate from the side effects of natural disasters, and to develop new strategies (Kimuli et.al., 2021).

National disaster risk management refers to the number of countries that have embraced and applied national disaster risk mitigation strategies by the Sendai Framework for Disaster Risk Reduction (SFDRR) 2015–2030 and aim to prevent the occurrence of disaster risk and enhance economic, social, health, and environmental resilience (UN, 2023). Economic development can be achieved in risky areas by using protective measures with an engineering-based approach to ensure disaster management in high-risk areas. International agreements that emerged with legal regulations and provisions are important factors that accelerate, support, and direct the development of disaster risk management systems. To have a globalized and properly functioning disaster management system, it is necessary to manage problems such as lack of capacity, local policies, political conflicts, and various economic fluctuations. To benefit from international agreements, it is necessary to adapt the existing principles and agreements to disaster risk management by considering the consequences of climate change, proceeding in parallel with the SDGs, and carrying out risk management practices at a multi-level without forgetting that the agreements are comprehensive. In addition, all stakeholders within the agreement should take an interdisciplinary approach and continue to make investments to manage disaster risk (Raikes et.al., 2022).

Local disaster risk management is the share of local governments that embrace and apply local disaster risk mitigation strategies in parallel with national disaster risk reduction strategies (UN, 2023). The vulnerability to severe natural occurrences and man-made disasters that hinder normal interactions and cause environmental damage is increasing around the world, and as a result, the importance of disaster risk management is once again evident. Measures should be taken for disaster risk management by using different methods in diverse regions. In this context, SFDRR, which provides a global framework for reducing disaster risk and increasing resilience to disasters in line with sustainable development, was developed by UN member countries. This framework, including strategizing based on community involvement and stakeholder management, disaster response-based management planning, post-disaster continuity management planning, and key sector continuity management planning, aims to prepare disaster risk reduction (DRR) strategies at both national and local levels by 2030. In a study conducted in South American countries

including Argentina, Bolivia, Colombia, Chile, Ecuador, Paraguay, and Peru which are the second most vulnerable in the world to natural disasters, DRR strategies, containing reducing risks, strengthening risk governance, investing in risk reduction, and preparing for disasters, were analysed using text-mining techniques. Difficulties were encountered during this work, such as a lack of coordination, resources, and awareness among different governments and the capacity to implement DRR strategies. The findings indicated that the significance of governments' consistency in implementing risk management planning strategies was evaluated as the most crucial one among the indicators examined. They stressed the significance of the existence of DRR plans, a theoretical approach, and a text-mining method to analyse strategies handled (Marcillo-Delgado et.al., 2021). Another study conducted in Pakistan examined the current state of school disaster risk reduction management in the city of Khyber Pakhtunkhwa. A mixed-method approach was used, including interviews, focus groups, and a survey of 100 people from 20 schools. Following the evaluation of results, it was determined that there is a lack of awareness about DRR among school personnel and students. To minimize the negative effects, suggestions such as developing and implementing school emergency plans, training school personnel and students on disaster preparedness, improving the physical infrastructure of schools, and making them more resistant to disasters should be recommended (Shah et.al., 2020).

### ***2.1.2. Integrate climate change measures into policy and planning***

Incorporation of climate change into national policies is the number of nations reporting the development or implementation of a comprehensive policy, strategy, or plan that enhances their capacity to adjust to the adverse impacts of climate change, encourages climate resilience, and supports the development of low-greenhouse gas emissions. Moreover, it contains countries with NDCs, long-term strategies, and national adaptation plans (UN, 2023). The northern tropics of Queensland, Australia, are among the regions most vulnerable to the impacts of climate change because of large fluctuations in precipitation, changes in evaporation, and often occurring extreme natural catastrophes like floods and droughts. In the study conducted in 2023 to mitigate the effects of climate change, local government implementers identified from various local government officials in the study area were interviewed, and the existing literature was examined. The current government policy was tried to be developed within the scope of Indicator 13.2.1 (Fig. 1). Local planning frameworks for adaptation to climate change involve various actions, like restricting construction in susceptible regions, evaluating and contrasting flood hazards, and allocating building levels

to expected floods. However, there are not enough resources, especially in terms of finance, to create and implement a strong plan for adaptation to climate change, and there are no rules for determining and allocating financial responsibility. If climate change adaptation measures are not properly applied at the local government level in the workplace, both the water sector and the local economy will encounter severe consequences. State and federal government policy organizations advise local governments to minimize their carbon footprints even though Australia has extremely high greenhouse gas emissions. Yet, this advice is only a recommendation and not a requirement. According to the study, local governments hold a crucial role in carrying out land use planning, policy or design guidelines, emission mitigations, and adaptation actions to address the negative impacts of climate change. It is presently the role of local government authorities in Australia to create strategic plans for climate change adaptation that are appropriate and agreeable to the local population, and they are leading the way in planning and executing climate change adaptation strategies. Thus, the evaluation of the existing situation contributes to improving plans for incorporating climate change into national policy in the research field (Biswas & Rahman, 2023).

### ***2.1.3. Build knowledge and capacity to meet climate change***

Climate change education is expressed as the “extent to which (i) global citizenship education and (ii) education for sustainable development are mainstreamed in (a) national education policies; (b) curricula; (c) teacher education; and (d) student assessment” (UN, 2023). We can implement education on climate change with global citizenship education, sustainable development education, national education policies, curriculum changes, teacher training, and student evaluations (The Danish Institute for Human Rights, 2016). Teachers encourage students to think creatively and help them develop a critical approach to climate change and respond to action. This training can be at the local or global level, including climate change mitigation policies, adaptation studies, and the relationships between these concepts. However, at this point, while developing positive attitudes in perspective, it is necessary to ensure that these attitudes turn into actions and behaviours. Being aware of the fact that climate change is a social problem besides being a scientific phenomenon, the efficiency of the process needs to ensure that new sustainable methods are integrated into the process by making students connect with daily life, to encourage students to reduce carbon emissions and educate students to engage in contributing to sustainable policies (Stevenson et. al., 2017; Tang, 2022).

In the study conducted by Tolppanen and co-workers (2022), a higher education course was conducted for climate change with the contributions of experts from a variety of branches, including online learning materials, reading assignments, quizzes, and project work. A questionnaire was administered to examine the course outcomes and how students' thinking, and behaviour changed (Tolppanen et.al., 2022). According to the results, it was determined that although the course was multidisciplinary, its effect on students was very limited. While the knowledge on the subject has increased, the actions taken have relatively changed. In other words, even though students were made aware of climate change, the desired effect was not achieved in their willingness to take mitigating measures. However, in the overall result, it is predicted that the carbon footprint of the students will decline at the end of the course.

#### ***2.1.4. Implement the UN Framework Convention on Climate Change***

The Green Climate Fund (“GCF” or “the Fund”) is an independent and multilateral financing institution established to provide climate finance in impartial shares to mitigation and adaptation initiatives by serving the United Nations Framework Convention on Climate Change (UNFCCC). The GCF was originally established by the UNFCCC, Conference of the Parties (COP) to support low-emission and climate-resilient development trajectories for sustainable development in developing countries and to reach the goal of limiting the global temperature increase below 2°C as mentioned in the Paris Agreement. GCF provides capacity building, technical assistance, and financing for a broad range of projects particularly in the areas of renewable energy, energy efficiency, sustainable agriculture, and climate-resilient infrastructure areas. This will enable developing countries to reduce their emissions, build resilience to climate change, and transition to a low-carbon economy (GCF, 2022).

Although the GCF started with high expectations, the differences in education levels in developing countries, the special interests of the countries, and the political problems over the financial policies cause slow progress and so, the desired result cannot be achieved. One reason may be that GCF dedicates only half of its capital to projects in progress. If the practices continue in the same way, the GCF will not have a noticeable effect in realizing the SDG 13 commitments expected to be made by 2030 in the Paris Agreement. Although there are UN organizations that support climate action such as the UN Environment and Development Programs and the Global Environment Instrument, the budgets given are not sufficient to achieve the desired result. The fact that private climate finance does not increase over the years and remains in place prevents the desired result from being achieved. Only about 20% of alleged climate finance so far has

targeted adaptation, and the rest has gone to greenhouse gas reduction projects. In the upcoming period, if the 100-billion-dollar fund is mobilized and spent on useful projects, significant benefits can be provided especially for developing countries (Gechev, 2019; Roberts et.al., 2021). Improving the capitalization and resource allocation of GCF is of great importance. The GCF has changed since the 2016 Strategic Plan and this change is ongoing. The importance of the effective use of climate finance and the correct use of grants and loans to support climate-oriented local financial systems is evident at this point. As expected more positive results will be obtained when the experts' recommendations are considered (Amighini et.al., 2022).

### ***2.1.5. Promote mechanisms to raise capacity for planning and management***

Assistance for planning and management in least-developed countries is related to the number of least-developed countries and small island developing States with NDCs, long-term strategies, national adaptation plans, and adaptation communications, as notified to the secretariat of the UNFCCC (UN, 2023). Although less developed countries contribute relatively less to GHG emissions, they are particularly sensitive to climate change owing to their geopolitical location, their low capacity to cope with these natural disasters, their limited adaptation capacities to climate change because of various economic reasons, and lack of infrastructure, and the inadequacy of these countries in developing policies compatible with climate change (Huq et.al., 2004). In a study implemented in Nepal, it was determined that factors, such as inadequate resources, income, sanitation and food security, low employment, and lack of education and health facilities, increase climate vulnerability and trigger to decrease in the adaptive capacity of the communities living there. The study recommended policies and interventions to reduce the climate vulnerability of susceptible areas, such as improving access to fundamental services such as water, sanitation, and shelter; strengthening disaster risk management, and promoting climate-resilient livelihoods (Giri et.al., 2021).

## **3. Evolution of CO<sub>2</sub> emissions and mitigation policies**

It is accepted that the most remarkable contributors to climate change are population increase and urbanization. By 2050 and 2100, the population is predicted to reach 9.8 billion and 11.2 billion, respectively (UN, 2017). It is an inevitable fact that population growth accelerates the requirements for energy, water, food, and other resources and urbanization triggers infrastructure, transportation, and energy demands, as well, resulting in the release of GHG emissions into the atmosphere. Since population growth triggers urbanization, the

effect of population increases and urbanization on climate change cannot be distributed equally (Satterthwaite, 2009). The relationship between world population and GHG emissions in the years between 1990 and 2021 is presented (Fig. 2). As understood from figure, excluding for 2020, the COVID-19 pandemic year, GHG emissions showed an increasing trend with population growth.

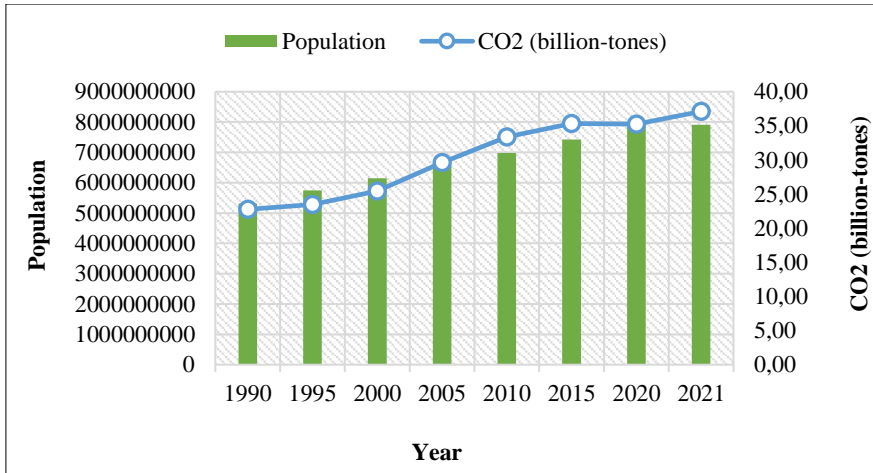


**Fig. 2.** The relationship between world population and GHG emissions in 1990 and 2021(adapted from Crippa et.al.,2022)

Evaluating carbon emissions by sectors are of great significance for determining the sources of emissions and taking measures accordingly. In this context, the JRC/IEA/PBL 2022 Report examined the CO<sub>2</sub> emissions of countries worldwide between the years 1990 and 2021 considering the sectors which consist of the power industry, combustion for industrial processing, and fuel production, buildings, transportation, and other sectors (industrial processes, agriculture soils, and waste) (EPA, 2021). The Global Emissions by Economic Sector data for 2021 is demonstrated (Fig. 3).

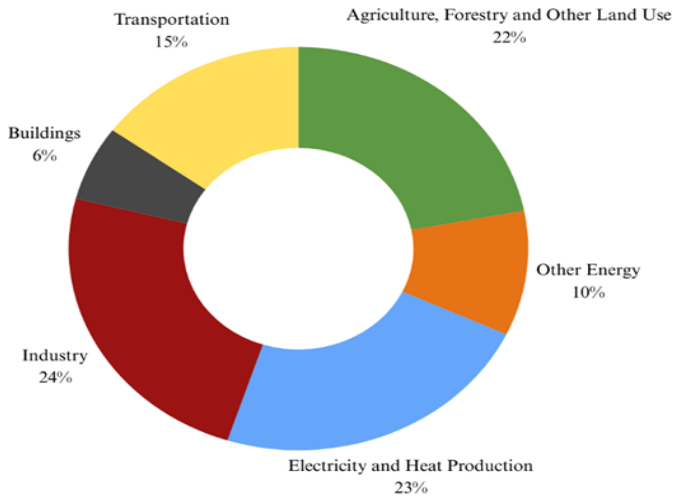


**Fig. 3.** Global Emissions by Economic Sector (adapted from EPA, 2021)

The biggest polluters, including the EU-27, the US, and Japan, all show a decrease in emissions in 2021 compared to 1990 (27.3%, 6.2%, and 7.4% respectively). On the contrary, China and India increased their CO<sub>2</sub> emissions 5.1 and 4.4 times, respectively, and in all countries in the world CO<sub>2</sub> emissions per capita have risen by approximately 13%, from 4.26 t CO<sub>2</sub>/person to 4.81 t CO<sub>2</sub>/person between 1990 and 2021.

Total greenhouse gas emissions per year mean the analysis of annual GHG emissions and advocate reduction targets (UN, 2023). Under this scope, China, the United States, the EU27, India, Russia, and Japan were the countries that emitted the most CO<sub>2</sub> emissions in the world for the year of 2021 (Fig. 4). China, which has the highest carbon emissions among all countries, emitted 12466,316 Mt CO<sub>2</sub>/yr in 2021 and constitutes 32.9% of the world’s total emissions. When compared according to years, it was observed that other countries, except Australia, increased their emissions between 2020 and 2021 (5.3% increase in the world total). Brazil and India, with an increase of 11% and 10.5% in their CO<sub>2</sub> emissions between the years of 2020 and 2021, respectively are the countries with the highest rise in CO<sub>2</sub> emissions. In 2022, global CO<sub>2</sub> emissions rose by 1.5% compared to 2021 and reached 36.1 Gt CO<sub>2</sub> (Crippa et al., 2022). Such an increase in emissions exhausted 13-36% of the carbon budget prepared to protect the 1.5 °C limit, which indicates that countries’ emission limits will be exceeded with a 67% probability by seven years. The sectoral distribution of emissions maintains consistent progress compared to previous years. Emissions in 2022 were caused by 39.3% power, 28.9% industry, 17.9% ground transportation, 9.9% residential, 3.1% international bunkers (international aviation and

shipping), and 0.9% domestic aviation sectors. It has been determined that emission increase rates have slowed down in other sectors except for international aviation. China, which is still the largest emitter of CO<sub>2</sub> in the world, reduced its emissions by 1.5% in 2022 for the first time. However, the country, which is still above 5.6% of pre-pandemic emission levels, needs to continue to pursue mitigation policies. The US, EU27, and India also increased their emissions by 3.2%, 0.5%, and 7%, respectively, compared to 2021. Russia, which is in the 5th place in terms of the highest CO<sub>2</sub> emission, increased its emissions between 2019 and 2021 but managed to catch an emission decrease of 1.8% in 2022.

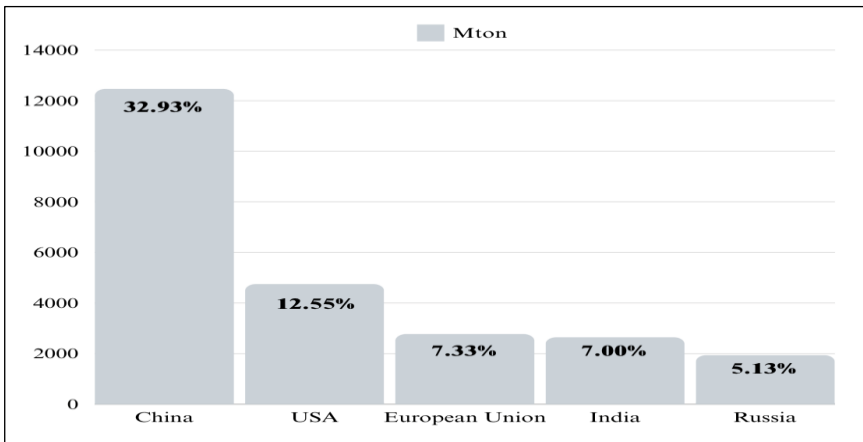


**Fig. 4.** The top 5 countries that emit the most CO<sub>2</sub> emissions in 2021(Crippa et.al., 2022)

China, India, Russia, Iran, Saudi Arabia, Brazil, and Türkiye are the countries with the highest increase in emissions in 2021 compared with 2019. Türkiye was the first order in this increasing trend (7.9%), while Mexico has shown the most substantial reduction in emissions, with a decrease of 13%. Despite this, Türkiye ranks at the bottom in the greenhouse gas emitters with Mexico, and Australia (1.2%, 1.1%, and 1% of fossil CO<sub>2</sub> emissions, respectively) (Crippa et.al., 2022). The results obtained indicate that we are on the path of growth beyond pre-pandemic emission levels. For this reason, it is thought that the peak of emissions has not been reached yet and that the increase in emissions will continue in the future (Liu et.al., 2023). On a sectoral basis, the other sectors category, which contains industrial processes, agricultural soils, and waste as mentioned above, increased by 101% between 1990 and 2021, while the power industry increased by 87% and the transport sector increased by 66%. These sectors were the primary contributors to the total 67% rise in CO<sub>2</sub> emissions.

Compared to 1990, China increased its total carbon emissions by 5.4% in 2021, while it experienced a huge increase of 414% on a sectoral basis (+915% transport and +767% power industry). The use of coal, which continues to make up the greatest portion of fossil fuel consumption, as well as the consumption of oil and gas are the primary causes of this emission increase in 2021. Compared to 1990, ranking second in total emissions, the United States' carbon emission percentage of the transport sector increased by 15%, while the carbon emission of the other industrial combustion sector decreased by 22%. Significant increases in coal and oil use led to a rise in CO<sub>2</sub> emissions in 2021. The findings are substantially more encouraging when we examine the EU27 nations on a sectoral level. In 2021, the other industrial combustion (combustion for industrial manufacturing and fuel production) category reduced fossil CO<sub>2</sub> emissions by 41%, followed by the power industry by 39% and buildings by 32%. All countries, particularly those with the highest emissions, should be required to conduct research aimed at reducing their carbon footprint to meet their commitments (Liu et.al., 2023).

The countries' maximum share of GHG emissions based on the sectors and the reduction policies under SDG 13 are presented (Tables 1-4) in terms of sectors including energy, electricity generation/consumption, agriculture, and transportation, respectively. In the selection of countries, the most emitter ones including China, the United States, the EU27, India, Russia, and Japan in 2021, and those showing the highest increase in fossil CO<sub>2</sub> emissions in 2021 than in 2019 consisting of China, India, Russia, Iran, Saudi Arabia, Brazil, and Türkiye are considered. In the evaluation of the EU27, Germany, was selected as the major contributor to the EU27's overall fossil CO<sub>2</sub> emissions, with a share of 24%.

**Table 1.** Mitigation actions under SDG 13 for the highest carbon emissions emitters from the energy sector

Country	Mitigation Action under SDG 13
Japan	<p>Following the implementation of the 5th Strategic Energy Plan, larger shares of renewable energy, and the restart of nuclear power.                      Carbon capture utilization and storage studies.                      Investing in greenhouse gas reduction projects.                      Lowering prices on CO<sub>2</sub> emissions from energy use than many other International Energy Agency (IEA) member countries.                      Presentation of the Green Growth Strategy in line with Carbon Neutrality in 2050.                      Introduction of Feed-In-Tariff in the field of renewable energy usage in 2012.                      Increase in biomass energy, solar, and wind power production.                      International hydrogen supply chain.                      Electricity and gas market reform (Ihara et al., 2020; IEA, 2023d).</p>
Germany	<p>Implementing the Climate Action Law to assure Germany's national greenhouse gas reduction targets.                      Renewable Energy Sources Act was implemented to sustain become widespread of renewable energy over the long term.                      Various measures have been implemented to improve research and development in the energy sector.                      Incentive to capture carbon and increase energy efficiency.                      Formation of climate cabinet.                      Adopting the Climate Action Programme 2030, which contains a progressive carbon pricing system for specific sectors.                      Passage of the Act on the Further Development of the Electricity Market.                      Establishing a Commission on Growth, Structural Change and Employment.                      Launching the National Platform Future of Mobility, to provide advice on tackling transport sector emissions (IEA, 2023a).</p>
Türkiye	<p>Increasing energy efficiency, use of renewable energy resources in buildings and industry, low carbon heating and cooling projects.                      Completion of the Tenth Development Plan and preparation for the Eleventh Development Plan.                      Laws on fossil fuels, energy efficiency, renewable energy resources, agriculture, sink areas, forestry, and construction.                      Prioritizing security of energy supply.                      Diversification of its energy mix.                      The Turkish Petroleum Law for domestic oil and gas production.                      Providing feed-in tariffs for renewable energy power plants like wind, solar, biomass, hydroelectric, and geothermal through the Renewable Energy Support Mechanism.                      Introduction of Renewable Energy Resource Areas.                      National Energy Efficiency Action Plan 2017-2023.                      Investments in electricity distribution (IEA, 2021; Talu &amp; Kocaman, 2018).</p>
Russia	<p>Long-term low-emissions development strategy in accordance with the Paris Agreement.                      Russia's updated climate pledge.                      Strategy for socio-economic growth of Russia by reducing greenhouse gas emissions by 2050.                      National Low-Carbon Strategy.                      Russian Federation's Energy Strategy for the term until 2035.                      Cancellation of low import duty.                      Climate Bill which commits MNCs to begin reporting their GHG emissions with quotas or penalties on large polluters from 2023.                      National Adaptation Programme and the third climate adaptation reporting strategy (IEA, 2023e; Climate Transparency, 2021; Zagoruichyk, 2022).</p>
Iran	<p>Providing 20% of electricity used by governmental/non-governmental entities from renewable sources.                      Law on the Sixth Five-Year Economic, Cultural, and Social Development Plan for 1396-1400 (2016-2021).                      Paying for the benefits of fossil fuel conservation.                      Renewable Electricity Compliance (IEA, 2023c).</p>
Saudi Arabia	<p>Global Methane Pledge signed at COP26.                      The Saudi Green Initiative to achieve a 50% stake of renewable energy in the power sector.                      Saudi Arabia Corporate Average Fuel Economy standards for cars implementation.                      Phase out fossil fuel heavy-duty vehicles.                      Qualitative goals are to increase the use of public transport and enhance the railways' efficiency with a modal shift in transport.                      Renovation of existing buildings with some measures to promote retrofitting.                      King Salman Energy Park                      The NEOM giga project in the Kingdom's Red Sea coast.                      9th Development Plan (Climate Transparency, 2022c; IEA, 2023f).</p>

Table 1 details the mitigation actions of Japan, Germany, Türkiye, Russia, Iran, and Saudi Arabia under SDG 13. In 2021, the energy sector was the largest source of global net carbon emissions (Statista, 2023). The energy sector accounted for 86.8% of overall GHG emissions (1,015 Mt CO<sub>2</sub>e/yr) in Japan (Ministry of the Environment Japan et.al., 2023). In Germany, the energy sector contributed 34% of the total GHG emissions (745.6 Mt CO<sub>2</sub>/yr) in 2022, followed by industry at 22% and transport at 20% (UBA, 2022). Türkiye emitted 71.3% of its CO<sub>2</sub> emissions from the energy sector in 2021, with 32.7% from electricity and heat generation (TUIK, 2023). Russia's energy sector was the highest emitter in 2021, responsible for 29% of total emissions, followed by industry and other energy-related sectors at 24% and 22%, respectively (Climate Transparency, 2021). In Iran, the electricity and heating sectors released 202.91 million tons of CO<sub>2</sub> in 2019, representing about 32% of total GHG emissions (Ritchie et.al., 2020). The energy sector accounted for 68% of Saudi Arabia's carbon emissions in 2019, with fuel combustion being the major driver (Climate Transparency, 2022c).

**Table 2.** Mitigation actions under SDG 13 for the highest carbon emissions emitters from electricity generation

Country	Mitigation Action under SDG 13
China	<ul style="list-style-type: none"> <li>Continuing to address overcapacity and accelerate the green and low-carbon transition of industries.</li> <li>Energetically developing service industry and supporting strategic emerging industries.</li> <li>Checking total energy usage and energy intensity.</li> <li>Advancing energy conservation in industry, information technology, transport, and buildings.</li> <li>Promoting energy conservation technologies and products.</li> <li>Controlling non-carbon dioxide GHG emissions in the agricultural, industrial, and waste sectors.</li> <li>Enhancing the carbon sink capacity of ecosystems.</li> <li>Deeping pilot and demonstration programs.</li> <li>Strengthening the Coordinated Control of GHG and Air Pollutants.</li> <li>Strengthening environmental regulations.</li> <li>The Work Plan for Greenhouse Gas Emissions Control in the 13th Five-year Plan Period has been created.</li> <li>National Adaptation to Climate Change Strategy 2035 has been started (NDRC of China, 2021; CIKD, 2021).</li> </ul>
India	<ul style="list-style-type: none"> <li>Developing solar energy production and increasing studies with the National Solar Mission.</li> <li>National Green Hydrogen Mission.</li> <li>Revised Domestic Gas Pricing.</li> <li>Improving energy efficiency.</li> <li>Development of sustainable habitat standards with the National Mission on Sustainable Habitat.</li> <li>Creation of National Mission on Strategic Knowledge for Climate Change.</li> <li>Using water resources efficiently with the National Water Mission.</li> <li>Switching to renewable energy.</li> <li>Reducing deforestation.</li> <li>Improving agricultural practices with National Mission for Sustainable Agriculture.</li> <li>Promoting public transportation (IEA, 2023b; MoEFCC, 2021).</li> </ul>

Table 2 outlines the mitigation actions undertaken by China and India in line with SDG 13. Electricity generation is another major source of carbon emissions, particularly in countries with large populations like China and India. In 2021, the highest GHG emissions in China came from electricity generation (44%) and

industrial combustion (27%) (Crippa et.al., 2022). Similarly, in India, the electricity and heat sector contributed the most to GHG emissions in 2019, accounting for 37% of the total (Tiseo, 2023).

**Table 3.** Mitigation actions under SDG 13 for the highest carbon emissions emitters from agriculture

Country	Mitigation Action under SDG 13
Brazil	Developing agricultural risk and vulnerability tracking systems. Readying Ecosystem-based Adaptation in areas at risk of extreme incidents. Expand the scope of the National Drinking Water Surveillance Programme. Diagnosing vulnerability to climate change of indigenous populations and lands. Brazil's 10-Year Energy Expansion Plan. The law that instituted the National Climate Change Policy. Brazil's National Adaptation Plan on climate change. Adaptation strategies in the agricultural sector. State funds were created by 16 Federation Units. Land use changes in various forms. Global Methane Pledge. Net-zero deforestation goal. Fully decarbonized power sector goal. Emission reductions across sectors. Curbing illegal deforestation (Climate Transparency, 2022a; WBG,2023).
Indonesia	National Long-Term Development Plan, The National Energy Plan (2017), and the National Action Plan on Climate Change Adaptation 2019 were implemented. An average of USD 940 million in public financing was provided to energy projects between 2019 and 2020. Investments were made in geothermal and hydroelectric renewable energy programs. A presidential regulation to establish a national framework for carbon pricing instruments, of which the ETS is one, was signed in October 2021. Besides biodiesel, in 2020 the government established ethanol blending targets of 10% for transportation and 5% for small businesses and agriculture, rising to 20% by 2025. Indonesia committed to ending deforestation by 2030 during COP26, but later withdrew the pledge because of the definitional issues, opting instead only to "halt and reverse forest loss and land degradation by 2030" (Climate Transparency, 2022b; IEA, 2022).
Democratic Republic of Congo	Democratic Republic of Congo mainly focuses on forestry, energy transport, agriculture, and the waste sector. In the National Determined Contribution Declaration, a 21% reduction in emissions from 2021 to 2030 is committed. Access to renewable energy from hydroelectricity instead of fossil fuels is supported. Improving the utilization of primary and secondary forests, creating sustainable financing models for community forest tenures, and finding alternatives to coal and land use. Technical assistance and capacity building are provided to government organizations to implement best practices and new perspectives for impactful policy development and data-driven decision-making (UNDP,2023; USAID,2022).

Table 3 outlines the mitigation actions taken by these countries under SDG 13. Brazil, Indonesia, and the Democratic Republic of Congo rank among the top countries with the highest carbon emissions in the agricultural sector. In Brazil, 2019 data indicates that 45% of sectoral emissions stemmed from agriculture, followed by 38% from the energy sector (Climate Transparency, 2022a). In Indonesia, the same year saw 65% of emissions from the energy sector, 15% from waste, and 14% from agriculture. Key sources of agricultural GHG emissions in Indonesia include rice cultivation (43%), cattle digestion (21%), and livestock manure (20%) (Climate Transparency, 2022b). In 2018, the Democratic Republic

of the Congo released 620 Mt CO<sub>2</sub>eq, largely due to deforestation, becoming the third largest emitter in the agricultural sector (FAO, 2021).

**Table 4.** Mitigation actions under SDG 13 for the highest carbon emissions emitters from transportation

Country	Mitigation Action under SDG 13
USA	The US Department of Energy funds for energy efficiency projects. Clean energy and carbon capture investments. Inflation Reduction Act of 2022. American Jobs Plan. Aviation Climate Action Plan. EPA AgSTAR program to encourage the use of biogas recovery systems to decrease methane emissions from livestock waste (IEA, 2023g).
Canada	Canada Net Zero Emissions Accountability Act Pan-Canadian Framework on Clean Growth and Climate Change Emissions Reduction Plan Commitment to provide USD 5.3 billion over five years in 2021 to keep helping developing countries impacted by climate change transition to sustainable development, after fully meeting its 2015 commitment to provide USD 2.65 billion in climate finance to developing countries. Efforts to phase out the use of coal-fired electricity generation and increase financing for emission-free electricity. Carbon pricing practices. Launching the \$8 billion Net-Zero Accelerator to promote the decarbonization of Canada's biggest industrial emitters, scale up clean technology, and boost Canada's industrial transformation across every sector. Commitment to provide \$3 billion in permanent public transit funding annually starting in fiscal 2026-27. Clean technology investments. Public awareness-raising efforts with civil society organizations (Government of Canada,2022).

Table 4 highlights the mitigation policies of the USA and Canada, the countries with the highest transport carbon emissions. Another sector with significant carbon emissions is transportation. In the United States, transportation is the largest source of emissions, accounting for 28% of GHG emissions in 2021, followed by electric power generation at 25% and industry at 23% (EPA, 2023). In Canada, transportation ranks second in terms of emissions, with 22% of overall GHG emissions in 2021, following the oil and gas sector at 28%, and preceding buildings at 13% and heavy industry at 11% (Government of Canada, 2022).

To prevent the increasing trend in air pollutant concentrations emitting into the atmosphere as soon as possible and to reach the 2030 and 2050 targets, countries started to work by making various commitments via international conferences. COP27, the 27th Conference of the Parties to the United Nations Framework Convention on Climate Change, was held in Sharm El-Sheikh, Egypt from November 6-18, 2022. At this conference, countries made a series of commitments to reduce greenhouse gas emissions and achieve the targets set in the Paris Agreement. In this context, they decided to work together to develop new technologies and solutions for climate change. However, the lack of ambitious commitments by some countries and their concerns about how to finance their action also led to some disagreements. Still, the commitments made

in COP27, which is a significant step in the fight against climate change, and the work to be done to achieve the goals set in the Paris Agreement are of great importance.

China, which has had the most greenhouse gas emissions for many years, has committed to achieving carbon neutrality before 2060 and peaking CO<sub>2</sub> emissions before 2030 and presented its strategies before COP26. By 2030, China aims to reduce its carbon intensity by more than 65% from the 2005 level, increase its forest stock to more than 6 billion cubic meters, reach 1,200 GW of installed wind and solar energy, and raise the proportion of non-fossil fuels in main energy consumption to 25%. China has announced that they will control coal use during the 14th Five-Year Plan (FYP; 2021-2025) period and will gradually reduce coal use in the 15<sup>th</sup> FYP period. However, looking at the data for 2021, China's annual coal production reached its highest level ever, and coal consumption increased by 4.6% due to the increase in energy demand. This means that CO<sub>2</sub> emissions in the energy sector increased by 5.8% in comparison with 2020. Although China's commitments are promising, its climate policy is seen as insufficient (Gregor & Ulrich, 2022).

Between 2005 and 2019, the USA, which managed to lower total greenhouse gas emissions by 11% and accounts for 26% of global emissions, is the second biggest emitter in the world after China. The USA launched its latest NDC in April 2021 after re-joining the Paris Agreement. This NDC sets an economy-wide target to lower net greenhouse gas emissions by 50% to 52% above 2005 levels by 2030, which is a much more ambitious target than in 2025. In addition, no quantitative targets were specified for 2035, other than the 100% carbon-free electricity target. In November 2021, the US committed to net zero by 2050 including energy efficiency, decarbonization of electricity, fuel switching, energy transitions, carbon sequestration, and CO<sub>2</sub> removal technologies in forests and soil, and presented its long-term strategies for non-CO<sub>2</sub> emission reductions. Later, the US enacted the Infrastructure Investment and Jobs Act, which provides \$7.5 billion in financing for electric vehicle charging stations. In addition, the United States passed the Inflation Reduction Act, which provides for investments of approximately US\$370 billion in energy security and climate action, and the Chips and Science Act, which authorizes approximately US\$170 billion in basic research funding, to accelerate the mitigation in greenhouse gas emissions. In addition, the US has established greenhouse gas emission standards for passenger cars and trucks and rules to limit and phase out hydrofluorocarbons (HFCs) over the next 15 years. However, despite all this, the climate policy of the USA is considered insufficient because it is not yet coherent with the global 1.5°C

temperature limit and it is foreseen that the current policies will not be able to achieve the 2030 targets (Gisela & Liselotte, 2022).

As globally the third biggest emitter of greenhouse gases, India doubled its greenhouse gas emissions between 2000 and 2019 as a consequence of population increase, urbanization, and energy demand brought by economic growth. India still has not presented a long-term strategy but is in the process of producing an action plan with ministries to achieve the net zero target by 2070. The country, which updated its NDC in 2022, lists 8 main objectives in this NDC, including the implementation of the LIFE vision to live a lifestyle in harmony with our planet and the pursuit of more climate-friendly strategies than other countries. These targets include reducing carbon intensity by 45% by 2030 in comparison with 2005 levels, providing ~50% cumulative non-fossil fuel-based electrical power installed capacity, generating an extra carbon sink of 2.5 to 3 billion tCO<sub>2</sub>e through afforestation, harmonization in sensitive sectors, focusing on measures, creating financial mobilization, capacity building, and technology transfer. However, India's climate policy is quite inadequate. It is said that India needs to increase its 2030 targets to reduce its emissions, set a clear zero target for 2050, and strengthen its climate policies (Angelos & Liselotte, 2022).

It is of great importance that Russia, which ranks among the countries with the highest carbon emissions, realizes its climate change policies. For this, key stakeholders in climate change policy processes play an important role. These stakeholders include Government, Businesses, NGOs, the public, and the international communities. The government is the primary actor in the policy process and has a significant effect on greenhouse gas emissions. The primary task of the government is to develop and apply policies to minimize greenhouse gas emissions. In the business world, especially in the field of energy, the industrial sector is a very important stakeholder in the implementation of climate policies, due to its contribution to greenhouse gases. Nongovernmental organizations have a significant impact on issues such as raising awareness on issues such as environmental protection, climate justice, and sustainability, monitoring policymakers, raising awareness, and pushing for change. The public is the group directly affected by the negative impacts of climate change. For this reason, it is crucial for the efficiency of the process that the public share their own needs and concerns in the policy-making process and try to reduce their emissions by contributing to the process. Finally, Russia, which is a party to international agreements such as UNFCCC and the Paris Agreement, is expected to comply with global efforts in the fight against climate change by realizing its commitments at the international level. For these commitments to be realized, policymakers must create inclusive and effective climate policies, taking into

account the views of different stakeholders. In this context, the steps already taken have not yielded the desired result. The government has been reluctant to engage with stakeholders and support policies as a business is concerned about the financial damage of the commitments made. Although NGOs are active in raising awareness and advocating policies on climate change, they don't have the power to influence the decision-making process. Even though steps are being taken that will have positive results in terms of the government and the business world, Russia needs to realize the importance of stakeholder participation and determine its priorities to realize the commitments given in international agreements (Yamawaki, 2020).

#### **4. Multinational Corporations and Sustainable Development Goals**

Cross-sectoral cooperation is essential for countries to achieve the SDGs and minimise the negative impacts of climate change. At this point, multinational corporations (MNCs) play a key role. MNCs working in alignment with the SDGs can increase engagement with stakeholders and capitalize on market opportunities potentially worth trillions while creating millions of jobs by 2030. To achieve these goals, the SDGs are used to set strategy and business objectives and conduct gap analysis, thereby driving business model innovation and sustainable growth. Moreover, business model innovation created by MNCs contributes to the achieving of the SDGs and creates a win-win effect. In tackling global challenges, a bridge is built between MNCs, governments, and non-profit organizations, and these structures benefit each other. This is where MNCs' innovation, technology, and strategic action skills are utilized (Rosati et.al., 2023). Within the scope of inter-sectoral cooperation and efforts to achieve SDGs, concrete steps should be taken to reduce carbon emissions. In this context, the European Union Emissions Trading System (EU ETS) comes to the fore. Adopted in 2005 as a result of the negotiations on the Kyoto Protocol, the EU ETS is the world's largest carbon market and has become the EU's most important tool in the fight against climate change. This system encourages emission reductions by imposing strict limits on the GHGs of MNCs in the energy and manufacturing industries (Pinkse & Kolk, 2007; dem Moore et al., 2019). The EU ETS covers 11,500 power plants and industrial facilities in 31 countries, and their carbon emissions account for almost 50 % of the EU's total emissions. However, there are differences in how firms respond to these regulations (Qi et al., 2023). After the EU ETS, intergovernmental emissions trading systems have varied greatly around the world. Some MNCs can utilise market rules more effectively to cope with carbon market regulations more efficiently and have higher carbon performance. In particular, under the EU ETS, MNCs have been found to have

better carbon performance on average than their local competitors (Nippa et al., 2021). However, the implementation of these systems at the company level and the fact that their institutional forms differ across countries have brought along certain challenges for MNCs (Pinkse & Kolk, 2007). The possibility that unilateral environmental regulations may impose significant costs on regulated MNCs, especially in carbon- and energy-intensive industries, divert resources away from productive activities, and ultimately jeopardise the international competitiveness of regulated firms raises concerns among economists, policymakers and industry representatives (dem Moore et al., 2019). Some negative climate behaviours of MNCs have also been observed in the context of the EU ETS. These behaviours include efforts to develop a corporate political strategy against stricter environmental regulations and actions such as overstating initial CO<sub>2</sub> emissions and hiding excess allowances for future more stringent systems (Nippa et al., 2021).

The environmental performance of MNCs is closely related to their strategies and practices towards their environmental responsibilities. As stakeholder concerns about global climate change increase, MNCs need to focus more on their environmental responsibilities and ensure that the information they provide in this context is in line with government regulations and social norms. In this way, MNCs endeavour to create a positive image by hiding their environmental failures and increasing their competitiveness. Since the Kyoto Protocol, MNCs' efforts to reduce carbon emissions have been supported by institutional pressure from governments and non-governmental organisations. This creates an obligation for MNCs to adjust their strategies and increase their investments in reducing carbon emissions. However, these investments are often limited by the desire for profit and question the commitment of MNCs to fulfil their environmental responsibilities. Environmental endeavours impose additional costs on MNCs, requiring more time and capital investment. For example, considering that the cost of CO<sub>2</sub> capture is quite expensive, it is understood that MNCs have difficulties in fulfilling their environmental commitments. In this context, the inconsistency between the environmental performance of MNCs and their disclosures reveals a form of behaviour called “greenwashing”. This behaviour, which reflects the understanding of magnifying underperformance, leads to the concealment of environmental mistakes and the highlighting of positive information. As a result, 86% of large MNCs are reported to be unbalanced in their sustainability practices and do not provide sufficient transparency on negative impacts (Peng et.al, 2023). It seems that MNCs can reduce investors' information inconsistency when they provide better transparency of environmental information. In particular, investors' willingness

to reduce their expected cost of equity if more environmental data are disclosed may contribute to increased confidence in this information. Furthermore, firms with better environmental performance may have a lower cost of equity by reducing their perceived environmental risks (Yu et al., 2021). The greenwashing behaviour of MNCs not only keeps their financial interests but also creates ethical problems when they fail to meet their environmental commitments. In this context, policymakers need to establish independent auditing systems regarding the level of environmental disclosure and develop financial penalty mechanisms for MNCs that fail to fulfil their environmental commitments (Peng et al., 2023; Yu et al., 2021).

Along with failure to meet environmental commitments creates ethical problems, carbon leakage and differences in regulations lead to economic and environmental challenges. Countries with relatively weaker regulations re-export carbon-intensive products to others with stricter regulations. Shifting economic activity to less regulated regions leads to job losses and reduced economic activity in highly regulated countries, creating carbon price differentials across regions. This so-called “carbon leakage” shows that policies are not only ineffective in terms of climate change but also costly in economic terms (dem Moore et al., 2019; Dechezleprêtre et al., 2022). With the increasing negative impacts of climate change, the EU ETS is expected to introduce stricter regulations. However, it is also thought that this will increase carbon leakage. That’s why, it is of great importance for governments and MNCs to favour regulations that do not cause carbon leakage (Dechezleprêtre et al., 2022). Many MNCs operate in less developed countries particularly Africa. MNCs are nowadays recognised as a major source of industrial growth and transfer of foreign technologies in host countries. However, the operations of MNCs through foreign direct investment have various negative environmental impacts on the host country (Balcilar et al., 2023).

For example, in Nigeria, whose economy is heavily dependent on the oil sector, mining and extraction activities are carried out. During the extraction of crude oil and the combustion of natural gases, a large amount of pollutant emissions is released into the atmosphere, and this is not limited to atmospheric degradation. Oil spills frequently occur in extraction areas, damaging agricultural land and water bodies and resulting in adverse impacts on terrestrial and marine ecotoxicities. The toxicity caused by these spills renders agricultural lands unproductive, puts underwater life at risk, and causes serious ecological degradation (Balcilar et al., 2023; Udemba & Angha, 2020). Between 1958 and 2016, there were 17 major oil spills in East Africa and 23 in West Africa. Most of these incidents were concentrated in the Niger Delta region of Nigeria and most

of them were not reported to official sources. It is recognised that MNCs can cause environmental damage in these regions where environmental laws and regulations are not sufficient (Balcilar et al., 2023). In developing countries, other pressing development challenges such as poverty, unemployment, and weak institutional frameworks exacerbate environmental pollution. Without strong institutional frameworks to guide environmental policies in host countries and ensure that MNEs comply with corporate social responsibility principles, the environmental pollution crisis may not be managed (Osabuohien et al., 2013). MNCs maintain their operations by utilising low regulations, and cheap resources and pollute the environment in the process (Udemba & Angha, 2020). Host countries should establish strong institutional frameworks to comply with environmental laws and prevent the negative impacts of MNCs (Osabuohien et al., 2013).

MNCs can play an important role in finding sustainable solutions to social and environmental problems by working in cooperation with the public sector by the stakeholders and decision-makers of governments mobilising resources and investments. The private sector shapes global climate governance through private regimes and public-private partnerships. By expanding the political authority of non-state actors, these partnerships contribute to agenda-setting, policy formulation, and implementation in international frameworks (Hori & Syugyo, 2020; Linares-Rodríguez et.al., 2023). For example, within the scope of SDG 13, MNCs in Colombia voluntarily disclose environmental data (Linares-Rodríguez et.al., 2023), while Türkiye contributes to advancing the sustainable development process through various policies and strategies in sectors like energy, industry, transportation, agriculture, waste, and forestry (Esen & Çalışkan, 2016). However, although they mostly adhere to the Global Reporting Initiative standards, their reporting does not reach the desired quality. The fact that MNCs in the Pacific region lag in the disclosure of SDG 13 indicates the need for urgent action plans from governments (Linares-Rodríguez et.al., 2023).

MNCs play an important role in green innovation and environmental research and development (R&D) activities to promote sustainable development and reduce carbon emissions. Green innovation is a critical approach for firms to effectively address concerns around environmental issues. Green innovation refers to innovation in the development and application of new technologies, products, services, organisational structures, or management practices aimed at promoting sustainable development. With the globalization of economic activities, MNCs are playing an increasingly crucial role in shaping the global environment, becoming key players in international relations. Research has shown that investments in R&D by MNCs contribute to reducing carbon

emissions for both local MNCs and MNCs themselves. For example, an empirical analysis examining the impact of the global diversification of Chinese MNCs between 2008 and 2020 on green innovation showed that global diversification has a positive and significant impact on green innovation. Moreover, factors such as the institutional quality of the host country, state ownership, and the academic background of the CEO further enhance this positive effect. These results suggest that global diversification facilitates MNCs' participation in green innovation activities and promotes environmental responsibility (Zhou & Lin, 2024). MNCs' efforts to mitigate carbon emissions on a global scale remain uncertain. However, MNCs often have the capability to finance extensive R&D capacities due to their easy access to international capital markets. Despite this, they may circumvent emission reductions by diversifying their production facilities across various geographical locations and relocating carbon-intensive activities among these facilities. The transition from traditional energy sources to renewable energy sources requires high R&D expenditures to develop rapid innovative technologies. MNCs rely heavily on R&D activities to improve their product innovation capabilities and tend to have the necessary resources to finance these large-scale expenditures (Gönenc & Poleska, 2022).

Scenario analyses based on methods outlined in international frameworks such as the UNFCCC and IEA are crucial for achieving the 2050 carbon neutrality targets. Climate change-oriented strategies are essential for business and ecological sustainability in all sectors. It is becoming increasingly inevitable for MNCs considering their performance towards 2050 to think about climate-related actions. While MNCs bear primary responsibility, international frameworks will continue to support and govern long-term vision and actions (Hori & Syugyo, 2020). To achieve these goals, gaps in various areas need to be filled. Closing the governance gap between government and regions is a first step. Improved governance mechanisms are needed to regulate highly polluting activities and support regions with low socioeconomic conditions. However, alliances between the public and private sectors should be strengthened. Cooperation is needed to ensure that concrete climate actions are aligned with regional plans and support carbon management (Linares-Rodríguez et al., 2023). Sustainable development strategies should be developed to combat climate change, the consequences of which affect political, economic, and social policies. Under the SDGs, the new business approach should be accountable, enable a low-carbon economy, and go hand in hand with adaptation strategies by proposing innovative solutions. So far, MNCs have made a substantial contribution to the fight against climate change by providing solutions. Businesses should engage in collaborative public and private sector efforts and initiatives to play a key role in tackling climate change

by overcoming barriers and fostering innovation. Strong corporate leadership and stakeholder engagement are essential to increase climate change impact and foster innovation in climate adaptation efforts (Esen & Çalışkan, 2016).

## **5. Conclusion**

Today, many studies focus on how SDGs can be achieved by 2050, and in other words, it has gained the most attention on how countries can successfully achieve the energy and climate policy targets to fulfil the goals of the Paris Agreement and the European Union Green Deal. If serious measures are not taken urgently, the earth will become an increasingly uninhabitable place for humans and all living things, and the situation will undoubtedly directly affect our future generations. Therefore, all nations must take responsibility, paving the way, and fulfil their responsibilities. In this context, due to extreme climatic events that raise a serious alarm about the severe danger awaiting humanity, a series of climate policies and efforts to take concrete steps on a global scale should be fulfilled by the decision-makers of countries. In this review paper, countries were evaluated considering CO<sub>2</sub> emissions they released into the atmosphere on a sectoral basis concerning their contribution to the global warming potential. Moreover, the countries, that caused the highest CO<sub>2</sub> emissions in recent years and tended to increase in terms of CO<sub>2</sub> emissions compared to previous years, were examined in terms of their commitments regarding the climate policies they will implement to combat global climate change. Additionally, the significance of multinational cooperation in driving mitigation and adaptation strategies considering the consistency with SDGs was addressed by closing the governance gap between government and regions.

The general contents of climate change mitigation and adaptation actions planned to be implemented by countries to reduce GHG emissions and achieve SDGs are summarized below:

- increasing energy efficiency,
- switching to renewable energy,
- clean energy and carbon capture investments,
- reducing deforestation,
- checking total energy usage and energy intensity.
- advancing energy conservation in industry, information technology, transport, and buildings,
- promoting energy conservation technologies and products.

The emission reduction policies of the countries summarized here are expected to provide ideas for policymakers and decision-makers to create new

road maps for steps toward carbon neutrality and to open the doors for multinational collaborations to share responsibilities by meeting under common ground to minimize the severe impacts of the global environmental issue on human beings.

While technological advances and economic growth continue sustainably, policies based on innovative and nature-friendly initiatives of multinational companies are of great importance in promoting sustainable development and supporting climate change mitigation and adaptation actions, with approaches that take environmental parameters into account. Realizing investments based on the concept of green innovation, policies that support the hierarchy and management with environmentally friendly approaches between the government and regions, taking into account corporate leadership and stakeholder participation, can be considered as aspects that multinational companies will take into consideration in achieving SDGs to minimize possible problems in the future.

## References

- Adedeji, O., Reuben O., & Olatoye O., (2014). Global climate change. *Journal of Geoscience and Environment Protection*, 2 (02), 114-122. <http://dx.doi.org/10.4236/gep.2014.22016>
- Altuğ, T., & Özkan, F., (2015). Sera Gazı Emisyonlarının İzlenmesi, Doğrulanması ve Raporlanması. *Verimlilik Dergisi*, (2), 67-86.
- Amighini, A., Giudici P., & Ruet J. (2022). Green finance: An empirical analysis of the Green Climate Fund portfolio structure. *Journal of Cleaner Production*, 350, 131383. <https://doi.org/10.1016/j.jclepro.2022.131383>
- Angelos, D., Liselotte, J. (2022). India's climate change policies: State of play ahead of COP27, EPRS: European Parliamentary Research Service. Belgium. Retrieved May 25, 2023, from <https://policycommons.net/artifacts/3131052/indias-climate-change-policies/3924285/>
- aus dem Moore, N., Großkurth, P., & Themann, M. (2019). Multinational corporations and the EU Emissions Trading System: The specter of asset erosion and creeping deindustrialization. *Journal of Environmental Economics and Management*, 94, 1-26. <https://doi.org/10.1016/j.jjeem.2018.11.003>
- Balat, M. (2007). Status of fossil energy resources: A global perspective. *Energy Sources, Part B: Economics, Planning, and Policy*, 2(1), 31-47. <https://doi.org/10.1080/15567240500400895>
- Balcilar, M., Usman, O., & Ike, G. N. (2023). Operational behaviours of multinational corporations, renewable energy transition, and environmental sustainability in Africa: Does the level of natural resource rents matter?. *Resources Policy*, 81, 103344. <https://doi.org/10.1016/j.resourpol.2023.103344>
- Biswas, R. R., & Rahman, A. (2023). Adaptation to climate change: A study on regional climate change adaptation policy and practice framework. *Journal of Environmental Management*, 336, 117666. <https://doi.org/10.1016/j.jenvman.2023.117666>
- Center for International Knowledge on Development (CIKD). (2021). China's Progress Report on Implementation of the 2030 Agenda for Sustainable Development. Retrieved June 1, 2023, from [https://www.fmprc.gov.cn/eng/topics\\_665678/2030kcxzfzyc/202109/P020211019152754484797.pdf](https://www.fmprc.gov.cn/eng/topics_665678/2030kcxzfzyc/202109/P020211019152754484797.pdf)
- Climate Transparency (2021). Climate Transparency Report: Comparing G20 Climate Action Towards Net Zero. Russian Federation Report. Retrieved

- June 16, 2023, from <https://www.climate-transparency.org/wp-content/uploads/2021/10/CT2021Russia.pdf>
- Climate Transparency (2022a). Climate Transparency Report: Comparing G20 Climate Action. Brazil Country Profile. Retrieved June 16, 2023, from <https://www.climate-transparency.org/wp-content/uploads/2022/10/CT2022-Brazil-Web.pdf>
- Climate Transparency (2022b). Climate Transparency Report: Comparing G20 Climate Action. Indonesia Country Profile. Retrieved June 16, 2023, from <https://www.climate-transparency.org/wp-content/uploads/2022/10/CT2022-Indonesia-Web.pdf>
- Climate Transparency (2022c). Climate Transparency Report: Comparing G20 Climate Action. Saudi Arabia Country Profile. Retrieved June 16, 2023, from <https://www.climate-transparency.org/wp-content/uploads/2022/10/CT2022-Saudi-Arabia-Web.pdf>
- Cohen, B., Cowie, A., Babiker, M., Leip, A., & Smith, P. (2021). Co-benefits and trade-offs of climate change mitigation actions and the *Sustainable Development Goals*. *Sustainable Production and Consumption*, 26, 805-813. <https://doi.org/10.1016/j.spc.2020.12.034>
- Crippa, M., Guizzardi, D., Banja, M., Solazzo, E., Muntean, M., Schaaf, E., Pagani, F., Monforti-Ferrario, F., Olivier, J., Quadrelli, R., Riskey Martin, A., Taghavi-Moharamli, P., Grassi, G., Rossi, S., Jacome Felix Oom, D., Branco, A., San-Miguel-Ayanz, J., & Vignati, E. (2022). CO2 emissions of all world countries - 2022 Report. *JRC Science for Policy Report, European Commission, EUR, 31182*.
- Dechezleprêtre, A., Gennaioli, C., Martin, R., Muûls, M., & Stoerk, T. (2022). Searching for carbon leaks in multinational MNCs. *Journal of Environmental Economics and Management*, 112, 102601. <https://doi.org/10.1016/j.jeem.2021.102601>
- Ellouz, F., & Barkouti, A. (2022). Trends on Carbon Footprint and Climate Change Research: A Bibliometric Study from 2000 to 2022. *African Journal of Advanced Pure and Applied Sciences (AJAPAS)*, 71-77.
- Esen, E., & Çalışkan, A. Ö. (2016). Company Policies to Adapt Climate Change Plan: A Case Study on Turkey. In *Climate Change and the 2030 corporate agenda for Sustainable Development* (Vol. 19, pp. 159-175). Emerald Group Publishing Limited. <https://doi.org/10.1108/s2051-503020160000019008>
- Federal Environment Agency (UBA). (2022). National Inventory Report for the German Greenhouse Gas Inventory 1990 – 2021.

- Filipović, S., Lior, N., & Radovanović, M. (2022). The green deal—just transition and sustainable development goals Nexus. *Renewable and Sustainable Energy Reviews*, 168, 112759. <https://doi.org/10.1016/j.rser.2022.112759>
- Food and Agriculture Organization (FAO). (2021). Emissions due to agriculture. Global, regional and country trends 2000–2018. FAOSTAT Analytical Brief Series No 18. Rome.
- Fuso Nerini, F., Sovacool, B., Hughes, N., Cozzi, L., Cosgrave, E., Howells, M., ... & Milligan, B. (2019). Connecting climate action with other Sustainable Development Goals. *Nature Sustainability*, 2(8), 674–680. <https://doi.org/10.1038/s41893-019-0334-y>
- Gechev, V. (2019). The Green Climate Fund—Projections vs. Reality. *Reality* (June 30, 2019). <http://dx.doi.org/10.2139/ssrn.3412561>
- Giri, M., Bista, G., Singh, P. K., & Pandey, R. (2021). Climate change vulnerability assessment of urban informal settlers in Nepal, a least developed country. *Journal of Cleaner Production*, 307, 127213. <https://doi.org/10.1016/j.jclepro.2021.127213>
- Gisela, G. & Liselotte, J. (2022). United States climate change policies: State of play ahead of COP27, EPRS: European Parliamentary Research Service. Belgium. Retrieved May 25, 2023, from <https://policycommons.net/artifacts/3131576/united-states-climate-change-policies/3924807/>
- Gomez-Echeverri, L. (2018). Climate and development: enhancing impact through stronger linkages in the implementation of the Paris Agreement and the Sustainable Development Goals (SDGs). *Philosophical Transactions of the Royal Society A: Mathematical, Physical and Engineering Sciences*, 376(2119), 20160444. <https://doi.org/10.1098/rsta.2016.0444>
- Gonenc, H., & Poleska, A. (2023). Multinationals, research and development, and carbon emissions: international evidence. *Climate Policy*, 23(8), 959–974. <https://doi.org/10.1080/14693062.2022.2135484>
- Government of Canada. (2022). Canada’s Eighth National Communication on Climate Change and Fifth Biennial Report. Retrieved May 24, 2023, from <https://unfccc.int/sites/default/files/resource/Canada%20NC8%20BR5%20EN.pdf>
- Green Climate Fund. (2022). GCF Appraisal Guidance: A comprehensive guide to the tools and due diligence processes used to review and assess concept notes and funding proposals. Retrieved May 24, 2023, from <https://www.greenclimate.fund/document/appraisal-guidance>

- Gregor, E. & Ulrich, J. (2022). China's climate change policies: State of play ahead of COP27, EPRS: European Parliamentary Research Service. Belgium. Retrieved May 25, 2023, from <https://policycommons.net/artifacts/3131200/chinas-climate-change-policies/3924433/>
- Hori, S., & Syugyo, S. (2020). The function of international business frameworks for governing MNCs' climate change-related actions toward the 2050 goals. *International Environmental Agreements: Politics, Law and Economics*, 20(3), 541-557. <https://doi.org/10.1007/s10784-020-09475-7>
- Huq, S., Reid, H., Konate, M., Rahman, A., Sokona, Y., & Crick, F. (2004). Mainstreaming adaptation to climate change in least developed countries (LDCs). *Climate Policy*, 4(1), 25-43. <https://doi.org/10.1080/14693062.2004.9685508>
- Ihara, I., Zhao, R., Pandyaswargo, A. H., & Onoda, H. (2020). Evaluating the Effectiveness of Japan's Climate Change Mitigation and Clean Technology Development Policies. *Indonesian Journal of Computing, Engineering, and Design (IJoCED)*, 2(1), 1-12. <https://doi.org/10.35806/ijoced.v2i1.98>
- Intergovernmental Panel on Climate Change (IPCC). (1990). *Climate Change. The IPCC Scientific Assessment*. Cambridge University Press, UK.
- Intergovernmental Panel on Climate Change (IPCC). (2007). *Climate Change 2007: The Physical Science Basis. Contribution of Working Group I to the Fourth Assessment Report of the Intergovernmental Panel on Climate Change*. [Solomon, S., D. Qin, M. Manning, Z. Chen, M. Marquis, K.B. Averyt, M. Tignor and H.L. Miller (eds.)]. Cambridge University Press, Cambridge, United Kingdom and New York, NY, USA, 996 pp.
- Intergovernmental Panel on Climate Change (IPCC). (2013). *Climate Change 2013: The Physical Science Basis. Contribution of Working Group I to the Fifth Assessment Report of the Intergovernmental Panel on Climate Change* [Stocker, T.F., D. Qin, G.-K. Plattner, M. Tignor, S.K. Allen, J. Boschung, A. Nauels, Y. Xia, V. Bex and P.M. Midgley (eds.)]. Cambridge University Press, Cambridge, United Kingdom and New York, NY, USA, 1535 pp.
- Intergovernmental Panel on Climate Change (IPCC). (2023). *Climate Change 2023: Synthesis Report. A Report of the Intergovernmental Panel on Climate Change. Contribution of Working Groups I, II and III to the Sixth Assessment Report of the Intergovernmental Panel on Climate Change* [Core Writing Team, H. Lee and J. Romero (eds.)]. IPCC, Geneva, Switzerland, (in press)

- International Energy Agency (IEA). (2021). Türkiye Energy Policy Review 2021. Retrieved June 18, 2023, from <https://www.iea.org/reports/turkey-2021>.
- International Energy Agency (IEA). (2022). An Energy Sector Roadmap to Net Zero Emissions in Indonesia International Energy Agency Special Report. Retrieved November 20, 2023, from <https://iea.blob.core.windows.net/assets/b496b141-8c3b-47fc-adb2-90740eb0b3b8/AnEnergySectorRoadmaptoNetZeroEmissionsinIndonesia.pdf>.
- International Energy Agency (IEA). (2023a). Germany Policies Database. Retrieved June 18, 2023, from <https://www.iea.org/policies?country=Germany>.
- International Energy Agency (IEA). (2023b). India Policies Database. Retrieved June 18, 2023, from <https://www.iea.org/policies?country=India>.
- International Energy Agency (IEA). (2023c). Iran Policies Database. Retrieved June 18, 2023, from <https://www.iea.org/policies?country=Iran>.
- International Energy Agency (IEA). (2023d). Japan Policies Database. Retrieved June 18, 2023, from <https://www.iea.org/countries/japan>.
- International Energy Agency (IEA). (2023e). Russia Policies Database. Retrieved June 18, 2023, from <https://www.iea.org/countries/russia#policies>.
- International Energy Agency (IEA). (2023f). Saudi Arabia Policies Database. Retrieved June 18, 2023, from <https://www.iea.org/policies?country=Saudi%20Arabia>.
- International Energy Agency (IEA). (2023g). United States Policies Database. Retrieved June 18, 2023, from <https://www.iea.org/policies?country=United%20States>.
- Kimuli, J. B., Di, B., Zhang, R., Wu, S., Li, J., & Yin, W. (2021). A multisource trend analysis of floods in Asia-Pacific 1990–2018: Implications for climate change in sustainable development goals. *International Journal of Disaster Risk Reduction*, 59, 102237. <https://doi.org/10.1016/j.ijdrr.2021.102237>
- Kozlowski, T. T. (Ed.). (1984). *Flooding and plant growth* (No. 581.5263 F631). New York: Academic Press.
- Leal Filho, W., & Mifsud, M. (2020). Concise guides to the United Nations sustainable development goals. *Emerald Publishing*.
- Linares-Rodríguez, M. C., Gambetta, N., & García-Benau, M. A. (2023). Climate action information disclosure in Colombian MNCs: A regional and sectorial analysis. *Urban Climate*, 51, 101626. <https://doi.org/10.1016/j.uclim.2023.101626>

- Liu, Z., Deng, Z., Davis, S., & Ciais, P. (2023). Monitoring global carbon emissions in 2022. *Nature Reviews Earth & Environment*, 1-2. <https://doi.org/10.1038/s43017-023-00406-z>
- Marcillo-Delgado, J. C., Alvarez-Garcia, A., & García-Carrillo, A. (2021). Analysis of risk and disaster reduction strategies in South American countries. *International Journal of Disaster Risk Reduction*, 61, 102363. <https://doi.org/10.1016/j.ijdrr.2021.102363>
- Ministry of Environment, Forest and Climate Change (MoEFCC). (2021). India: Third Biennial Update Report to the United Nations Framework Convention on Climate Change. Ministry of Environment, Forest and Climate Change, Government of India. Retrieved June 17, 2023, from [https://unfccc.int/sites/default/files/resource/INDIA\\_%20BUR-3\\_20.02.2021\\_High.pdf](https://unfccc.int/sites/default/files/resource/INDIA_%20BUR-3_20.02.2021_High.pdf).
- Ministry of the Environment Japan, Greenhouse Gas Inventory Office of Japan (GIO), Center for Global Environmental Research (CGER), National Institute for Environmental Studies (NIES). (2023). National Greenhouse Gas Inventory Report of Japan. Retrieved June 17, 2023, from [https://www.nies.go.jp/gio/en/archive/nir/jqjm1000001v3csj-att/NIR-JPN-2023-v3.0\\_gioweb.pdf](https://www.nies.go.jp/gio/en/archive/nir/jqjm1000001v3csj-att/NIR-JPN-2023-v3.0_gioweb.pdf).
- National Development and Reform Commission of the People's Republic of China (NDRC of China). (2021). China's policies and actions for addressing climate change. Retrieved June 13, 2023, from <http://www.ncsc.org.cn/yjcg/cbw/202111/P020211117418821628432.pdf>
- Nippa, M., Patnaik, S., & Taussig, M. (2021). MNE responses to carbon pricing regulations: Theory and evidence. *Journal of International Business Studies*, 52, 904-929. <https://doi.org/10.1057/s41267-021-00403-8>
- Olabi, A. G., Obaideen, K., Elsaid, K., Wilberforce, T., Sayed, E. T., Maghrabie, H. M., & Abdelkareem, M. A. (2022). Assessment of the pre-combustion carbon capture contribution into sustainable development goals SDGs using novel indicators. *Renewable and Sustainable Energy Reviews*, 153, 111710. <https://doi.org/10.1016/j.rser.2021.111710>
- Osabuohien, E. S., Efobi, U. R., & Gitau, C. M. (2013). External intrusion, internal tragedy: environmental pollution and multinational corporations in Sub-Saharan Africa. In *Principles and strategies to balance ethical, social and environmental concerns with corporate requirements* (pp. 93-118). Emerald Group Publishing Limited. [https://doi.org/10.1108/S2051-5030\(2013\)0000012010](https://doi.org/10.1108/S2051-5030(2013)0000012010)
- Owusu, P. A., & Asumadu-Sarkodie, S. (2016). A review of renewable energy sources, sustainability issues and climate change mitigation. *Cogent*

- Engineering*, 3(1), 1167990.  
<https://doi.org/10.1080/23311916.2016.1167990>
- Parris, T. M., & Kates, R. W. (2003). Characterizing and measuring sustainable development. *Annual Review of Environment and Resources*, 28(1), 559-586. <https://doi.org/10.1146/annurev.energy.28.050302.105551>
- Peng, X., Li, J., Tang, Q., Lan, Y. C., & Cui, X. (2024). Do environmental scores become multinational corporations' strategic “greenwashing” tool for window-dressing carbon reduction? A cross-cultural analysis. *Business Strategy and the Environment*, 33(3), 2084-2115. <https://doi.org/10.1002/bse.3586>
- Pinkse, J., & Kolk, A. (2007). Multinational corporations and emissions trading: Strategic responses to new institutional constraints. *European Management Journal*, 25(6), 441-452. <https://doi.org/10.1016/j.emj.2007.07.003>
- Qi, Y., Yuan, M., & Bai, T. (2023). Where will corporate capital flow to? Revisiting the impact of China's pilot carbon emission trading system on investment. *Journal of Environmental Management*, 336, 117671. <https://doi.org/10.1016/j.jenvman.2023.117671>
- Raikes, J., Smith, T. F., Baldwin, C., & Henstra, D. (2022). The influence of international agreements on disaster risk reduction. *International Journal of Disaster Risk Reduction*, 76, 102999. <https://doi.org/10.1016/j.ijdrr.2022.102999>
- Ridhosari, B., & Rahman, A. (2020). Carbon footprint assessment at Universitas Pertamina from the scope of electricity, transportation, and waste generation: toward a green campus and promotion of environmental sustainability. *Journal of Cleaner Production*, 246, 119172. <https://doi.org/10.1016/j.jclepro.2019.119172>
- Rio Declaration on Environment and Development (RDED). (1992). *Environmental Conservation*. 19(04), p.366.
- Ritchie, H., Rosado, P., & Roser, M. (2022). Natural disasters. *Our World in Data*. Retrieved June 18, 2023, from <https://ourworldindata.org/natural-disasters>
- Ritchie, H., Roser, M., Rosado-Merino, P. (2020). Iran: CO2 Country Profile. OurWorldInData.org. Retrieved June 18, 2023, from <https://ourworldindata.org/co2/country/iran>.
- Robert, K. W., Parris, T. M., & Leiserowitz, A. A. (2005). What is sustainable development? Goals, indicators, values, and practice. *Environment: science and policy for sustainable development*, 47(3), 8-21. <https://doi.org/10.1080/00139157.2005.10524444>

- Roberts, J. T., Weikmans, R., Robinson, S. A., Ciplet, D., Khan, M., & Falzon, D. (2021). Rebooting a failed promise of climate finance. *Nature Climate Change*, 11(3), 180-182. <https://doi.org/10.1038/s41558-021-00990-2>
- Rosati, F., Rodrigues, V. P., Cosenz, F., & Li-Ying, J. (2023). Business model innovation for the Sustainable Development Goals. *Business Strategy and the Environment*, 32(6), 3752-3765. <https://doi.org/10.1002/bse.3334>
- Ross, A. (2009). Modern interpretations of sustainable development. *Journal of law and society*, 36(1), 32-54. <https://doi.org/10.1111/j.1467-6478.2009.00455.x>
- Satterthwaite, D. (2009). The implications of population growth and urbanization for climate change. *Environment and urbanization*, 21(2), 545-567. <https://doi.org/10.1177/0956247809344361>
- Schleussner, C. F., Lissner, T. K., Fischer, E. M., Wohland, J., Perrette, M., Golly, A., ... & Schaeffer, M. (2016). Differential climate impacts for policy-relevant limits to global warming: the case of 1.5 C and 2 C. *Earth system dynamics*, 7(2), 327-351. <https://doi.org/10.5194/esd-7-327-2016>
- Scoones, I. (2016). The politics of sustainability and development. *Annual Review of Environment and Resources*, 41, 293-319. <https://doi.org/10.1146/annurev-environ-110615-090039>
- Shah, A. A., Gong, Z., Pal, I., Sun, R., Ullah, W., & Wani, G. F. (2020). Disaster risk management insight on school emergency preparedness—a case study of Khyber Pakhtunkhwa, Pakistan. *International Journal of Disaster Risk Reduction*, 51, 101805. <https://doi.org/10.1016/j.ijdr.2020.101805>
- Statista. (2023). Global greenhouse gas emissions by sector 2021. Statista. Retrieved July 26, 2024, from <https://www.statista.com/statistics/1341795/ghg-emissions-by-sector-globally/#:~:text=The%20biggest%20contributor%20to%20global,of%20GHG%20emissions%20in%202021.>
- Stevenson, R. B., Nicholls, J., & Whitehouse, H. (2017). What is climate change education?. *Curriculum Perspectives*, 37, 67-71. <https://doi.org/10.1007/s41297-017-0015-9>
- Talu, N., & Kocaman, H. (2018). Turkey's Climate Change Policy, Legal and Institutional Framework. Ankara. Retrieved June 17, 2023, from [https://www.iklimin.org/wp-content/uploads/2020/03/modul\\_04\\_en-1.pdf](https://www.iklimin.org/wp-content/uploads/2020/03/modul_04_en-1.pdf).
- Tang, K. H. D. (2022). A model of behavioral climate change education for higher educational institutions. *Environmental Advances*, 9, 100305. <https://doi.org/10.1016/j.envadv.2022.100305>

- Tiseo, I. (2023). Distribution of greenhouse gas emissions in India in 2019, by sector. Statista. Retrieved June 18, 2023, from <https://www.statista.com/statistics/955980/india-distribution-of-ghg-emissions-by-sector/>.
- Tolppanen, S., Kang, J., & Riuttanen, L. (2022). Changes in students' knowledge, values, worldview, and willingness to take mitigative climate action after attending a course on holistic climate change education. *Journal of Cleaner Production*, 373, 133865. <https://doi.org/10.1016/j.jclepro.2022.133865>
- Turkish Statistical Institute (TUIK). (2023). Türkiye Greenhouse Gas Emission Statistics, 1990-2021. Retrieved November 19, 2023, from <https://data.tuik.gov.tr/Bulten/Index?p=Sera-Gazi-Emisyon-Istatistikleri-1990-2021-49672&dil=1>.
- U.S. Agency for International Development (USAID). (2022). Democratic Republic of the Congo (DRC) Climate Change Country Profile Fact Sheet, U.S. Agency For International Development. Retrieved June 25, 2023, from: <https://www.usaid.gov/climate/country-profiles/democratic-republic-congo>.
- Udamba, E. N., & Agha, C. O. (2020). Abatement of pollutant emissions in Nigeria: a task before multinational corporations. *Environmental Science and Pollution Research*, 27(21), 26714-26724. <https://doi.org/10.1007/s11356-020-08908-9>
- UN (United Nations). (2016). The Sustainable Development Goals Report 2016. *New York: United Nations*.
- United Nations Development Programme (UNDP). (2023). Congo (Democratic Republic of). (n.d.). UNDP Climate Promise. Retrieved June 14, 2023, from <https://climatepromise.undp.org/what-we-do/where-we-work/congo-democratic-republic>.
- United Nations. (2016). Goals, targets and indicators. The Danish Institute for Human Rights. Retrieved June 14, 2023, from <https://sdg.humanrights.dk/en/goals-and-targets?page=3>.
- United States Environmental Protection Agency (EPA). (2021). Sources of Greenhouse Gas Emissions. Retrieved June 18, 2023, from <https://www.epa.gov/ghgemissions/sources-greenhouse-gas-emissions>
- United States Environmental Protection Agency (EPA). (2023). Inventory of U.S. Greenhouse Gas Emissions and Sinks: 1990-2021. Retrieved June 18, 2023, from <https://www.epa.gov/ghgemissions/inventory-us-greenhouse-gas-emissions-and-sinks-1990-2021>

- World Bank Group (WBG). (2023). Brazil Country Climate and Development Report.  
<https://openknowledge.worldbank.org/server/api/core/bitstreams/fd36997e-3890-456b-b6f0-d0cee5fc191e/content>.
- Yamawaki, D. (2020). A Stakeholder Analysis of Climate Change Policies in Russia. *Russian and East European Studies*.  
<https://doi.org/10.5823/jarees.2020.126>
- Yu, E. P. Y., Tanda, A., Luu, B. V., & Chai, D. H. (2021). Environmental transparency and investors' risk perception: Cross-country evidence on multinational corporations' sustainability practices and cost of equity. *Business Strategy and the Environment*, 30(8), 3975-4000.  
<https://doi.org/10.1002/bse.2852>
- Zagoruichyk, A. (2022). The Carbon Brief Profile: Russia. Retrieved June 14, 2023, <https://www.carbonbrief.org/the-carbon-brief-profile-russia/>.
- Zhou, C., & Lin, F. (2024). Does global diversification promote or hinder green innovation? Evidence from Chinese multinational corporations. *Technovation*, 129, 102905.  
<https://doi.org/10.1016/j.technovation.2023.102905>

## Chapter 4

### Sustainable Energy Management Through Machine Learning Models for Natural Gas Consumption Prediction

**Didem GULERYUZ<sup>1</sup>**

**Fatmanur BİLGEN<sup>2</sup>**

---

<sup>1</sup> Assoc. Prof. Dr., Bayburt University, Faculty of Applied Sciences, Management Information Systems, [dguleryuz@bayburt.edu.tr](mailto:dguleryuz@bayburt.edu.tr), ORCID: 0000-0003-4198-9997

<sup>2</sup> Undergraduate Student (Graduate), Bayburt University, Faculty of Applied Sciences, Management Information Systems, [bilgenfatmanur33@gmail.com](mailto:bilgenfatmanur33@gmail.com), 0009-0008-2055-7451.

## **1. Introduction**

In contemporary times, energy has emerged as a matter of critical importance, impacting all of humanity. Remarkably, the global emphasis on “sustainable development” has underscored the necessity for the efficient production and consumption of current energy resources, minimizing environmental impacts, and transitioning to clean, inexhaustible energy sources such as solar, wind, biomass, and geothermal energy. Energy is a fundamental component of modern economic and social structures, underpinning the sustainability of various sectors, including industry, transportation, comfortable living spaces, and healthcare services (IEA, 2021). Global energy demand continues to rise steadily, driven by rapid population growth and economic expansion (Stern, 2011). This increase necessitates the effective and efficient management of energy resources, the mitigation of environmental impacts, and the assurance of energy security. Traditional fossil fuels pose significant concerns regarding environmental pollution and greenhouse gas emissions, highlighting the urgent need to revise energy policies and strategies. In this context, renewable energy sources are gaining increasing prominence to ensure environmental sustainability and energy security. Integrating inexhaustible resources such as solar, wind, biomass, and geothermal energy plays a pivotal role in reducing dependence on fossil fuels and combating global warming (UN, 2015). Turkey is a rapidly growing country in energy consumption and demand, with a significant portion of its energy needs met through imports. This reliance heightens risks and dependency concerning energy security. Consequently, Turkey’s energy strategies aim to diversify energy sources and enhance domestic energy production. Among these strategies, natural gas holds a prominent position. As a fossil fuel, natural gas offers lower carbon emissions and higher efficiency than other fossil fuels, making it a viable alternative for reducing environmental impacts. Furthermore, its economic predictability and cost-effectiveness significantly strengthen energy security and balance energy costs. The dual challenges of global warming and environmental pollution caused by fossil fuel consumption and the finite nature of fossil fuels have intensified the focus on renewable energy research. Despite being a fossil fuel, natural gas, with its relatively lower carbon emissions, is considered a more accessible and environmentally friendly energy source for Turkey. Accurately forecasting natural gas demand, particularly during the winter months in colder regions, is paramount in supporting sustainable energy policies and climate action. Bayburt, located in Turkey's Black Sea Region, experiences a pronounced winter climate. The harsh winter conditions, which necessitate substantial energy consumption, highlight the critical role of natural gas in meeting regional energy demands. Bayburt’s cold climate significantly increases natural gas demand

during winter months (AKSA, 2024). Understanding the factors influencing natural gas consumption in Bayburt is crucial for effectively managing energy resources and ensuring environmental sustainability. In this context, global energy consumption and demand trends, alongside Turkey’s energy strategies, clearly emphasize the critical role of natural gas as an energy resource. From both environmental sustainability and energy security perspectives, natural gas’s economic and ecological advantages stand out prominently (UN, 2015). Figure 1 illustrates the changes in natural gas consumption globally and in Turkey between 2005 and 2023. This visualization provides a foundation for understanding the impact of global and local energy policies on natural gas demand. The data highlights the increase in energy consumption and the consequent necessity of sustainable energy management policies and underscores the urgency of transitioning from fossil fuels to renewable energy sources.



**Figure 1.** Natural Gas Consumption in Turkey and the World: The 2005-2023 Period

Since 2005, a significant upward trend has been observed in global natural gas consumption. This increase in energy demand is closely associated with rapidly industrializing economies, growing populations, and rising energy needs. However, an examination of the data reveals periods where the consumption growth rate has slowed. These fluctuations can be attributed to global economic crises, the increased adoption of renewable energy sources, and policies aimed at reducing fossil fuel consumption due to environmental concerns. Nonetheless, the overall trend demonstrates that natural gas continues to play a vital role in energy production. In Turkey, natural gas consumption has shown a growth pattern consistent with global trends over 2005–2023. The primary drivers of this

increase include population growth, urbanization, the widespread adoption of natural gas for residential heating, and its significant role as an input in industry and energy production. Aligned with Turkey's energy strategies, natural gas is prioritized as an energy source due to its lower carbon emissions and higher efficiency than other fossil fuels. The consumption data for natural gas between 2005 and 2023 underscores a steady global increase, with Turkey reflecting a parallel rise in energy consumption. Turkey's natural gas consumption fluctuations can be directly linked to energy policies and economic dynamics. In this context, accurately forecasting natural gas demand is critical for energy management and cost balancing. Effective and sustainable management of energy resources is pivotal for Turkey to achieve its long-term development goals. Accelerating industrial transformation, designing more efficient production processes, developing sustainable energy solutions, and adopting innovative production systems will support environmental sustainability and enhance Turkey's global competitiveness. Accurate natural gas demand forecasting is vital for efficiently utilising resources, reducing environmental impacts, and developing sustainable energy policies. The prediction of natural gas demand is inherently complex, nonlinear, and multivariate. Traditional methods have shown limited success in addressing these challenges. Machine learning-based models such as Support Vector Regression (SVR) and Gaussian Process Regression (GPR) offer robust alternatives for modelling such intricate systems. Optimization algorithms like Grid Search and Random Search further enhance prediction accuracy by optimizing the hyperparameters of these models.

This study applies optimized SVR and GPR models to predict the increased natural gas demand during winter months in Bayburt province. The primary objective is to evaluate the performance of these models and analyze their applicability in energy management processes. SVR and GPR models are distinguished by their ability to model nonlinear relationships effectively, and their performance has been further improved through optimization using Grid Search and Random Search algorithms. Accurate forecasting of natural gas demand is crucial for ensuring environmental sustainability, managing energy costs, enabling local energy policies, and achieving long-term economic goals. This study aims to model the heightened energy needs during winter in Bayburt by considering the region's climatic and demographic conditions. The prediction models derived from this study are expected to significantly contribute to local governments' energy planning and management processes. Data science and artificial intelligence-based prediction models have gained increasing importance in recent years across various applications. These models enable the effective modelling of nonlinear and complex relationships, yielding successful results,

particularly in dynamic and multivariate systems such as energy management. Accordingly, an AI-based model for predicting natural gas consumption is anticipated to contribute to energy planning and management processes significantly. These contributions will support the efficient use of resources and facilitate the achievement of sustainable development goals. A systematic review of previous studies reveals that efforts to predict natural gas consumption can be categorized into two main approaches: statistical methods and AI-based models. While statistical methods excel in predictions based on strong correlations, their limited capacity to model nonlinear relationships renders them inadequate for complex systems.

In contrast, AI-based methods effectively model nonlinear and multivariate relationships, offering significant advantages, especially when working with large datasets. Table 1 systematically presents academic studies on natural gas consumption prediction and the methods employed. These studies represent both statistical models and AI-based approaches. Notably, methods such as Support Vector Regression (SVR), Artificial Neural Networks (ANN), and Long Short-Term Memory (LSTM) have emerged as prominent AI techniques in natural gas consumption prediction in recent years (Liu et al., 2021). Integrating AI-based models into the energy sector aims to improve energy management processes and energy security, contributing to economic and environmental sustainability. In this context, an AI-based natural gas forecasting model explicitly developed for Bayburt province can serve as an effective tool for understanding and managing local energy demand dynamics. Using data science and AI-based prediction models in energy management is crucial to achieving sustainable development goals by enabling more accurate demand forecasting and efficient resource utilization. Studies on natural gas consumption prediction hold a significant place in the literature, providing valuable insights into developing new methods and improving existing models. By leveraging machine learning techniques, this study is expected to not only optimize existing systems but also foster the development of innovative energy management strategies. It contributes to Turkey's energy security objectives and supports the broader global transition toward sustainable energy systems.

**Table 1.** Review of Academic Studies and Methodologies on Natural Gas Consumption Prediction

Study Topic	Method/Scope	Source
Forecasting Models for Industrial Natural Gas Consumption	Statistical modelling, trend analyses	(Sánchez-Úbeda & Berzosa, 2007)
Long-Term Data Usage for Short-Term Forecasting	Time series, machine learning methods	(Svoboda et al., 2021)
Estimation of the Difference Between Natural Gas Production and Consumption in the USA	Wavelet transformation, LSTM	(Liu C. et al., 2021)
Analysis of Univariate Forecasting Methods for Industrial Natural Gas Consumption	ARIMA, ETS, Neural Network	(Naim & Mahara, 2018)
History and Future Challenges in Natural Gas Consumption Forecasting	Artificial neural networks, SVR	(Liu J. et al., 2021)
Statistical Methods for Forecasting Natural Gas Consumption	Statistical models, nonlinear regression	(Vondráček et al., 2008)
White-Box Modeling for Daily Natural Gas Consumption Forecasting	PCA, k-means with white-box modelling	(Wei et al., 2021)
Hybrid Model Application for Daily Natural Gas Consumption Forecasting	LSTM, improved SSA	(Wei et al., 2019)
Forecasting Natural Gas Consumption with Ensemble Learning Methods	Deep learning, ARIMA-based ensemble models	(Wang et al., 2024)
Hybrid Model for Annual Natural Gas Consumption Forecasting	Support vector machines, AFSA	(Gao & Shao, 2021)
Artificial Neural Network Combination Models for Natural Gas Consumption Forecasting	Artificial neural networks, modular systems	(Khotanzad et al., 2000)
Bayesian Modeling for Forecasting Natural Gas Consumption in China	Bayesian modeling	(Zhang & Yang, 2015)

Evaluating the applications of studies on natural gas consumption forecasting offers valuable insights into the methods and trends shaping this critical field. Below, summaries of various studies in the literature are presented. Forecasting natural gas consumption is crucial for ensuring energy security, optimizing supply chains, and enabling effective resource management. In this context, statistical models and AI-based approaches offer complementary solutions (Teke, 2022). While statistical models excel in trend analyses, AI methods demonstrate superior performance in capturing nonlinear and multivariate relationships. The literature highlights the effectiveness of these methods in addressing both short-term operational needs and long-term planning objectives, contributing significantly to advancements in energy efficiency and sustainability. A wide range of research emphasizing the practical applications and comparative

advantages of various modelling approaches underscores the importance of these methods in energy policy and decision-making processes.

Forecasting natural gas consumption is pivotal for energy management, resource planning, and achieving sustainability goals. The literature encompasses a broad methodological spectrum, including statistical models and AI-based approaches (Efe & Efe, 2023), applied and evaluated for natural gas consumption forecasting. These studies propose various methods to enhance forecast accuracy, analyze diverse data types, and broaden the applicability of models. Sánchez-Úbeda and Berzosa (2007) developed a model for forecasting industrial natural gas consumption. The model aimed to improve forecast accuracy by analyzing time series' trend, seasonal, and daily variation components. Its flexible structure demonstrated applicability to extensive datasets and provided high computational efficiency. Another study by Svoboda et al. (2021) focused on using long-term data for short-term forecasts. By employing time series and machine learning algorithms, the study presented a dataset that improved forecast accuracy and was valuable for comparative model analysis. Hybrid models have been proposed to address seasonal and complex variables in natural gas consumption. Liu C. et al. (2021) combined Wavelet Transformation (WT), Sparse Autoencoder (SAE), and Long Short-Term Memory (LSTM) methods to estimate the difference between natural gas production and consumption in the USA. This model effectively captured nonlinear relationships and enhanced forecast accuracy. Similarly, Wei et al. (2019) developed a hybrid model based on Singular Spectrum Analysis (SSA) and LSTM to forecast daily natural gas consumption. By reducing noise in time series data, this model improved prediction performance. Traditional methods have also proven effective in forecasting natural gas consumption. Vondráček et al. (2008) conducted a study using statistical models to forecast natural gas consumption for individual customers. Nonlinear regression methods were employed and tested on a large customer dataset. Similarly, Naim and Mahara (2018) compared univariate methods such as ARIMA, Holt-Winters, and Simple Exponential Smoothing, demonstrating that the ARIMA model achieved high accuracy. AI-based methods have gained prominence for effectively modelling nonlinear and multivariate relationships. Liu J. et al. (2021) reviewed the historical development of AI-based methods in natural gas consumption forecasting. They identified Artificial Neural Networks (ANN) as the most successful method for short-term predictions. Wang et al. (2024) developed an ensemble learning-based forecasting model by integrating ARIMA, HFCM, and LSTM models. This model contributed significantly to energy management with its resilience to noise and high accuracy. Hybrid methods have been suggested for annual natural gas consumption forecasting.

Gao and Shao (2021) developed a model based on Support Vector Machines (SVM) and the Improved Artificial Fish Swarm Algorithm (IAFSA). This model offered low error rates, supporting decision-making processes in energy planning. Khotanzad et al. (2000) aimed to improve forecast accuracy using artificial neural network combinations. This approach demonstrated strong performance through the integration of different neural network models. Finally, a study by Zhang and Yang (2015) utilized the Bayesian Modeling Approach (BMA) to forecast natural gas consumption in China. The study achieved higher accuracy than traditional models and provided a comprehensive analysis by integrating economic factors into the forecasting process. These studies illustrate how statistical and AI-based approaches have been applied and advanced in natural gas consumption forecasting. While highlighting the advantages and limitations of different methods, the literature offers innovative solutions to enhance forecast accuracy and contribute to energy management objectives.

Forecasting natural gas consumption in small-scale regions with dynamic consumption models, such as Bayburt, is crucial for the efficient use of energy resources and sustainable planning. However, the existing literature includes limited studies specifically addressing small provinces. Comprehensive analyses of the application of machine learning methods to such datasets are scarce. This study aims to offer an innovation by employing Support Vector Regression (SVR) and Gaussian Process Regression (GPR) methods to forecast natural gas consumption in Bayburt. These models have been optimized using Grid Search and Random Search techniques, and their forecasting performances have been compared in detail.

The applicability of machine learning-based prediction models to environmental and economic problems, especially in regions with limited datasets like Bayburt, has not been adequately explored in the literature. In this context, a comparative analysis of metaheuristic optimization algorithms, such as Grid Search and Random Search, has been conducted to optimize the performance of SVR and GPR methods for small datasets.

The research addresses gaps in the literature regarding natural gas consumption forecasting in small cities. The results highlight the effectiveness of optimized SVR and GPR models in capturing complex and nonlinear consumption relationships. Beyond a theoretical contribution, the study is a practical guide for energy management and planning processes, providing an innovative perspective on energy policy and resource allocation decisions. The primary objective is to develop a machine learning-based forecasting model capable of predicting natural gas consumption in Bayburt. By enabling deep data analysis and precise modelling, machine learning methods enhance the accuracy

of energy demand predictions. In particular, applying these algorithms to understand the dynamic and complex nature of natural gas demand offers significant energy planning and management benefits. Accurate forecasting in Bayburt will help optimize local energy management strategies and support the development of sustainable energy policies. This research distinguishes itself from previous studies in two key aspects. First, it is the first to employ optimized Support Vector Regression (SVR) and Gaussian Process Regression (GPR) models for natural gas demand forecasting. Second, the hyperparameters, typically determined by model developers, are optimized using Grid Search and Random Search algorithms, further improving the predictive performance of the models.

The study comprises four main sections. The second section details the methods and materials used in the research, including explanations of the SVR and GPR methods employed for forecasting natural gas consumption in Bayburt. It also discusses the Grid Search and Random Search techniques for optimizing these models and the metrics applied to evaluate model performance. The third section analytically examines the results of SVR, GPR, and their optimized versions, providing a comparative evaluation of these models' forecasting performances. The fourth and final section discusses the implications of the findings about the study's objectives, emphasizing the potential contributions of these models to energy management and planning processes, particularly in regions like Bayburt with small-scale datasets.

## **2. Material and Methods**

### **2.1. Data Collection Process**

This study analysed data related to energy demand and demographic variables in Bayburt province to forecast natural gas consumption. One of the input variables, average monthly temperature, was utilized as a critical indicator to evaluate the impact of seasonal variations—mainly heating needs during colder months—on natural gas consumption. Population size emerges as another significant input variable, providing insights into the influence of demographic structure on energy demand. The output variable, natural gas consumption volume, represents monthly natural gas usage in Bayburt and is a fundamental indicator in energy management and resource planning processes. The relationship between natural gas consumption and heating needs is closely tied to variations in air temperatures. During the winter, when low temperatures persist for extended periods, increased heating needs lead to a noticeable rise in natural gas consumption. Conversely, during the summer months, consumption drops to minimal levels as temperatures rise. In this context, air temperature is a key

variable for understanding and predicting consumption behaviours. Figure 2 illustrates the monthly average temperature trends in Bayburt between 2020 and 2024.

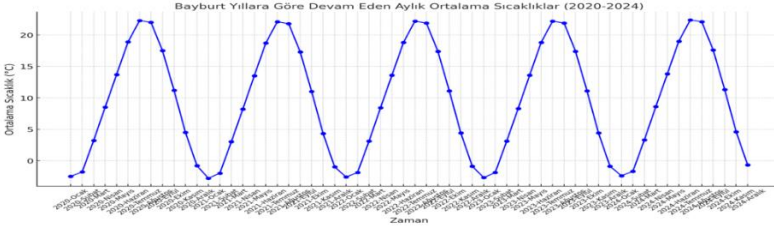


**Figure 2.** Monthly Average Temperature Trends in Bayburt (2020–2024)

The graph reflects the monthly temperature trends in Bayburt, highlighting the seasonal impacts on energy demand. It is observed that temperatures generally fall below freezing during the winter months, while in summer, average temperatures hover around 22°C. These temperature trends provide key insights into the seasonal fluctuations in natural gas consumption. The dataset used in this study spans the years 2020–2024 and consists of monthly collected data. This dataset enables the inclusion of seasonal dynamics and temporal patterns in the analysis, and it has been split for model training and testing to assess performance and generalizability. The dataset used in this study was constructed using data from multiple reliable sources to ensure accuracy and comprehensiveness. Monthly natural gas consumption data for Bayburt was obtained from the regional natural gas distribution company, AKSA Natural Gas Distribution Co. Population data was sourced from the Turkish Statistical Institute (TÜİK), providing demographic information essential for understanding energy demand dynamics.

Additionally, the Turkish State Meteorological Service's official website retrieved average monthly temperature data, representing the climatic conditions that significantly influence natural gas consumption. The sources of these datasets are summarized in Table 2, ensuring transparency and traceability in the data collection process. This multi-source approach enhances the robustness of the analysis and provides a solid foundation for modelling natural gas demand in Bayburt. The relationships between input variables -such as air temperatures and population size-and the output variable, which represents natural gas consumption, were analyzed using machine learning techniques. The study aims to develop a model capable of accurately predicting natural gas consumption in Bayburt and contributing to energy planning and sustainable management strategies. This comprehensive approach enables a deeper understanding of natural gas consumption dynamics and facilitates the more effective shaping of

energy management policies. The impact of climatic variables like air temperatures on energy demand has enhanced the model's predictive capacity. The study holds the potential to offer innovative solutions for energy management in small-scale local administrations like Bayburt.

Table 2 details the abbreviations, units, and data sources for the variables used in this study. These inputs have been integrated into the model to comprehensively analyse the energy and demographic factors influencing natural gas consumption in Bayburt. The variables included in the study serve as a critical knowledge base for the development of energy planning and sustainable management strategies.

**Table 2.** Variable Abbreviations, Units, and Sources

Variable	Abbr.	Unit	Source
Air Temperature (°C)	Temp	Degrees Celsius	(MeteoService, 2024)
Population	Pop	People	(TURKSTAT, 2024)
Natural Gas Consumption	GasCons	Cubic Meters	(Aksa, 2024)

These variables play a crucial role in achieving energy management and environmental sustainability goals in alignment with the Sustainable Development Goals (SDGs). Average monthly temperature, a critical variable for understanding seasonal changes in natural gas consumption, contributes to developing energy efficiency strategies under SDG 7 (Affordable and Clean Energy) and SDG 13 (Climate Action). Population size provides an opportunity to analyze the impact of demographic structure on energy demand, shedding light on urban energy planning and infrastructure development policies in connection with SDG 11 (Sustainable Cities and Communities) and SDG 9 (Industry, Innovation, and Infrastructure). The output variable, natural gas consumption, facilitates the design of strategies for more efficient use of energy resources and reducing carbon emissions in line with SDG 12 (Responsible Consumption and Production). Analyzing these variables enables a deeper understanding of factors influencing local energy demand and contributes to developing more sustainable and environmentally friendly energy management systems. Table 3 presents detailed descriptive statistics and key statistical measures for the input and output variables used in the study. Among the input variables, average monthly temperature provides significant insights with minimum, maximum, mean, and standard deviation values, particularly regarding fluctuations in energy demand during Bayburt's cold winter months. This variable has been considered a critical indicator for modelling the impact of seasonal changes on energy demand. The

other input variable, population size, reflects demographic changes during the analysis period and helps to understand long-term trends and growth dynamics in energy demand. The mean, minimum, and maximum values for population size in Table 3 provide important context for assessing the level of urban development in Bayburt and its impact on energy consumption. The output variable, natural gas consumption, plays a key role in understanding the energy demand structure in Bayburt, with monthly minimum, maximum, and mean values presented. Natural gas consumption variation has been associated with seasonal differences, population growth, and infrastructure development. Additionally, measures such as the standard deviation highlight the fluctuations in energy demand and the variation that must be considered during the modelling process.

The key statistical measures presented in Table 3 are essential for enhancing the model's reliability and better understanding the inputs and outputs' role in the analysis process. Descriptive statistics provide a foundation for a more detailed understanding of the dynamics influencing natural gas consumption, guiding the structuring of the model and the interpretation of results. This information contributes to developing effective strategies for sustainable energy management and long-term energy planning.

**Table 3.** Descriptive Statistics

Statistical Measures	Air Temperature (°C)	Population	Natural Gas Consumption (m <sup>3</sup> )
<b>Mean</b>	9.61666	84310.0	274842.47
<b>Std</b>	8.9316	1542.40	3048294.36
<b>Min</b>	-2.8	81910.0	274842.47
<b>%25</b>	2.05	83658.25	1361361.24
<b>%50</b>	9.75	84641.5	2754184.07
<b>%75</b>	7.8	85293.25	6874089.05
<b>Max</b>	22.3	86047.0	9468265.37

The air temperature data in the dataset has an average of 9.62°C, with values ranging from -2.8°C to 22.3°C. These values reflect the pronounced seasonal and climatic variations in Bayburt throughout the year. The standard deviation, calculated as 8.93°C, indicates a wide dispersion in temperature values. This variation is primarily associated with low temperatures in winter and higher temperatures in the summer. The dynamic nature of temperature data significantly impacts energy demand and natural gas consumption. For instance, it can be stated that low temperatures increase heating needs, leading to noticeable rises in natural gas consumption levels. Modelling temperature variations plays a critical role in forecasting energy demand.

The population data for Bayburt during the analyzed period ranges between 81,910 and 86,047 people, with an average population of 84,310 people. The standard deviation, calculated as just 1,542 people, reveals no significant fluctuations in the population structure of Bayburt. This stability indicates that population data can be considered reliable for forecasting energy demand. However, long-term factors such as urbanization, migration trends, and population growth should also be considered for their potential impact on energy demand. The stability in Bayburt's population allows for the development of more predictable strategies in energy management and infrastructure planning.

The natural gas consumption volumes in the dataset exhibit a wide range, varying from 274,842.47 cubic meters to 9,468,265.37 cubic meters. The average natural gas consumption is calculated as 4,182,053.42 cubic meters, providing a general idea of Bayburt's total energy demand. However, the standard deviation, recorded at 3,048,294.36 cubic meters, is notably high, indicating significant seasonal and periodic fluctuations in energy consumption. These fluctuations may arise from increased heating needs during winter months, changes in population, climatic conditions, or industrial activities. While energy consumption intensifies during winter due to increased heating demand, lower consumption patterns are observed in summer. These descriptive statistics contribute to understanding energy demand dynamics, specifically in Bayburt. The relationship between air temperatures, population size, and natural gas consumption is critical for energy management and resource planning. Considering seasonal changes and population movements allows for more accurate predictions of natural gas consumption. Such comprehensive analyses play a guiding role in developing sustainable energy policies and efficiently utilising resources.

The dataset was divided into training and testing sets using an 80-20 split to ensure sufficient data for model training and evaluation. To enhance the reliability of the results, a 3-fold cross-validation technique was applied, which systematically partitions the data to minimize overfitting and improve model generalization. The balance of the dataset was also assessed to ensure that the distribution of values across variables did not introduce bias into the model. Furthermore, a min-max normalization process was performed, scaling the data within a specified range to standardize the features and improve the performance of the machine learning algorithms. These steps collectively ensured a robust and unbiased modelling process, contributing to the accuracy and reliability of the results.

## **2.2. Support Vector Regression (SVR)**

Support Vector Regression (SVR) is based on the foundation of Support Vector Machines (SVM). SVR is suitable not only for classification problems but also for solving regression problems. While the primary goal of SVM is to find a hyperplane that separates data between two classes with the maximum margin, SVR extends this concept by finding a hyperplane that encompasses the data in a regression problem while minimizing deviations. SVR attempts to keep prediction errors within a specific range (epsilon-tube) and optimizes the hyperplane using a penalty function for errors outside this tube. To handle non-linear data, SVR employs kernel functions, which enable the model to achieve successful results even with datasets containing non-linear relationships. A linear hyperplane can be established by transforming data into a higher-dimensional space through kernel functions. Studies have shown that SVR provides a robust regression method, particularly for non-linear and noisy datasets (Özden & Güteryüz, 2021).

## **2.3. Gaussian Process Regression (GPR)**

Gaussian Process Regression (GPR) is a probabilistic regression model that models the distribution of the predicted data. Like SVR, GPR relies on kernel functions to measure the similarity between data points, offering a flexible approach to solving non-linear problems. GPR models the relationship between data points using Gaussian processes, allowing the data to be represented within a certain uncertainty range. GPR adopts a probabilistic approach to predict the relationship between inputs and outputs, assuming that the inputs are derived from a Gaussian distribution. A significant advantage of GPR is its ability to estimate uncertainties, making it particularly useful for researchers aiming to calculate confidence intervals for predicted values (Güteryüz & Özden, 2023a). Additionally, Gaussian processes are effective in dealing with noise in the dataset.

## **2.4. Hyperparameter Optimization in Hybrid Models: Grid Search and Random Search Methods**

Hyperparameter optimization is a fundamental process for improving the performance of machine learning models and ensuring better adaptability to datasets. In this context, Grid Search and Random Search are two widely used methods for optimizing the hyperparameters of machine learning models. Grid Search is an optimization approach that systematically tests all possible combinations of hyperparameters within a defined range. This method aims to identify the best-performing hyperparameters by evaluating every combination.

The main advantage of Grid Search is its comprehensive coverage, increasing the likelihood of reaching the global optimum. However, the computational cost of Grid Search can be high, especially for large hyperparameter spaces, making it time-consuming. For this reason, Grid Search is typically preferred for smaller, constrained hyperparameter ranges.

On the other hand, Random Search tests a randomly selected subset of hyperparameter combinations instead of the entire hyperparameter space. This approach significantly reduces computational costs and achieves faster results than Grid Search, particularly in large hyperparameter spaces. The primary advantage of Random Search is its ability to discover influential regions of the hyperparameter space more efficiently when only a portion of the space determines model performance. However, randomness introduces the risk of overlooking some essential combinations (Banerjee, 2019; Liashchynskiy & Liashchynskiy, 2019).

Both methods are widely applied in models like Support Vector Regression (SVR) and Gaussian Process Regression (GPR). Hyperparameter optimization is critical in enhancing these models' predictive accuracy and generalization capacity, which are frequently preferred for modeling non-linear and complex systems.

#### 2.4.1 GS-SVR and GS-GPR

Hyperparameter optimization is a critical process for improving machine learning model performance. Grid Search (GS) provides a systematic approach for hyperparameter optimization and is commonly applied to models like SVR and GPR. By testing all combinations within a defined range, GS aims to select the hyperparameters that deliver the best performance.

SVR, known for its ability to model non-linear relationships, uses kernel functions to transform data into higher-dimensional spaces, effectively capturing non-linear patterns. Key hyperparameters in SVR include (Smola & Schölkopf, 2004):

- **Penalty parameter (C):** Controls the model's tolerance for errors.
- **Epsilon ( $\epsilon$ ):** Defines a threshold for prediction accuracy.
- **Kernel type:** Determines the structure of relationships between data points.

In contrast, GPR uses a probabilistic approach and estimates both prediction accuracy and uncertainties. Key hyperparameters in GPR include:

- **Noise level:** Controls the model's sensitivity to data noise.
- **Length scale:** Determines the model's ability to learn finer details in the data.

GS-optimized SVR and GPR systematically evaluate hyperparameter combinations, searching for the global optimum. While GS-SVR delivers rapid results for large datasets, GS-GPR excels in small datasets, mainly due to its ability to estimate uncertainties. Both models are effective tools for modelling complex systems like energy demand forecasting.

### **2.4.2 RS-SVR and RS-GPR**

Random Search (RS) is an efficient method to reduce computational costs during hyperparameter optimization. Instead of evaluating the entire hyperparameter space, RS tests a randomly selected subset of combinations. This method provides faster results than Grid Search while maintaining lower computational costs. RS-SVR optimizes the Support Vector Regression model by randomly selecting hyperparameter combinations such as  $C$ ,  $\epsilon$ , and kernel parameters. Optimizing these parameters enhances the accuracy and generalization capacity of the SVR model. Particularly in large datasets and non-linear relationship modelling, RS-SVR stands out as a fast and effective method. RS-GPR optimizes the hyperparameters of the Gaussian Process Regression model, including kernel functions, noise level, and length scale, through random combinations. Compared to Grid Search, RS-GPR achieves results with lower computational costs. RS-GPR performs exceptionally well for small datasets and provides an advantage in estimating uncertainties, making it ideal for complex systems like energy demand forecasting.

RS-SVR and RS-GPR models apply to dynamic and complex systems such as energy demand forecasting and environmental modelling. The flexibility of Random Search enables it to deliver effective solutions across wide hyperparameter ranges while reducing computational costs and achieving accurate, generalizable predictions. Grid Search (GS) and Random Search (RS)-optimized SVR and GPR models enhance machine learning by improving accuracy and generalization capacity. These models offer reliable predictions in dynamic systems such as energy demand, contributing to the development of sustainable management strategies.

## **3. Findings and Performance Comparisons**

MAE (Mean Absolute Error), RMSE (Root Mean Square Error), and  $R^2$  (Coefficient of Determination) are statistical measures frequently used to evaluate the performance of a model (Chai & Draxler, 2014). MAE expresses how much, on average, the model's predictions deviate from the actual values and measures the accuracy of each prediction. RMSE, by squaring the errors, gives more weight to large deviations and makes the impact of significant errors more

prominent. This measure provides a critical evaluation, especially when considerable errors are substantial.  $R^2$ , on the other hand, measures the variance in the data that the model can explain; as its value approaches 1, it indicates a high explanatory power of the model, while values closer to 0 show inadequacy (Gülyüz&Özden, 2023b; Teke et al., 2023; Akkaş et al., 2018; Şen et al., 2023). When these three metrics are used together, they comprehensively evaluate the model’s accuracy and reliability. This study calculated the MAE, RMSE, and  $R^2$  values for all developed models and analyzed them comparatively. Table 4 presents the performance results of the developed models for both the training and testing phases, evaluated using three key statistical metrics: RMSE (Root Mean Square Error),  $R^2$  (Coefficient of Determination), and MAE (Mean Absolute Error).

**Table 4.** Comparative Performance Analysis of Developed Models

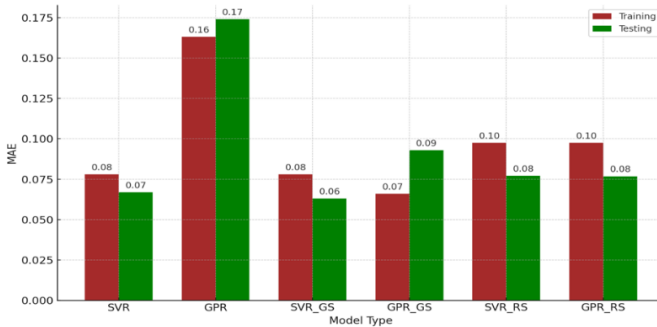
Model Type		RMSE	$R^2$	MAE
Training Phase	SVR	0,081	0,85	0,078
	GPR	0,126	0,54	0,163
	SVR_GS	0,083	0,84	0,078
	GPR_GS	0,080	0,90	0,066
	SVR_RS	0,115	0,73	0,098
	GPR_RS	0,115	0,73	0,098
Testing Phase	SVR	0,098	0,83	0,067
	GPR	0,138	0,49	0,174
	SVR_GS	0,096	0,86	0,063
	GPR_GS	0,114	0,78	0,093
	SVR_RS	0,113	0,80	0,077
	GPR_RS	0,112	0,81	0,077

In this study, which aimed to predict natural gas consumption, various hyperparameter optimization methods, such as Grid Search and Random Search, were applied using Support Vector Regression (SVR) and Gaussian Process Regression (GPR) algorithms. The results presented in the table provide a comparative analysis of the performance of different machine learning models. Support Vector Regression (SVR), Gaussian Process Regression (GPR), and their optimized versions with Grid Search (GS) and Random Search (RS) were evaluated during both the training and testing phases. The performance metrics

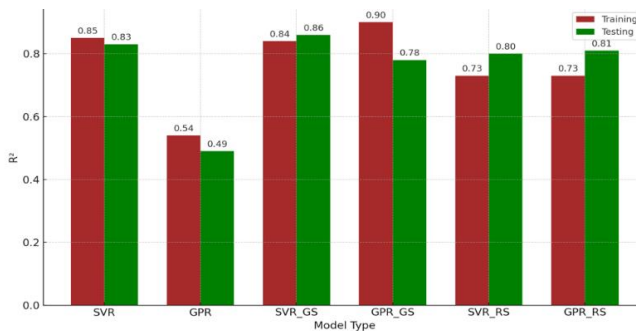
used include Root Mean Square Error (RMSE),  $R^2$  (Coefficient of Determination), and Mean Absolute Error (MAE). This evaluation is a significant guide for understanding the accuracy and generalization capacity of the models.

During the training phase, the SVR model demonstrated strong performance with low RMSE and MAE values and a high  $R^2$  score (85%). SVR stood out with its ability to effectively model non-linear relationships. In contrast, the GPR model lagged behind SVR, with a relatively low  $R^2$  value (54%) and higher error rates (RMSE: 0.1263, MAE: 0.1631). However, among the models optimized with Grid Search, GPR\_GS provided the best results. Optimizing GPR with Grid Search significantly improved its performance, increasing the  $R^2$  value to 90% during the training phase.

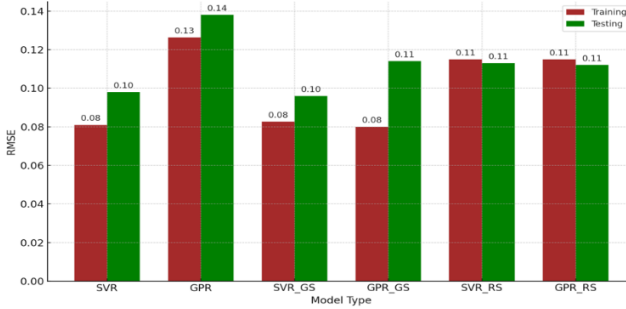
In the models optimized with Random Search, SVR\_RS and GPR\_RS exhibited lower performance than Grid Search. This outcome indicates that Grid Search provides a more comprehensive optimization, enhancing model accuracy. The comparison of RMSE,  $R^2$ , and MAE values during the testing phases is visualized in Figure 3. The figure demonstrates the superior performance of the Grid Search-optimized SVR (SVR\_GS) model.



(a)



(b)



(c)

**Figure 3.** Performance Comparison of Machine Learning Models Across Metrics (a: MAE, b:  $R^2$ , c: RMSE )

In the testing phase, the SVR model again demonstrated effective performance, proving its strong generalization capacity with an  $R^2$  value of 83% and low error rates (RMSE: 0.098, MAE: 0.0669). The GPR model, similar to its performance in the training phase, showed lower performance in the testing phase, with an  $R^2$  value of 49% and higher error rates (RMSE: 0.138, MAE: 0.174), indicating limited generalization capacity. Among the models optimized with Grid Search, SVR\_GS achieved the highest accuracy during the testing phase with an  $R^2$  value of 86% and significantly reduced error rates (RMSE: 0.096, MAE: 0.063). While the GPR\_GS model provided better results during the testing phase ( $R^2$ : 78%, RMSE: 0.114), it still lagged behind the SVR-based models. For models optimized with Random Search, RS optimization improved the performance of both SVR and GPR models during the testing phase, but it was not as effective as Grid Search.

Overall, SVR models outperformed GPR models in training and testing phases, providing higher accuracy. SVR's ability to effectively model non-linear relationships and maintain low error rates highlights its superiority. Grid Search optimization led to significant improvements, particularly for GPR models, whereas its impact on SVR models was more limited. Although the Random Search method offered faster and more cost-effective optimization, it demonstrated lower performance than Grid Search. These findings indicate that SVR models, especially those supported with Grid Search optimization, should be preferred in dynamic processes such as energy demand forecasting. However, GPR models optimized with Grid Search could provide a suitable approach for applications requiring uncertainty analysis. Both models serve as practical tools for energy management and resource planning processes.

The findings of this study demonstrate the accuracy and effectiveness of the machine learning models used to forecast natural gas consumption for Bayburt province. In particular, improving SVR and GPR models with optimization methods such as Grid Search and Random Search has enabled more accurate

energy demand predictions. The results provide important insights into improving energy management and ensuring the more efficient use of resources. These findings serve as a strategic guide for managing energy demand at the local level and achieving sustainable development goals (SDGs). Specifically, the predictability of energy consumption contributes to SDG 7 (Affordable and Clean Energy) and SDG 13 (Climate Action). Accurate forecasting models support the prevention of energy waste, reduce carbon emissions, and play a critical role in facilitating the transition to renewable energy sources. In this context, the findings have the potential to guide the shaping of local energy policies from a sustainability perspective and contribute to the global energy transition.

#### **4. Conclusion and Recommendations**

This study highlights the importance of accurately forecasting natural gas consumption for Bayburt province to ensure adequate energy management at the local level and contribute to broader goals such as sustainable development and combating climate change. Advanced machine learning models such as Support Vector Regression (SVR) and Gaussian Process Regression (GPR), along with optimization techniques like Grid Search and Random Search, demonstrate the potential to improve prediction accuracy in dynamic and complex systems. Conducted in a small-scale city like Bayburt, this study plays a pioneering role in developing regional energy strategies. The results indicate that Grid Search-optimized SVR models outperformed other models in training and testing phases, proving to be a suitable method for high-accuracy forecasts in regions with limited data resources. However, in scenarios requiring uncertainty analysis, GPR models emerge as valuable tools for risk analysis and planning under uncertain conditions.

Bayburt's small size, along with its unique economic, social, and climatic structure compared to larger metropolitan areas, further underscores the importance of this study. Understanding energy consumption dynamics in small-scale settlements is crucial for the efficient use of limited resources and the development of regional strategies for energy management. Additionally, in regions with low population density, such as Bayburt, the effects of seasonal temperature changes on natural gas consumption are more pronounced. Therefore, this study's models and analytical methods provide a successful example of energy demand forecasting in small-scale regions like Bayburt.

The findings of this study are directly aligned with the Sustainable Development Goals (SDGs). By facilitating energy management and the efficient use of resources, the study supports SDG 7 (Affordable and Clean Energy). Accurate predictions of natural gas demand minimize energy waste, promote optimal resource utilization, and contribute to achieving SDG 12 (Responsible

Consumption and Production). Furthermore, improving the accuracy of energy forecasts helps align energy policies with SDG 13 (Climate Action) by reducing greenhouse gas emissions. Integrating climatic variables, particularly temperature, into forecasting models highlights the importance of considering climate variability in energy planning processes. The findings of this study are particularly significant for regions like Bayburt, where energy demand is heavily influenced by seasonal temperature changes. Bayburt's small-scale structure enhances the direct applicability of these findings. By incorporating climatic and demographic factors into machine learning models, the study allows for a better understanding of the relationship between energy consumption and environmental dynamics. This approach contributes to the development of local energy strategies for regions like Bayburt and supports the global transition toward more sustainable energy systems.

In conclusion, this study demonstrates the applicability of data-driven approaches for improving energy efficiency and combating climate change in small-scale cities like Bayburt. The presented methodologies and findings provide a foundation for future studies to optimise energy systems, reduce emissions, and achieve sustainable development goals. The findings of this study not only provide a framework for forecasting energy demand in Bayburt and offer critical insights for global sustainable energy management strategies. Accurate prediction of natural gas consumption enhances energy efficiency, prevents resource wastage, and optimizes fossil fuel consumption, thereby reducing carbon emissions. This is particularly critical for achieving SDG 7 (Affordable and Clean Energy) and SDG 13 (Climate Action). The machine learning-based models employed in this study offer a universally applicable methodology for predicting energy demand in different geographies. Accurate forecasting models also facilitate the integration of renewable energy sources into power grids, ensuring energy security and enabling the design of sustainable energy systems.

The methods developed for small-scale regions like Bayburt present a highly applicable model for energy management in less-developed areas. Accurate forecasting of energy demand in such regions is essential for ensuring energy equity and supporting local economic and environmental sustainability. Additionally, this study contributes to developing policies that enhance energy accessibility, reduce global carbon emissions, and strengthen the resilience of energy networks. As a result, the findings provide a valuable guide for designing and managing global energy systems more sustainably.

Future research could integrate renewable energy sources (e.g., solar, wind, and biomass) and hybrid energy systems into machine learning-based prediction models (Liu et al., 2021). In this context, incorporating renewable energy

production data (e.g., solar radiation and wind speeds) into energy demand forecasting processes could enhance model accuracy while providing a more sustainable framework for resource utilization. Modelling the interactions between renewable sources and conventional energy systems within hybrid energy systems could contribute significantly to managing seasonal and regional energy imbalances. Therefore, future studies can comprehensively examine the intersection of machine learning and energy management, contributing to sustainable development goals at both local and global scales.

### **Acknowledgements**

We gratefully acknowledge the support provided by the TÜBİTAK 2209-A University Students Research Projects Support Program under application number 1919B012206511.

## References

- Akkaş, N., Onar, V., Teke, Ç., İlhan, E., & Aslanlar, S. (2018). Welding Time Effect on Nugget Sizes in Resistance Spot Welding of SPA-C Steel Sheets Used in Railway Vehicles. *Acta Physica Polonica A*, 134(1), 235–237.
- AKSA. (2024). Aksa Doğal Gaz Dağıtım A.Ş., Bayburt. Unpublished company data.
- Banerjee, A. (2019). Intuitive Hyperparameter Optimization : Grid Search, Random Search and Bayesian Search. <https://towardsdatascience.com/intuitive-hyperparameter-optimization-grid-search-random-search-and-bayesian-search-2102dbfaf5b>
- Chai, T., & Draxler, R. R. (2014). Root mean square error (RMSE) or mean absolute error (MAE)? – Arguments against avoiding RMSE in the literature. *Geoscientific Model Development*, 7(3), 1247–1250. <https://doi.org/10.5194/gmd-7-1247-2014>
- Efe, B., & Efe, Ö. F. (2023). The fine-Kinney method is based on fuzzy logic for the natural gas pipeline project risk assessment. *Soft Computing*, 27, 16465–16482. <https://doi.org/10.1007/s00500-023-09108-6>
- Gao, F., & Shao, X. (2021). Forecasting annual natural gas consumption via the application of a novel hybrid model. *Environmental Science and Pollution Research*, 28(17), 21411–21424. <https://doi.org/10.1007/s11356-020-12275-w>
- Güleryüz, D., & Özden, E. (2023a). Kamu sağlık harcamalarının tahmini: Destek vektör makineleri ve Gauss süreç regresyonu. In Ş. Karabulut (Ed.), *İktisat uygulamalarının ampirik analizi* (pp. 27-42). Yaz Yayınları. ISBN: 978-625-6524-90-3.
- Güleryüz, D., & Özden, E. (2023b). Tarımsal veriler ışığında sürdürülebilir su yönetimi: Makine öğrenmesi tahmin modelleri. In İ. Cengizler & S. Duman (Eds.), 3. *Tarım, Orman ve Su Bilimlerinde İleri ve Çağdaş Çalışmalar* (pp. 135-153). Duvar Yayınları. ISBN: 978-625-6585-92-8.
- IEA (International Energy Agency). (2021). *World energy outlook 2021*. Retrieved from <https://www.iea.org/reports/world-energy-outlook-2021>
- Khotanzad, A., Elragal, H. M., & Lu, T.-L. (2000). Combination of artificial neural-network forecasters for prediction of natural gas consumption. *IEEE Transactions on Neural Networks*, 11 2, 464–473. <https://api.semanticscholar.org/CorpusID:12216677>
- Liashchynskiy, P., & Liashchynskiy, P. (2019). Grid Search, Random Search, Genetic Algorithm: A Big Comparison for NAS. 2017, 1–11. <http://arxiv.org/abs/1912.06059>

- Liu, C., Wu, W.-Z., Xie, W., Zhang, T., & Zhang, J. (2021). Forecasting natural gas consumption of China by using a novel fractional grey model with time power term. *Energy Reports*, 7, 788–797. <https://doi.org/https://doi.org/10.1016/j.egy.2021.01.082>
- Liu, J., Wang, S., Wei, N., Chen, X., Xie, H., & Wang, J. (2021). Natural gas consumption forecasting: A discussion on forecasting history and future challenges. *Journal of Natural Gas Science and Engineering*, 90, 103930. <https://api.semanticscholar.org/CorpusID:233701713>
- MeteoService (2024) Turkish State Meteorological Service. Accessed 1 Oct 2024 <https://www.mgm.gov.tr/>
- Naim, I., & Mahara, T. (2018). Comparative Analysis of Univariate Forecasting Techniques for Industrial Natural Gas Consumption. *International Journal of Image, Graphics and Signal Processing*, 10, 33–44. <https://api.semanticscholar.org/CorpusID:55321785>
- Özden, E., & Guleryuz, D. (2022). Optimized Machine Learning Algorithms for Investigating the Relationship Between Economic Development and Human Capital. *Computational Economics*, 60(1), 347–373. <https://doi.org/10.1007/s10614-021-10194-7>
- Sánchez-Úbeda, E. Fco., & Berzosa, A. B. (2007). Modeling and forecasting industrial end-use natural gas consumption☆. *Energy Economics*, 29, 710–742. <https://api.semanticscholar.org/CorpusID:154624151>
- Smola, A. J., & Schölkopf, B. (2004). A tutorial on support vector regression. *Statistics and Computing*, 14(3), 199–222. <https://doi.org/10.1023/B:STCO.0000035301.49549.88>
- Stern, D. I. (2011). The role of energy in economic growth. *Annals of the New York Academy of Sciences*, 1219(1), 26–51. <https://doi.org/10.1111/j.1749-6632.2010.05921.x>
- Svoboda, R., Kotik, V., & Plato, J. (2021). Short-term natural gas consumption forecasting from long-term data collection. *Energy*, 218, 119430. <https://api.semanticscholar.org/CorpusID:229450910>
- Şen, H., Efe, Ö. F., & Efe, B. (2023). Estimation Of Occupational Accidents In Turkey Until 2030. *Natural Resources and Technology*, 17(1), 26–32.
- Teke, Ç. (2022). Yapay zeka. In M. Baş, İ. Erdoğan Tarakçı, & R. Aslan (Eds.), *Dijitalleşme* (pp. 147-157). Efe Akademi Yayınları. ISBN: 978-625-6995-74-1.
- Teke, Ç., Akkurt, I., Arslankaya, S., Ekmekci, I., & Gunoglu, K. (2023). Prediction of gamma ray spectrum for  $^{22}\text{Na}$  source by feed forward back propagation ANN model. In *Radiation Physics and Chemistry* (Vol. 202,

- p. 110558). Elsevier BV.  
<https://doi.org/10.1016/j.radphyschem.2022.110558>
- TURKSTAT (Turkish Statistical Institute). (2024). Population statistics. Retrieved from <https://www.turkstat.gov.tr/>
- UN (United Nations). (2015). Transforming our world: The 2030 agenda for sustainable development. Retrieved from <https://sustainabledevelopment.un.org>
- Vondráek, J., Pelikán, E., Konár, O., ermáková, J., Eben, K., Malý, M., & Brabec, M. (2008). A statistical model for the estimation of natural gas consumption. *Applied Energy*, 85, 362–370. <https://api.semanticscholar.org/CorpusID:108641690>
- Wang, Q., Luo, Z., & Li, P. (2024). Natural Gas Consumption Forecasting Based on Homoheterogeneous Stacking Ensemble Learning. *Sustainability*. <https://api.semanticscholar.org/CorpusID:273242423>
- Wei, N., Li, C., Peng, X., Li, Y., & Zeng, F. B. (2019). Daily natural gas consumption forecasting via the application of a novel hybrid model. *Applied Energy*. <https://api.semanticscholar.org/CorpusID:164739028>
- Wei, N., Yin, L., Li, C., Li, C., Chan, C. W., & Zeng, F. B. (2021). Forecasting the daily natural gas consumption with an accurate white-box model. *Energy*, 232, 121036. <https://api.semanticscholar.org/CorpusID:236410903>
- Wordbank. (2023). Data Bank. Retrieved from <https://databank.worldbank.org>
- Zhang, W., & Yang, J. (2015). Forecasting natural gas consumption in China by Bayesian Model Averaging. *Energy Reports*, 1, 216–220. <https://api.semanticscholar.org/CorpusID:109935539>

## Chapter 5

### The Role of Chaotic Maps in Metaheuristic Optimization Algorithms: A Study on AVOA

Osman ALTAY<sup>1</sup>  
Elif VAROL ALTAY<sup>2</sup>

---

<sup>1</sup> Assoc. Prof. Dr., Manisa Celal Bayar University, Hasan Ferdi Turgutlu Technology Faculty, Software Engineering, ORCID: 0000-0003-3989-2432, [osman.altay@cbu.edu.tr](mailto:osman.altay@cbu.edu.tr)

<sup>2</sup>Assoc. Prof. Dr., Manisa Celal Bayar University, Hasan Ferdi Turgutlu Technology Faculty, Software Engineering, ORCID: 0000-0001-8087-2754, [elif.altay@cbu.edu.tr](mailto:elif.altay@cbu.edu.tr)

# **The Role of Chaotic Maps in Metaheuristic Optimization Algorithms: A Study on AVOA**

## **Abstract**

This study comprehensively examines the integration of chaotic maps in order to improve the performance of the African Vulture Optimization Algorithm (AVOA), which stands out among nature-inspired metaheuristic algorithms. AVOA was developed by taking inspiration from energy-efficient flight techniques and hunting behaviors of African vultures and achieves successful results in global optimization problems. However, it has limitations such as being trapped in local minima and not being able to scan the search space comprehensively enough. In order to overcome these problems, it is proposed to integrate chaotic systems into AVOA as chaotic maps. The exploration phase of AVOA incorporates 10 distinct chaotic maps, including Circle, Chebyshev, Logistic, Gauss/mouse, Iterative, Sine, Piecewise, Sinusoidal, Singer, and Tent. These maps aim to improve both exploration and exploitation balance by increasing the initial population diversity of the algorithm. We comprehensively evaluate the proposed methods using the CEC'17 benchmark test functions. We divide these functions into unimodal, multimodal, hybrid, and compositional categories, and comprehensively test the convergence performance, local optima compression tendency, and solution quality of the algorithm. When chaotic maps are added to CAVOA algorithms, they work better than AVOA algorithms, especially in unimodal and hybrid functions, according to the results.

**Keywords-** Optimization, Chaotic map, Metaheuristic optimization algorithm, CEC'17 functions

## 1. Introduction

Optimization is of critical importance to solve problems frequently encountered in disciplines such as engineering [1], [2], energy [3], [4], logistics [5], economics [6], [7], medical [8] [9], [10], bioinformatics [11], [12], and artificial intelligence [13]. In particular, finding the optimum solution in high-dimensional and nonlinear problems creates difficulties in terms of both time and computational cost. Traditional optimization methods may be stuck in local minima and inadequate in finding the global optimum in such problems [14]. In this context, innovative approaches such as nature-inspired algorithms and chaotic systems have attracted the attention of researchers to provide effective solutions to optimization problems.

The African Vultures Optimization Algorithm (AVOA) is a metaheuristic algorithm derived from the energy-efficient flying techniques and predatory activities of African vultures. This algorithm has attained encouraging outcomes in global optimization challenges by presenting a novel method to equilibrate exploration and exploitation processes. However, when addressing complex and multi-dimensional problems, algorithms like AVOA may be susceptible to local minima. Improving the search process and increasing the population's diversity are two things that are absolutely necessary in order to overcome this constraint. Local minima may be efficiently reduced by including chaotic maps into metaheuristic algorithms. This is accomplished by increasing the variety of the population at the beginning of the search process, which in turn makes the search process more efficient.

Chaotic systems are complex mathematical systems that exhibit chaotic behavior despite being deterministic. Integrating these systems into optimization algorithms in the form of chaotic maps enables a broader search in the solution space. In the literature, chaotic maps have been shown to be successfully used in algorithms such as bird swarm optimization [15], slime mold optimization algorithm [16], and grasshopper optimization algorithm [17], arithmetic optimization algorithm [18], dragonfly algorithm [19], vortex search algorithm [20], crow search algorithm [21], hunger games search algorithm [22], transient search optimization [23], chimp optimization [24], whale optimization algorithm [25], Henry gas solubility optimization algorithm [26]. However, studies on the integration of chaotic dynamics in AVOA are quite limited.

The performance of the algorithms used in solving optimization problems varies from problem to problem. The No Free Lunch (NFL) Theorem states that no optimization algorithm can be equally effective for all problems. This theorem reveals that a single algorithm cannot provide the best results for all types of optimization problems and that specific algorithms or developments suitable for

different problems should be developed [27]. In this context, nature-inspired algorithms such as AVOA, although successful for certain problem classes, may show limitations such as getting stuck in local minima or insufficient solution quality when it comes to complex and multimodal problems. In light of the NFL Theorem, the integration of chaotic maps to improve the performance of the AVOA algorithm is considered an important step to increase the general applicability of the algorithm and make it effective for a wider range of problems.

Although AVOA has been proven to be a powerful optimization algorithm in the literature, there is a need for methods that will prevent it from getting stuck in local minima and scan the search space more effectively. Integrating chaotic maps with AVOA offers a potential solution to close this gap. In this study, different types of chaotic maps (for example, Chebyshev, Gauss/mouse, Circle, Iterative, Sine, Logistic, Sinusoidal, Piecewise, Singer, and Tent maps) have been examined in order to improve the performance of the AVOA algorithm, and the effects of these maps on the performance of AVOA have been analyzed in detail. The aim is to improve the solution quality, convergence speed, and the risk of getting stuck in local minima of the algorithm. In this context, the aim of this study, supported by both theoretical and experimental analyses, is to reveal the superiority of optimization algorithms enriched with chaotic maps and to emphasize the potential of such innovative methods to solve complex problems.

The rest of the paper is organized as follows: In the second section, the African vultures method is discussed and examined in detail. In the third section, chaotic maps are included, and the maps used are explained. In the fourth section, information about the proposed method is given and its equations are shown. In the fifth section, experimental results are performed, and the proposed method is analyzed in detail in CEC'17 functions. In addition, Friedman and Wilcoxon sign rank statistical analyses are performed. In the last section, the sixth section, the results of the study are given and information about future studies is given.

## **2. Chaotic AVOA Algorithm**

AVOA consists of 6 stages. These stages are explained below, respectively [28].

### **2.1. Identifying the best vulture within a group**

After establishing the initial population, the fitness of each solution is evaluated. The best solution is named the best vulture in the first group, and the next best solution is named the best vulture in the second group. The remaining solutions then migrate towards the optimal solutions of both groups, as per Equation (1). Every time the fitness iteration is changed, the whole population is reassessed.

$$R(i) = \begin{cases} BestVulture_1 if p_i = L_1 \\ BestVulture_2 if p_i = L_2 \end{cases} \quad (1)$$

In Equation (1), the chance of selecting certain vultures to guide the remaining vultures towards one of the optimal solutions within each group is computed, where  $L_1$  and  $L_2$  The parameters to be assessed prior to the search process must have values ranging from 0 to 1, with their total equaling 1. The likelihood of selecting the optimal solution is determined by using the Roulette wheel to choose the best answers from each group, as shown by Equation (2).

$$p_i = \frac{F_i}{\sum_{i=1}^n F_i} \quad (2)$$

An  $\alpha$ -numeric parameter near 1 and  $\beta$ -numeric parameter near 0 in AVOA will result in heightened intensification. If the  $\beta$ -numeric parameter approaches 1 and the  $\alpha$ -numeric parameter approaches 0, it results in increased variety in AVOA.

## 2.2. The vulture starvation rate

The mathematical modeling for this step used Equation (4). It was used to transition from the exploration phase to the exploitation phase, influenced by the satiety or hunger rate of vultures. The satiety rate exhibits a declining tendency, and Equation (4) was used to represent this phenomenon.

$$t = h \times \left( \sin^w \left( \frac{\pi}{2} \times \frac{iteration_i}{maxiterations} \right) + \cos \left( \frac{\pi}{2} \times \frac{iteration_i}{maxiterations} \right) - 1 \right) \quad (3)$$

$$F = (2 \times rand_1 + 1) \times z \times \left( 1 - \frac{iteration_i}{maxiterations} \right) + t \quad (4)$$

In Equations (3) and (4),  $h$  is a stochastic variable inside the interval of -2 to 2,  $F$  signifies that the vultures are satisfied,  $z$  is a random value between -1 and 1 that varies with each iteration, iteration represents the current iteration number, max iterations indicate the total number of iterations, and  $rand_1$  has a stochastic value ranging from 0 to 1. When the  $z$  value falls below 0, it indicates that the vulture is malnourished, and when it rises to 0, it signifies that the vulture is satisfied.

## 2.3. Exploration

In the AVOA, vultures may explore several random regions, determined by two distinct techniques, with a parameter known as  $P_1$  used to choose between them. This parameter must be assigned a value prior to the search operation and should range between 0 and 1, dictating the use of each of the two techniques. To choose any strategy in the  $rand_{p_1}$  exploration phase, a random number between 0 and 1 is created. The Equation (6) is used if this number is greater than or equal to the  $P_1$  parameter. If  $rand_{p_1}$  is less than the parameter  $P_1$ , then Equation (8) is used. In this scenario, each vulture does a random search in its environment based on its degree of satiation. This approach is shown in Equation (5).

$$P(i + 1) = \begin{cases} \text{Equation(6)} & \text{if } P_1 \geq rand_{p1} \\ \text{Equation(8)} & \text{if } P_1 < rand_{p1} \end{cases} \quad (5)$$

$$P(i + 1) = R(i) - F \times D(i) \quad (6)$$

$$D(i) = |R(i) \times X - P(i)| \quad (7)$$

As per Equation (6), vultures engage in a random search for sustenance within a range defined by one of the optimal cultures from the two groups, where  $P(i + 1)$  denotes the vulture's position vector in the next iteration, and  $F$  represents the rate of vulture satiation, denotes the vulture's position vector in the next iteration. In Equation (7),  $R(i)$  denotes one of the optimal vultures, chosen by the application of Equation (1) in the present iteration. Additionally,  $X$  is the location where vultures disperse unpredictably to safeguard their meal from competing vultures.  $X$  serves as a coefficient vector that amplifies random motion, varying with each iteration, and is derived from the formula  $X = 2 \times rand$ , where  $rand$  represents a random integer within the range of 0 to 1.  $P(i)$  denotes the current vector location of the vulture.

$$P(i + 1) = rand_2 \times ((ub - lb) \times rand_3 + lb) + R(i) - F \quad (8)$$

In Equation (8),  $R(i)$  denotes one of the optimal vultures identified using Equation (1) in the present iteration.  $F$  is the vulture satiation rate derived from Equation (4) in the present iteration, whereas  $rand_2$  is a random number ranging from 0 to 1.  $ub$  and  $lb$  indicate the upper and lower bounds of the variables, respectively. Employing Equation (8) in the AVOA yields a basic model for the stochastic creation of solutions inside the interval  $(lb, ub)$ .  $rand_3$  is used to enhance the randomness coefficient. If  $rand_3$  approaches 1, it distributes the answers in like ways, introducing a stochastic motion in combination with the  $lb$ . It generates a substantial random coefficient proportional to the size of the search environment to enhance diversity and investigate various areas of the search space.

## 2.4. Exploitation

The efficiency phase of the AVOA is examined at this juncture. If the value of  $|F|$  is less than one, the AVOA transitions onto the exploitation phase, consists of two phases, each utilizing a different approach. There are two parameters,  $P_2$  and  $P_3$ , that determine the strategy used in each internal stage. Parameter  $P_2$  is used to choose the strategies accessible in the first phase, whereas parameter  $P_3$  is employed to pick the methods accessible in the subsequent phase. Both parameters must be assigned values of 0 and 1 prior to starting the search operation. The vultures' foraging behaviors, analyzed in section 3, are structured and tailored to mathematical challenges.

Exploitation: The AVOA commences the first part of the Exploitation stage when the value  $|F|$  ranges from 1 to 0.5. During the first phase, two distinct rotational aerial and siege combat techniques are used.  $P_2$  is used to ascertain the selection of each strategy, which must be evaluated prior to the execution of the search operation, with the value required to be between 0 and 1. At the start of this phase, a random number,  $rand_{p_2}$ , is created within the range of 0 to 1. If this amount is larger than or equal to the parameter  $P_2$ , the Siege-fight tactic is implemented gradually. However, if this random number is less than the parameter  $P_2$ , a rotational flying strategy is implemented. This process is shown in Equation (9).

$$P(i + 1) = \begin{cases} \text{Equation(10)} & \text{if } P_2 \geq rand_{p_2} \\ \text{Equation(13)} & \text{if } P_2 < rand_{p_2} \end{cases} \quad (9)$$

Food Competition: When  $|F|$  is  $\geq 0.5$ , the vultures are adequately satisfied and possess sufficient energy. The congregation of several vultures around a single food source may lead to significant disputes over food procurement. Conversely, the weaker vultures attempt to exhaust and get sustenance from the healthier vultures by congregating around them and instigating little skirmishes. Equations (10) and (11) are used to represent this phase.

$$P(i + 1) = D(i) \times (F + rand_4) - d(t) \quad (10)$$

$$d(t) = R(i) - P(i) \quad (11)$$

$D(i)$  is computed using Equation (7), whereas  $F$  represents the satiation rate of vultures, determined by Equation (4).  $rand_4$  is a stochastic variable ranging from 0 to 1, used to augment the random coefficient. In Equation (11),  $R(i)$  represents one of the optimal vultures from the two groups chosen using Equation (1) in the present iteration, while  $P(i)$  denotes the current vector location of the vulture, which facilitates the calculation of the distance between the vulture and one of the optimal vultures in the two groups.

### 2.5. Rotating flight of Vultures:

The spiral model has been used to mathematically represent circular flight. The rotational flight is articulated by Equations (12) and (13).

$$S_1 = R(i) \times \left( \frac{rand_5 \times P(i)}{2\pi} \right) \times \cos(P(i))$$

$$S_2 = R(i) \times \left( \frac{rand_6 \times P(i)}{2\pi} \right) \times \sin(P(i)) \quad (12)$$

$$P(i + 1) = R(i) - (S_1 + S_2) \quad (13)$$

In Equations (12) and (13),  $R(i)$  represents the position vector of one of the two optimal vultures in the current iteration, derived from Equation (1). Cosine and sine denote the functions of cosine and sine, respectively.  $rand_5$  and  $rand_6$

are random numbers ranging from 0 to 1.  $S_1$  and  $S_2$  are derived using Equation (12). Ultimately, the position of the vultures is revised using Equation (13).

## 2.6. Exploitation (Second Phase):

During the second phase of exploitation, the motions of the two vultures attract many species of vultures to the food supply, resulting in a siege and intense competition for sustenance. If the absolute value of  $F$  is less than 0.5, this step of the algorithm is run. At the start of this phase,  $rand_{p_3}$  is produced, representing a random integer within the interval of 0 to 1. If  $rand_{p_3}$  is higher than or equal to the parameter  $P_3$ , the plan involves accumulating several kinds of vultures around the food supply. If the resultant number is less than the parameter  $P_3$ , the aggressive siege-fight strategy is executed. This approach is shown in Equation (14).

$$P(i + 1) = \begin{cases} Eq(16) & \text{if } p_3 \geq rand_{p_3} \\ Eq(17) & \text{if } p_3 < rand_{p_3} \end{cases} \quad (14)$$

The aggregation of several vulture species around the feeding source: The aggregation of vultures towards the feeding source is analyzed. Vultures can experience starvation, leading to intense competition for food that may attract many vulture species to a single resource. Equations (15) and (16) have been used to model this vulture movement.

$$\begin{aligned} A_1 &= BestVulture_1(i) - \frac{BestVulture_1(i) \times P(i)}{BestVulture_1(i) - P(i)^2} \times F \\ A_2 &= BestVulture_2(i) - \frac{BestVulture_2(i) \times P(i)}{BestVulture_2(i) - P(i)^2} \times F \end{aligned} \quad (15)$$

In Equation (15),  $BestVulture_1(i)$  denotes the optimal vulture of the first group in the current iteration, while  $BestVulture_2(i)$  signifies the optimal vulture of the second group in the same iteration.  $F$  represents the vulture satiation rate, computed via Equation (4), and  $P(i)$  indicates the current vector position of a vulture.

$$P(i + 1) = \frac{A_1 + A_2}{2} \quad (16)$$

The aggregate of all vultures is executed using Equation (16), with  $A_1$  and  $A_2$  derived from Equation (15), and  $P(i + 1)$  representing the vector of the vulture's location in the subsequent iteration.

Aggressive vultures in pursuit of food converge from all directions towards the dominant vulture. Equation (17) serves to represent this motion.

$$P(i + 1) = R(i) - |d(t)| \times F \times Levy(d) \quad (17)$$

In Equation (16),  $d(t)$  denotes the distance of the vulture to one of the optimal vultures in the two groups, derived by Equation (11). The Levy flight (LF) equation is shown in Equation (18).

$$LF(x) = 0.01 \times \frac{u \times \sigma}{v^\beta}, \sigma = \left( \frac{\Gamma(1+\beta) \times \sin\left(\frac{\pi\beta}{2}\right)}{\Gamma(1+\beta) \times \beta \times 2\left(\frac{\beta-1}{2}\right)} \right)^{\frac{1}{\beta}} \quad (18)$$

In Equation (18),  $d$  denotes the issue dimensions,  $u$  and  $v$  are random variables ranging from 0 to 1, and  $\beta$  is a constant value of 1.5.

### 3. Chaotic Maps

Chaotic maps constitute a significant area within the science of dynamical systems and serve as instruments often used for the mathematical description of deterministic chaos. These maps include consecutive repetitions of a mathematical function that defines the system's state. Chaotic maps exhibit profound sensitivity to beginning circumstances, a phenomenon termed the butterfly effect, whereby little alterations may result in significant disparities over time. Chaotic maps are used to simulate processes characterized by unpredictability and disorder across several domains, including physics, economics, biology, and engineering, facilitating the comprehension of complicated system dynamics within these disciplines. Chaotic maps and their properties used in the paper are shown in Table 1.

**Table 1.** Variables and equations of chaotic maps

CM No	CM Name	CM Equation
1	Chebyshev map	$X_{n+1} = \cos(kc \cos^{-1} x_n)$
2	Circle map	$X_{n+1} = X_n + b - \left(\frac{a}{2\pi}\right) \sin(2\pi X_n) \text{ mod}(1)$ $a = 0.5$ and $b = 0.2$
3	Gauss map	$X_{n+1} = \begin{cases} 0, & X_n = 0 \\ \frac{1}{x_n \text{ mod}(1)}, & X_n \in (0,1), \frac{1}{x_n \text{ mod}(1)} = \frac{1}{x_n} - \left\lfloor \frac{1}{x_n} \right\rfloor \end{cases}$
4	Iterative map	$X_{n+1} = \sin\left(\frac{a\pi}{x_n}\right), a = 0.7$
5	Logistic map	$X_{n+1} = aX_n(1 - X_n), a = 4$
6	Piecewise map	$x_{n+1} = \begin{cases} \frac{x_n}{P}, & 0 \leq x_n < P \\ \frac{x_n - P}{0.5 - P}, & P \leq x_n < 0.5 \\ \frac{1 - P - x_n}{0.5 - P}, & 0.5 \leq x_n < 1 - P \\ \frac{1 - x_n}{P}, & 1 - P \leq x_n < 1 \end{cases}, P = 0.4$
7	Sine map	$X_{n+1} = \frac{a}{4} \sin(\pi x_n), 0 < a \leq 4$
8	Singer map	$X_{n+1} = \mu(7.86x_n - 23.31x_n^2 + 28.75x_n^3 - 13.302875x_n^4), \mu = 1.07$
9	Sinusoidal map	$X_{n+1} = ax_n^2 \sin(\pi X_n), a = 2.3$ and $X_0 = 0.7$
10	Tent map	$f(x) = \begin{cases} X_n/0.7, & X_n < 0 \\ 10/3 X_n(1 - X_n), & \text{otherwise} \end{cases}$

#### 4. Chaotic AVOA

A primary issue of metaheuristic optimization algorithms is maintaining population diversity and avoiding premature convergence. For these algorithms to provide successful answers, they must achieve a delicate equilibrium between exploration and exploitation processes. Integrating chaotic maps into algorithms is one of the most effective methods to enhance population variety and improve solution quality. Chaotic maps enhance the search precision and convergence rate of metaheuristic algorithms by allowing a broader search space. Metaheuristic algorithms typically have two primary phases: exploration and exploitation. The exploration step inhibits the algorithm from being ensnared in local optima by extensively surveying the search space. The exploitation phase, conversely, seeks to identify the optimal solution within a specific portion of the search space by concentrating on the most promising locations. Nonetheless, an algorithm too focused on exploitation may get ensnared in local optima, while excessive emphasis on exploration might render the search arbitrary and unproductive.

Recently proposed AVOA is popularly applied in many different problems in the literature. Although AVOA method has proven itself in the literature, it has some disadvantages in the exploration phase. In order to eliminate these disadvantages, chaotic maps are used in the exploration phase of AVOA. Equations 19 and 20 are obtained by applying 10 different chaotic maps instead of random in Equation 7 and  $rand_2$  in Equation 8 in the exploration phase of AVOA.

$$D(i) = |2 \times CMV \times R(i) - P(i)| \quad (19)$$

$$P(i + 1) = R(i) - F + CMV \times ((ub - lb) \times rand_3 + lb) \quad (20)$$

The CMV, or sequentially produced chaotic map value, is used here. The suggested techniques using ten distinct chaotic maps are as follows: Chebyshev map (CAVOA-1), circle map (CAVOA-2), Gaussian map (CAVOA-3), iterative map (CAVOA-4), logistic map (CAVOA-5), piecewise map (CAVOA-6), sinus map (CAVOA-7), singer map (CTSO-8), sinusoidal map (CAVOA-9), and tent map (CAVOA-10).

#### 5. Results and Discussions

The suggested methodologies were used to the CEC'17 test functions to assess their performance. The findings were meticulously compared under this subject, and the performance analyses of the methodologies were conducted. The parameter values of CAVOA are taken as the default values in the AVOA article. All applications were developed using MATLAB R2021a, licensed from Manisa Celal Bayar University, and all testing were conducted on a machine equipped

with an Intel(R) Core (TM) i9–10900k CPU @ 3.70 GHz (10 CPUs), 48 GB RAM, running Windows 10–64 bit.

The IEEE Congress on Evolutionary Computation (CEC) test functions were used to evaluate the efficacy of the suggested ten distinct CAVOA and AVOA methodologies. CEC'17 test functions include 29 distinct functions, including unimodal, multimodal, hybrid, and composition categories. Unimodal functions (f1 and f3) assess the convergence performance of the method, whereas multimodal functions (f4–f10) analyze potential early convergence issues and local optima entrapment. Hybrid and composition functions (f11–f20 and f21–f30) are used to assess the capacity to circumvent local optima, characterized by several local optima, and to evaluate the equilibrium between exploration and exploitation.

**Table 2.** Results of experiments on CEC'17 test functions

f1		AVG	STD	MAX	MIN	f3		AVG	STD	MAX	MIN
	AVOA	4.75E+03	6.17E+03	1.99E+04	1.09E+02		AVOA	3.70E+04	7.16E+03	5.10E+04	2.32E+04
	CAVOA-1	4.17E+03	5.56E+03	1.84E+04	1.13E+02		CAVOA-1	3.42E+04	7.47E+03	4.92E+04	1.32E+04
	CAVOA-2	5.35E+03	6.19E+03	2.16E+04	1.05E+02		CAVOA-2	3.70E+04	7.06E+03	4.98E+04	1.70E+04
	CAVOA-3	5.99E+03	6.63E+03	2.10E+04	1.07E+02		CAVOA-3	3.43E+04	5.09E+03	4.62E+04	2.69E+04
	CAVOA-4	4.19E+03	4.96E+03	1.74E+04	1.13E+02		CAVOA-4	3.36E+04	5.09E+03	4.39E+04	2.23E+04
	CAVOA-5	<b>3.45E+03</b>	4.85E+03	2.02E+04	1.02E+02		CAVOA-5	3.33E+04	8.31E+03	5.57E+04	1.60E+04
	CAVOA-6	7.59E+03	8.25E+03	3.09E+04	1.22E+02		CAVOA-6	3.68E+04	7.79E+03	5.60E+04	2.41E+04
	CAVOA-7	3.70E+03	5.12E+03	2.00E+04	1.17E+02		CAVOA-7	3.49E+04	7.02E+03	4.78E+04	2.20E+04
	CAVOA-8	3.86E+04	1.88E+05	1.03E+06	1.08E+02		CAVOA-8	3.82E+04	6.01E+03	4.99E+04	2.73E+04
	CAVOA-9	5.03E+03	4.87E+03	1.96E+04	1.08E+02		CAVOA-9	<b>3.29E+04</b>	7.60E+03	5.23E+04	1.91E+04
	CAVOA-10	3.80E+03	4.65E+03	1.54E+04	1.06E+02		CAVOA-10	3.42E+04	7.31E+03	4.78E+04	2.06E+04
f4		AVG	STD	MAX	MIN	f5		AVG	STD	MAX	MIN
	AVOA	5.10E+02	2.86E+01	5.56E+02	4.03E+02		AVOA	7.28E+02	5.02E+01	8.04E+02	6.33E+02
	CAVOA-1	<b>5.06E+02</b>	2.84E+01	5.70E+02	4.07E+02		CAVOA-1	7.27E+02	4.31E+01	8.08E+02	6.21E+02
	CAVOA-2	5.15E+02	2.46E+01	5.53E+02	4.17E+02		CAVOA-2	7.33E+02	3.83E+01	8.20E+02	6.49E+02
	CAVOA-3	5.10E+02	2.88E+01	5.58E+02	4.04E+02		CAVOA-3	7.28E+02	4.42E+01	8.08E+02	6.58E+02
	CAVOA-4	5.10E+02	2.82E+01	5.62E+02	4.06E+02		CAVOA-4	7.25E+02	4.20E+01	8.16E+02	6.66E+02
	CAVOA-5	5.17E+02	2.23E+01	5.69E+02	4.72E+02		CAVOA-5	<b>7.15E+02</b>	4.87E+01	8.23E+02	5.86E+02
	CAVOA-6	5.16E+02	2.86E+01	5.83E+02	4.69E+02		CAVOA-6	7.33E+02	4.20E+01	8.05E+02	6.41E+02
	CAVOA-7	5.11E+02	2.32E+01	5.88E+02	4.66E+02		CAVOA-7	7.26E+02	4.66E+01	8.45E+02	6.47E+02
	CAVOA-8	5.08E+02	3.55E+01	5.94E+02	4.15E+02		CAVOA-8	7.20E+02	4.00E+01	8.07E+02	6.41E+02
	CAVOA-9	5.17E+02	2.43E+01	5.79E+02	4.54E+02		CAVOA-9	7.25E+02	4.25E+01	8.00E+02	6.53E+02
	CAVOA-10	5.18E+02	2.36E+01	5.79E+02	4.72E+02		CAVOA-10	7.24E+02	4.10E+01	8.04E+02	6.53E+02
f6		AVG	STD	MAX	MIN	f7		AVG	STD	MAX	MIN
	AVOA	<b>6.49E+02</b>	7.02E+00	6.66E+02	6.35E+02		AVOA	1.15E+03	7.55E+01	1.29E+03	9.97E+02
	CAVOA-1	6.54E+02	9.75E+00	6.74E+02	6.31E+02		CAVOA-1	1.16E+03	7.34E+01	1.36E+03	1.04E+03
	CAVOA-2	6.53E+02	7.91E+00	6.77E+02	6.38E+02		CAVOA-2	1.16E+03	6.62E+01	1.29E+03	1.07E+03
	CAVOA-3	6.54E+02	7.90E+00	6.66E+02	6.34E+02		CAVOA-3	1.18E+03	9.45E+01	1.32E+03	9.89E+02
	CAVOA-4	6.51E+02	8.57E+00	6.68E+02	6.32E+02		CAVOA-4	<b>1.13E+03</b>	9.48E+01	1.26E+03	9.32E+02
	CAVOA-5	6.54E+02	9.89E+00	6.81E+02	6.43E+02		CAVOA-5	1.15E+03	7.81E+01	1.29E+03	9.69E+02
	CAVOA-6	6.51E+02	8.68E+00	6.71E+02	6.35E+02		CAVOA-6	<b>1.13E+03</b>	7.99E+01	1.28E+03	9.82E+02
	CAVOA-7	6.50E+02	1.01E+01	6.69E+02	6.32E+02		CAVOA-7	1.16E+03	7.42E+01	1.31E+03	1.03E+03
	CAVOA-8	6.52E+02	7.56E+00	6.69E+02	6.39E+02		CAVOA-8	1.17E+03	7.59E+01	1.30E+03	9.75E+02
	CAVOA-9	6.54E+02	8.05E+00	6.71E+02	6.40E+02		CAVOA-9	1.19E+03	6.76E+01	1.34E+03	1.06E+03
	CAVOA-10	6.50E+02	7.59E+00	6.67E+02	6.36E+02		CAVOA-10	1.15E+03	7.71E+01	1.27E+03	1.00E+03
f8		AVG	STD	MAX	MIN	f9		AVG	STD	MAX	MIN

	AVOA	9.71E+02	3.37E+01	1.04E+03	9.05E+02		AVOA	5.06E+03	7.41E+02	6.88E+03	3.54E+03
	CAVOA-1	9.64E+02	2.07E+01	1.00E+03	9.11E+02		CAVOA-1	5.53E+03	7.11E+02	7.89E+03	4.39E+03
	CAVOA-2	9.67E+02	3.13E+01	1.03E+03	9.03E+02		CAVOA-2	5.07E+03	7.38E+02	6.42E+03	3.28E+03
	CAVOA-3	9.68E+02	3.97E+01	1.04E+03	9.02E+02		CAVOA-3	5.56E+03	9.12E+02	8.26E+03	4.05E+03
	CAVOA-4	9.62E+02	2.98E+01	1.03E+03	9.18E+02		CAVOA-4	5.23E+03	5.03E+02	6.67E+03	4.40E+03
	CAVOA-5	9.69E+02	3.87E+01	1.03E+03	8.82E+02		CAVOA-5	5.61E+03	9.54E+02	8.10E+03	3.80E+03
	CAVOA-6	9.73E+02	2.93E+01	1.04E+03	9.27E+02		CAVOA-6	5.07E+03	6.14E+02	6.13E+03	3.76E+03
	CAVOA-7	<b>9.60E+02</b>	2.55E+01	1.01E+03	9.18E+02		CAVOA-7	5.49E+03	9.33E+02	7.59E+03	3.65E+03
	CAVOA-8	9.64E+02	3.33E+01	1.03E+03	8.99E+02		CAVOA-8	5.25E+03	6.77E+02	6.95E+03	3.89E+03
	CAVOA-9	9.67E+02	2.74E+01	1.03E+03	9.28E+02		CAVOA-9	5.33E+03	8.83E+02	8.50E+03	4.20E+03
	CAVOA-10	9.72E+02	3.95E+01	1.05E+03	8.96E+02		CAVOA-10	<b>5.03E+03</b>	8.31E+02	7.14E+03	3.39E+03

**Table 2.** Results of experiments on CEC'17 test functions (continued)

f10		AVG	STD	MAX	MIN	f11		AVG	STD	MAX	MIN
	AVOA	5.37E+03	8.52E+02	7.44E+03	3.90E+03		AVOA	<b>1.25E+03</b>	5.13E+01	1.34E+03	1.15E+03
	CAVOA-1	5.61E+03	7.98E+02	7.04E+03	4.35E+03		CAVOA-1	<b>1.25E+03</b>	3.80E+01	1.32E+03	1.18E+03
	CAVOA-2	<b>5.33E+03</b>	8.51E+02	6.86E+03	3.66E+03		CAVOA-2	1.27E+03	5.79E+01	1.45E+03	1.17E+03
	CAVOA-3	<b>5.33E+03</b>	6.84E+02	6.35E+03	3.96E+03		CAVOA-3	1.26E+03	5.44E+01	1.39E+03	1.19E+03
	CAVOA-4	5.50E+03	8.04E+02	7.51E+03	3.75E+03		CAVOA-4	1.26E+03	5.82E+01	1.36E+03	1.16E+03
	CAVOA-5	5.50E+03	8.64E+02	7.24E+03	3.61E+03		CAVOA-5	1.26E+03	4.46E+01	1.35E+03	1.17E+03
	CAVOA-6	5.50E+03	6.14E+02	6.86E+03	4.10E+03		CAVOA-6	<b>1.25E+03</b>	5.26E+01	1.33E+03	1.15E+03
	CAVOA-7	5.51E+03	6.28E+02	7.24E+03	4.12E+03		CAVOA-7	1.26E+03	5.42E+01	1.38E+03	1.17E+03
	CAVOA-8	5.51E+03	6.08E+02	6.55E+03	4.25E+03		CAVOA-8	1.28E+03	6.45E+01	1.40E+03	1.16E+03
	CAVOA-9	5.76E+03	6.50E+02	6.77E+03	4.22E+03		CAVOA-9	<b>1.25E+03</b>	4.32E+01	1.33E+03	1.16E+03
	CAVOA-10	5.68E+03	8.07E+02	7.16E+03	4.19E+03		CAVOA-10	1.26E+03	4.08E+01	1.33E+03	1.17E+03
f12		AVG	STD	MAX	MIN	f13		AVG	STD	MAX	MIN
	AVOA	6.00E+06	6.78E+06	3.57E+07	6.45E+05		AVOA	1.41E+05	7.42E+04	2.89E+05	4.63E+04
	CAVOA-1	6.26E+06	7.09E+06	3.25E+07	2.56E+05		CAVOA-1	1.36E+05	1.15E+05	4.36E+05	1.65E+04
	CAVOA-2	7.61E+06	8.03E+06	3.77E+07	1.73E+05		CAVOA-2	<b>1.04E+05</b>	5.85E+04	2.90E+05	3.58E+04
	CAVOA-3	6.12E+06	4.92E+06	2.15E+07	4.65E+05		CAVOA-3	1.06E+05	7.53E+04	4.05E+05	2.72E+04
	CAVOA-4	8.15E+06	6.39E+06	2.89E+07	4.35E+05		CAVOA-4	1.57E+05	1.12E+05	5.12E+05	7.20E+04
	CAVOA-5	6.68E+06	4.64E+06	2.10E+07	8.08E+05		CAVOA-5	1.10E+05	6.83E+04	2.96E+05	1.77E+04
	CAVOA-6	6.66E+06	4.24E+06	1.84E+07	1.96E+06		CAVOA-6	1.34E+05	7.32E+04	3.01E+05	1.97E+04
	CAVOA-7	7.24E+06	5.54E+06	2.60E+07	4.83E+05		CAVOA-7	1.32E+05	7.99E+04	4.03E+05	3.97E+04
	CAVOA-8	<b>5.88E+06</b>	4.04E+06	1.73E+07	4.64E+05		CAVOA-8	1.17E+05	7.25E+04	2.90E+05	1.40E+04
	CAVOA-9	9.11E+06	9.03E+06	3.63E+07	8.05E+05		CAVOA-9	1.51E+05	7.92E+04	3.99E+05	5.22E+04
	CAVOA-10	6.94E+06	4.36E+06	1.64E+07	6.78E+05		CAVOA-10	1.52E+05	1.23E+05	5.78E+05	6.12E+03
f14		AVG	STD	MAX	MIN	f15		AVG	STD	MAX	MIN
	AVOA	3.07E+05	3.47E+05	1.18E+06	5.03E+03		AVOA	4.00E+04	2.42E+04	1.02E+05	9.65E+03
	CAVOA-1	<b>2.30E+05</b>	2.51E+05	9.82E+05	3.45E+03		CAVOA-1	4.62E+04	3.39E+04	1.52E+05	1.21E+04
	CAVOA-2	4.46E+05	4.96E+05	2.13E+06	5.08E+04		CAVOA-2	<b>3.59E+04</b>	2.52E+04	9.65E+04	6.25E+03
	CAVOA-3	3.56E+05	3.76E+05	1.13E+06	3.51E+03		CAVOA-3	4.29E+04	3.17E+04	1.31E+05	1.14E+04
	CAVOA-4	3.63E+05	3.45E+05	1.42E+06	7.90E+03		CAVOA-4	4.00E+04	2.71E+04	1.14E+05	6.39E+03
	CAVOA-5	2.68E+05	2.57E+05	8.75E+05	1.22E+04		CAVOA-5	3.79E+04	2.15E+04	1.03E+05	1.25E+04
	CAVOA-6	4.27E+05	4.45E+05	1.57E+06	7.34E+03		CAVOA-6	4.89E+04	3.64E+04	1.58E+05	1.04E+04
	CAVOA-7	3.37E+05	3.77E+05	1.57E+06	2.85E+03		CAVOA-7	5.24E+04	4.31E+04	1.90E+05	9.19E+03
	CAVOA-8	4.37E+05	5.50E+05	2.14E+06	1.95E+04		CAVOA-8	4.75E+04	2.83E+04	1.44E+05	8.37E+03
	CAVOA-9	4.62E+05	5.25E+05	2.22E+06	7.30E+03		CAVOA-9	4.25E+04	3.14E+04	1.66E+05	5.24E+03
	CAVOA-10	4.14E+05	4.68E+05	1.64E+06	1.81E+04		CAVOA-10	3.86E+04	2.87E+04	1.14E+05	6.94E+03
f16		AVG	STD	MAX	MIN	f17		AVG	STD	MAX	MIN
	AVOA	3.08E+03	3.54E+02	4.25E+03	2.39E+03		AVOA	2.51E+03	2.26E+02	3.09E+03	2.12E+03
	CAVOA-1	3.10E+03	3.76E+02	3.79E+03	2.45E+03		CAVOA-1	<b>2.41E+03</b>	2.75E+02	2.90E+03	1.92E+03
	CAVOA-2	3.14E+03	3.17E+02	3.65E+03	2.36E+03		CAVOA-2	2.55E+03	2.60E+02	3.25E+03	2.13E+03
	CAVOA-3	3.27E+03	3.88E+02	4.17E+03	2.60E+03		CAVOA-3	2.59E+03	2.66E+02	3.16E+03	2.02E+03
	CAVOA-4	3.19E+03	5.08E+02	4.37E+03	2.46E+03		CAVOA-4	2.48E+03	2.85E+02	2.89E+03	1.79E+03
	CAVOA-5	3.14E+03	4.55E+02	3.95E+03	2.33E+03		CAVOA-5	2.54E+03	2.67E+02	3.18E+03	2.02E+03
	CAVOA-6	3.08E+03	3.16E+02	3.79E+03	2.56E+03		CAVOA-6	2.54E+03	2.55E+02	2.98E+03	2.02E+03
	CAVOA-7	3.09E+03	4.07E+02	3.85E+03	2.35E+03		CAVOA-7	2.45E+03	2.32E+02	3.07E+03	2.08E+03
	CAVOA-8	<b>3.04E+03</b>	3.56E+02	3.94E+03	2.29E+03		CAVOA-8	2.52E+03	3.00E+02	3.19E+03	2.00E+03
	CAVOA-9	3.10E+03	3.46E+02	3.86E+03	2.39E+03		CAVOA-9	2.60E+03	2.65E+02	3.13E+03	2.06E+03
	CAVOA-10	3.30E+03	3.31E+02	4.24E+03	2.65E+03		CAVOA-10	2.49E+03	2.36E+02	2.99E+03	2.09E+03

All functions in the CEC'17 test suite have lower and upper limits ranging from  $-100$  to  $100$ . To provide a fair assessment under uniform circumstances, the evaluation count was set at  $1000$ , and the population size was determined to be  $30$ . In all trials, algorithms were executed  $30$  times, and the findings for mean (AVG), standard deviation (STD), maximum (max), and minimum (MIN) values are shown in a comparison format in Table 2.

Upon examining Table 2 based on the mean value, it becomes evident that CAVOAs failed to achieve superiority in two of the problems. However, in 8 of these problems, CAVOAs achieved the best results alongside AVOA and outperformed AVOA in the remaining 19. Upon closer examination, we find that CAVOAs outperformed AVOA in all unimodal functions. In multimodal functions, CAVOAs performed better in 8 of them, equal in 1 of them, and worse in 1 of them. In hybrid and composition functions, CAVOAs performed better in 12 of them, equal in 7 of them, and worse in 1 of them.

**Table 2.** Results of experiments on CEC'17 test functions (continued)

f18		AVG	STD	MAX	MIN	f19		AVG	STD	MAX	MIN
	AVOA	1.67E+06	1.66E+06	7.64E+06	9.72E+04		AVOA	6.08E+04	6.12E+04	2.53E+05	4.28E+03
	CAVOA-1	1.59E+06	1.64E+06	6.17E+06	2.35E+04		CAVOA-1	7.11E+04	6.82E+04	2.66E+05	2.87E+03
	CAVOA-2	1.56E+06	1.65E+06	6.16E+06	1.94E+05		CAVOA-2	7.51E+04	9.59E+04	3.93E+05	5.83E+03
	CAVOA-3	1.31E+06	1.32E+06	4.47E+06	8.12E+04		CAVOA-3	<b>2.82E+04</b>	2.41E+04	1.11E+05	2.23E+03
	CAVOA-4	<b>1.23E+06</b>	1.70E+06	7.14E+06	2.54E+04		CAVOA-4	4.91E+04	7.33E+04	3.82E+05	3.35E+03
	CAVOA-5	1.45E+06	1.51E+06	5.57E+06	5.56E+04		CAVOA-5	4.71E+04	4.69E+04	1.96E+05	2.42E+03
	CAVOA-6	1.42E+06	1.21E+06	4.77E+06	1.21E+05		CAVOA-6	5.27E+04	7.74E+04	3.76E+05	3.15E+03
	CAVOA-7	1.75E+06	1.76E+06	5.38E+06	1.23E+05		CAVOA-7	5.29E+04	4.66E+04	1.87E+05	6.76E+03
	CAVOA-8	1.33E+06	1.33E+06	5.57E+06	8.86E+04		CAVOA-8	6.75E+04	7.18E+04	2.91E+05	3.12E+03
	CAVOA-9	2.06E+06	2.33E+06	1.09E+07	9.07E+04		CAVOA-9	4.49E+04	4.60E+04	2.16E+05	3.78E+03
	CAVOA-10	1.50E+06	1.49E+06	6.97E+06	1.06E+05		CAVOA-10	7.44E+04	5.21E+04	1.80E+05	5.67E+03
f20		AVG	STD	MAX	MIN	f21		AVG	STD	MAX	MIN
	AVOA	2.76E+03	2.62E+02	3.35E+03	2.22E+03		AVOA	<b>2.51E+03</b>	4.55E+01	2.61E+03	2.42E+03
	CAVOA-1	2.73E+03	2.04E+02	3.06E+03	2.31E+03		CAVOA-1	2.53E+03	4.24E+01	2.62E+03	2.45E+03
	CAVOA-2	2.77E+03	2.18E+02	3.15E+03	2.40E+03		CAVOA-2	2.53E+03	6.05E+01	2.70E+03	2.43E+03
	CAVOA-3	2.73E+03	2.14E+02	3.20E+03	2.34E+03		CAVOA-3	2.54E+03	6.25E+01	2.75E+03	2.45E+03
	CAVOA-4	2.73E+03	2.03E+02	3.18E+03	2.36E+03		CAVOA-4	2.52E+03	4.39E+01	2.61E+03	2.43E+03
	CAVOA-5	2.75E+03	1.97E+02	3.14E+03	2.36E+03		CAVOA-5	2.52E+03	5.07E+01	2.63E+03	2.43E+03
	CAVOA-6	<b>2.72E+03</b>	2.35E+02	3.09E+03	2.29E+03		CAVOA-6	2.52E+03	4.82E+01	2.62E+03	2.42E+03
	CAVOA-7	<b>2.72E+03</b>	2.33E+02	3.27E+03	2.30E+03		CAVOA-7	2.53E+03	6.48E+01	2.73E+03	2.42E+03
	CAVOA-8	2.75E+03	2.56E+02	3.16E+03	2.22E+03		CAVOA-8	2.52E+03	4.14E+01	2.64E+03	2.45E+03
	CAVOA-9	2.77E+03	1.82E+02	3.06E+03	2.27E+03		CAVOA-9	2.55E+03	5.33E+01	2.67E+03	2.42E+03
	CAVOA-10	2.74E+03	1.95E+02	3.11E+03	2.27E+03		CAVOA-10	<b>2.51E+03</b>	5.82E+01	2.64E+03	2.40E+03
f22		AVG	STD	MAX	MIN	f23		AVG	STD	MAX	MIN
	AVOA	5.48E+03	2.54E+03	8.86E+03	2.30E+03		AVOA	<b>2.94E+03</b>	8.87E+01	3.19E+03	2.82E+03
	CAVOA-1	5.29E+03	2.38E+03	8.48E+03	2.30E+03		CAVOA-1	2.98E+03	9.68E+01	3.16E+03	2.81E+03
	CAVOA-2	<b>5.10E+03</b>	2.52E+03	8.24E+03	2.30E+03		CAVOA-2	2.98E+03	9.33E+01	3.19E+03	2.85E+03
	CAVOA-3	6.21E+03	1.84E+03	7.94E+03	2.30E+03		CAVOA-3	2.99E+03	8.57E+01	3.23E+03	2.88E+03
	CAVOA-4	5.55E+03	2.37E+03	8.23E+03	2.30E+03		CAVOA-4	2.97E+03	7.40E+01	3.13E+03	2.85E+03
	CAVOA-5	5.41E+03	2.27E+03	8.10E+03	2.30E+03		CAVOA-5	<b>2.94E+03</b>	8.09E+01	3.23E+03	2.83E+03
	CAVOA-6	5.83E+03	2.43E+03	8.78E+03	2.30E+03		CAVOA-6	2.96E+03	7.59E+01	3.09E+03	2.81E+03
	CAVOA-7	5.63E+03	2.30E+03	8.46E+03	2.30E+03		CAVOA-7	2.98E+03	7.51E+01	3.12E+03	2.84E+03
	CAVOA-8	6.22E+03	2.11E+03	8.21E+03	2.30E+03		CAVOA-8	2.97E+03	8.46E+01	3.13E+03	2.81E+03
	CAVOA-9	6.02E+03	2.13E+03	8.61E+03	2.30E+03		CAVOA-9	2.98E+03	8.07E+01	3.15E+03	2.77E+03
	CAVOA-10	5.52E+03	2.73E+03	8.62E+03	2.30E+03		CAVOA-10	2.97E+03	9.73E+01	3.23E+03	2.78E+03
f24		AVG	STD	MAX	MIN	f25		AVG	STD	MAX	MIN
	AVOA	3.14E+03	1.02E+02	3.35E+03	2.96E+03		AVOA	2.92E+03	2.82E+01	2.99E+03	2.88E+03
	CAVOA-1	3.16E+03	1.10E+02	3.39E+03	2.97E+03		CAVOA-1	<b>2.91E+03</b>	2.59E+01	2.99E+03	2.88E+03
	CAVOA-2	<b>3.13E+03</b>	8.51E+01	3.32E+03	2.98E+03		CAVOA-2	2.92E+03	2.11E+01	2.95E+03	2.89E+03

CAVOA-3	3.17E+03	1.10E+02	3.43E+03	3.00E+03	CAVOA-3	<b>2.91E+03</b>	2.10E+01	2.96E+03	2.88E+03
CAVOA-4	3.17E+03	8.88E+01	3.31E+03	2.97E+03	CAVOA-4	<b>2.91E+03</b>	1.90E+01	2.97E+03	2.88E+03
CAVOA-5	3.17E+03	8.83E+01	3.30E+03	2.98E+03	CAVOA-5	<b>2.91E+03</b>	1.78E+01	2.94E+03	2.89E+03
CAVOA-6	3.15E+03	8.71E+01	3.33E+03	3.02E+03	CAVOA-6	2.92E+03	2.74E+01	2.98E+03	2.88E+03
CAVOA-7	3.14E+03	7.82E+01	3.29E+03	2.96E+03	CAVOA-7	<b>2.91E+03</b>	2.07E+01	2.96E+03	2.89E+03
CAVOA-8	<b>3.13E+03</b>	8.90E+01	3.35E+03	2.97E+03	CAVOA-8	2.92E+03	3.08E+01	3.01E+03	2.88E+03
CAVOA-9	3.16E+03	9.88E+01	3.33E+03	2.95E+03	CAVOA-9	<b>2.91E+03</b>	1.77E+01	2.95E+03	2.88E+03
CAVOA-10	3.15E+03	6.96E+01	3.30E+03	3.02E+03	CAVOA-10	2.92E+03	2.51E+01	2.99E+03	2.88E+03

Table 3 presents the average Friedman mean rank values all benchmark functions.

**Table 2.** Results of experiments on CEC'17 test functions (continued)

f26	AVG	STD	MAX	MIN	f27	AVG	STD	MAX	MIN
AVOA	<b>6.48E+03</b>	1.35E+03	8.30E+03	2.80E+03	AVOA	3.28E+03	3.62E+01	3.39E+03	3.23E+03
CAVOA-1	6.76E+03	1.24E+03	8.30E+03	2.80E+03	CAVOA-1	3.29E+03	3.92E+01	3.42E+03	3.23E+03
CAVOA-2	7.00E+03	7.44E+02	8.44E+03	5.70E+03	CAVOA-2	3.30E+03	5.26E+01	3.49E+03	3.23E+03
CAVOA-3	6.76E+03	1.32E+03	8.58E+03	2.80E+03	CAVOA-3	3.32E+03	5.74E+01	3.44E+03	3.24E+03
CAVOA-4	6.69E+03	1.18E+03	8.20E+03	3.21E+03	CAVOA-4	3.28E+03	3.05E+01	3.34E+03	3.22E+03
CAVOA-5	6.51E+03	1.21E+03	8.26E+03	3.14E+03	CAVOA-5	<b>3.27E+03</b>	3.70E+01	3.36E+03	3.22E+03
CAVOA-6	6.76E+03	1.31E+03	9.13E+03	3.15E+03	CAVOA-6	3.29E+03	4.67E+01	3.46E+03	3.21E+03
CAVOA-7	6.60E+03	1.00E+03	8.41E+03	3.61E+03	CAVOA-7	3.30E+03	5.44E+01	3.43E+03	3.22E+03
CAVOA-8	6.65E+03	1.14E+03	8.27E+03	2.80E+03	CAVOA-8	3.28E+03	2.76E+01	3.33E+03	3.24E+03
CAVOA-9	6.91E+03	1.68E+03	8.99E+03	2.80E+03	CAVOA-9	3.31E+03	6.00E+01	3.48E+03	3.23E+03
CAVOA-10	6.64E+03	1.76E+03	9.37E+03	2.80E+03	CAVOA-10	3.28E+03	3.36E+01	3.37E+03	3.22E+03
f28	AVG	STD	MAX	MIN	f29	AVG	STD	MAX	MIN
AVOA	<b>3.26E+03</b>	3.79E+01	3.38E+03	3.20E+03	AVOA	4.36E+03	3.34E+02	5.04E+03	3.73E+03
CAVOA-1	<b>3.26E+03</b>	2.21E+01	3.30E+03	3.21E+03	CAVOA-1	4.38E+03	2.50E+02	4.78E+03	3.81E+03
CAVOA-2	3.27E+03	3.73E+01	3.35E+03	3.21E+03	CAVOA-2	4.29E+03	2.53E+02	4.79E+03	3.85E+03
CAVOA-3	<b>3.26E+03</b>	2.30E+01	3.30E+03	3.21E+03	CAVOA-3	4.39E+03	2.64E+02	4.96E+03	3.89E+03
CAVOA-4	3.28E+03	2.29E+01	3.34E+03	3.23E+03	CAVOA-4	4.33E+03	3.25E+02	4.89E+03	3.85E+03
CAVOA-5	3.27E+03	2.05E+01	3.32E+03	3.22E+03	CAVOA-5	4.30E+03	3.37E+02	5.06E+03	3.82E+03
CAVOA-6	<b>3.26E+03</b>	2.25E+01	3.31E+03	3.21E+03	CAVOA-6	4.36E+03	2.77E+02	4.94E+03	3.80E+03
CAVOA-7	3.27E+03	2.84E+01	3.38E+03	3.22E+03	CAVOA-7	<b>4.24E+03</b>	3.18E+02	4.89E+03	3.61E+03
CAVOA-8	3.27E+03	2.85E+01	3.37E+03	3.21E+03	CAVOA-8	4.34E+03	2.91E+02	4.74E+03	3.74E+03
CAVOA-9	3.27E+03	2.63E+01	3.35E+03	3.21E+03	CAVOA-9	4.32E+03	3.17E+02	4.96E+03	3.78E+03
CAVOA-10	3.27E+03	2.53E+01	3.33E+03	3.22E+03	CAVOA-10	4.28E+03	2.52E+02	4.89E+03	3.83E+03
f30	AVG	STD	MAX	MIN					
AVOA	7.53E+05	4.57E+05	1.66E+06	1.26E+05					
CAVOA-1	5.67E+05	4.23E+05	1.66E+06	6.44E+04					
CAVOA-2	6.99E+05	4.56E+05	2.05E+06	1.60E+05					
CAVOA-3	5.60E+05	3.60E+05	1.65E+06	7.74E+04					
CAVOA-4	<b>5.25E+05</b>	3.38E+05	1.14E+06	9.03E+04					
CAVOA-5	7.99E+05	5.51E+05	2.35E+06	6.36E+04					
CAVOA-6	8.33E+05	5.21E+05	1.97E+06	1.61E+05					
CAVOA-7	7.62E+05	4.33E+05	1.97E+06	1.11E+05					
CAVOA-8	8.13E+05	6.39E+05	2.62E+06	7.88E+04					
CAVOA-9	7.59E+05	4.73E+05	1.78E+06	1.30E+05					
CAVOA-10	8.54E+05	4.72E+05	1.96E+06	2.06E+05					

**Table 3.** Results of Friedman rank

Friedman	f1	f3	f4	f5	f6	f7	f8	f9	f10	f11	f12	f13	f14	f15	f16
AVOA	5.73	6.63	5.57	6.23	4.63	6.00	6.33	5.30	4.90	5.40	5.13	6.80	5.53	5.80	5.27
CAVOA-1	5.70	5.77	5.37	5.77	6.80	6.10	5.93	6.97	6.17	5.40	5.13	5.73	5.17	6.13	5.83
CAVOA-2	6.57	6.63	6.93	6.80	6.50	5.63	6.17	5.33	5.10	7.00	5.87	5.17	6.97	5.00	5.97
CAVOA-3	6.50	5.77	6.13	6.17	6.70	6.70	5.77	7.03	5.47	5.73	5.50	5.13	6.17	5.80	6.83
CAVOA-4	6.10	5.17	5.37	5.87	5.60	5.17	5.53	5.60	5.83	5.80	6.93	6.60	6.47	5.77	6.13

CAVOA-5	5.13	5.47	6.40	5.23	6.33	5.90	6.30	7.30	6.07	6.00	6.13	5.17	5.47	5.87	6.13
CAVOA-6	7.20	6.37	6.23	6.63	5.60	5.13	6.67	5.33	6.47	6.17	6.23	6.10	6.53	6.60	5.77
CAVOA-7	5.63	6.10	5.97	5.77	5.63	6.00	5.27	7.13	6.03	6.20	6.33	6.17	5.37	6.60	5.77
CAVOA-8	4.83	7.50	5.20	5.73	6.33	6.30	5.37	5.63	6.17	6.63	5.63	5.57	5.87	7.10	4.97
CAVOA-9	6.87	5.00	6.33	5.97	6.83	7.60	6.30	5.43	7.07	5.87	6.57	7.00	6.37	6.17	5.97
CAVOA-10	5.73	5.60	6.50	5.83	5.03	5.47	6.37	4.93	6.73	5.80	6.53	6.57	6.10	5.17	7.37

**Table 3.** Results of Friedman rank (continued)

Friedman	f17	f18	f19	f20	f21	f22	f23	f24	f25	f26	f27	f28	f29	f30
AVOA	5.83	6.50	6.67	6.23	4.73	5.90	4.70	5.37	6.33	5.53	5.53	5.47	6.47	6.30
CAVOA-1	4.40	6.27	6.57	5.77	6.53	5.53	6.63	6.20	5.43	6.30	6.40	5.70	6.80	4.87
CAVOA-2	6.03	6.27	6.10	6.13	6.20	5.77	6.30	5.43	6.03	6.43	6.50	5.77	5.40	6.03
CAVOA-3	6.87	5.43	4.60	5.80	6.67	6.23	6.77	6.70	5.87	6.37	8.03	5.07	6.57	4.73
CAVOA-4	6.07	4.87	5.43	5.60	5.37	5.97	6.07	6.53	4.80	5.97	5.43	6.77	5.83	4.60
CAVOA-5	6.40	5.77	5.40	6.27	5.93	5.43	4.80	6.57	5.80	5.33	4.33	6.27	5.87	6.37
CAVOA-6	6.27	6.13	5.03	5.87	6.17	6.07	5.83	5.80	6.47	6.10	5.97	5.57	6.63	6.60
CAVOA-7	5.50	6.30	6.17	5.47	5.93	5.77	6.70	5.33	6.60	4.90	6.17	6.03	5.07	6.37
CAVOA-8	5.70	6.00	6.73	6.37	5.73	6.87	6.27	5.47	5.87	5.70	5.70	6.53	6.53	6.50
CAVOA-9	7.40	6.53	5.67	6.57	7.33	6.30	6.30	6.33	6.07	7.20	6.63	6.73	5.70	6.37
CAVOA-10	5.53	5.93	7.63	5.93	5.40	6.17	5.63	6.27	6.73	6.17	5.30	6.10	5.13	7.27

## 6. Conclusion

This study illustrates that chaotic maps may be efficiently used to address the issue of AVOA being confined to local minima and to enhance solution quality. Chaotic maps enhance the algorithm's capacity to converge to the global optimum by augmenting the initial variety of the population. The analysis shows that chaotic maps not only improve the performance of AVOA but also provide a more effective balance between the exploration and exploitation phases of the algorithm. The achievements, such as high convergence speed for single-mode functions, prevention of local optima squeeze in multi-mode functions, and increased solution quality in hybrid functions, clearly prove the value of the integration of chaotic maps. The results of this study provide important guidance for future development efforts on nature-inspired algorithms, as well as increasing the applicability of AVOA for a wider range of problems. Looking forward, it is thought that research on the integration of chaotic maps into other meta-heuristic algorithms or the use of different chaotic dynamics in optimization problems may provide new contributions to the literature.

Although 10 different chaotic maps, such as Chebyshev, Logistic, Tent, Sine and Piecewise were considered in the study, the effect of other chaotic maps found in the literature or new chaotic dynamics that have not yet been discovered on AVOA can be examined. In particular, the effect of more complex and multifaceted chaotic systems on optimization algorithms can be investigated. Hybrid approaches can be developed with other meta-heuristic algorithms to improve the performance of the Chaotic AVOA (CAVOA) algorithm. Instead of using a fixed chaotic map, an adaptive or dynamic chaotic map selection mechanism can be developed. This approach can ensure that the most appropriate chaotic map is selected at each stage of the algorithm or in different problem types. In this way, the effect of chaotic maps can be used more efficiently. CAVOA algorithms can be combined with parallel computing and cloud-based platforms and applied to large-scale optimization problems.

## References

- [1] T. Gurgenc and O. Altay, "Surface roughness prediction of wire electric discharge machining ( WEDM )-machined AZ91D magnesium alloy using multilayer perceptron , ensemble neural network , and evolving product-unit neural network", *Materials Testing*, 64(3), 350-362, 2022.
- [2] O. Altay and T. Gurgenc, "GJO-MLP: a novel method for hybrid metaheuristics multi-layer perceptron and a new approach for prediction of wear loss of az91d magnesium alloy worn at dry, oil, and h-bn nanoadditive oil", *Surface Review and Letters (SRL)*, 31(06), 1-16, 2024.
- [3] E. Varol, E. Gurgenc, O. Altay, and A. Dikici, "Geothermics Hybrid artificial neural network based on a metaheuristic optimization algorithm for the prediction of reservoir temperature using hydrogeochemical data of different geothermal areas in Anatolia ( Turkey )," *Geothermics*, vol. 104, no. May, p. 102476, 2022, doi: 10.1016/j.geothermics.2022.102476.
- [4] E. Gurgenc and O. Altay, "AOSMA-MLP : A Novel Method for Hybrid Metaheuristics Artificial Neural Networks and a New Approach for Prediction of Geothermal Reservoir Temperature", *Applied Sciences*, 14(8), 3534, 2024.
- [5] C. Boonmee, M. Arimura, and T. Asada, "International Journal of Disaster Risk Reduction Facility location optimization model for emergency humanitarian logistics," *Int. J. Disaster Risk Reduct.*, vol. 24, no. February, pp. 485–498, 2017, doi: 10.1016/j.ijdr.2017.01.017.
- [6] S. A. Jalae, A. Shakibaei, H. R. Horry, H. Akbarifard, A. Ghaseminejad, and F. N. Robati, "MethodsX A new hybrid metaheuristic method based on biogeography-based optimization and particle swarm optimization algorithm to estimate money demand in Iran," *MethodsX*, vol. 8, p. 101226, 2021, doi: 10.1016/j.mex.2021.101226.
- [7] L. Calvet, R. De Torre, A. Goyal, and M. Marmol, "Modern Optimization and Simulation Methods in Managerial and Business Economics : A Review", *Administrative Sciences*, 2020, doi: 10.3390/admsci10030047.
- [8] H. Gündoğdu, O. Altay, "Evaluation of Performance of Feature Selection of Meta-Heuristic Optimization Methods in Medical Data. *Computer Science*", *Journal of Computer Science*, pp. 58–66, 2023.
- [9] E. V. Altay and B. Alatas, "Association analysis of Parkinson disease with vocal change characteristics using multi-objective metaheuristic optimization," *Med. Hypotheses*, vol. 141, p. 109722, Aug. 2020, doi: 10.1016/j.mehy.2020.109722.
- [10] E. V. Altay and B. Alatas, "A novel clinical decision support system for liver fibrosis using evolutionary multi-objective method based numerical

- association analysis,” *Med. Hypotheses*, vol. 144, p. 110028, Nov. 2020, doi: 10.1016/j.mehy.2020.110028.
- [11] R. M. Aziz, “Nature - inspired metaheuristics model for gene selection and classification of biomedical microarray data,” *Med. Biol. Eng. Comput.*, pp. 1627–1646, 2022, doi: 10.1007/s11517-022-02555-7.
- [12] L. Calvet, S. Benito, and A. A. Juan, “On the role of metaheuristic optimization in bioinformatics,” vol. 30, pp. 2909–2944, 2023, doi: 10.1111/itor.13164.
- [13] O. Altay and E. Varol, “A novel hybrid multilayer perceptron neural network with improved grey wolf optimizer,” *Neural Comput. Appl.*, vol. 35, no. 1, pp. 529–556, 2023, doi: 10.1007/s00521-022-07775-4.
- [14] E. V. Altay and B. Alatas, “Differential evolution and sine cosine algorithm based novel hybrid multi-objective approaches for numerical association rule mining,” *Inf. Sci. (Ny)*, vol. 554, pp. 198–221, 2021, doi: 10.1016/j.ins.2020.12.055.
- [15] E. Varol Altay and B. Alatas, "Bird swarm algorithms with chaotic mapping", *Artificial Intelligence Review*, 53(2), 1373-1414, 2020. doi: 10.1007/s10462-019-09704-9.
- [16] O. Altay, "Chaotic slime mould optimization algorithm for global optimization", *Artificial Intelligence Review*, 55(5), 3979-4040, 2021. doi: 10.1007/s10462-021-10100-5.
- [17] S. Arora and P. Anand, “Chaotic grasshopper optimization algorithm for global optimization,” *Neural Comput. Appl.*, vol. 31, no. 8, pp. 4385–4405, 2019, doi: 10.1007/s00521-018-3343-2.
- [18] X.-D. Li, J.-S. Wang, W.-K. Hao, M. Zhang, and M. Wang, “Chaotic arithmetic optimization algorithm,” *Appl. Intell.*, 52(14), 16718-16757, 2022, doi: 10.1007/s10489-021-03037-3.
- [19] G. I. Sayed, A. Tharwat, and A. E. Hassanien, “Chaotic dragonfly algorithm: an improved metaheuristic algorithm for feature selection,” *Appl. Intell.*, vol. 49, no. 1, pp. 188–205, 2019, doi: 10.1007/s10489-018-1261-8.
- [20] F. S. Gharehchopogh, I. Maleki, and Z. A. Dizaji, "Chaotic vortex search algorithm: metaheuristic algorithm for feature selection", *Evolutionary Intelligence*, 15(3), 1777-1808, 2021. doi: 10.1007/s12065-021-00590-1.
- [21] R. M. Rizk-Allah, A. E. Hassanien, and S. Bhattacharyya, “Chaotic crow search algorithm for fractional optimization problems,” *Appl. Soft Comput. J.*, vol. 71, pp. 1161–1175, 2018, doi: 10.1016/j.asoc.2018.03.019.
- [22] F. Kutlu Onay and S. B. Aydemir, “Chaotic hunger games search

- optimization algorithm for global optimization and engineering problems,” *Math. Comput. Simul.*, vol. 192, pp. 514–536, 2022, doi: 10.1016/j.matcom.2021.09.014.
- [23] O. Altay and E. V. Altay, “A novel chaotic transient search optimization algorithm for global optimization , real-world engineering problems and feature selection”, *PeerJ Computer Science*, 9, e1526, 2023, doi: 10.7717/peerj-cs.1526.
- [24] Y. Wang, H. Liu, G. Ding, and L. Tu, "Adaptive chimp optimization algorithm with chaotic map for global numerical optimization problems", *The Journal of Supercomputing*, 79(6), 2023. doi: 10.1007/s11227-022-04886-6.
- [25] G. Kaur and S. Arora, “Chaotic whale optimization algorithm,” *J. Comput. Des. Eng.*, vol. 5, no. 3, pp. 275–284, 2018, doi: 10.1016/j.jcde.2017.12.006.
- [26] B. Sultan et al., “A novel chaotic Henry gas solubility optimization algorithm for solving real - world engineering problems,” *Eng. Comput.*, vol. 38, no. s2, pp. 871–883, 2022, doi: 10.1007/s00366-020-01268-5.
- [27] E. V. Altay, "Hybrid Archimedes optimization algorithm enhanced with mutualism scheme for global optimization problems", *Artificial Intelligence Review*, 56(7), 6885-6946, 2023. doi: 10.1007/s10462-022-10340-z.
- [28] B. Abdollahzadeh, F. Soleimani, and S. Mirjalili, “Computers & Industrial Engineering African vultures optimization algorithm : A new nature-inspired metaheuristic algorithm for global optimization problems,” *Comput. Ind. Eng.*, vol. 158, no. January, p. 107408, 2021, doi: 10.1016/j.cie.2021.107408.

## **Chapter 6**

### **Numerical Investigation of The Effect Of Different Volume Concentrations Of Binary Hybrid Nanofluids On Entropy Generation In A Circular Heat Exchanger Tube**

**Fatma OFLAZ<sup>1</sup>**

---

<sup>1</sup> Firat University, Faculty of Technology, Automotive Engineering, Elazığ, Turkey  
Email: [fteber@firat.edu.tr](mailto:fteber@firat.edu.tr), ORCID NO: 0000-0002-9636-5746

## **Numerical investigation of the effect of different volume concentrations of binary hybrid nanofluids on entropy generation in a circular heat exchanger tube**

### **Abstract**

In this study, the effects of changes in volume concentration on entropy generation were numerically examined for binary Graphene- $\text{Al}_2\text{O}_3$  nanofluids prepared at five different volume concentrations ranging from 0.1% to 1% with a 50:50 mixing ratio. Under turbulent flow conditions, a constant heat flux of 30  $\text{kW/m}^2$  was applied to the tube test section, and experiments were conducted at Reynolds numbers ranging from 20000 to 80000. The  $k$ - $\epsilon$  RNG solution method was used, and grid validation was performed. The thermophysical properties of the hybrid nanofluids were determined based on well-established correlations found in the existing literature. The results showed a decreasing trend in entropy generation with increasing volume concentration of the binary nanofluid. Volume concentrations where  $N_s$  value remained below 1 were determined, indicating minimal irreversibility and thermodynamic advantages in the system. The lowest entropy production number of 0.8 was achieved at a Reynolds number of 20000 using 1% Graphene- $\text{Al}_2\text{O}_3$  water nanofluid. Total entropy production analysis exhibited decreasing values in the range of % 52.15 -12.21 compared to water for binary GnP- $\text{Al}_2\text{O}_3$  nanofluids with the increase in Reynolds number. It was observed that adding GNP- $\text{Al}_2\text{O}_3$  water nanofluids to pure water reduced total irreversibility, and the increase in concentration contributed significantly to the decrease in the total entropy generation.

**Keywords:** Entropy generation, Binary nanofluids, Heat transfer enhancement

## 1. Introduction

Researchers have focused on developing and improving the efficiency of thermal systems due to the growing demand for energy efficiency and the need to reduce energy consumption. Traditional heat transfer fluids, such as water, ethylene glycol, and oils, often have limitations regarding their heat transfer capabilities [1]. This has prompted scientists to seek innovative ways to enhance their thermal performance. One such approach involves the use of nanofluids. Nanofluids are engineered colloidal suspensions of nanosized solid particles (such as metals, oxides, or carbon-based materials like graphene or carbon nanotubes) dispersed in traditional base fluids [2]. These nanoparticles have unique thermal properties, including higher thermal conductivity than conventional fluids. By adding these nanoparticles to the base fluids, beneficial effects such as enhanced thermal conductivity, improved heat transfer performance, uniform heat distribution, reduced system size, and energy savings are achieved [3]. The shift from using single-type (mono) nanoparticles to hybrid nanofluids in research and development is driven by the need for better performance and cost-effectiveness. While using mono nanoparticles in base fluids has shown promising results in improving heat transfer and thermal conductivity, there is room for further optimization. Hybrid nanofluids are made by dispersing two or more different types of nanoparticles into a base fluid. The goal of creating hybrid nanofluids is to combine the beneficial properties of different nanoparticles to achieve even better performance than with single nanoparticles alone [4]. This study aimed to combine graphene and  $\text{Al}_2\text{O}_3$  nanoparticles in a hybrid nanofluid to merge the extraordinary thermal conductivity of graphene with the cost-effectiveness and stability of  $\text{Al}_2\text{O}_3$ . This combination allows the hybrid nanofluid to achieve enhanced thermohydraulic performance compared to using only  $\text{Al}_2\text{O}_3$ , while being more cost-effective than using only graphene. This approach increases heat transfer performance while keeping costs manageable. Graphene boosts thermal efficiency, while  $\text{Al}_2\text{O}_3$  provides stability and reduces expenses, resulting in a balanced, high-performance, and economical nanofluid suitable for various applications. Rea et al. studied the heat transfer performance of alumina water nanofluid under laminar flow conditions. They found that the use of alumina at 6% volume concentration showed a 27% increase in heat transfer coefficient compared to water [5]. Guo et al. [6] examined how the stability of hybrid nanofluids, specifically a blend of  $\text{Al}_2\text{O}_3$  and  $\text{TiO}_2$  nanoparticles in water ( $\text{Al}_2\text{O}_3$ - $\text{TiO}_2$ /W), influences their flow boiling heat transfer performance. At a low concentration of 0.03% by volume, this  $\text{Al}_2\text{O}_3$ - $\text{TiO}_2$ /W nanofluid achieved up to a 61.9% improvement in heat transfer compared to water alone. A computational fluid

dynamics model was used to analyze a concentric tube counter-flow heat exchanger operating under turbulent conditions with nanofluids. The model incorporates twisted tape turbulators in the annular section and within the tube, combined with various nanofluids. Findings showed that, with a 3% volume concentration, the overall heat transfer coefficient ( $U$ ) improved by 6.03% for CNTs/H<sub>2</sub>O nanofluid, 16.74% for Al<sub>2</sub>O<sub>3</sub>/H<sub>2</sub>O nanofluid, and 6.74% for SiO<sub>2</sub>/H<sub>2</sub>O nanofluid, compared to results without twisted tape turbulators [7]. Additionally, scientists have recently begun conducting extensive research on graphene nanoparticles, as they enable groundbreaking advancements in technology and scientific research by providing unique flexibility and performance improvements in areas where traditional materials fall short. Balaji et al. [8] conducted an experimental study on the convective heat transfer properties of water-based hybrid nanofluids containing equal parts Graphene Nanoplatelets and Multi-Walled Carbon Nanotubes. The investigation covered volume concentrations of 0.01%, 0.05%, 0.1%, 0.15%, and 0.2%. Results showed that the thermal conductivity of the nanofluid with 0.2% volume concentration increased by 25% compared to the base fluid. Additionally, they found that the convective heat transfer coefficient demonstrated a significant enhancement of 85%. Naghash et al. [9] conducted an investigation into the improvement of the convective heat transfer coefficient for nanofluids formulated using high-surface-area graphene, focusing on laminar flow within the developing region. Their findings reveal that at a 0.1 wt.% concentration, the nanofluid's thermal conductivity remains nearly unchanged, showing only a 3.8% increase. However, the convective heat transfer coefficient exhibits a notable improvement, with a 34% increase. The effects of Graphene oxide (GO)/water, Al<sub>2</sub>O<sub>3</sub>/water, and GO-Al<sub>2</sub>O<sub>3</sub>/water hybrid nanofluids were studied at weight concentrations of 0.01%, 0.02%, and 0.03% to assess improvements in heat transfer and thermal efficiency in a plate heat exchanger compared to pure water [10]. At the highest concentration of 0.03%, thermal efficiency ( $\eta$ ) was maximized, reaching 37% with GO, 21% with Al<sub>2</sub>O<sub>3</sub>, and 26% with the GO-Al<sub>2</sub>O<sub>3</sub> hybrid. GO nanoparticles showed the greatest enhancement in heat exchanger performance, achieving an optimized increase of 15.94%, followed by the hybrid at 11.86%, and Al<sub>2</sub>O<sub>3</sub> at 7.4%. Zolfalizadeh et al. [11] explored the effects of varying concentrations of graphene-water nanosheets on heat exchanger performance. At a concentration of 0.06% by weight, the nanofluid achieved the maximum increases in heat transfer coefficient, efficiency, and heat transfer rate, with gains of 22.47%, 8.88%, and 15.65%, respectively, over the base fluid. However, higher nanofluid concentration and increased flow rate resulted in a notable rise in pressure drop. Entropy generation analysis optimizes thermal systems by minimizing energy

losses (irreversibility), aiming for efficient design through reduced entropy generation [12,13]. Improved heat transfer lowers entropy, enhancing efficiency, but often increases pressure drop due to fluid friction, which adds energy loss [14]. This approach balances heat transfer improvements with flow resistance to achieve optimal system performance. Many studies have focused on examining the entropy generation of thermal systems. Singh et al. [15] focused on increasing the heat and exergy efficiency of parabolic trough solar collectors through the use of a hybrid nanofluid based on water with Graphene-ZrO<sub>2</sub> nanoparticles at varying volume concentrations. Experimental findings revealed notable enhancements in both thermal energy capture (68.72%) and exergy efficiency (16.7%), underscoring the promise of graphene-ZrO<sub>2</sub>/water hybrid nanofluids as an effective approach to improving the performance of parabolic trough solar collector systems. Keklikcioğlu et al. [16] assessed the second law efficiency of a heat exchanger tube under continuous heat flux and turbulent flow, using a hybrid nanofluid with GnP and Fe<sub>3</sub>O<sub>4</sub> nanoparticles and modified coiled wires as passive enhancement techniques. Various mass fractions of the nanoparticles were tested alongside barrel-type and hourglass-type coiled wire inserts. Results showed significant improvement in second law efficiency with these combined methods, achieving a maximum efficiency of 0.416 and a minimum entropy generation number of 0.118. Differences between barrel and hourglass inserts were minimal, primarily due to increased frictional losses with the hourglass type. Anand [17] analyzed entropy generation in nanofluid flow within a tube immersed in an isothermal fluid, using water-Al<sub>2</sub>O<sub>3</sub> and ethylene glycol-Al<sub>2</sub>O<sub>3</sub> nanofluids. The study showed that adding nanoparticles reduced entropy from heat transfer but increased it from fluid friction. Karabulut et al. [18] conducted a study on entropy generation and exergy gain in a thermal system featuring a copper straight pipe with a constant heat load, utilizing Graphene Oxide-Water nanofluid. The findings revealed that incorporating GO-Water nanofluid at an average concentration of 0.02% resulted in a significant 93.43% decrease in entropy production along the pipe. Varma et al. [19] the effect of duct shape on thermo-hydraulic performance using Al<sub>2</sub>O<sub>3</sub> nanofluids with computational fluid dynamics. The serpentine duct improved heat transfer by 86% compared to the circular duct, while the elliptical duct had the best performance due to lower pressure drop. Entropy analysis showed the highest increase in the square duct and the lowest in the elliptical duct. Taşkesen et al.[20] studied numerically forced convection in various channel shapes (cylindrical, square, rectangular, and triangular) using Fe<sub>3</sub>O<sub>4</sub>/water nanofluid under laminar flow. The findings indicated that cylindrical channels provide the highest heat transfer efficiency, achieving up to 77.6% better performance than triangular channels. Nanofluids

with higher nanoparticle concentrations exhibit reduced entropy generation rates compared to those with lower concentrations and to the base fluid. Specifically, a nanofluid with 5% nanoparticle concentration results in a 12.1% reduction in entropy generation, while 2% and 1% concentrations lead to 5.5% and 2.9% reductions, respectively, compared to pure water.

The literature indicates that various hybrid nanofluids have been studied in thermal systems to assess entropy generation and exergy gain. However, no research has specifically addressed entropy generation analysis for Graphene- $\text{Al}_2\text{O}_3$  nanofluid in heat exchanger tubes with different volume fractions under turbulent flow, particularly within a Reynolds number range of 20000 to 80000. Therefore, in this study, entropy production and exergy analysis were carried out for Graphene- $\text{Al}_2\text{O}_3$ /water nanofluid using a 10 mm inner diameter pipe applied at a constant heat flux of  $30 \text{ kW/m}^2$ . The working fluid was prepared by adding graphene and  $\text{Al}_2\text{O}_3$  nanoparticles, mixed in a 50:50 ratio, to water at volume concentrations of 0.1%, 0.3%, 0.5%, 0.7%, and 1%. The results were compared with the existing studies with other nanofluids, showing reasonable alignment and consistency. The main aim of this study is to determine the ideal conditions for minimizing entropy generation in a thermal system using second law thermodynamic analysis. In thermodynamics, the second law addresses irreversibility, which is closely related to entropy generation. Lower entropy production signifies a more efficient energy transfer process, where less energy is wasted as heat. By examining the system under various factors, such as different nanoparticle concentrations and flow rates, this study seeks to identify configurations that decrease entropy generation, thus improving the system's efficiency.

## **2. Material and Method**

### **2.1. Numerical Procedure**

The study conducted numerical simulations using the finite volume method in ANSYS Fluent 19. To improve the accuracy of turbulent flow modeling and better capture fluid mixing and instability, the  $k\text{-}\epsilon$  RNG turbulence model was employed for single-phase flow simulations. The SIMPLE (Semi-Implicit Method for Pressure-Linked Equations) algorithm was utilized to solve the pressure and velocity fields iteratively, ensuring fluid flow stability. For precise and accurate convective flow calculations, the QUICK (Quadratic Upstream Interpolation for Convective Kinematics) scheme was implemented. The convergence criterion was evaluated as  $1 \times 10^{-6}$ . The Equations 1, 2, and 3 used for this purpose are generally as follows :

Mass Conservation

$$\nabla(\rho\vec{V}) = 0$$

(1)

Momentum Conservation

$$\nabla(\rho\vec{V}\vec{V}) = -\nabla P + \nabla(\mu\nabla\vec{V})$$

(2)

Energy Conservation

$$\nabla(\rho c_p \vec{V}T) = \nabla(k\nabla T)$$

(3)

The k-ε turbulence model utilizes transport equations for  $k$  and  $\varepsilon$ , provided in Equations 4 and 5, respectively.

$$\frac{\partial(\rho k)}{\partial t} + \nabla \cdot (\rho U k) = \nabla \cdot \left( \left( \mu + \frac{\mu_t}{\sigma_k} \right) \nabla k \right) + P_k - \rho \varepsilon \quad (4)$$

$$\frac{\partial(\rho \varepsilon)}{\partial t} + \nabla \cdot (C_{\varepsilon 2} \rho \varepsilon) = \nabla \cdot \left( \left( \mu + \frac{\mu_t}{\sigma_\varepsilon} \right) \nabla \varepsilon \right) + \frac{\varepsilon}{k} (C_{\varepsilon 1} P_k) - P_k \quad (5)$$

$P_k$  defined as;

$$P_k = \mu_t \nabla U \cdot (\nabla U + \nabla U^T) - \frac{2}{3} \nabla \cdot U (3\mu_t \nabla \cdot U + \rho k) \quad (6)$$

In this turbulence model, the constant coefficients are as follows:  $C_\mu=0.087$ ,  $C_{\varepsilon 1}=1.43$ ,  $C_{\varepsilon 2}=1.90$ ,  $\sigma_k=1$ ,  $\sigma_\varepsilon=1.3$

$$\mu_t = \rho c_\mu k^2 / \varepsilon \quad (7)$$

## 2.2. Numerical Model and Boundary Conditions

For the CFD analysis, the 3D test tube model was divided into three main sections: inlet, test, and outlet sections. The study was conducted under turbulent flow conditions with Reynolds numbers between 20000 and 80000 using a 50:50 mixture of Graphene- $\text{Al}_2\text{O}_3$ /water nanofluid at 0.1%, 0.3%, 0.5%, 0.7% and 1% volume concentrations. A constant heat flux of  $30 \text{ kW/m}^2$  was applied to the test section and the inlet temperature was set as 300.15 K.

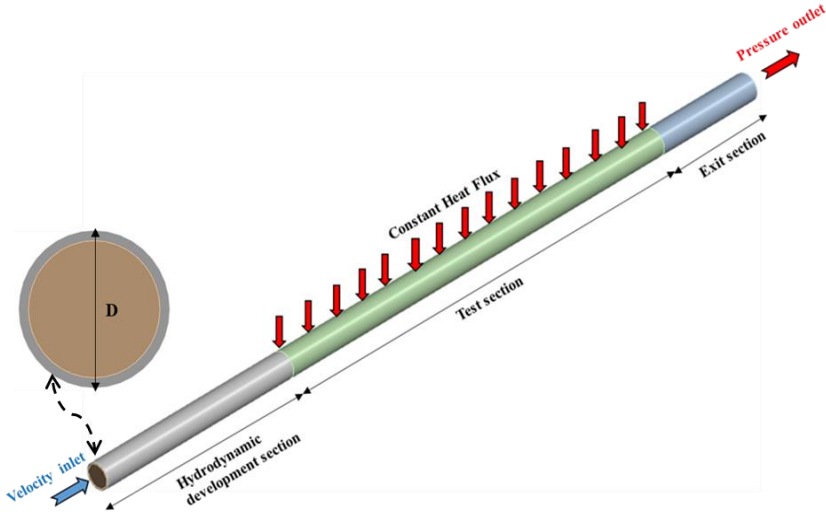


**Fig.1.** Numerical model

The tube diameter was 10 mm. The inlet region, designed to ensure that the flow reaches uniformity, was set at ten times the tube diameter (100 mm), which provides a transition from the initial unsteady state to a stable flow profile. The test section where the data were collected was 1000 mm long and served as the primary region for the measurements. At the outlet, a section five times the tube diameter (50 mm) was included to stabilize the outlet by preventing turbulence at the end of the tube. This structure provides a consistent flow pattern necessary for accurate data collection, reducing irregularities that could affect measurement reliability.

### 2.3. Thermophysical properties of hybrid nanofluids

The density [21], specific heat [22], thermal conductivity [23] and dynamic viscosity [24] equations used to calculate the thermophysical properties of hybrid nanofluids are given in equations 8, 9, 10, 11.

$$\rho_{hnf} = \varphi_{p1}\rho_{p1} + \varphi_{p2}\rho_{p2} + (1 - \varphi_{p1} - \varphi_{p2}) \rho_f \quad (8)$$

$$Cp_{hnf} = \frac{\varphi_{p1}(\rho_{p1}cp_{p1}) + \varphi_{p2}(\rho_{p2}cp_{p2}) + (1 - \varphi_{p1} - \varphi_{p2})(\rho_f cp_f)}{\rho_{nf}} \quad (9)$$

$$\mu_{hnf} = \mu_{bf}(1 - \varphi_{p1} - \varphi_{p2})^{-2.5} \quad (10)$$

$$k_{hnf} = \frac{(\varphi_{p1}k_{p1} + \varphi_{p2}k_{p2})/\varphi_{nf} + 2k_{bf} + 2(\varphi_{p1}k_{p1} + \varphi_{p2}k_{p2}) - 2(\varphi_{nf}k_{bf})}{(\varphi_{p1}k_{p1} + \varphi_{p2}k_{p2})/\varphi_{nf} + 2k_{bf} - 2(\varphi_{p1}k_{p1} + \varphi_{p2}k_{p2}) + \varphi_{nf}k_{bf}} \quad (11)$$

Table 1 lists the thermophysical properties of the base fluid and nanoparticles. These properties were incorporated into Equations (1-6) to calculate the density, specific heat, viscosity, and thermal conductivity of the hybrid nanofluids.

Table 1. Thermal and physical characteristics of the base fluid and nanoparticles

Propertie	Water	GnP	Al <sub>2</sub> O <sub>3</sub>
$\rho(\text{kg/m}^3)$	998.2	2250	3980
$C_p(\text{J/kg})$	4182	790	777
$k(\text{W/mK})$	0.6	3000	38

## 2.4. Governing equations

Once the thermophysical properties of the hybrid nanofluids were calculated, these values were input into ANSYS Fluent 19 for simulation purposes. The analyses yielded data, which were then used to compute several key parameters that describe the flow and heat transfer behavior. The Reynolds number was determined as shown in Equation 12.

$$Re = \frac{\rho U_{av} D}{\mu} \quad (12)$$

$U_{av}$  denotes the mean fluid velocity within the tube, and  $\rho$ ,  $\mu$  represent the hybrid nanofluid density and dynamic viscosity.

the total Nusselt number is defined as follows and  $k$  represent the thermal conductivity of the hybrid nanofluid.

$$Nu = \frac{hD}{k} \quad (13)$$

Equation 14 provides the formula for calculating the friction coefficient.

$$f = \frac{\Delta P}{\frac{1}{2} \rho U^2 \frac{L}{D}} \quad (14)$$

Here,  $\Delta P$  represent the difference in fluid pressure, and  $L$  signifies the length of the test region.

Entropy generation minimization involves designing and refining a system by analyzing fluid flow, heat and mass transfer, and material properties to reduce inefficiencies. Exergy analysis, on the other hand, employs thermodynamic principles to quantify how real systems deviate from ideal, perfectly efficient systems. This approach helps identify energy losses and areas for performance improvement. The total entropy generation rate in a tube can be expressed as the

sum of entropy generation due to heat transfer and fluid friction [26,27], as shown in Equation 15.

$$S'_{gen} = S'_{gen, heat} + S'_{gen, friction} \quad (15)$$

represents total entropy generation in a tube, combining:

$S'_{gen, heat}$  : Entropy from heat transfer, caused by temperature differences.

$S'_{gen, friction}$  : Entropy from fluid friction, due to pressure losses in flow.

Reducing these terms helps make the system more efficient by minimizing thermal and frictional irreversibilities.

$$\dot{S}'_{gen} = \frac{q'^2}{\pi T^2 k Nu} + \frac{32 \dot{m}^3 f}{\pi^2 \rho^2 T D^5} \quad (16)$$

T and  $\rho$  given in Equation 16 express the bulk properties.

$$N_s = \frac{S'_{gen,n}}{S'_{gen,s}} \quad (17)$$

The ratio of  $N_s$  given in Equation 17 compares entropy generation in a modified system  $S'_{gen,n}$  to a standard system  $S'_{gen,s}$ :

$N_s < 1$  : The modified system is more efficient (lower entropy generation),

$N_s = 1$  : No efficiency improvement,

$N_s > 1$  : The modified system is less efficient (higher entropy generation).

The Bejan number (Be) is a dimensionless parameter used to evaluate the performance of thermal systems by quantifying entropy generation. It is defined as the ratio of entropy generation due to heat transfer to the total entropy generation. The formula is:

$$Be = \frac{\dot{S}'_{gen,\Delta T}}{\dot{S}'_{gen,\Delta T} + \dot{S}'_{gen,\Delta P}} \quad (18)$$

where:  $\dot{S}'_{gen,\Delta T}$  represents entropy generation due to heat transfer (temperature differences),

$\dot{S}'_{gen,\Delta P}$  entropy generation due to fluid friction (pressure differences).

The Bejan number helps identify the dominant source of irreversibility in the system, guiding improvements to enhance system efficiency.

$Be = 1$  : Entropy generation is entirely due to heat transfer,

$Be = 0$  : Entropy generation is entirely due to fluid friction,

$0 < Be < 1$  : Both heat transfer and fluid friction contribute to entropy generation.

## 2.5. Mesh Independence Test and Validation

In numerical simulations, verifying mesh independence is crucial for ensuring reliable results. Mesh independence confirms that the solution does not significantly change with further increases in mesh density. For this study, the

impact on Nusselt number (Nu) and friction factor (f) at a Reynolds number of 20000 was evaluated.

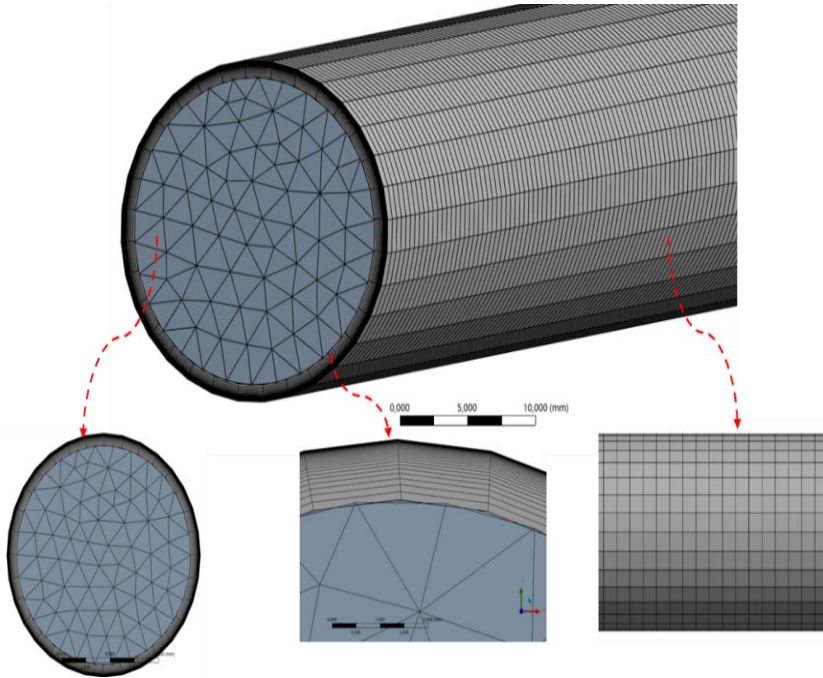


**Fig.2.** Mesh structure of the numerical model

Achieving a suitable  $y^+$  value in the recommended range of  $5 < y^+ < 30$  especially for high Reynolds numbers, ensures accurate boundary layer resolution. Then, the heat transfer efficiency was analyzed under defined boundary conditions and a mesh of 1,400,000 cells was selected after observing a deviation of less than 2% in Nu and f. The  $y^+$  value of the mesh was determined as 1.92 and the structure in Figure 2 was selected for further analysis.

In numerical studies, validating method accuracy is essential, often done by comparing results with established reference equations. In this study, the Gnielinski [28] and Blasius [29] equations were used, as outlined in equations 19 and 20, to verify the reliability of the numerical model. Results from these equations were compared to the simulation data, showing strong agreement as shown in Fig. 3 and Fig. 4. The maximum deviation observed was 13% for the Nusselt number and 7.2% for the friction coefficient.

$$Nu = \frac{(f/8)(Re_D - 1000)Pr}{1 + 12.7(f/8)^{1/2}(Pr^{2/3} - 1)} \quad (19)$$

$$f = 0.316 Re^{-0.25} \quad (20)$$

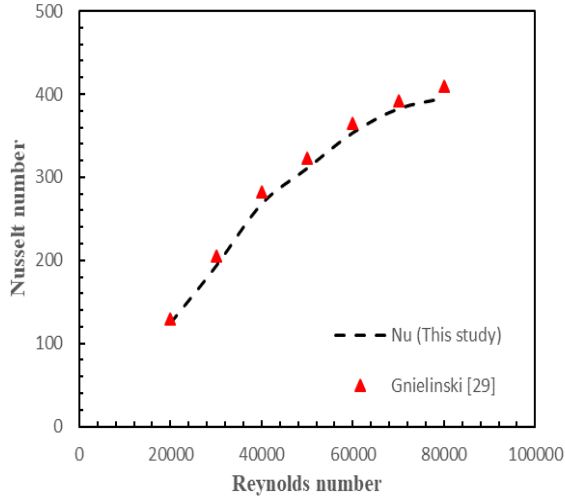


**Fig.3.** Validation of Nusselt number

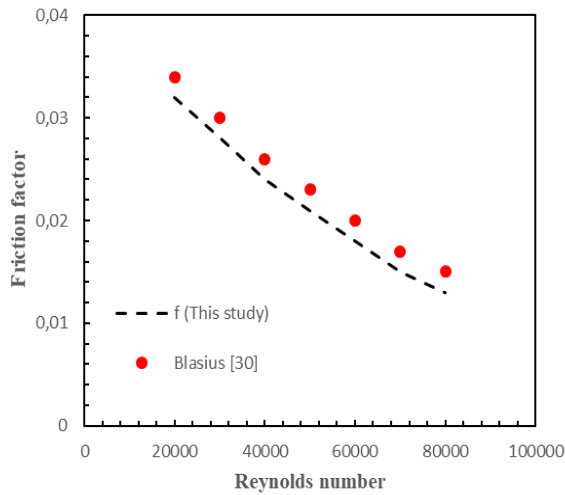
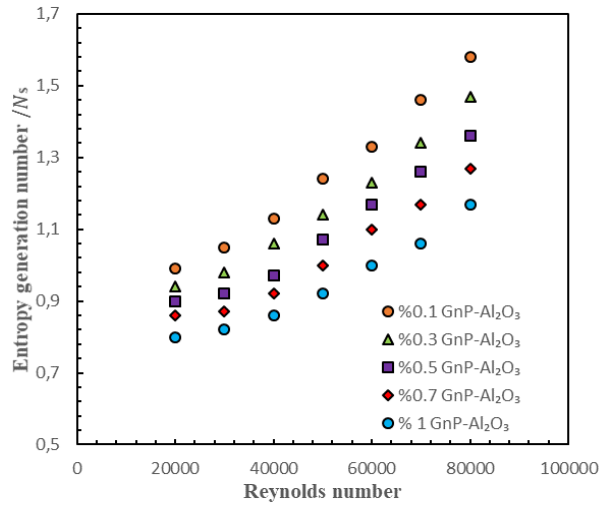


**Fig.4.** Validation of Friction factor

### 3. Results and Discussion

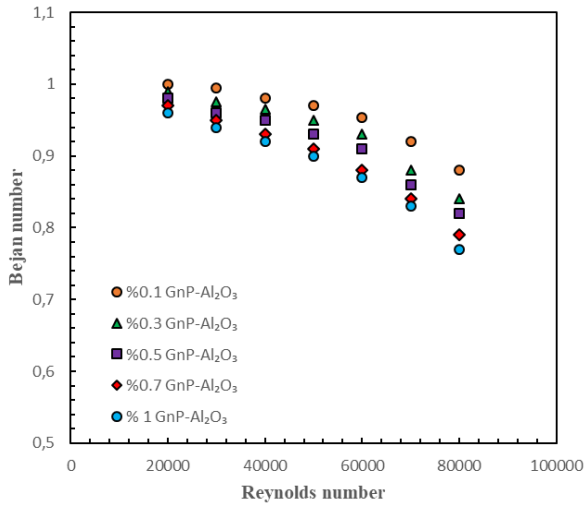
#### 3.1. Entropy Generation Analysis

Passive techniques in heat exchangers are designed to increase heat transfer rates without the need for additional external energy. These techniques include surface modifications, inserts, extended surfaces, or using advanced fluids like nanofluids, which enhance turbulence and improve heat exchange.



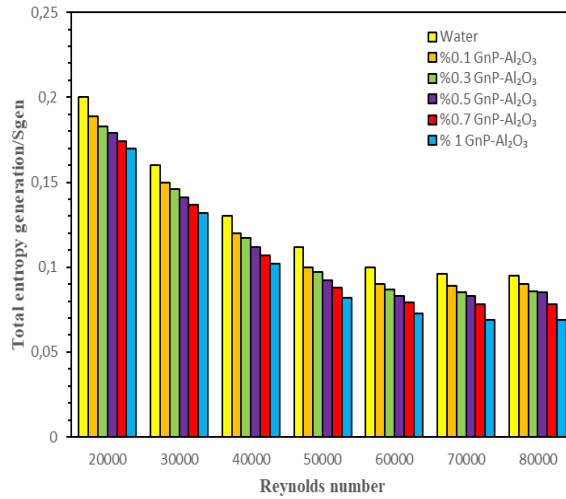
**Fig.5.** The change of the entropy generation number versus the Reynolds number

The use of nanofluids increases heat transfer due to higher thermal conductivity but can increase fluid viscosity, leading to higher pressure drops and greater entropy generation. The second law of thermodynamics analysis is crucial to comprehensively evaluating the effectiveness of these passive enhancement methods. This approach assesses not only the improvements in heat transfer but also the drawbacks associated with increased pressure drop by examining entropy generation [27]. By focusing on both thermal performance and energy losses, this analysis helps determine whether a passive technique is efficient and thermodynamically optimal for the system, ensuring a balance between improved heat transfer and minimized energy consumption. As shown in Figure 5, the entropy generation number increased with higher Reynolds numbers due to frictional irreversibility becoming more significant at high flow velocities. At very high flow rates, the frictional losses from increased fluid viscosity and turbulence become dominant, leading to an overall increase in the entropy generation number. As seen in Figure 5, for all cases where the  $N_s$  value remained below 1, this represented a thermodynamically advantageous state in which irreversibilities in the system were minimized. This indicated that the heat exchanger operated efficiently with an appropriate balance between heat transfer enhancement and frictional losses. The lowest entropy generation number was obtained as 0.8 using 1% Graphene- $\text{Al}_2\text{O}_3$  water nanofluid at the lowest Reynolds number of 20000. The Bejan number is another crucial factor in thermal systems because it identifies the main source of entropy generation—whether it's due to heat transfer or frictional losses.



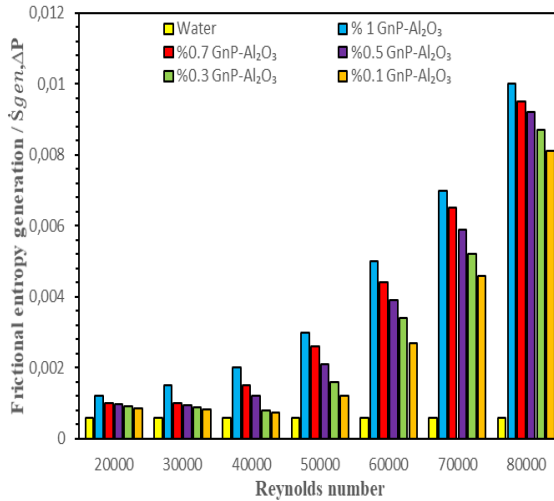
**Fig.6.** The change of the bejan number versus the Reynolds number

This optimizes system efficiency by pinpointing where energy losses occur, guiding design adjustments to reduce irreversibility, and balancing trade-offs between heat transfer enhancement and frictional losses for a more efficient system. Figure 6 shows the variation of Bejan number with Reynolds number and nanoparticle concentration. The Bejan number indicates the balance between heat transfer efficiency and total entropy generation. When the Bejan number is close to 1, heat transfer dominates entropy generation, signifying that frictional losses have minimal impact. As seen in Figure 6, the Be values approach 1 at lower Reynolds numbers, indicating that heat transfer is the primary factor in entropy generation for GnP-Al<sub>2</sub>O<sub>3</sub>-water nanofluids. However, as the Reynolds number increases, Be values decrease. This trend is explained by the increased frictional effects at higher Reynolds numbers. Consequently, frictional losses play a more significant role in entropy generation, becoming more influential than heat transfer in this regime.



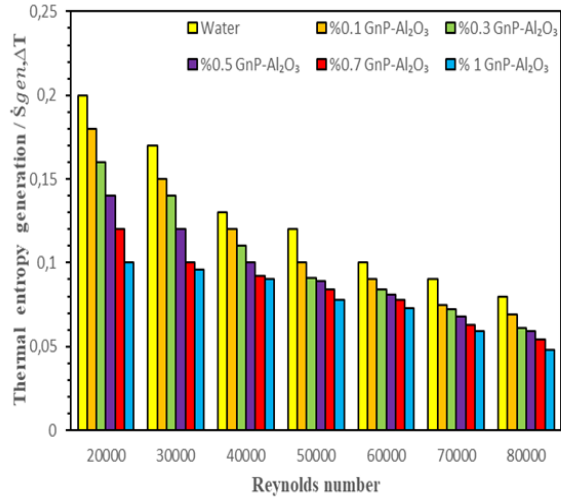
**Fig.7.** The change of the total entropy generation number versus the Reynolds number

Figure 7 illustrates how total entropy generation in the nanofluids varied with increasing Reynolds number and nanoparticle concentration. The data showed that total entropy generation decreased as both Reynolds number and nanoparticle concentrations increased. This reduction can be attributed primarily to the enhanced thermal conductivity of the nanofluids compared to the base fluid. Enhanced thermal conductivity improves heat transfer efficiency, which in turn reduces the temperature gradients within the fluid. Additionally, as  $Re$  increases, the flow becomes more turbulent, leading to better mixing and more uniform temperature distribution in the fluid. This improved mixing further reduces temperature gradients, contributing to lower total entropy generation. Compared to water, it was observed that the total entropy production decreased by 12.21%, 24.63%, 36.62%, 44.13%, and 52.15% at 0.1, 0.3, 0.5, 0.7, and 1% volume fractions of GnP-Al<sub>2</sub>O<sub>3</sub> nanofluids, respectively.



**Fig.8.** The change of the frictional entropy generation number versus the Reynolds number

As seen in Figure 8, frictional entropy generation increased with higher Reynolds numbers and nanoparticle concentrations. Higher Reynolds numbers enhanced the fluid velocity, increasing internal friction and frictional entropy generation. Additionally, higher nanoparticle concentrations made the fluid denser, leading to more collisions and interactions, which raised frictional resistance and frictional entropy generation [30]. As shown in Figure 9, thermal entropy generation decreased with higher Reynolds numbers and increased nanoparticle concentrations because they enhanced heat transfer. Higher Reynolds numbers improve fluid mixing and reduce the thermal boundary layer, lowering temperature gradients. Increased nanoparticle concentrations boost thermal conductivity, enabling efficient heat dissipation and further reducing temperature gradients, ultimately minimizing thermal entropy generation [31,32]. Maximum thermal entropy generation reductions were observed as 11.3%, 23.36%, 34.9%, 44.6, and 51.2% for volume fractions of GnP-Al<sub>2</sub>O<sub>3</sub> nanofluids 0.1%, 0.3%, 0.5%, 0.7%, and 1%, respectively, compared to water at the 20000 Reynolds number.



**Fig.9.** The change of the thermal entropy generation number versus the Reynolds number

### 3.2. Comparison with the literature

In this study, nanofluids prepared by adding GnP-Al<sub>2</sub>O<sub>3</sub> nanoparticles in the ratio of (50:50) were compared with the best configurations in the literature. Kanti et al. [33] carried out the entropy analysis of hybrid nanofluids having 0.1-0.75% volume fraction by adding red mud and graphene oxide nanoparticles in the ratio of (50:50). Marulasiddeshi et al. [34] prepared hybrid nanofluids containing Al<sub>2</sub>O<sub>3</sub>-CuO nanoparticles in the volume fraction range of 0-1% and carried out entropy generation analysis in the Reynolds number range of 7000-44662. Sundar et al. [35] prepared reduced graphene oxide nanoparticles with 0.5-2.0% volume fraction and carried out thermal entropy generation and exergy efficiency analyses. As seen in Figure 10, entropy generation decreases with increasing Reynolds number. This is because a higher Reynolds number makes the flow more turbulent, promoting better mixing within the fluid and reducing the temperature gradient, which in turn lowers entropy generation.

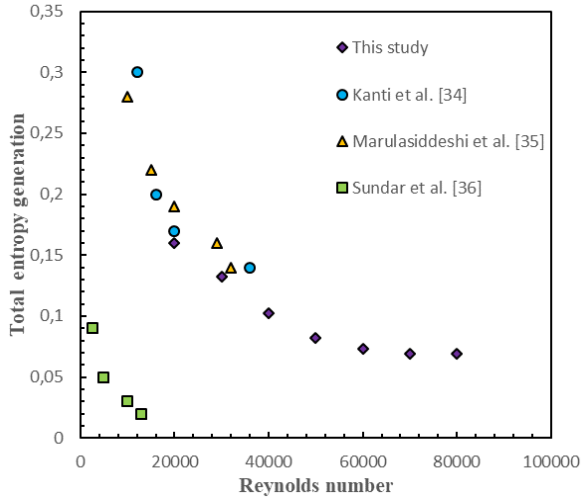


**Fig.10.** Comparison of total entropy generation with literature data

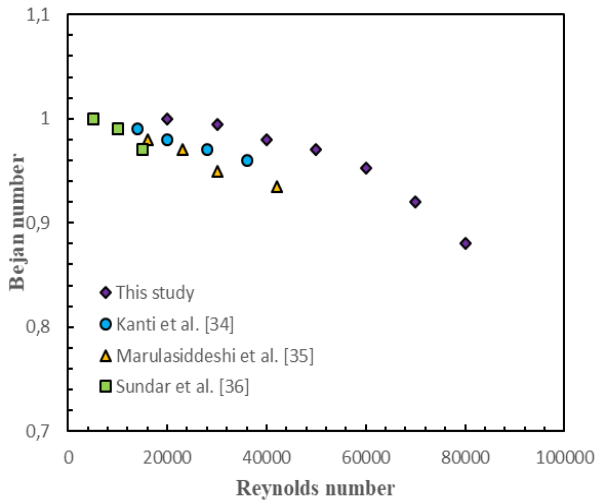


**Fig.11.** Comparison of Bejan number with literature data

As seen in Figure 10, the lowest entropy production at the same Reynolds number among the obtained values was observed in the  $\text{GnP-Al}_2\text{O}_3$  nanofluids used in this study. As seen in Figure 11, the Bejan number in the studies shows the same trend with increasing Reynolds number. At lower Reynolds numbers, Be values are close to 1, indicating that heat transfer is the main contributing factor to entropy generation.

#### 4. Conclusions

This study focused on analyzing the entropy generation of water-based graphene and  $\text{Al}_2\text{O}_3$  hybrid nanofluids at five different volume concentrations (ranging from 0.1% to 1%) in a circular tube, using CFD software. The analysis was performed under turbulent flow conditions with the  $k-\varepsilon$  RNG turbulence model, applying a constant surface heat flux, and varying the Reynolds number between 20000 and 80000. The results showed that as the volume fraction of the hybrid nanofluid increased, the dimensionless entropy generation followed a decreasing trend. The lowest entropy production number of 0.8 was achieved at a Reynolds number of 20000 using 1% Graphene- $\text{Al}_2\text{O}_3$  water nanofluid. Total entropy production analysis exhibited decreasing values in the range of % 52.15 -12.21 compared to water for binary GnP- $\text{Al}_2\text{O}_3$  nanofluids with the increase in Reynolds number. With higher nanofluid concentration, the system became thermodynamically more efficient and entropy production decreased. To summarize the reasons for this situation: The enhanced thermal conductivity and micro-convection of the nanofluids lower temperature gradients, while optimized concentration minimizes viscous dissipation. In turbulent flow, higher Reynolds numbers increase mixing and further reduce entropy production. Overall, these effects allow the system to operate closer to reversible conditions, with minimal energy lost, making the heat transfer process more thermodynamically efficient.

## References

- [1] Barai, R., Kumar, D., and Wankhade, A. 2023. Heat transfer performance of nanofluids in heat exchanger: a review. **Journal of Thermal Engineering**. **9** (1), 86–106.
- [2] Bacha, H. Ben, Ullah, N., Hamid, A., and Shah, N.A. 2024. A comprehensive review on nanofluids: Synthesis, cutting-edge applications, and future prospects. **International Journal of Thermofluids**. **22** (November 2023), 100595.
- [3] Rahman, M.A., Hasnain, S.M.M., Pandey, S., Tapalova, A., Akylbekov, N., and Zairov, R. 2024. Review on Nanofluids: Preparation, Properties, Stability, and Thermal Performance Augmentation in Heat Transfer Applications. **ACS Omega**.
- [4] Keklikcioğlu, O. 2021. Grafen-Demir Oksit Hibrit Nanoakışkanı Kullanılan Bir Isı Değiştirici Borusunun Entropi Üretim Analizi. **European Journal of Science and Technology**. (24), 398–404.
- [5] Rea, U., McKrell, T., Hu, L. wen, and Buongiorno, J. 2009. Laminar convective heat transfer and viscous pressure loss of alumina-water and zirconia-water nanofluids. **International Journal of Heat and Mass Transfer**. **52** (7–8), 2042–2048.
- [6] Guo, W., Zhai, Y., Huang, X., and Li, Z. 2024. Optimizing stability and enhancing flow boiling heat transfer performance of Al<sub>2</sub>O<sub>3</sub>-TiO<sub>2</sub>/water hybrid nanofluids. **Experimental Thermal and Fluid Science**. **155** (July 2023), 111177.
- [7] Saini, R., Gupta, B., Prasad Shukla, A., Singh, B., Baredar, P., and Bisen, A. 2023. CFD analysis of heat transfer enhancement in a concentric tube counter flow heat exchanger using nanofluids (SiO<sub>2</sub>/H<sub>2</sub>O, Al<sub>2</sub>O<sub>3</sub>/H<sub>2</sub>O, CNTs/H<sub>2</sub>O) and twisted tape turbulators. **Materials Today: Proceedings**. **76** 418–429.
- [8] Balaji, T., Rajendiran, S., Selvam, C., and Lal, D.M. 2021. Enhanced heat transfer characteristics of water based hybrid nanofluids with graphene nanoplatelets and multi walled carbon nanotubes. **Powder Technology**. **394** 1141–1157.
- [9] Naghash, A., Sattari, S., and Rashidi, A. 2016. Experimental assessment of convective heat transfer coefficient enhancement of nanofluids prepared from high surface area nanoporous graphene. **International Communications in Heat and Mass Transfer**. **78** 127–134.
- [10] Behrozifard, A., Goshayeshi, H.R., Zahmatkesh, I., Chaer, I., Salahshour, S., and Toghraie, D. 2024. Experimental optimization of the performance of a plate heat exchanger with Graphene oxide/water and Al<sub>2</sub>O<sub>3</sub>/water

- nanofluids. **Case Studies in Thermal Engineering**. **59** (April), 104525.
- [11] Zolfalizadeh, M., Heris, S.Z., Pourpasha, H., Mohammadpourfard, M., and Meyer, J.P. 2023. Experimental Investigation of the Effect of Graphene/Water Nanofluid on the Heat Transfer of a Shell-and-Tube Heat Exchanger. **International Journal of Energy Research**. **2023**.
- [12] Bejan, A. 1996. Entropy Generation Minimization. **CRC Press, Boca Taron**.
- [13] Şahin, A.Z. 1998. A second law comparison for optimum shape of duct subjected to constant wall temperature and laminar flow. **Heat and Mass Transfer/Waerme- Und Stoffuebertragung**. **33** (5–6), 425–430.
- [14] Moghaddami, M., Mohammadzade, A., and Esfehiani, S.A.V. 2011. Second law analysis of nanofluid flow. **Energy Conversion and Management**. **52** (2), 1397–1405.
- [15] Singh, P.K., Manikandan, R., Kumar, R., Verma, R., Kulandaivel, A., Kamesh, V. V, et al. 2024. Enhancing Thermal Energy and Exergy Harvesting in Concentrated Solar Power Systems using Graphene-ZrO<sub>2</sub>/Water Hybrid Nanofluid: An Experimental Study. **Process Safety and Environmental Protection**. **191** (PA), 1461–1471.
- [16] Mertaslan, O.M. and Keklikcioglu, O. 2024. Investigating heat exchanger tube performance: second law efficiency analysis of a novel combination of two heat transfer enhancement techniques. **Journal of Thermal Analysis and Calorimetry**. (0123456789),.
- [17] Anand, V. 2015. Entropy generation analysis of laminar flow of a nanofluid in a circular tube immersed in an isothermal external fluid. **Energy**. **93** 154–164.
- [18] Karabulut, K., Ocak, N. 2023. Investigation of entropy generation and exergy gain of GO-water nanofluid depending on working conditions. **EJONS INTERNATIONAL JOURNAL**. **7**(1).
- [19] Varma, A. and Nidhul, K. 2024. Thermo-hydraulic and entropy generation analysis of nanofluid flow with variable properties in various duct cross sections: a 3-D two-phase approach. **Journal of Thermal Analysis and Calorimetry**. **149** (9), 4209–4225.
- [20] Taskesen, E., Tekir, M., Gedik, E., and Arslan, K. 2021. Numerical investigation of laminar forced convection and entropy generation of Fe<sub>3</sub>O<sub>4</sub>/water nanofluids in different cross-sectioned channel geometries. **Journal of Thermal Engineering**. **7** (7), 1752–1767.
- [21] Pak, B.C. and Cho, Y.I. 1998. Hydrodynamic and heat transfer study of dispersed fluids with submicron metallic oxide particles. **Experimental Heat Transfer**. **11** (2), 151–170.

- [22] Xuan, Y. and Roetzel, W. 2000. Conceptions for heat transfer correlation of nanofluids. **International Journal of Heat and Mass Transfer**. **43** (19), 3701–3707.
- [23] Xu, J.Z., Gao, B.Z., and Kang, F.Y. 2016. A reconstruction of Maxwell model for effective thermal conductivity of composite materials. **Applied Thermal Engineering**. **102** 972–979.
- [24] H.C., B. 1952. The viscosity of concentrated suspensions and solutions. **J. Chem. Phys.** **20** 571.
- [25] Sajjad, R., Hussain, M., Khan, S.U., Rehman, A., Khan, M.J., Tlili, I., et al. 2024. CFD analysis for different nanofluids in fin prolonged heat exchanger for waste heat recovery. **South African Journal of Chemical Engineering**. **47** (July 2023), 9–14.
- [26] Bejan, A. 2001. Thermodynamic optimization of geometry in engineering flow systems. **Exergy Int J.** **1**:269–77.
- [27] Bejan, A. 1995. Entropy generation minimization: the method of thermodynamic optimization of finite-size systems and finite-time processes. **1st Ed. Bejan A, Editor. New York: CRC Press LLC.**
- [28] Gnielinski, V. 1976. New equations for heat and mass transfer in turbulent pipe and channel flow. **Int. Chem. Eng.** **16** 359–368.
- [29] H. Blasius 1913. The Law of Similarity for Frictions in Liquids, "Notices of research in the field of engineering. **Not. Res. F. Eng.,** **131** 1–41.
- [30] Kanti, P.K., Sharma, K. V., Minea, A.A., and Kesti, V. 2021. Experimental and computational determination of heat transfer, entropy generation and pressure drop under turbulent flow in a tube with fly ash-Cu hybrid nanofluid. **International Journal of Thermal Sciences**. **167** (March), 107016.
- [31] Ahammed, N., Asirvatham, L.G., and Wongwises, S. 2016. Entropy generation analysis of graphene–alumina hybrid nanofluid in multiport minichannel heat exchanger coupled with thermoelectric cooler. **International Journal of Heat and Mass Transfer**. **103** 1084–1097.
- [32] Humnic, G. and Humnic, A. 2020. Entropy generation of nanofluid and hybrid nanofluid flow in thermal systems: A review. **Journal of Molecular Liquids**. **302**.
- [33] Kanti, P.K., Vicki Wanatasanappan, V., Mahjoub Said, N., and Sharma, K. V. 2024. Stability, thermophysical properties, forced convective heat transfer, entropy minimization and exergy performance of a novel hybrid nanofluid: Experimental study. **Journal of Molecular Liquids**. **410** (April), 125571.
- [34] H B, M., Kanti, P.K., Prakash, S.B., and Sridhara, S.N. 2023.

- Investigation of entropy generation and thermohydraulic characteristics of Al<sub>2</sub>O<sub>3</sub>–CuO hybrid nanofluid flow in a pipe at different inlet fluid temperatures. **International Journal of Thermal Sciences**. **193** (July), 108541.
- [35] Sundar, L. S., Chandra Mouli, K. V., Mewada, H. K., & Sousa, A.C. 2024. Thermal entropy generation and exergy efficiency analysis of rGO/water nanofluid in a tube under turbulent regime using experimental and fully connected neural network. **Diamond and Related Materials**. **145**, 11106.

## **Chapter 7**

### **Investigating the Effect of Dimpled Tubes on Thermal Performance and Flow Resistance**

**Fatma OFLAZ<sup>1</sup>**

---

<sup>1</sup> Firat University, Faculty of Technology, Automotive Engineering, Elazığ, Turkey  
Email: [fteber@firat.edu.tr](mailto:fteber@firat.edu.tr), ORCID NO: 0000-0002-9636-5746

## 1. Introduction

The incorporation of dimpled tubes into heat exchanger designs is one of the commonly used methods to enhance heat transfer and thermal performance. The use of surface dimples can significantly increase heat transfer by promoting more efficient fluid dynamics. The dimples inside the tubes cause localized disturbances in the fluid flow, generating turbulence. This turbulence enhances the mixing of fluid layers near the tube walls, which significantly improves heat transfer [1]. In smooth tubes, a boundary layer often forms where the fluid near the wall remains relatively stagnant, reducing heat transfer efficiency. However, the dimples disrupt this boundary layer, allowing for more direct contact between the fluid and the tube surface, leading to more effective heat exchange. Several previous studies have demonstrated that corrugated tube heat exchangers offer significantly better thermal performance compared to traditional smooth tubes [2–5]. Farsad et al. [6] compared the heat transfer performance between a Dimpled-Protruded tube and a smooth tube. Their findings indicated that the small vortices generated in the dimpled tube enhanced interfacial heat transfer. The rough surface of the dimpled tube led to a significant 36.21% increase in heat transfer, though it also resulted in higher friction losses. Firoozi et al. [7] conducted a numerical study on the hydrothermal performance of flow within tubes featuring spherical dimples, exploring various geometrical parameters. They analyzed a three-dimensional steady flow using both water and water-based nanofluids as working fluids, with Reynolds numbers ranging from 500 to 4000. Their findings indicated a notable improvement in overall performance, particularly when using water-based nanofluids, as a result of optimizing the dimple parameters. The maximum thermal enhancement factor (TEF) achieved was approximately 3.1. Li et al. focused on optimizing the geometry of dimpled tubes to improve the thermal hydraulic performance in single-phase flow. Their study revealed that the modified surfaces provide a larger heat transfer area and increased turbulence, which leads to enhanced heat exchange efficiency [8]. Nazari et al. [9] investigated how dimple depth, quantity, and arrangement impact flow and heat transfer properties in turbulent flow. Their findings showed that the average Nusselt number was greater for dimpled surfaces compared to smooth plates. However, a drawback of this method is the increased pressure drop, attributed to higher frictional drag and the formation of recirculation zones within the dimples. Manoram et al. [10] conducted both numerical and experimental studies to examine the impact of dimples and their design variables on the hydrothermal performance of a solar thermal collector. They used simulations to explore changes in dimple pitch-to-diameter ratio, dimple count, and mass flow rate. The results showed that the Nusselt number increased by a factor of 2.5 for

the dimpled tube with a pitch-to-diameter ratio of 3 and a mass flow rate of 2.5 kg/min. However, this configuration also caused the friction factor to rise by 11.1% compared to the smooth reference tube. Zheng et al. [11] carried out a numerical study on the impact of dimples in helically coiled mini-tubes, focusing on performance evaluation criteria (PEC) and entropy generation. The results showed that the dimpled tubes had a two-fold increase in both heat transfer and friction coefficients. They also noted that the introduction of dimples significantly lowered the entropy generation and reduced the maximum wall temperature. Sabir et al. [12] conducted a numerical study on the hydrothermal performance of tubes featuring dimples with different geometric pitches across a range of Reynolds numbers. Their findings revealed that the performance of dimpled tubes varies considerably with changes in dimple pitch and Re. Specifically, they discovered that the ellipsoidal 45° and teardrop dimpled tubes, when optimized for pitch, improved thermal-hydraulic performance by as much as 45.7% and 31.2%, respectively. Nascimento et al. [13] utilized shallow square dimples in flat tubes to investigate heat transfer enhancements in compact heat exchangers, with potential applications in vehicle radiators. Their study achieved augmentation factors as high as 2.28, allowing for greater heat dissipation without increasing the pumping power. The hydrothermal performance of models with varying dimple diameters, spaced at specific intervals along the tube, was assessed under single-phase flow conditions for Reynolds numbers between 3000 and 8000 [14]. The study revealed that dimpled tubes enhanced heat transfer relative to smooth tubes, with the Nusselt number doubling in comparison. The highest overall performance metrics were 1.22 for Model A and 1.33 for Model B. The thermo-hydraulic performance of Fe<sub>3</sub>O<sub>4</sub>/H<sub>2</sub>O nanofluid flow within dimpled tubes under the effect of a magnetic field was numerically investigated by Gürdal et al. [15]. The objective of the study was to generate comprehensive numerical data on turbulent flow behavior within spherical dimpled tubes, contributing to the optimization and design of advanced, highly efficient thermal energy storage systems. Simulations were conducted with Reynolds numbers ranging from 10000 to 50000 under a constant heat flux of 20 kW/m<sup>2</sup>. The results indicated that the Nusselt number increased as the Reynolds number increased and the pitch ratio decreased. Among the different dimple geometries, the one with a pitch-to-diameter ratio (P/d) of 7.50 was found to be the most effective. Kaood et al. [16] conducted a numerical study on the flow characteristics within dimpled conical tube heat exchangers with varying diameter ratios. Their investigation analyzed the Nusselt number (Nu), friction factor (f), and thermal enhancement factor (TEF) across different diameter ratios and a wide range of Reynolds numbers. The results showed that tubes with a nozzle configuration and

a diameter ratio of 1.5 achieved the highest TEF, with an improvement of approximately 30% compared to the reference tube geometry. Eimsa et al. [17] studied the thermo-hydraulic performance of dimpled tubes equipped with twisted tape inserts, using  $\text{TiO}_2$ -water nanofluids as the working fluid. The experimental results demonstrated that the combination of dimpled tubes and twisted tapes provided higher heat transfer rates compared to using dimpled tubes alone. The findings also showed that dimple angle, twist ratio, and  $\text{TiO}_2$ -water nanofluid concentration had a significant impact on the overall performance. Among the tested configurations, the dimpled tube with a  $45^\circ$  dimple angle achieved the greatest heat transfer enhancement. Heat transfer, represented by the Nusselt number (Nu), increased with a lower twist ratio and higher nanofluid concentrations. Keklikcioğlu [18] evaluated the heat transfer and fluid flow characteristics in tubes with circular dimples using hybrid nanofluids. The study emphasized that the combined use of hybrid nanofluids and dimples significantly increased heat transfer efficiency, with the Nusselt number increasing as the Reynolds number increased. Although the presence of dimples led to an increase in friction factors, the overall thermohydraulic performance remained positive, resulting in a net energy gain. The study concluded that combining hybrid nanofluids with dimpled tube surfaces enhanced heat exchanger efficiency by improving both thermal and hydraulic performance.

This study aims to investigate how the use of dimple protrusions on the outer surface of a heat exchanger tube can enhance heat transfer rates. These dimples are arranged in a pattern with varying pitch distances. The heat exchanger tube is filled with water maintained at a constant temperature to evaluate the effect of the dimple arrangement on overall heat transfer performance. The primary function of the dimples is to disturb the flow, increase turbulence, and improve heat exchange efficiency.

## **2. Material and Methods**

### **2.1. Numerical model and boundary conditions**

In this study, the 3D test tube analyzed using CFD software is divided into three sections: the inlet, test, and outlet regions, as shown in Figure 1. The analysis was conducted under turbulent conditions, with Reynolds numbers ranging from 10000 to 50000, and a constant heat flux of  $30 \text{ kW/m}^2$  was applied to the test region. Boundary conditions for the system were defined by a velocity inlet at the entry and a pressure outlet at the exit, where the outlet pressure was set to zero gauge pressure.

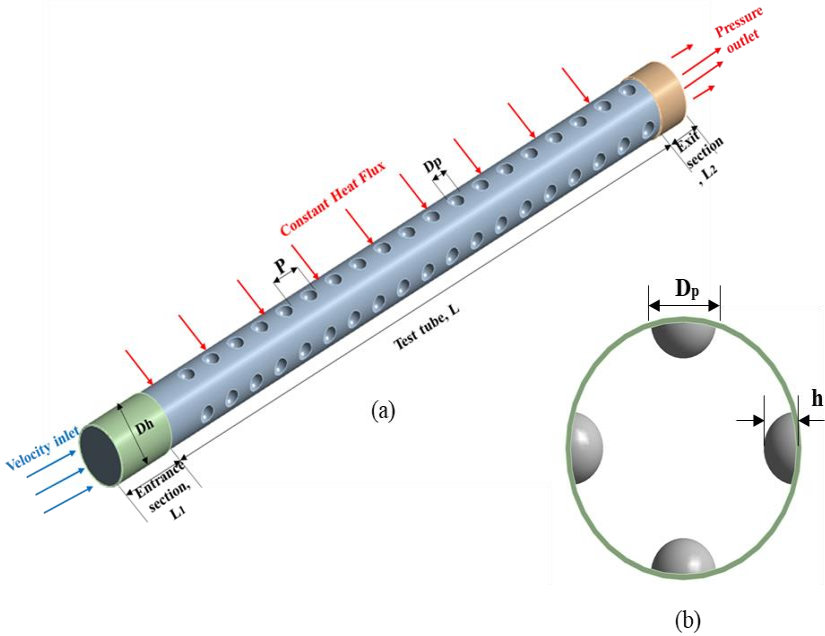


**Fig.1.** (a) Geometrical characteristics of the numerical model, (b) Dimpled pipe (Front View)

The inlet temperature was 293.15 K and the inlet velocity was varied based on the Reynolds numbers. The tube's dimensions were chosen to ensure hydrodynamically and thermally fully developed flow, with a wall thickness of 2 mm and an internal diameter ( $D_h$ ) of 20 mm. Dimples, each 4 mm in diameter, were placed on the tube's surface. The dimple diameter ( $D_p$ ), depth ( $h$ ), and pitch ( $P$ ) are illustrated in Table 2. The entrance region, designed to allow the flow to become uniform, is defined as ten times the tube diameter (200 mm), meaning the flow starts unstable but transitions to laminar over this distance. The test region, where flow is stabilized and measurements are taken, extends 1000 mm and serves as the critical area for collecting experimental data. The exit region, modelled to be five times the tube diameter (100 mm), facilitates a smooth flow at the tube's end. This arrangement prevents chaotic exit flow, which could compromise the reliability of experimental data. The water used as the working fluid is assumed to be incompressible, steady, and in continuous flow and its 293.15 K properties are given in the Table 1. These parameters were carefully selected to optimize flow conditions and enhance the accuracy of the obtained results.

Table 1. Properties of water at 293.15 K [19].

Water (293.15 K)	$\rho$	$\mu$	$c_p$	$k$
	998.0 kg/m <sup>3</sup>	1.002E-3 kg/ms	4185 j/kgK	0.598 w/mK

The geometric parameters of the numerical model are explained in Figure 1 (a), (b), and the values of these parameters are provided in Table 2.

Table 2. Values of geometrical characteristics of numerical model.

Defination	Symbol	Value (mm)
Tube Diameter	Dh	20
Dimple diameter	Dp	4
Dimple pitch	P	10-40
Dimple height	h	1.5
Test Section	L	1000
Entrance Section	L1	200
Exit Section	L2	100

## 2.2. Solution methodology

In this study, numerical analysis was performed using the finite volume method, a commonly applied approach for addressing fluid flow and heat transfer challenges, within ANSYS Fluent 19. The k- $\epsilon$  RNG (Re-Normalization Group) turbulence model was selected due to its effectiveness in modeling turbulent flows, particularly in scenarios involving significant flow separation and swirling. The SIMPLE (Semi-Implicit Method for Pressure Linked Equations) algorithm was employed to solve the flow equations. This algorithm is widely used to couple pressure and velocity in incompressible flow simulations. For convective transport evaluation, the QUICK (Quadratic Upstream Interpolation for Convective Kinematics) scheme was utilized, offering enhanced accuracy compared to simpler schemes. The convergence criteria were set at  $1 \times 10^{-6}$  for continuity (to ensure mass conservation), velocity, energy, and the turbulence parameters k (turbulent kinetic energy) and  $\epsilon$  (turbulent dissipation rate), ensuring precise and reliable results. The k- $\epsilon$  RNG model relies on three essential conservation equations: mass, momentum, and energy, which are fundamental for characterizing fluid flow. These are mathematically represented in Equations 1, 2, and 3, corresponding to the laws of mass conservation, momentum conservation, and energy conservation, respectively.

Mass Conservation

$$\nabla(\rho\vec{V}) = 0 \quad (1)$$

Momentum Conservation

$$\nabla(\rho\vec{V}\vec{V}) = -\nabla P + \nabla(\mu\nabla\vec{V}) \quad (2)$$

Energy Conservation

$$\nabla(\rho c_p \vec{V}T) = \nabla(k\nabla T) \quad (3)$$

The k-ε turbulence model determines the values of k and ε by solving differential equations that describe the behavior of these turbulent properties.

$$\frac{\partial(\rho k)}{\partial t} + \nabla \cdot (\rho U k) = \nabla \cdot \left( \left( \mu + \frac{\mu_t}{\sigma_k} \right) \nabla k \right) + P_k - \rho \varepsilon \quad (4)$$

$$\frac{\partial(\rho \varepsilon)}{\partial t} + \nabla \cdot (\rho U \varepsilon) = \nabla \cdot \left( \left( \mu + \frac{\mu_t}{\sigma_\varepsilon} \right) \nabla \varepsilon \right) + \frac{\varepsilon}{k} (C_{\varepsilon 1} (P_k) - C_{\varepsilon 2} \rho \varepsilon) \quad (5)$$

$P_k$  defined as;

$$P_k = \mu_t \nabla U \cdot (\nabla U + \nabla U^T) - \frac{2}{3} \nabla \cdot U (3\mu_t \nabla \cdot U + \rho k) \quad (6)$$

The constant coefficients in this turbulence model are given as:  $C_\mu = 0.087$ ,  $C_{\varepsilon 1} = 1.43$ ,  $C_{\varepsilon 2} = 1.90$ ,  $\sigma_k = 1$ , and  $\sigma_\varepsilon = 1.3$ .

$$\mu_t = \rho C_\mu k^2 / \varepsilon \quad (7)$$

### 2.3. Data acquisition

In the analysis conducted using ANSYS Fluent 19, the resulting data were utilized to calculate several key parameters, including the Reynolds number (Re), Nusselt number (Nu), friction factor (f), and the thermohydraulic performance coefficient. These parameters are essential for assessing the flow and heat transfer characteristics of the system. Here's an explanation of each:

**Reynolds Number (Re):** The Reynolds number is a dimensionless quantity that indicates whether the flow is laminar or turbulent. It is calculated based on the fluid velocity, characteristic length (in this case, the tube diameter), and fluid properties such as density and viscosity. The equation 8 for Re is typically given by:

$$Re = \frac{\rho v D}{\mu} \quad (8)$$

where  $\rho$  is the fluid density,  $v$  is the fluid velocity,  $D$  is the characteristic length, and  $\mu$  is the dynamic viscosity of the fluid.

**Nusselt Number (Nu):** The Nusselt number represents the ratio of convective to conductive heat transfer. It helps quantify the heat transfer enhancement in the system. Nu can be calculated using the relation between the heat transfer coefficient, characteristic length, and the thermal conductivity of the fluid as shown in equation 9:

$$Nu = \frac{hD}{k} \quad (9)$$

where  $h$  is the convective heat transfer coefficient,  $D$  is the characteristic length, and  $k$  is the thermal conductivity of the fluid.

**Friction Factor (f):** The friction factor quantifies the resistance to fluid flow due to friction along the surface of the tube. It is related to pressure loss in the system and can be calculated from the equation 10, typically used for turbulent flows:

$$f = \frac{\Delta P}{\frac{1}{2}\rho v^2 \frac{L}{D}} \quad (10)$$

where  $\Delta P$  is the pressure drop,  $\rho$  is the fluid density,  $v$  is the velocity,  $D$  is the tube diameter, and  $L$  is the length of the tube.

**Thermohydraulic Performance Coefficient:** This coefficient combines both the thermal and hydraulic performance of the system, giving a comprehensive view of how efficiently the system operates. It is typically expressed as a ratio of the Nusselt number to the friction factor, often normalized with respect to a smooth tube as shown in equation 11 :

$$\eta = (Nu/Nu_o) (f/f_o)^{1/3} \quad (11)$$

where  $Nu_o$  and  $f_o$  are the Nusselt number and friction factor for the reference smooth tube.

### 3. Results and Discussion

#### 3.1. Mesh independence

In order to guarantee that the numerical results are not influenced by the mesh size or the number of computational cells, a grid independence study was performed before conducting the main numerical analysis. This process involves running simulations using multiple grid resolutions, ranging from coarse to fine, to assess how the solution changes with varying grid densities. The goal of this study is to identify a grid size that provides accurate and stable results without further refinement significantly altering the outcomes. By comparing key parameters, such as pressure, temperature, and velocity, across different grid sizes, the smallest grid that yields consistent results is selected. This ensures that the solution is "grid-independent," meaning that any further increase in the number of cells will not significantly impact the accuracy of the results, thereby optimizing computational resources while maintaining precision in the analysis. The  $y^+$  value is a key parameter that assesses the mesh quality, and an appropriate  $y^+$  value ensures that the mesh accurately resolves the boundary layer. For high Reynolds number flows, the optimal range for  $y^+$  is  $5 < y^+ < 30$  [20], which is crucial for capturing flow details within the boundary layer effectively. Several

mesh structures were tested at a Reynolds number of 10000, and the model with 1,92 million elements was selected for all analyses, where deviations in Nu and f remained under 2%. In this study, the  $y^+$  value for the mesh structure was calculated as 1.43.

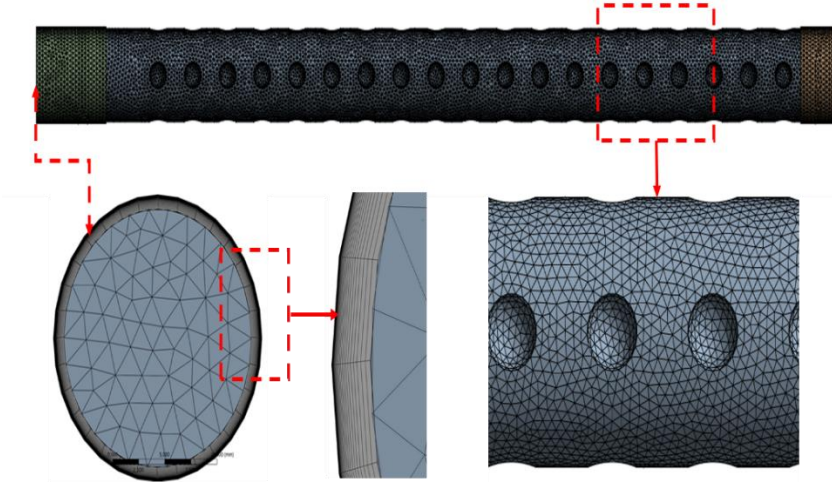


**Fig. 2.** Mesh structure of the numerical model

### 3.2. Validation of the numerical procedure

Before beginning the primary research, the numerical analysis was validated by comparing the results with established data from the literature. This validation process is critical to ensuring the accuracy and reliability of the numerical model. Specifically, the numerical results for a smooth tube were compared against well-known empirical correlations. For the Nusselt number (Nu), which measures heat transfer efficiency, the results were compared with the correlations developed by Gnielinski [21] and Petukhov [22]. These correlations are commonly used for predicting the average Nu number in smooth tubes under turbulent flow conditions.

$$Nu = \frac{(f/8)(Re_D - 1000)Pr}{1 + 12.7(f/8)^{\frac{1}{2}}\left(\frac{2}{Pr^{\frac{2}{3}} - 1}\right)} \quad (12)$$

$$Nu = \frac{(f/8)Re Pr}{1.07 + 12.7(f/8)^{\frac{1}{2}}\left(\frac{2}{Pr^{\frac{2}{3}} - 1}\right)} \quad (13)$$

Figure 3 illustrates that the Nusselt number increases as the Reynolds number increases. This is attributed to the enhanced turbulent mixing with higher Reynolds numbers, leading to more efficient heat transfer. Figure 3 shows that the numerical results align closely with the established equations when evaluating

the Nusselt number. For the smooth heat exchanger tube using water as the working fluid, the maximum observed error in the Nusselt number is  $\pm 11.35\%$ .

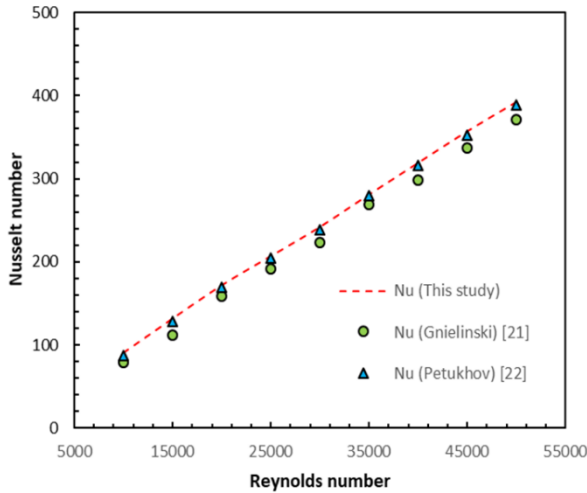


**Fig.3.** Comparison of Nusselt Number numerical results with literature

For the friction factor ( $f$ ), which indicates the resistance to fluid flow, the numerical results were compared with the correlations provided by Petukhov [22] and Blasius [23]. These correlations are widely recognized for their accuracy in estimating the average friction factor for smooth tubes in turbulent regimes. The equations used in the validation procedure are given in Equations (12), (13), (14), and (15). By comparing the numerical results with these established correlations, the accuracy of the simulation model can be confirmed. If the results closely align, it indicates that the numerical analysis can reliably predict heat transfer and flow behavior, ensuring confidence in subsequent analyses involving more complex geometries or conditions.

$$f = 0.316Re^{-0.25} \tag{14}$$

$$f = (0.790 \ln Re - 1.64)^{-2} \tag{15}$$

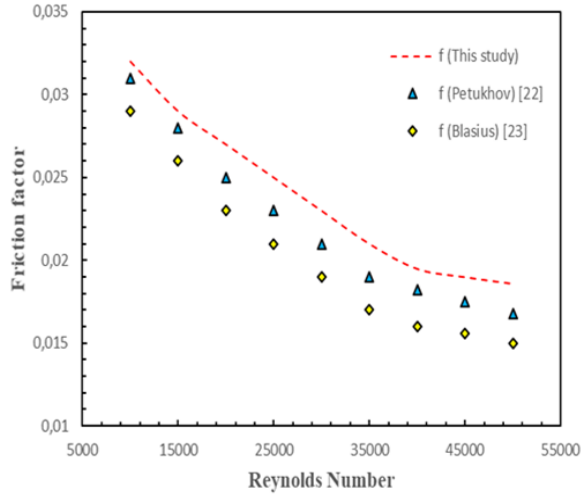


**Fig.4.** Comparison of Friction factor numerical results with literature

Figure 4 shows that the friction coefficient is inversely proportional to the Reynolds number and decreases with increasing Re values. The maximum deviation value in f is 13.22%.

### 3.3. Heat transfer and friction factor

Reducing the pitch length between dimples results in more dimples on the surface, which disrupts the fluid flow and creates turbulence. This turbulence breaks up the boundary layer, where the fluid tends to move more slowly near a smooth surface. The dimples generate eddies, enhancing the mixing of cooler and hotter fluid layers, thus improving heat transfer. With more dimples, there is increased surface area and interaction between the fluid and the surface, allowing for better local heat exchange. The heightened turbulence near the wall encourages more efficient heat removal from the surface to the fluid, increasing heat transfer performance. In this study, the dimples on the pipe surface were placed at four different distances ( $P=10\text{mm}$ ,  $P=20\text{ mm}$ ,  $P=30\text{ mm}$ ,  $P=40\text{ mm}$ ) and the effect of increasing the dimple distances on the Nusselt number and friction factor is shown in Figure 5 and Figure 6. The maximum Nusselt number was obtained as 392.52 at a Reynolds number of 50000 with a pitch length of 10 mm. The maximum friction factor, on the other hand, was recorded as 0.0332 at a Reynolds number of 10000 with the same pitch length of 10 mm.

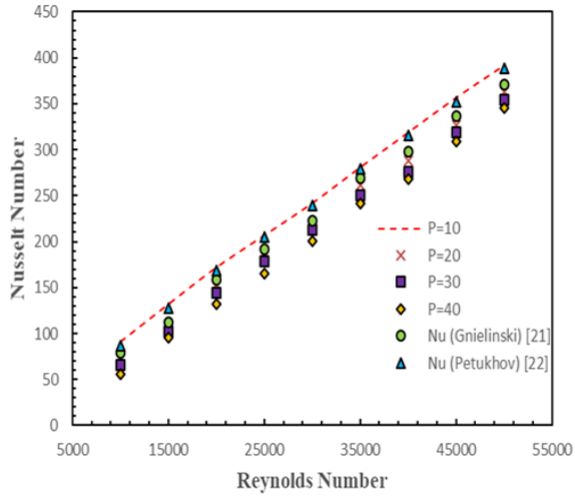


**Fig.5.** Variation of Nusselt number via Reynolds number for dimples at different distances

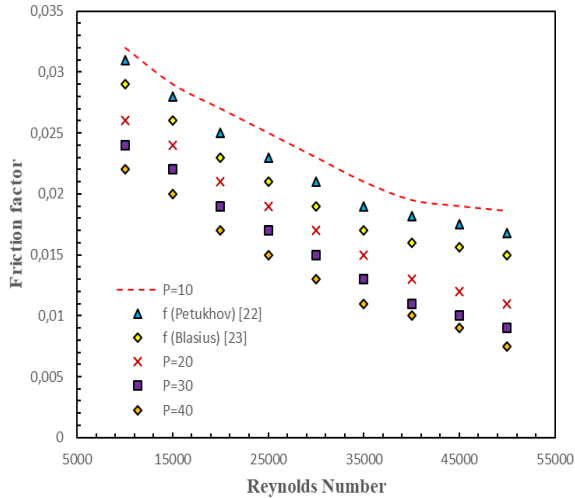


**Fig.5.** Variation of friction factor via Reynolds number for dimples at different distances

### 3.4. Thermohydraulic performance (THP)

The coefficient of thermohydraulic performance (THP) is a key metric in thermal systems because it balances the benefits of enhanced heat transfer against the drawback of increased pressure drop. While heat transfer improvements can boost efficiency, they often raise pressure drop, requiring more energy for pumping. The THP accounts for both factors, showing whether the energy gained from improved heat transfer outweighs the extra pumping energy needed. A THP greater than 1 indicates a net energy gain, making the system more efficient.

Figure 6 shows that thermohydraulic performance decreases with increasing Reynolds number because higher Re leads to higher fluid velocity, which

increases turbulence and heat transfer, but also causes a much higher pressure drop. This higher pressure drop requires more pumping energy, reducing system efficiency. In contrast, at lower  $Re$ , the pressure drop is less severe, leading to better overall performance despite lower heat transfer. The thermal performance of all arrangements of dimples on the tube is above 1. The  $P=10$  mm configuration achieved the best thermohydraulic performance with a coefficient of 1.27 at the lowest Reynolds number. Figure 7 compares the thermal performance results of the current study with those from previous studies in the literature and provides a visual reference to evaluate differences or similarities in performance.

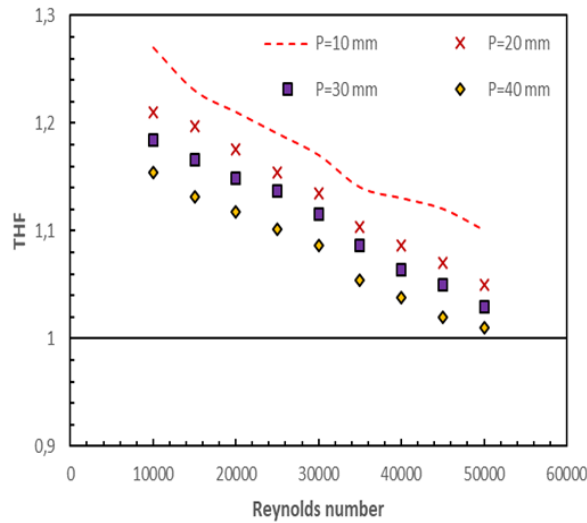


**Fig.6.** Variation of thermohydraulic performance with respect to distance between dimple

#### 4. Conclusions

The effects of dimples placed at different distances on the thermohydraulic performance of a tube were examined. The findings from the study are expressed below.

✓ All dimple geometries demonstrated a thermal performance greater than 1. The 10 mm pitch configuration was proven to be the most efficient, reaching a THF value of 1.27 at a Reynolds number of 10,000, while the lowest performance was recorded for the 40 mm pitch configuration, with a THF value of 1.15 at the same Reynolds number.

✓ Nusselt number increased with Reynolds number in all configurations because higher Reynolds numbers correspond to higher fluid velocities, leading to increased turbulence. This turbulence allows for better fluid mixing, enhancing heat transfer and improving the rate of heat transfer from the surface to the fluid.

✓ The friction factor increased with the number of dimples because more dimples create additional surface roughness, which adds more resistance to fluid flow. This increased resistance results in a higher pressure drop, as more energy is required to push the fluid through the system due to the added friction.

✓ Despite the increased pressure drop caused by the additional friction from more dimples, the thermohydraulic performance coefficient exceeded 1 in all configurations. This indicates a net energy gain because improvements in heat transfer efficiency (shown by the increased Nusselt number) outweigh the extra energy cost associated with pumping. The enhanced turbulence and mixing caused by the dimples lead to a significant increase in heat transfer, compensating for the higher pressure drop and resulting in an overall more energy-efficient system.

## References

- [1] Mangrulkar, C.K., Dhoble, A.S., Chamoli, S., Gupta, A., and Gawande, V.B. 2019. Recent advancement in heat transfer and fluid flow characteristics in cross flow heat exchangers. **Renewable and Sustainable Energy Reviews**. **113** (September 2017), 109220.
- [2] Wang, Y., He, Y., and Lei, Y. 2009. Heat Transfer and Friction Characteristics for Turbulent Flow of Dimpled Tubes. (6), 956–963.
- [3] Suresh, S., Chandrasekar, M., and Sekhar, S.C. 2011. Experimental studies on heat transfer and friction factor characteristics of CuO / water nanofluid under turbulent flow in a helically dimpled tube. **Experimental Thermal and Fluid Science**. **35** (3), 542–549.
- [4] Sabir, R., Mahabat, M., Ahmed, N., Ul, I., and Brabazon, D. 2020. Assessment of thermo-hydraulic performance of inward dimpled tubes with variation in angular orientations. **Applied Thermal Engineering**. **170** (October 2019), 115040.
- [5] Xie, S., Guo, Z., Gong, Y., Dong, C., Liu, J., and Ren, L. 2022. International Journal of Thermal Sciences Numerical investigation of thermal-hydraulic performance of a heat exchanger tube with helical dimples. **International Journal of Thermal Sciences**. **177** (February), 107530.
- [6] Farsad, S., Mashayekhi, M., Zolfagharnasab, M.H., Lakhi, M., Farhani, F., Zareinia, K., et al. 2022. The effects of tube Dimples-Protrusions on the thermo-fluidic properties of turbulent forced-convection. **Case Studies in Thermal Engineering**. **35** 102033.
- [7] Firoozi, A.O., Majidi, S., and Ameri, M. 2020. A numerical assessment on heat transfer and flow characteristics of nanofluid in tubes enhanced with a variety of dimple configurations. **Thermal Science and Engineering Progress**. **19** (April),.
- [8] Li, M., Khan, T.S., Al-Hajri, E., and Ayub, Z.H. 2016. Single phase heat transfer and pressure drop analysis of a dimpled enhanced tube. **Applied Thermal Engineering**. **101** 38–46.
- [9] Nazari, S., Zamani, M., and Moshizi, S.A. 2018. Comparative study on the influence of depth, number and arrangement of dimples on the flow and heat transfer characteristics at turbulent flow regimes. **Heat and Mass Transfer/Waerme- Und Stoffuebertragung**. **54** (9), 2743–2760.
- [10] Manoram, R.B., Moorthy, R.S., and Raganathan, R. 2021. Investigation on influence of dimpled surfaces on heat transfer enhancement and friction factor in solar water heater. **Journal of Thermal Analysis and Calorimetry**. **145** (2), 541–558.

- [11] Zheng, L., Xie, Y., and Zhang, D. 2018. Numerical investigation on heat transfer and flow characteristics in helically coiled mini-tubes equipped with dimples. **International Journal of Heat and Mass Transfer**. **126** 544–570.
- [12] Sabir, R., Khan, M.M., Sheikh, N.A., and Ahad, I.U. 2022. Effect of dimple pitch on thermal-hydraulic performance of tubes enhanced with ellipsoidal and teardrop dimples. **Case Studies in Thermal Engineering**. **31** (February), 101835.
- [13] Nascimento, I.P. and Garcia, E.C. 2016. Heat transfer performance enhancement in compact heat exchangers by using shallow square dimples in flat tubes. **Applied Thermal Engineering**. **96** 659–670.
- [14] Falih, A.H., Khalaf, B.S., and Freegah, B. 2024. Investigate the Impact of Dimple Size and Distribution on the Hydrothermal Performance of Dimpled Heat Exchanger Tubes. **Frontiers in Heat and Mass Transfer** . **22** (2), 597–613.
- [15] Gürdal, M., Pazarlıoğlu, H.K., Tekir, M., Arslan, K., and Gedik, E. 2022. Numerical investigation on turbulent flow and heat transfer characteristics of ferro-nanofluid flowing in dimpled tube under magnetic field effect. **Applied Thermal Engineering**. **200** (October 2021),.
- [16] Kaood, A., ElDegwy, A., and Aboulmagd, A. 2024. Hydrothermal and entropy generation performance of convergent tubes with various dimple shapes. **International Journal of Thermal Sciences**. **197** (August 2023), 108842.
- [17] Wongcharee, K., Kunrarak, K., Kumar, M., and Chuwattabakul, V. 2019. Heat transfer enhancement of TiO<sub>2</sub>-water nanofluid flow in dimpled tube with twisted tape insert. 2987–3001.
- [18] Keklikcioğlu, O. 2024. Augmentation of thermohydraulic performance in a dimpled tube using ternary hybrid nanofluid. **European Mechanical Science**. **8** (1), 38–46.
- [19] Cengel, Y.A., John, C.. 2012. Fluid Mechanics: Fundamentals and Applications. **MCGraw-Hill Education**.
- [20] Ao, S.I., Castillo, O., Douglas, C., Dagan Feng, D., and Korsunsky, A.M. 2017. Proceedings of the international multiconference of engineers and computer scientists 2017. **Lecture Notes in Engineering and Computer Science**. **2227**.
- [21] Gnielinski, V. 1976. New equations for heat and mass transfer in turbulent pipe and channel flow. **International Chemical Engineering**,. **27** 359–368.
- [22] B.S. Petukhov 1970. Heat Transfer and Friction in Turbulent Pipe Flow

with Variable Physical Properties. **Advances in Heat Transfer**. **6** 503–564.

- [23] H. Blasius 1913. The Law of Similarity for Frictions in Liquids, "Notices of research in the field of engineering. **Not. Res. F. Eng.**, **131** 1–41.

## Chapter 8

### Advancing Clean Energy: The Integration of Renewable Energy Sources, Smart Grids, and the Role of Electric Vehicles

**Şafak Melih ŞENOCAK<sup>1</sup>**  
**Yasin VAROL<sup>2</sup>**

---

**1** Şafak Melih ŞENOCAK, Lecturer, Osmaniye Korkut Ata University, Osmaniye Vocational School  
e-mail: [mlhsnck@gmail.com](mailto:mlhsnck@gmail.com), ORCID ID: <https://orcid.org/0000-0003-0602-2836>

**2** Prof. Dr. Yasin VAROL, Firat University, Technology Faculty, Elazig  
e-mail: [yvarol@gmail.com](mailto:yvarol@gmail.com), ORCID ID: <https://orcid.org/0000-0003-2989-7125>

# **Advancing Clean Energy: The Integration of Renewable Energy Sources, Smart Grids, and the Role of Electric Vehicles**

## **Summary**

This study provides a comprehensive evaluation of the integration of renewable energy sources, smart grid technologies, and the role of electric vehicles in energy systems. The environmental and economic benefits of renewable energy sources are discussed alongside the technical, economic, and social challenges encountered during their integration into energy systems. The study highlights the critical role of smart grids in ensuring the reliable and efficient integration of renewable energy sources while emphasizing the future needs for the development of advanced energy management systems. The potential of electric vehicles (EVs) to enhance energy sustainability is explored, with a particular focus on the contributions of Vehicle-to-Grid (V2G) technology in energy storage, load balancing, and the integration of renewable energy sources. However, the challenges associated with V2G implementation, such as battery lifespan concerns, high investment costs, and social barriers, are also addressed. Through advanced communication and management models, smart grids aim to make energy systems more flexible, reliable, and environmentally friendly. This study outlines a roadmap for future energy management strategies shaped by renewable energy sources, smart grids, and electric vehicle technologies. It underscores the opportunities offered by this integration in achieving environmental sustainability and enhancing energy security.

**Keywords:** smart grids, electric vehicles (EV), renewable energy integration, vehicle to grid (V2G) technology, energy sustainability

## **1. Introduction**

Renewable energy stands as one of the most ideal solutions to mitigate the growing issue of greenhouse gas emissions while promoting an environmentally friendly approach. Many countries actively utilize renewable energy in the development and production of next-generation technologies (Sen & Ganguly, 2017). Energy plays a critical role in sustaining life on Earth, with energy transformation processes at the core of this system. The production of usable energy involves converting energy into various forms, relying on both renewable and non-renewable sources. Today, a significant portion of global energy demand is met by non-renewable resources such as fossil fuels (oil, natural gas, and coal). However, the finite nature of these resources and their environmental impacts have heightened interest in energy transitions. Among non-renewable resources, uranium used in nuclear energy production offers a notable alternative due to its high energy density. Nevertheless, increasing the use of sustainable and renewable energy sources in energy production has become an essential requirement from both environmental and economic perspectives. The utilization of renewable energy sources such as solar, biomass, hydro, and wind varies significantly depending on a country's geographical, economic, and technological conditions. For instance, nations with high solar energy potential prioritize this resource, while regions rich in water resources emphasize hydropower. Similarly, the adoption of biomass and wind energy is influenced by factors such as the availability of natural resources, government policies, and infrastructure investments. These variations necessitate flexible and regionally focused approaches in national energy strategies, ensuring the effective integration of renewable energy sources (Martinot, Dienst, Weiliang, & Qimin, 2007). The integration of renewable energy sources into existing electricity grids presents significant technical and operational challenges, such as outages, voltage fluctuations, and energy losses. To overcome these difficulties and enhance the efficiency of energy supply, smart grid systems have been developed. Traditional electricity distribution infrastructure was designed during an era when energy was relatively inexpensive and accessible, and its fundamental structure has been supported by only limited upgrades aimed at meeting increasing electricity demand over time. However, the rapid growth in energy demand and the widespread adoption of renewable energy sources have necessitated a transition to a more modern, flexible, and dynamic infrastructure. Smart grids play a pivotal role in this transformation by maintaining the balance between energy production and distribution, thereby facilitating the effective integration of renewable energy sources. These advanced systems are instrumental in addressing the limitations of traditional grids and ensuring a more sustainable and reliable energy future.

(Dileep, 2020). The existing traditional electricity grid operates with significant inefficiencies, converting only one-third of the energy from fuel into electricity while failing to recover usable waste heat. Approximately 8% of production is lost during transmission, and 20% of generation capacity is reserved solely to meet peak demand periods. Furthermore, the centralized and unidirectional nature of this energy system makes it highly vulnerable to cascading failures, where a single issue can disrupt the entire network. The fundamental operation of public utility systems remains largely unchanged from a century ago, relying on the transfer of energy from centralized power plants to households through public grids and maintaining reliability via stored reserve capacity. However, this system is environmentally and economically unsustainable. Inefficient energy use, a high carbon footprint, and harmful emissions have made this structure a significant source of pollution and greenhouse gas emissions. To address modern energy demands, a transition to a more sustainable and flexible energy infrastructure has become imperative. This shift is essential not only to reduce environmental impacts but also to ensure the reliability and adaptability of energy systems in the face of growing demand and the integration of renewable energy sources. (Farhangi, 2010). The system known as the smart grid aims to address the fundamental shortcomings of the existing energy infrastructure and transform the processes of energy generation, transmission, and consumption into a more efficient, reliable, and sustainable structure. Smart grids overcome the unidirectional and centralized nature of traditional systems by offering innovative features such as bidirectional energy flow, real-time monitoring, demand-side management, and the integration of renewable energy sources. These aspects are expected to provide long-term solutions to the technical and environmental challenges faced by the energy sector. A smart grid is a modern electricity network model that operates by leveraging information and communication technologies. It collects and analyzes data on the energy usage behaviors of suppliers and consumers. This information is automatically processed to make electricity production and distribution more efficient, reliable, economical, and sustainable. Beyond optimizing energy flow, the smart grid enables users to manage their energy consumption more consciously. With these capabilities, it aims to reduce the inefficiencies of the current infrastructure and facilitate the integration of renewable energy sources (Siano, 2014). Most smart grids are strategically established in locations far from densely populated areas and close to natural resources suitable for energy production, such as dam sites or near fuel sources, to ensure the effective utilization of renewable energy. These grids are often designed on a large scale to benefit from economies of scale. The electricity generated is stepped up to higher voltage levels to facilitate integration into the

transmission network. This high-voltage energy is transmitted through the grid, typically reaching wholesale customers, such as companies operating local distribution networks. During this process, the energy may cross international borders, traveling over considerable distances. The structure of smart grids is specifically designed to enhance efficiency and reliability in energy generation and transmission processes. (Hossain et al., 2016). When the power reaches a substation, its voltage level is stepped down from the transmission level. Upon exiting the substation, it enters the distribution cables. Finally, when it arrives at the service location, the voltage is further reduced from the distribution level to the required service voltage. Table 1 briefly highlights the differences between a traditional power grid and a smart grid.

**Table 1.** Conventional grid versus smart grid (Tuballa & Abundo, 2016)

Feature	Traditional Grid	Smart Grid
Operation System	Mechanically operated	Digitized
Transmission Direction	One-way	Two-way
Generation Structure	Centralized Power Generation	Distributed Generation
Connection Type	Radially connected	Distributed
Number of Sensors	Few sensors	Many sensors
Monitoring Capability	Limited monitoring capabilities	Closely monitored
Control Mechanism	Manual control	Automated control
Automated control	Fewer security concerns	Vulnerable to security issues
Response Time	Slow response actions	Fast response

## 2. An Overview of Renewable Energy Sources

There are various renewable energy sources available worldwide, and the primary characteristic of these energy sources is that they are naturally available and generally free of cost. This study will provide a detailed examination of all renewable energy technologies and explain their production capacities on a global scale.

### 2.1. Wind Energy

Wind energy is harnessed by converting the kinetic energy of air flow into mechanical energy through turbines, which is then transformed into electrical energy. Examples of wind power applications include windmills, wind pumps, and sails used to propel ships. Today, large-scale wind farms stand out as systems where hundreds of wind turbines are integrated into the transmission grid for electricity generation. Offshore wind farms offer advantages such as access to stronger and more stable wind resources and reduced visual impact compared to onshore wind turbines. However, offshore projects pose economic challenges due

to the high costs associated with construction and maintenance. On the other hand, small-scale onshore wind farms are designed for more isolated areas and are utilized to meet localized energy needs. Additionally, small home-scale wind turbines are becoming increasingly popular for individual electricity generation and are often supported by utility companies. The versatile applications of wind energy make it a vital option for both large-scale and individual energy solutions, contributing to its growing prominence in the global energy landscape. (Hossain et al., 2016). Wind energy is actively utilized in 83 countries worldwide as an economically viable resource. In 2010, more than 2.5% of global electricity demand was met by wind energy, with an annual growth rate exceeding 25%. From a cost perspective, wind energy has reached a level where its production costs per unit are competitive with those of new coal and natural gas facilities. These attributes make wind energy an attractive option both economically and environmentally (Gasch & Twele, 2012).

### **2.1.2. Wind Turbine Technology**

A wind turbine can be defined as a device that converts the kinetic energy of wind into electrical energy, typically through methods referred to as wind power. If the turbine is used to convert mechanical energy into electricity, it is referred to as a wind power plant or "wind turbine." In cases where the mechanical power is employed for tasks such as operating machinery, pumping water, or grinding grain, the device is known as a windmill. Similarly, when this energy is used for charging batteries, the turbine functions as a charging device. Advancements in wind energy technology have led to significant progress in the engineering designs of both vertical and horizontal axis wind turbines. Small turbines have been developed for specialized applications, such as charging batteries or providing auxiliary power for boats. On the other hand, large-scale turbine arrays play a critical role in meeting the increasing energy demands by generating electricity through wind power. These large wind farms are recognized as a key component of renewable energy production and contribute significantly to achieving sustainability goals in the energy sector. (P., 2008).

### **2.2. Solar Energy**

A wind turbine is a device that converts the kinetic energy of wind into electrical energy, typically through methods known as wind power. If the turbine is used to convert mechanical energy into electricity, it is called a wind power plant or "wind turbine." When mechanical power is utilized for tasks such as operating machinery, pumping water, or grinding grain, the device is referred to as a windmill. Similarly, when this energy is employed for charging batteries, the

turbine functions as a charging device. Advancements in wind energy technology have significantly improved the engineering designs of both vertical and horizontal axis wind turbines. Small turbines are designed for specific applications, such as charging batteries or providing auxiliary power for boats. Meanwhile, large-scale turbine arrays are essential in addressing the growing energy demands by generating electricity from wind power. These extensive wind farms are vital components of renewable energy systems and play a major role in achieving sustainability objectives within the energy sector (Hossain et al., 2016).

### **2.2.2. Photovoltaic**

Photovoltaic (PV) technology refers to solar cells as devices that generate direct current (DC) and electrical power based on the flow of sunlight. Solar cells operate on the principle of the photovoltaic effect, capturing energy from sunlight and converting it into electrical current. A PV system is built around a PV cell, a semiconductor device that transforms solar energy into DC electricity. These cells are typically interconnected to form a PV module with a capacity ranging from 50 to 200 W. When combined with additional components such as inverters, batteries, electrical components, and mounting systems, these modules constitute a PV system. PV systems are highly modular and can be scaled to deliver power ranging from a few watts to several megawatts. In solar PV technologies, silicon-based modules remain the most widely used systems. In recent years, however, technologies known as thin-film modules, made from non-silicon semiconductor materials, have gained prominence. While thin-film modules generally offer lower efficiency compared to silicon modules, their reduced costs provide a distinct advantage. Additionally, concentrated PV (CPV) technology, which focuses sunlight onto smaller areas, has emerged as a high-efficiency solution, achieving up to 40% efficiency and nearing full market deployment. Meanwhile, innovative technologies like organic PV cells are still in the research and development stage, holding the potential to create new opportunities in the solar energy sector in the future. (Bhuiyan, Sugita, Hashimoto, & Yamamoto, 2012). Solar PV combines two significant advantages. Firstly, module production can be conducted in large-scale facilities, enabling economies of scale and reducing costs. Secondly, PV is an exceptionally modular technology, easily adaptable to applications ranging from small systems to large-scale installations. One of PV's greatest advantages over concentrated solar power (CSP) is its ability to harness not only direct sunlight but also diffuse solar radiation. This capability allows solar PV to generate energy without requiring a completely clear sky, making it effective across a much broader geographical range compared to CSP.

### 2.3. Hydroelectric Energy

Hydroelectric power is a renewable energy source derived from the energy of moving water. Flowing water is captured and converted into electricity using turbines. Dams are the most commonly used method for hydroelectric generation. However, more innovative hydroelectric technologies that utilize wave and tidal energy are becoming increasingly prevalent, emerging as significant alternatives in the energy sector. In the future of smart grid systems, hydroelectric power may play a vital role as a major energy storage resource and establish a strong market for power semiconductors as a component of renewable energy. Figure 1 illustrates the operational principles of a hydroelectric facility.

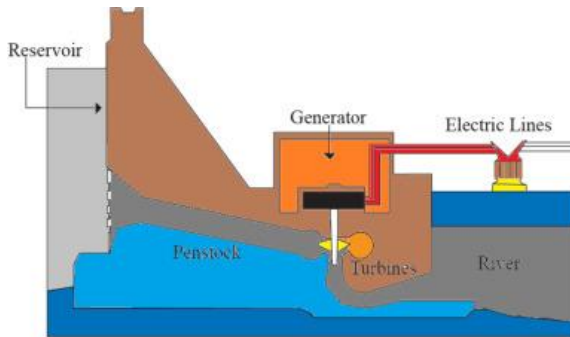


**Figure 1.** Diagram of a Hydroelectric Power Generation Facility (Hossain et al., 2016)

Hydroelectric power plants are categorized into three main types based on their operating principles and water flow models: Run-of-River (RoR), Reservoir, and Pumped Storage Hydroelectric Plants. These systems can be built on varying scales, from small to large, depending on the hydrological regime and topographical features of the basin.

**Run-of-River (RoR) Plants:** These plants primarily harness energy from the natural flow of a river to generate electricity. Some RoR facilities may include short-term storage capacities to partially adapt to changes in demand. However, their production capacity is directly dependent on the river's flow and precipitation levels, which can result in significant daily, monthly, or seasonal variations in output.

**Reservoir Plants:** Equipped with water storage capabilities, these plants store energy for future use. Reservoirs help stabilize fluctuations in inflow, making energy production more sustainable. The generation facilities are typically located downstream, connected to the reservoir via pipelines. The size and design of the reservoir are determined by the geographical characteristics of the region in which it is located.

Pumped Storage Plants: These plants act as energy storage systems rather than primary energy sources. During periods of low demand, water is pumped from a lower reservoir to an upper reservoir, and during peak demand, it flows back to generate electricity. Although the pumping process results in energy losses, making these plants net energy consumers, they provide large-scale energy storage solutions. Currently, pumped storage systems are among the most widely used and highest-capacity energy storage technologies globally. Globally, a significant portion of electricity generation relies on hydroelectric power. Figure 2 illustrates the current and projected hydroelectric production for various regions.

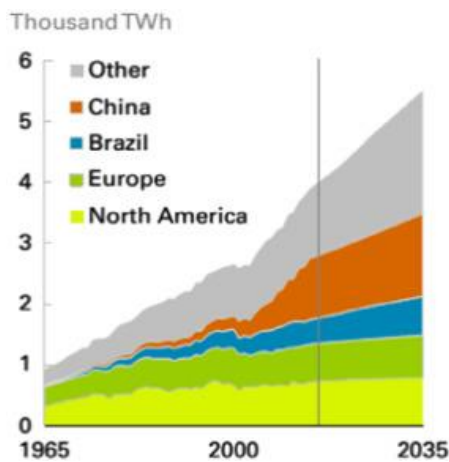


Figure 2. Hydroelectric Distribution by Region (Hossain et al., 2016)

When examining Figure 2, it is evident that since the year 2000, hydroelectric energy production has gained momentum across all regions. Furthermore, this upward trend is projected to continue accelerating through 2035.

### 3. Challenges of Renewable Energy Sources

Renewable energy sources are inherently intermittent. The uncontrollable nature, limited dispatchability, and intermittent characteristics of the most common renewable energy sources, such as wind and solar, necessitate specialized ancillary services like spinning reserves and other regulatory operations to ensure reliability and meet operational demands. Furthermore, one of the primary challenges of renewable energy integration is the potential for rapid fluctuations in power output. When combined with existing load variability, this increases the stochastic nature of the entire power grid. As a result, both the complexity of operations and the need for enhanced support systems must be

addressed through upgrades and improvements. The current power grid operates as a centralized system, focusing on bulk power generation, transmission, and distribution. However, this structure is insufficient for providing scalable energy measurement and production management that can accommodate the rapidly changing requirements of renewable energy sources. Similarly, operational complexity at the distribution level typically excludes production management and is limited to maintaining the quality of the supplied power. Systematic integration of renewable energy sources at both the generation and distribution levels requires comprehensive and coordinated system upgrades to monitor, control, and regulate these processes effectively. In particular, the distribution level demands significant improvements in monitoring and control systems to ensure the flexible and efficient operation of small-scale renewable energy-based generation systems. These upgrades aim to enhance system reliability, ensure operational safety, and enable optimization in energy management, ultimately paving the way for a more robust and sustainable energy infrastructure (Manditereza & Bansal, 2016). The primary objective can be defined as ensuring optimized power flow and supply quality while reducing stochastic complexity within energy systems. Achieving this requires managing the uncertainties introduced by renewable energy integration, enhancing system flexibility, and maintaining high-quality standards throughout all processes, from energy production to distribution. While the current power grid is designed to handle load fluctuations, the stability, controllability, and other ancillary support traditionally provided by conventional synchronous generators are significantly diminished with RE integration. Maintaining grid stability under these conditions necessitates the adaptation or transformation of synchronous generator capacities. This transformation must be systematically implemented, considering the rapid fluctuations and temporal variability of RE sources. Particularly, wind turbines experience continuous fluctuations in output due to varying wind speeds, making production predictability heavily reliant on weather data. Consequently, more advanced control systems and power-balancing strategies are essential to enhance the reliability and flexibility of the grid. High levels of wind energy penetration can lead to overproduction, especially during peak hours. Addressing this challenge requires accurate hourly forecasts of energy supply and effective management of other energy unit commitments to maintain balance in energy provision. Accurate forecasting of wind and solar energy production necessitates the use of advanced equipment and intelligent algorithms to facilitate unit commitment calculations. Moreover, regional planning procedures for integrating intermittent energy sources must be further refined to meet energy market requirements. These enhancements contribute to creating more flexible

and adaptive energy grids, ensuring the efficient utilization of energy derived from renewable sources and fostering a sustainable energy infrastructure. (Lee, Ban, & Kim, 2022). To effectively plan and manage renewable energy production, detailed evaluation and research of short- and long-term weather forecasts are essential. These forecasts are critical for predicting the inherently variable output of renewable energy sources and maintaining the balance between energy supply and demand. Accurate forecasting models not only enhance the reliability of energy grids but also support the flexibility and efficiency of energy systems, ensuring a more stable and sustainable energy infrastructure. (Khalid, 2018; Naz et al., 2019; Sarshar, Moosapour, & Joorabian, 2017). Unlike conventional generators, the unpredictability of renewable energy (RE) sources restricts their ability to operate at full capacity, particularly during peak demand hours. This limitation makes the energy grid more vulnerable to instabilities and power outages while imposing additional strain through increased load demands. Consequently, energy grids incorporating RE sources must be equipped with advanced energy management systems that account for electricity supply, demand, unit pricing, storage, and production costs. Furthermore, when RE output constitutes less than 5-10% of total demand, the grid may consider this production as noise. This highlights the importance of adapting energy management strategies and infrastructure to maximize the potential benefits of RE sources, ensuring both system reliability and operational efficiency. (Sgouridis et al., 2016). Similarly, the intermittent and variable nature of renewable energy (RE) sources poses significant challenges in planning the daily operations of electricity grids. This variability complicates the balance between energy production and demand, necessitating a more flexible and predictable planning approach to maintain grid reliability and efficiency. The inherent characteristics of RE sources amplify the need for innovative solutions and advanced forecasting methods in energy management systems. The fluctuations of RE generation across different time scales compel grid operators to adjust system operations in real-time, over a few hours, or on a day-ahead basis. As RE output changes every minute, traditional generation systems must continuously adapt to meet load demands. This cyclical operation places strain on generators, reducing their efficiency and negatively impacting overall system performance. These challenges become even more pronounced when coupled with fluctuating load demands. Rapid variations in wind and solar energy production can disrupt hourly load-following schedules and disturb the second-to-second balance between supply and demand. Therefore, reducing the costs associated with managing the intermittent nature of RE sources has become a fundamental objective for grid operations. More flexible and adaptive energy systems are

critical to overcoming these challenges and maximizing the efficiency and potential of renewable energy sources (Alhammad, Khan, Alismail, & Khalid, 2021).

In conclusion, when a wind turbine is properly positioned, appropriately sized, and efficiently operated, it can replace conventional synchronous generators in the power grid. However, the unpredictable power fluctuations inherent to wind turbines must be considered, as they can impact energy flow and operational stability within the grid. Such fluctuations necessitate more dynamic and flexible approaches in energy management processes. Furthermore, these challenges extend beyond energy production, affecting various aspects of electrical power systems and transforming processes of identification, optimization, design, and implementation into a multidisciplinary field of engineering and energy science. Successfully integrating renewable energy sources requires inevitable interdisciplinary collaboration and innovation, highlighting the complexity and interconnected nature of modern energy systems. (Ichikawa et al., 2019; Qays et al., 2022; Reddy, Kumar, Mallick, Sharon, & Lokeswaran, 2014; W. Wang, Yuan, Sun, & Wennersten, 2022).

#### **4. Overview of Smart Grids**

The grid is a network of interconnected lines that facilitate the transmission and distribution of electricity. A smart grid, on the other hand, is defined as a modern electrical grid that leverages analog or digital information and communication technologies. In the context of renewable energy, a smart grid serves as a communication and management platform that integrates electricity generated from renewable energy sources into the grid. However, this integration introduces several challenges, including stability issues, complex operational processes, and the need for remote control mechanisms. The electrical power system is a cornerstone of modern societal infrastructure, reaching nearly all homes, workplaces, and institutions in both developed nations and emerging economies such as Malaysia, China, and India. The electricity generation and distribution network is unified yet complex, and no single organization has complete control over these large-scale systems or the capacity to assess, monitor, and manage them in real time. The power grid encompasses not only the transmission of energy from power plants to substations but also the distribution of energy from substations to individual consumers. Smart grid systems incorporate a wide array of technologies, ranging from monitoring and analysis to automation, load control, and renewable energy integration. These systems enable the integration and management of distributed energy resources such as microgrids, renewable energy sources, solid oxide fuel cells, and battery storage

systems. They also require advanced satellite technologies, communication infrastructures, computing systems, and global positioning systems (GPS) for deploying devices such as phasor measurement units (PMU), digital frequency recorders (DFR), and dynamic swing recorders (DSR). Wide-Area Management Systems (WAMS) for large regions, such as the New York area, enable more efficient and secure management of energy systems. However, ensuring the security and protection of these devices demands integrated analytical methods and the development of appropriate safety standards. Additionally, fostering new potential electricity markets for consumers and addressing economic factors are critical needs in smart grid systems. These technologies signify a comprehensive transformation across all grid operations, from transmission to sub-transmission and distribution, paving the way for more efficient, reliable, and sustainable energy systems (Massoud Amin, 2011). The structure and distribution of the smart grid are illustrated in Figure 3. The diagram highlights the placement and function of distributed generation units within an energy grid, including offshore wind farms, solar power plants, fossil fuel-based power plants, and combined heat and power (CHP) systems. These components serve as fundamental elements of modern energy infrastructure, playing a critical role in energy generation and management. The Smart Grid (SG) utilizes advanced metering infrastructure (AMI) or Supervisory Control and Data Acquisition (SCADA) systems to manage these generation units through remote monitoring and control mechanisms. The figure also demonstrates that the SG operates as both a transmission and distribution network, integrating components such as microgrids, smart homes, smart buildings, and electric vehicles through smart meters to optimize energy usage. The depicted data center acts as a hub, facilitating communication among grid components and coordinating energy flow, thereby enabling more efficient management of energy consumption and production. Smart grids not only enhance energy transmission and distribution but also facilitate the integration of renewable energy sources, thereby promoting environmental sustainability. These systems enable bidirectional communication between data and energy networks, offering greater flexibility and dynamism in managing the balance between energy supply and demand. In this context, smart grids emerge as a cornerstone of modern energy systems, driving innovation and efficiency in the evolving energy landscape.

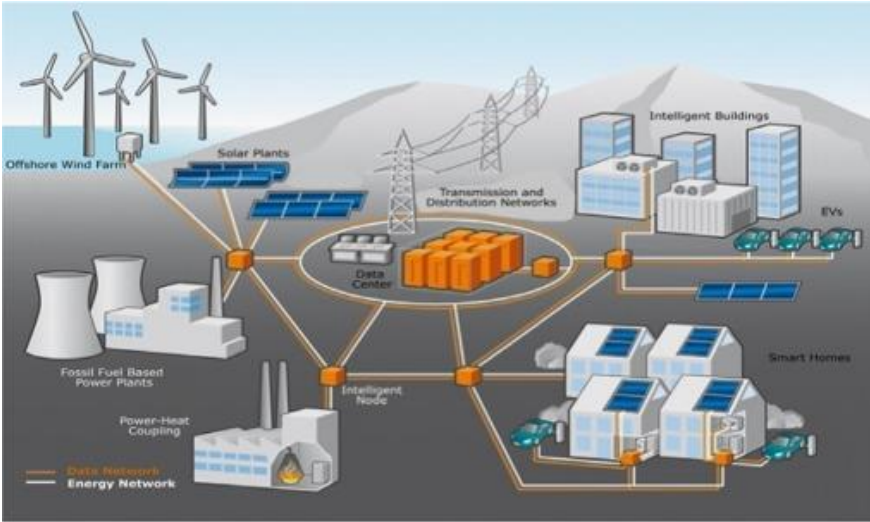


**Figure 3.** Production and Distribution within the Smart Grid Structure (Colak, Kabalci, Fulli, & Lazarou, 2015)

## 5. Integration of Renewable Energy On Smart Grids

Electric power systems worldwide face multifaceted challenges, including aging infrastructure, increasing energy demand, broader integration of renewable energy sources, enhanced supply security, and the need to reduce carbon emissions. These issues necessitate making power grids more resilient, flexible, and sustainable. While many renewable energy studies have explored clean energy sources, integrating renewable energy into power systems remains a critical challenge in modernizing and transforming the grid into a smart grid. Some grids are already highly congested, making it difficult to transport power from wind farms to meet consumption demands. Renewable energy sources are inherently intermittent and variable by nature. Traditionally, electricity flowed in a single direction, from a power plant to the consumer. However, with additional sources from alternative energies, electricity must now enter the grid from multiple points. Integrating wind, solar, and other alternative sources into the distribution grid and directing them to their destinations require grid automation, bidirectional power flow, and advanced controls. Coordinated efforts are essential to adapt solar photovoltaic and wind energy technologies effectively. Furthermore, new devices in smart grid systems must be compatible with existing equipment to ensure seamless integration. Achieving this integration will enable the transition to a more robust and sustainable energy infrastructure capable of supporting modern energy demands while accommodating renewable energy sources efficiently. (Gaviano, Weber, & Dirmeier, 2012). Smart grid technologies

not only provide innovative solutions to address these challenges but also contribute significantly to making energy systems more efficient, cost-effective, and environmentally friendly. Advanced features such as enhanced monitoring, data analytics, and automation optimize energy production, transmission, and distribution, enabling more effective management of the energy supply-demand balance. Consequently, smart grid technologies play a pivotal role in the transformation of modern energy systems. By integrating smart grid tools and technologies into the electrical infrastructure, bidirectional energy and data flows are facilitated. This capability allows for more flexible and dynamic management of both energy and communication processes. These new features enhance efficiency, strengthen reliability, improve interoperability between different components, and bolster overall system security. Such advancements are essential for making modern energy grids more sustainable and resilient. Feasibility and applicability studies conducted worldwide provide crucial insights to support the development of grid-connected renewable energy systems in specific regions. These studies serve as vital tools for assessing the energy potential of various locations and identifying the most suitable renewable energy solutions. For instance, an analysis using HOMER energy optimization software successfully demonstrated the feasibility of an 80 kW solar PV-grid-connected system in Jos, Nigeria. Such evaluations enable the optimization of renewable energy systems tailored to local conditions, paving the way for the development of sustainable energy solutions. (Adaramola, 2014).

General renewable energy research forms the cornerstone of the Smart Grid concept. In this context, a study conducted in Senegal developed a rural electrification kit, serving as the foundation for the establishment of microgrids in remote villages without access to electricity. (Alzola et al., 2009). The study revealed that hybrid microgrids with high renewable energy content present a promising solution for rural electrification in developing countries. Trends in renewable energy growth in India, on the other hand, provide valuable insights into goal-setting and capacity-building processes in this field. These trends underscore an increasing need for proper sizing, accurate installation, efficient operation, and regular maintenance of renewable energy systems. Such research serves as a guide for the integration of renewable energy sources and the expansion of energy access. (Pillai & Banerjee, 2009).

## **6. The Role of Smart Grids in Electric Vehicle Integration**

Electric vehicle (EV) technology has garnered increasing attention from governments and the public due to rising environmental concerns and the escalating costs of fossil fuels. Integrating EVs with smart grids powered by

renewable energy sources promotes cleaner energy usage while supporting environmental sustainability by reducing the carbon footprint. This integration not only facilitates the transformation of energy systems into more environmentally friendly frameworks but also strengthens the synergy between the transportation and energy sectors, paving the way for a more sustainable future (Kasaei, Gandomkar, & Nikoukar, 2017). However, the integration of the transportation sector with the electric grid brings various challenges to energy systems. For instance, the widespread adoption of EVs can significantly increase the load on the electric grid, particularly during charging processes. Nevertheless, the anticipated penetration of EVs holds the potential to enable V2G applications, facilitating bidirectional energy flow between the grid and vehicles. This technology can enhance the grid's load balancing and energy storage capacity, thereby supporting the flexibility and sustainability of energy systems. Implementing V2G technology, however, requires advanced infrastructure, appropriate technological advancements, and well-defined regulatory frameworks. The integration of EVs into smart grids significantly reduces the dependency on fossil fuels in the transportation sector while also contributing to the reduction of greenhouse gas (GHG) emissions. V2G technology is categorized into unidirectional and bidirectional modes based on the direction of energy flow. These modes offer distinct capabilities in optimizing grid operations and maximizing the utility of renewable energy sources (Yilmaz & Krein, 2012, 2013). Unidirectional V2G regulates the charging rate of each EV by employing a communication system between the grid operator and the EV. This mechanism helps prevent issues such as grid overload, system imbalances, and voltage drops, ensuring a more stable and efficient operation of the electric grid. (Fasugba & Krein, 2011; E. Sortomme, 2012). This structure serves as a fundamental approach to controlling EV charging processes to optimize the load on the grid.

From the perspective of the electrical grid, EV batteries can be considered not only as an electrical load but also as an energy storage unit. Building on this concept, bidirectional V2G enables energy exchange between EV batteries and the electrical grid. This technology allows EVs not only to charge but also to feed stored energy back into the grid when needed. Bidirectional V2G facilitates enhanced reliability and sustainability of the energy system for utility companies, helping them manage energy resources more flexibly in the process. (Gallardo-Lozano, Milanés-Montero, Guerrero-Martínez, & Romero-Cadaval, 2012). This flexibility provides a significant advantage in meeting energy demand and integrating renewable energy sources. V2G technology represents a complex unit commitment problem, characterized by diverse and often conflicting objectives and constraints. As a result, implementing V2G necessitates the use of

optimization techniques. While various optimization methods have been proposed in the literature, Genetic Algorithm (GA) and Particle Swarm Optimization (PSO) emerge as the two prominent techniques for V2G applications. These optimization methods operate by considering specific constraints to achieve V2G's operational objectives, which include services such as peak load shaving, load balancing, voltage regulation, and profit maximization. GA and PSO provide effective tools to ensure the energy grid operates more efficiently and flexibly, addressing the complex structure of energy systems and the diverse requirements of V2G. These methods play a critical role in enhancing grid reliability while maximizing economic benefits for users.

### **6.1. Unidirectional and Bidirectional V2G**

Unidirectional V2G is a technology that operates with a single-directional power flow between the EV and the grid, managing the charging rate of the EV battery (Romo & Micheloud, 2015; Yilmaz & Krein, 2013). Unidirectional V2G technology offers a streamlined approach to managing grid load by focusing solely on the controlled charging of EV batteries. Its implementation is cost-efficient due to the simplicity of the required infrastructure, which typically involves integrating a basic control device to regulate charging rates. This accessibility makes it an attractive and practical option for energy providers and EV owners alike, particularly in the early stages of V2G adoption. Beyond its simplicity, unidirectional V2G provides crucial ancillary services to the grid, such as frequency regulation and spinning reserves, thereby enhancing grid reliability and operational flexibility. While its scope is more limited compared to bidirectional V2G, its ability to support grid stability with minimal investment positions it as a vital stepping stone toward more advanced energy integration strategies. This foundational role underscores its importance in fostering the gradual adoption of V2G technologies in diverse energy markets (Akhtar, Al-Awami, & Khalid, 2013; Guille & Gross, 2009). This technology not only enhances the efficiency of energy systems but also helps prevent issues such as grid overloading by effectively managing the charging process. Additionally, unidirectional V2G holds significant potential for maximizing profits and minimizing carbon emissions through the application of optimization techniques. By aligning energy usage with grid demands, it supports a more sustainable and economically viable energy system while contributing to global efforts to reduce environmental impact (Ghofrani, Arabali, & Etezadi-Amoli, 2012; Eric Sortomme & El-Sharkawi, 2011). However, the services provided by this system are limited to offering auxiliary support to the grid. Advanced functionalities such as peak load shaving, reactive power support, voltage regulation, and frequency

stabilization can only be achieved through bidirectional V2G technology. While unidirectional V2G serves as a crucial starting point, transitioning to bidirectional systems is necessary to deliver more comprehensive and impactful services. This evolution would enable greater flexibility, improved grid stability, and enhanced integration of renewable energy sources, aligning with the long-term objectives of modern energy management systems.

Bidirectional V2G is a technology that facilitates two-way power flow between EVs and the electrical grid, offering a multitude of benefits. This approach not only allows EVs to draw energy from the grid for charging but also enables them to supply stored energy back to the grid when needed. By leveraging this bidirectional capability, V2G technology contributes to improved grid stability, optimized energy utilization, and enhanced flexibility in managing energy demand and supply. (Ferreira, Miranda, Araujo, & Lopes, 2011). As illustrated in Figure 4, a typical bidirectional EV battery charger comprises an AC/DC converter and a DC/DC converter. The AC/DC converter operates by converting alternating current (AC) from the grid into direct current (DC) during charging mode, while in discharging mode, it converts DC from the battery back into AC to feed power back to the grid. The DC/DC converter, on the other hand, manages the bidirectional power flow by utilizing current control techniques. It functions as a buck converter during charging and as a boost converter during discharging. This configuration ensures efficient and controlled energy exchange between the EV battery and the electrical grid.

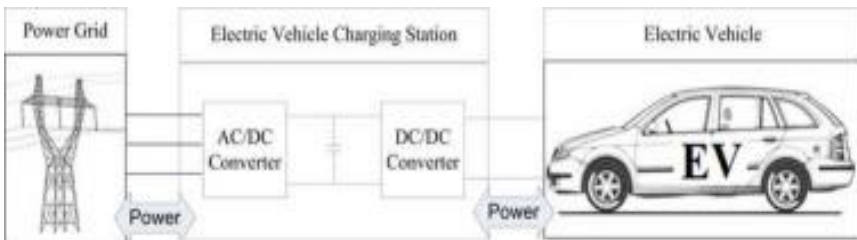


**Figure 4.** V2G power diagram (Tan, Ramachandaramurthy, & Yong, 2016)

Bidirectional V2G provides greater flexibility and functionality for power systems, offering benefits such as active power support, reactive power compensation, power factor regulation, and support for renewable energy integration. For instance, active power support enables essential grid services like peak load shaving and load balancing. (Ghosh, Thomas, & Wicker, 2013; Z. Wang & Wang, 2013). However, implementing bidirectional V2G faces several challenges, with battery degradation being a significant concern due to frequent charge and discharge cycles, which can shorten battery lifespan (Dogger,

Roossien, & Nieuwenhout, 2011). Additionally, the complexity of bidirectional chargers increases the need for additional hardware, leading to high investment costs. Furthermore, social barriers play a significant role in the implementation of bidirectional V2G. For instance, EV owners often prefer to keep their batteries at high charge levels for unexpected travel, which can limit participation in bidirectional V2G services (Fasugba & Krein, 2011). Despite these challenges, the flexibility and innovative features offered by bidirectional V2G hold significant potential for enhancing the sustainability of energy systems and optimizing grid operations. However, for this technology to achieve widespread adoption, technical, economic, and social barriers must be effectively addressed.

## **6.2. Advantages and Disadvantages of V2G Technology**

V2G technology manages bidirectional power flow between EVs and the electricity grid, offering various benefits to energy systems. This technology presents a critical solution for maintaining the energy supply-demand balance, supporting the integration of renewable energy sources, and enhancing the flexibility of energy systems. V2G services include functionalities such as ancillary services, active power support, reactive power compensation, and renewable energy support. Unidirectional V2G controls charging rates to provide services like frequency regulation and spinning reserves, while bidirectional V2G utilizes energy stored in EV batteries for more advanced functions such as peak shaving and load balancing. Additionally, bidirectional V2G can regulate voltage through reactive power compensation and act as a backup energy storage unit to mitigate fluctuations in renewable energy generation.

However, the implementation of V2G technology faces several challenges. The frequent charging and discharging cycles of EV batteries negatively impact battery life, posing a significant obstacle. High investment costs, particularly due to the complexity of bidirectional chargers and infrastructure upgrade requirements, present an economic barrier. Moreover, social barriers, such as range anxiety and unforeseen travel needs of EV owners, limit participation in V2G services. Despite these challenges, V2G technology holds great potential for enhancing the sustainability of energy systems and optimizing energy efficiency. To successfully implement this technology, overcoming technical, economic, and social hurdles is imperative.

## **7. Recommendations and Future Research**

Today's energy systems are undergoing a profound transformation, shifting from fossil fuels to renewable energy sources. This transition necessitates future

power grids to accommodate the large-scale integration of renewable energy sources, bringing both challenges and opportunities. While Advanced Metering Infrastructure (AMI) plays a critical role in this transition, its effective implementation is hindered by strategic shortcomings such as information gaps, the management of data collected from smart meters, and the lack of standardized communication protocols. Improved energy transmission, enhanced distribution control, and real-time information flow are essential to benefit both energy consumers and utility providers.

The integration of renewable energy sources into smart grids not only enhances the sustainability of energy supply but also improves the flexibility of energy systems. However, technical challenges such as unpredictable generation profiles, voltage fluctuations, harmonic distortions, and the impacts of energy storage systems on the grid need to be addressed. Energy Management Systems (EMS) require further research, particularly regarding the planning and control measures of battery systems. These systems will enhance the sustainability of energy transport and ensure better compatibility of EV operations with smart grids.

Additionally, investigating the most efficient use of renewable energy sources and addressing uncertainties surrounding technologies like Virtual Power Plants (VPP) is crucial. Robust communication and management models are imperative for the effective operation of VPPs and EVs. Understanding the impact of communication disruptions on grid operations will also be an important research area to improve the reliability of energy systems.

Furthermore, more studies should explore how advanced technologies such as Artificial Intelligence (AI) can be utilized in smart grids and buildings for data collection, analysis, and transmission. AI-powered energy management systems have the potential to optimize the integration of renewable energy sources, making energy use more efficient and environmentally friendly. Thus, AI and smart grids will emerge as fundamental components of a sustainable and reliable energy infrastructure. These innovative approaches are vital for maintaining the balance of energy supply and demand and for reducing carbon emissions.

## **8. Conclusion**

The integration of renewable energy sources into energy systems lies at the heart of efforts to enhance the sustainability of energy transitions, reshaping global energy systems through innovative approaches. Smart grid technologies play a pivotal role in this transformation by delivering greater efficiency, flexibility, and reliability across energy generation, transmission, and consumption processes. The integration of EVs into smart grids not only

contributes to reducing carbon emissions but also provides innovative solutions for demand-side management and the optimized utilization of renewable energy sources.

This study comprehensively addresses the technical, economic, and social challenges encountered in adapting renewable energy sources and discusses the technological advancements and management strategies required to overcome these barriers. Notably, the advancement of energy storage technologies is critical for enhancing grid flexibility. VPPs and V2G technologies emerge as effective tools to optimize the integration of renewable energy sources and render energy systems more dynamic. However, significant obstacles must be addressed to enhance the feasibility of these technologies. For instance, the inherent variability of renewable energy sources necessitates more sophisticated planning and forecasting systems to maintain the balance between energy supply and demand. Additionally, for widespread adoption of V2G technologies, critical challenges such as battery degradation, high investment costs, and social acceptance must be overcome. Developing advanced energy management systems and integrating artificial intelligence-based analytical methods into energy infrastructure hold substantial promise in addressing these challenges.

In conclusion, the integration of renewable energy sources, smart grid technologies, and electric vehicles presents a transformative paradigm that supports the goals of environmental sustainability, economic efficiency, and operational reliability in energy systems. Future research should focus on enhancing the interoperability of these technologies and optimizing the integration across diverse energy systems. Aligning energy policies with this transformation and developing innovative financing models will be crucial in accelerating this transition. Such advancements represent significant strides toward a sustainable energy future.

## REFERENCES

- Adaramola, M. S. (2014). Viability of grid-connected solar PV energy system in Jos, Nigeria. *International Journal of Electrical Power & Energy Systems*, 61, 64–69.
- Akhtar, G. M. A., Al-Awami, A. T., & Khalid, M. W. (2013). Coordinating emission-aware energy trading with V2G services. In *Eurocon 2013* (pp. 1293–1298).
- Alhammad, H. I., Khan, K. A., Alismail, F., & Khalid, M. (2021). Capacity Optimization and Optimal Placement of Battery Energy Storage System for Solar PV Integrated Power Network. In *2021 IEEE Energy Conversion Congress and Exposition (ECCE)* (pp. 847–852).
- Alzola, J. A., Vechiu, I., Camblong, H., Santos, M., Sall, M., & Sow, G. (2009). Microgrids project, Part 2: Design of an electrification kit with high content of renewable energy sources in Senegal. *Renewable Energy*, 34(10), 2151–2159.
- Bhuiyan, A. G., Sugita, K., Hashimoto, A., & Yamamoto, A. (2012). InGaN Solar Cells: Present State of the Art and Important Challenges. *IEEE Journal of Photovoltaics*, 2(3), 276–293.
- Colak, I., Kabalci, E., Fulli, G., & Lazarou, S. (2015). A survey on the contributions of power electronics to smart grid systems. *Renewable and Sustainable Energy Reviews*, 47, 562–579.
- Dileep, G. (2020). A survey on smart grid technologies and applications. *Renewable Energy*, 146, 2589–2625.
- Dogger, J. D., Roossien, B., & Nieuwenhout, F. D. J. (2011). Characterization of Li-Ion Batteries for Intelligent Management of Distributed Grid-Connected Storage. *IEEE Transactions on Energy Conversion*, 26(1), 256–263.
- Farhangi, H. (2010). The path of the smart grid. *IEEE Power and Energy Magazine*, 8(1), 18–28.
- Fasugba, M. A., & Krein, P. T. (2011). Cost benefits and vehicle-to-grid regulation services of unidirectional charging of electric vehicles. In *2011 IEEE Energy Conversion Congress and Exposition* (pp. 827–834).
- Ferreira, R. J., Miranda, L. M., Araujo, R. E., & Lopes, J. P. (2011). A new bi-directional charger for vehicle-to-grid integration. In *2011 2nd IEEE PES International Conference and Exhibition on Innovative Smart Grid Technologies* (pp. 1–5).
- Gallardo-Lozano, J., Milanés-Montero, M. I., Guerrero-Martínez, M. A., & Romero-Cadaval, E. (2012). Electric vehicle battery charger for smart grids. *Electric Power Systems Research*, 90, 18–29.

- Gasch, R., & Twele, J. (Eds.). (2012). *Wind Power Plants*. Berlin, Heidelberg: Springer Berlin Heidelberg.
- Gaviano, A., Weber, K., & Dirmeier, C. (2012). Challenges and Integration of PV and Wind Energy Facilities from a Smart Grid Point of View. *Energy Procedia*, 25, 118–125.
- Ghofrani, M., Arabali, A., & Etezadi-Amoli, M. (2012). Electric drive vehicle to grid synergies with large scale wind resources. In *2012 IEEE Power and Energy Society General Meeting* (pp. 1–6).
- Ghosh, D. P., Thomas, R. J., & Wicker, S. B. (2013). A Privacy-Aware Design for the Vehicle-to-Grid Framework. In *2013 46th Hawaii International Conference on System Sciences* (pp. 2283–2291).
- Guille, C., & Gross, G. (2009). A conceptual framework for the vehicle-to-grid (V2G) implementation. *Energy Policy*, 37(11), 4379–4390.
- Hossain, M. S., Madloul, N. A., Rahim, N. A., Selvaraj, J., Pandey, A. K., & Khan, A. F. (2016). Role of smart grid in renewable energy: An overview. *Renewable and Sustainable Energy Reviews*, 60, 1168–1184.
- Ichikawa, H., Yokogawa, S., Kawakita, Y., Sawada, K., Sogabe, T., Minegishi, A., & Uehara, H. (2019). An Approach to Renewable-Energy Dominant Grids via Distributed Electrical Energy Platform for IoT Systems. In *2019 IEEE International Conference on Communications, Control, and Computing Technologies for Smart Grids (SmartGridComm)* (pp. 1–6).
- Kasaei, M. J., Gandomkar, M., & Nikoukar, J. (2017). Optimal management of renewable energy sources by virtual power plant. *Renewable Energy*, 114, 1180–1188.
- Khalid, M. (2018). Economic Dispatch Using Functional Network Wind Forecast Model. In *2018 IEEE 27th International Symposium on Industrial Electronics (ISIE)* (pp. 502–507).
- Lee, H., Ban, J., & Kim, S. W. (2022). Microgrid Optimal Scheduling Incorporating Remaining Useful Life and Performance Degradation of Distributed Generators. *IEEE Access*, 10, 39362–39375.
- Manditereza, P. T., & Bansal, R. (2016). Renewable distributed generation: The hidden challenges – A review from the protection perspective. *Renewable and Sustainable Energy Reviews*, 58, 1457–1465.
- Martinot, E., Dienst, C., Weiliang, L., & Qimin, C. (2007). Renewable Energy Futures: Targets, Scenarios, and Pathways. *Annual Review of Environment and Resources*, 32(1), 205–239.
- Massoud Amin, S. (2011). Smart Grid: Overview, Issues and Opportunities. Advances and Challenges in Sensing, Modeling, Simulation, Optimization and Control. *European Journal of Control*, 17(5–6), 547–567.

- Naz, A., Javaid, N., Rasheed, M. B., Haseeb, A., Alhussein, M., & Aurangzeb, K. (2019). Game Theoretical Energy Management with Storage Capacity Optimization and Photo-Voltaic Cell Generated Power Forecasting in Micro Grid. *Sustainability*, 11(10), 2763.
- P., M. (2008). Part 1-Early History Through 1875. Retrieved from <http://www.telosnet.com/wind/early.html>
- Pillai, I. R., & Banerjee, R. (2009). Renewable energy in India: Status and potential. *Energy*, 34(8), 970–980.
- Qays, M. O., Ahmed, M. M., Parvez Mahmud, M. A., Abu-Siada, A., Muyeen, S. M., Hossain, M. L., ... Rahman, M. M. (2022). Monitoring of renewable energy systems by IoT-aided SCADA system. *Energy Science & Engineering*, 10(6), 1874–1885.
- Reddy, K. S., Kumar, M., Mallick, T. K., Sharon, H., & Lokeswaran, S. (2014). A review of Integration, Control, Communication and Metering (ICCM) of renewable energy based smart grid. *Renewable and Sustainable Energy Reviews*, 38, 180–192.
- Romo, R., & Micheloud, O. (2015). Power quality of actual grids with plug-in electric vehicles in presence of renewables and micro-grids. *Renewable and Sustainable Energy Reviews*, 46, 189–200.
- Sarshar, J., Moosapour, S. S., & Joorabian, M. (2017). Multi-objective energy management of a micro-grid considering uncertainty in wind power forecasting. *Energy*, 139, 680–693.
- Sen, S., & Ganguly, S. (2017). Opportunities, barriers and issues with renewable energy development – A discussion. *Renewable and Sustainable Energy Reviews*, 69, 1170–1181.
- Sgouridis, S., Abdullah, A., Griffiths, S., Saygin, D., Wagner, N., Gielen, D., ... McQueen, D. (2016). RE-mapping the UAE's energy transition: An economy-wide assessment of renewable energy options and their policy implications. *Renewable and Sustainable Energy Reviews*, 55, 1166–1180.
- Siano, P. (2014). Demand response and smart grids—A survey. *Renewable and Sustainable Energy Reviews*, 30, 461–478.
- Sortomme, E. (2012). Combined bidding of regulation and spinning reserves for unidirectional Vehicle-to-Grid. In *2012 IEEE PES Innovative Smart Grid Technologies (ISGT)* (pp. 1–7).
- Sortomme, Eric, & El-Sharkawi, M. A. (2011). Optimal Charging Strategies for Unidirectional Vehicle-to-Grid. *IEEE Transactions on Smart Grid*, 2(1), 131–138.
- Tan, K. M., Ramachandaramurthy, V. K., & Yong, J. Y. (2016). Integration of electric vehicles in smart grid: A review on vehicle to grid technologies

- and optimization techniques. *Renewable and Sustainable Energy Reviews*, 53, 720–732.
- Tuballa, M. L., & Abundo, M. L. (2016). A review of the development of Smart Grid technologies. *Renewable and Sustainable Energy Reviews*, 59, 710–725.
- Wang, W., Yuan, B., Sun, Q., & Wennersten, R. (2022). Application of energy storage in integrated energy systems — A solution to fluctuation and uncertainty of renewable energy. *Journal of Energy Storage*, 52, 104812.
- Wang, Z., & Wang, S. (2013). Grid Power Peak Shaving and Valley Filling Using Vehicle-to-Grid Systems. *IEEE Transactions on Power Delivery*, 28(3), 1822–1829.
- Yilmaz, M., & Krein, P. T. (2012). Review of benefits and challenges of vehicle-to-grid technology. In *2012 IEEE Energy Conversion Congress and Exposition (ECCE)* (pp. 3082–3089).
- Yilmaz, M., & Krein, P. T. (2013). Review of the Impact of Vehicle-to-Grid Technologies on Distribution Systems and Utility Interfaces. *IEEE Transactions on Power Electronics*, 28(12), 5673–5689.

## **Chapter 9**

### **Detection Damages in the Presence of Electric and Magnetic Fields Using Computer-Aided Tap Test**

**Imran ORAL<sup>1</sup>**

---

<sup>1</sup>Assoc.Prof.Dr.; Department of Physics Education, Necmettin Erbakan University, Konya, Türkiye.  
oralimran@erbakan.edu.tr, <https://orcid.org/0000-0002-5299-5068>

\* This study was supported by the Scientific Research Projects (BAP) Coordinating Office of Necmettin Erbakan University (grant number 161210018). The author is grateful for the assistance from Necmettin Erbakan University, Türkiye.

## **Abstract**

This study aimed to determine, using the Computer-Aided Tap Tester (CATT), the effects of electrical and magnetic fields, material thickness, and material type on the detection of damage in aluminum honeycomb panels of different thicknesses, wood (Poplar and Pine), and iron materials. For this purpose, the CATT system was utilized to measure the contact durations between the surfaces of intact materials and the tapper, determine the stiffness values of the material surfaces, and generate contour images. After introducing various types of damage to the materials, the CATT system was used again to measure the contact durations and stiffness values of the damaged material surfaces, and new contour images were generated. By comparing the contour images of intact and damaged materials, the effects of thickness, electrical field, magnetic field, and material type on damage detection were evaluated. The analysis of the contour images revealed that damage in thick aluminum honeycomb panels was more easily detected compared to those in thin aluminum honeycomb panels. Additionally, based on the contour images obtained from the materials, it was found that, when performed in the presence of electrical and magnetic fields, CATT made a significant contribution to detecting damages, particularly in honeycomb panel structures with conductive inner cores.

**Keywords:** Computer-aided tap testing, Damage, Electric field, Magnetic field, Honeycomb panels.

## INTRODUCTION

Non-destructive testing (NDT) techniques enable damage detection without compromising material integrity while also reducing maintenance and repair costs. Tap testing is a traditional NDT method that involves striking a material's surface with a small hammer or a coin. The physical principles of the coin-tapping technique are well-documented (Bowkett & Thanapalan, 2017). In tap-testing, it has been reported that the contact duration between the tapper and the material surface is longer in damaged regions than in undamaged ones in a composite material containing defects such as damaged cores or delamination (Gryzagoridis & Findeis, 2013). The prolonged contact time in the damaged area is because the damaged region provides less support than the intact portion of the material.

Manual tap testing is a method based on the auditory perception of the human ear. Consequently, the sensitivity and reliability of this technique depend on the tester's ability to hear accurately. To eliminate the dependence on human auditory perception, numerous studies have been conducted, leveraging advancements in electronic technology (Barnard, 2015; Cawley, 1991; Cawley & Adams, 1989; Gryzagoridis & Findeis, 2015; Hsu, Barnard, Peters, & Dayal, 1999, 2000). For example, in a study conducted by Hsu et al. (2000) at Iowa State University, the Computer-Aided Tap Tester (CATT) system was developed to eliminate reliance on human auditory perception. Additionally, devices such as "The Woodpecker," developed by Mitsui Heavy Industries, and "The Rapid Damage Detection Device (RD3)," created by Boeing Company, are computer-aided applications designed to remove the human auditory factor from impact testing. The research by Hsu et al. (2000) provides a detailed explanation of the CATT system and its principles of operation. Later, the scientists, who introduced the CATT system, further enhanced it in their subsequent work by making it semi-automatic. They incorporated a motorized impact probe and new software featuring position encoding into the system (Barnard, Foreman, & Hsu, 2009). This new version was user-friendly, was relatively low-cost, offered a fourfold increase in scanning speed, and provided higher image quality.

Barnard (2015) conducted drop tests at varying heights on a honeycomb panel with a hexagonal core, generating damages at different energy levels, which were successfully detected using the CATT system. Similar studies on tap testing have been carried out by various researchers (Barnard, 2015; Cawley, 1991; Gryzagoridis & Findeis, 2015; Hsu, 2009). However, none of these studies were conducted in the presence of electrical and magnetic fields. Therefore, no research has explored the effects of performing tap testing in the presence of electric and magnetic fields on damage detection. Yet, since all materials consist of stable physical particles like electrons, protons, and neutrons, they inherently

exhibit magnetic and electrical properties to varying degrees. Therefore, when materials are exposed to electric and magnetic fields, changes in their internal structures are expected. This is because the effects of electric fields (Campbell, Fahmy, & Conrad, 1999; Kumar & Singh, 1997; Liu, Chen, Wang, & Wang, 2001) and magnetic fields (Alshits et al., 2017; Golovin, 2004; Roman, 2004) on the mechanical properties of materials have been extensively studied over time. For instance, Liu et al. (2001) investigated the impact of an electric field on the tensile properties and microstructure of an aluminum-lithium (Al-Li) alloy containing cerium (Ce). Their findings revealed that the ductility of the Al-Li alloy with Ce improved when exposed to an electric field. Similarly, a study by Skvortsov, Pshonkin, Nikolaev, and Kulakov (2023) examined the effects of a constant magnetic field on the creep behavior of an aluminum alloy containing ferromagnetic inclusions. The research indicated that exposing the aluminum alloy to a 0.7 T magnetic field for at least 30 minutes increased its creep rate by up to 20% (Skvortsov et al., 2023). These studies demonstrate that the mechanical properties of magnetorheological and electrorheological materials change in the presence of external magnetic (Carlson & Jolly, 2000) and electric fields (Jagadish & Ravikumar, 2013). Furthermore, it has been shown that various magnetic parameters, such as Curie temperature (Chiba, Yamanouchi, Matsukura, & Ohno, 2003), magnetic anisotropy (Chiba et al., 2008; Endo, Kanai, Ikeda, Matsukura, & Ohno, 2010), and coercive force (Weisheit et al., 2007), can also be altered by applying an external electric field.

This study was conducted to investigate the effects of parameters such as electrical and magnetic fields, as well as material thickness, on the detection of damage in various materials, including aluminum honeycomb panels, wood (Poplar and Pine), and metal (iron), using the CATT method. For this purpose, 2D contour images were generated using the contact durations between the surfaces of both intact and damaged materials, the tapper, as well as the local stiffness values of the materials. The data obtained were evaluated by comparing these contour images.

## **MATERIALS AND METHODS**

The computer-aided tap tests were conducted using a CATTV5\_3-ASI (USA) brand CATT system. As shown in Figure 1, the CATT system consists of a power module, a hand tapping instrument equipped with a steel accelerometer, a laptop computer (Acer One 10 model), software (ASI CATTV5\_3 program), connecting cables, and grids of various sizes. For this study, 15cm x 15cm x 1cm and 15cm x 15cm x 3cm aluminum honeycomb panels sourced from Hexagon, Turkiye, iron materials obtained from Konya Metal Industry, Poplar, and Pine wood

materials from Konya Carpenter Industry, and acetate sheets with a 0.5 cm grid were used. Additionally, experiments utilized strip and neodymium magnets, two 1.5 V batteries with a battery holder, aluminum foil, tape, a millimeter-scaled ruler, and conductive wires.

The experimental setups used in this study are presented in Figure 1, while the materials and their dimensions are shown in Figure 2.

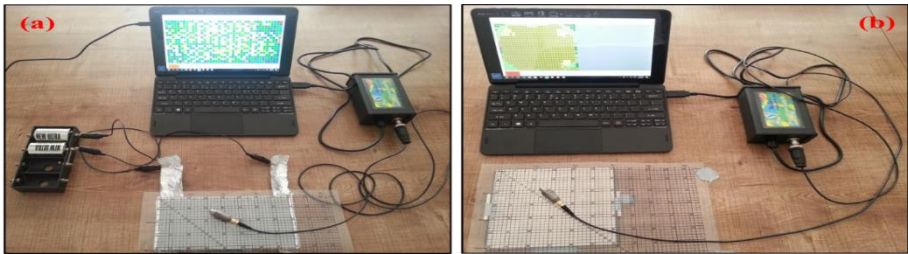


**Figure 1.** Experimental setups used in the research: (a) Tap test setup in electric field, (b) Tap test setup in magnetic field.

### Material Inspection with Computer-Aided Tap Tester (CATT) System

In the simple harmonic motion model of a grounded spring, the contact time ( $\tau$ ) is related to the local stiffness ( $k$ , the spring constant) as follows (Hsu et al., 2000):

$$k = \left(\frac{\pi}{\tau}\right)^2 \cdot m_T \quad (1)$$

Research has shown that when there is no damage to the material surface, the contact time between the tapper tip and the surface is short; however, if there is damage to the surface, this contact time significantly increases (Hsu et al., 2000).

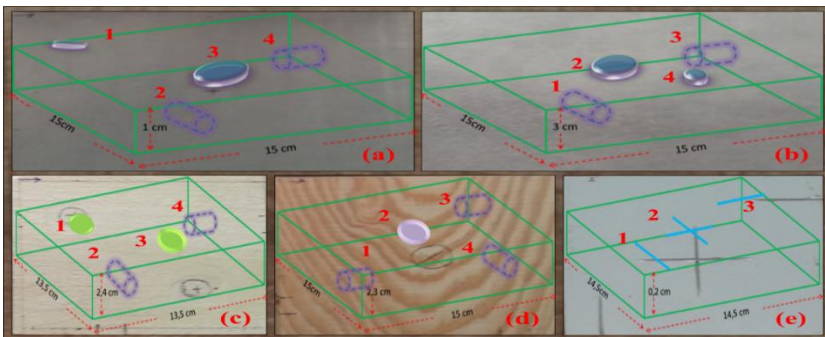


**Figure 2.** Materials used in the study and the locations of the created defects: (a) Thin aluminum, (b) Thick aluminum, (c) Poplar wood, (d) Pine wood, (e) Iron Material.

The  $k$  value in Newtons per meter at different points of the material, determined from this contact time ( $\tau$ ), can then be plotted as an image of the stiffness of the material. By utilizing the obtained contact time or stiffness values, 2D contour images of the examined material surface can be obtained, as well as 3D images.

The damage to the materials used in the study was inflicted with an electric drill and a hammer. These materials and the different types of defects created in various regions of these materials are shown in Figure 2.

The 2D contour images of each material used in the study were obtained using CATT under three conditions: in the absence of any field, in the electric field, and in the magnetic field, before any damage was created. The same process was repeated after the defects given in Figure 2 above were created in the materials, and the contour images of all the damaged materials were obtained with respect to both contact time and stiffness.

### **Performing the Tap Test with CATT**

Before performing the tap test on a material surface with CATT, the setup shown in Figure 1 was established without any electric or magnetic field. Then, the ASI CATTV5\_3 software program, installed on an Acer One 10 model computer, was opened, and a scanning window with 0.5 cm grid spacing was created, according to the dimensions of each material being examined. After verifying that the system was working, the tap test was carried out on the material surface in the selected area size, in the CATT program. During each tap, the contact time between the point struck in the scanning window and the accelerometer was measured in microseconds ( $\mu\text{s}$ ) and displayed on the screen in different colors. After the scanning was completed, impacts were repeated at the desired points to conclude the impact test. The obtained data were then saved to the computer with the desired naming convention. Using both the obtained contact times and the local stiffness values derived from them, 2D and 3D images of the examined materials were plotted.

## **EXPERIMENTAL FINDINGS**

The data collected for investigating the effects of material thickness, electric field, magnetic field, and material type on the determination of various types of defects in different materials using the CATT system have been evaluated.

### **The Effect of Material Thickness on Defect Detection with CATT**

To investigate the effect of material thickness on defect detection, two aluminum honeycomb panels with different thicknesses were used in this study.

The inner core, top, and bottom surface plates of these panels are made of aluminum, but the panels have thicknesses either 1 cm or 3 cm. The defect-free and defective images of the two aluminum honeycomb panels were compared and evaluated. The inner core and the top and bottom surface plates of these two panels are made of aluminum. The obtained 2D contour graphs of the thin aluminum in its defect-free and defective states are shown in Figures 3a and 3b, while the 2D contour graphs of the thick aluminum panel in its defect-free and defective states are shown in Figures 3c and 3d.

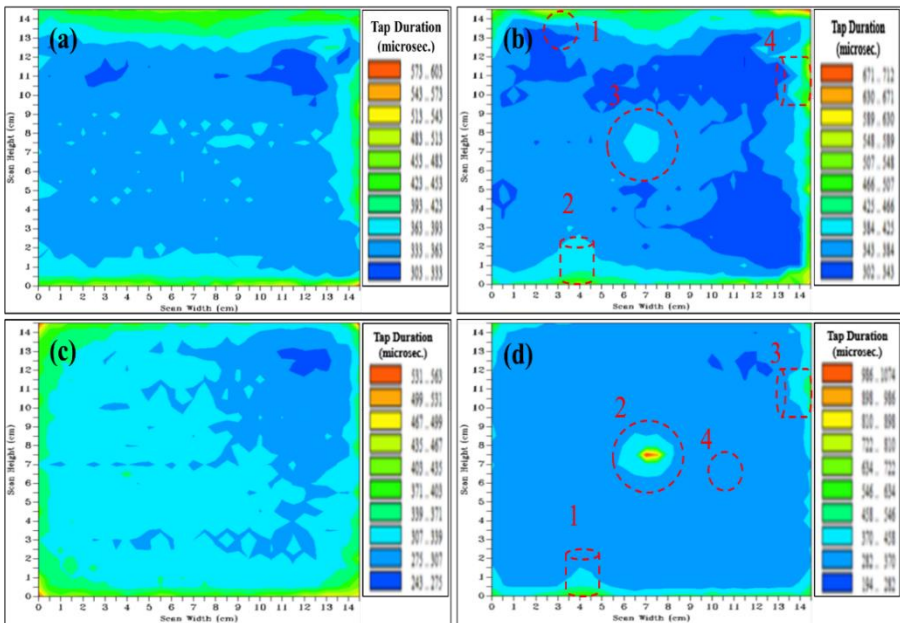


**Figure 3.** Images obtained based on contact times in aluminum honeycomb panels of different thicknesses: a) Thin - Intact, b) Thin - Damaged, c) Thick - Intact, d) Thick - Damaged.

In the thin intact aluminum, apart from the green and red regions obtained from the edge effects, dark blue (303-333  $\mu\text{s}$ ), light blue (333-363  $\mu\text{s}$ ), and turquoise (363-393  $\mu\text{s}$ ) regions were observed, and the contact times obtained for these regions provide information about the material's top plate, adhesive layer beneath the plate, and the inner core. After the damage was created, as seen in Figure 3b obtained again with CATT, it can be observed that damaged regions 2, 3, and 4, as indicated in Figure 2a, were detectable but not very clearly, while damage 1 could not be clearly detected. In the thin damaged aluminum, new shapes arising from the defects appeared, apart from the green and red regions from the edge effects, in the dark blue, light blue, and turquoise regions, which were also visible in the intact sample. Furthermore, after damage occurred in the

thin aluminum, the contact times in the previously observed dark blue, light blue, and turquoise regions were also found to have increased. For example, the contact time in dark blue regions increased from 333  $\mu\text{s}$  to 343  $\mu\text{s}$ , in light blue regions from 364  $\mu\text{s}$  to 384  $\mu\text{s}$ , and in turquoise regions from 393  $\mu\text{s}$  to 425  $\mu\text{s}$ .

In thick intact aluminum, apart from the green and red regions obtained from edge effects, dark blue (243-275  $\mu\text{s}$ ), light blue (275-307  $\mu\text{s}$ ), and turquoise (307-339  $\mu\text{s}$ ) regions were observed. The contact times for these regions provide information about the material's top plate, the adhesive layer beneath the plate, and the inner core. After the damage was created, as seen in Figure 3d, it can be observed, obtained again with CATT, that damage 1, 2, and 3, as indicated in Figure 2b, were detectable, while damage 4 could not be clearly detected. In the thick damaged aluminum, new turquoise (370-458  $\mu\text{s}$ ), green (634-810  $\mu\text{s}$ ), yellow (810-898  $\mu\text{s}$ ), orange (898-986  $\mu\text{s}$ ), and red (986-1074  $\mu\text{s}$ ) regions emerged due to defects, including turquoise (370-458  $\mu\text{s}$ ), green (634-810  $\mu\text{s}$ ), yellow (810-898  $\mu\text{s}$ ), orange (898-986  $\mu\text{s}$ ), and red (986-1074  $\mu\text{s}$ ). These appeared alongside existing green and red regions resulting from edge effects. After damage was created in the thick aluminum, the contact times in the previously observed dark blue, light blue, and turquoise regions increased, like thin aluminum. For example, the contact time in dark blue regions increased from 275  $\mu\text{s}$  to 282  $\mu\text{s}$ , in light blue regions from 307  $\mu\text{s}$  to 370  $\mu\text{s}$ , and in turquoise regions from 339  $\mu\text{s}$  to 458  $\mu\text{s}$ .

### **Effect of Electric and Magnetic Fields on Contact Time**

Studies related to CATT testing and general tap testing have never been carried out in an electric or magnetic field. However, most materials are affected by the electric charges present in their structures when subjected to both electric and magnetic fields. Conductive and ferromagnetic materials are expected to undergo changes in their structures when exposed to electric and magnetic fields. This is because the electric charges and electric dipoles in their structures can align parallel or opposite to the electric field. Similarly in ferromagnetic materials, the magnetic dipoles align in a way that supports the external magnetic field. Regardless of the material type, when subjected to electric and magnetic fields, some changes, to varying degrees, are expected. Can the expected changes in the internal structures of materials in the presence of electric or magnetic fields be used to detect defects present on the surfaces and in the internal structures of the materials? To answer this question, the 2D contour images of the intact Poplar and Pine wood, shown in Figures 2c-d, were first obtained with contact times determined separately for each point on the material surface, in the absence of any field (Figure 4a), in an electric field (Figure 4b), and in a magnetic field

(Figure 4c). Similarly, after creating the defects indicated in Figures 2c-d for the Poplar and Pine wood materials, the 2D contour images were obtained with contact times determined separately for each point on the material surface without a field (Figure 4d), in an electric field (Figure 4e), and in a magnetic field (Figure 4f). For both Poplar and Pine wood materials, the contact times taken in the absence of any field, as well as in the presence of an electric and magnetic field, differed, as seen in Figure 4.

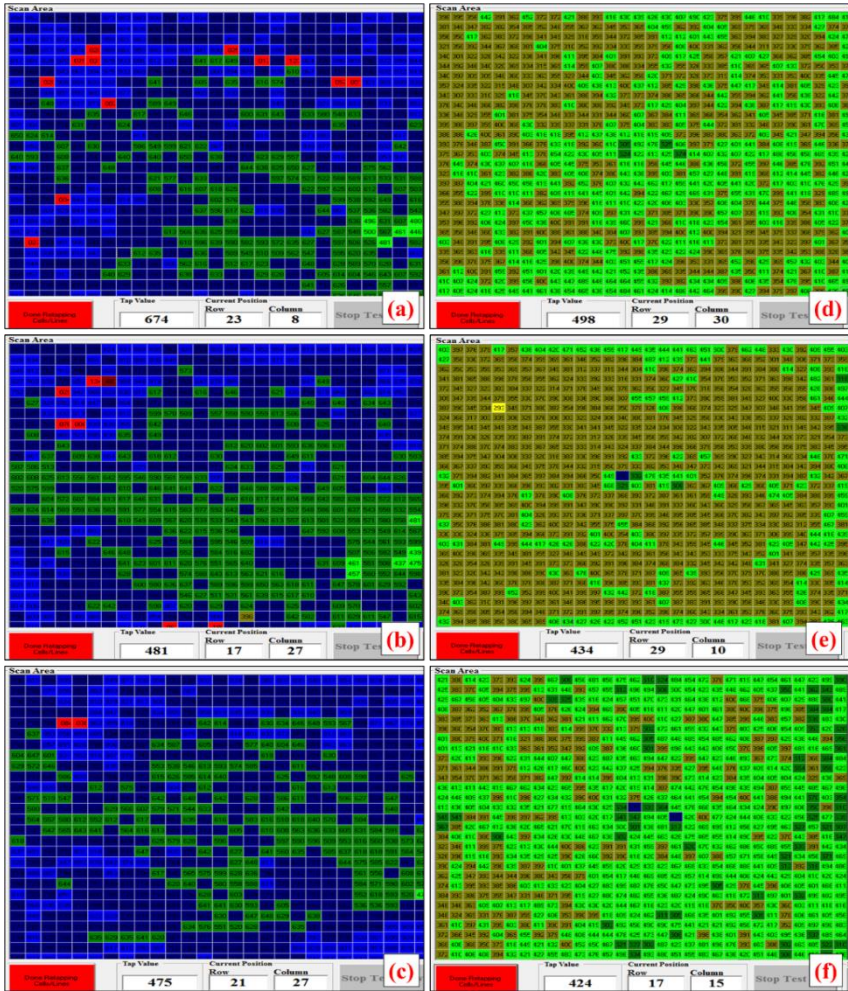


**Figure 4.** Images of the contact time values obtained for damaged Poplar and Pine wood materials: a) No field, b) In the presence of an electric field, c) In the presence of a magnetic field.

Upon examining the data in Figure 4, the data show that the contact time obtained for the damaged Poplar and Pine wood materials were different in the absence of any field, in an electric field, and in a magnetic field. These data

indicate that both the electric and magnetic fields influence the obtained images. Therefore, this method was applied to all defects created in the materials.

### **Effect of Electric and Magnetic Fields on Defect Detection with CATT**

Contour images obtained using contact time and stiffness values for the intact and damaged states of the thick aluminum material. The inner core and top and bottom surface plates of this material are made of aluminum, as shown in Figure 2b, are provided in Figures 5 and 6, respectively. The 3D images drawn using the contact times obtained in the electric and magnetic fields for the thick aluminum material shown in Figure 2b are presented in Figure 7. Additionally, contour images of the contact times and stiffness values obtained with CATT, both without and with electric and magnetic fields, for the iron material shown in Figure 2e, are provided in Figure 8.

The tap test performed in the electric field on the intact thick aluminum revealed the material surface and structure with dark blue (254-294  $\mu\text{s}$ ), light blue (294-334  $\mu\text{s}$ ), and turquoise (334-374  $\mu\text{s}$ ) regions. Similarly, because of the tap test performed in the magnetic field on the intact thick aluminum, dark blue (252-297  $\mu\text{s}$ ), light blue (297-342  $\mu\text{s}$ ), and turquoise (342-387  $\mu\text{s}$ ) regions successfully revealed the material surface and structure. It can be observed that the contact times obtained from tap tests conducted in both electric (E) and magnetic (B) fields were higher (Figure 5a, c) when compared to the contact times from the impact test conducted on the thick aluminum honeycomb panel without any field (Figure 3c).

As a result of the tap test performed in the electric field on the damaged thick aluminum, the dark blue (266-336  $\mu\text{s}$ ), light blue (336-406  $\mu\text{s}$ ), and turquoise (406-476  $\mu\text{s}$ ) regions; along with the green and red (476-966  $\mu\text{s}$ ) regions appearing as an indicator of the damage, revealed the material structure and the four damaged areas shown in Figure 2b. Similarly, the tap test performed in the magnetic field on the damaged thick aluminum clearly revealed the material structure and the four damaged areas shown in Figure 2b. The dark blue (261-309  $\mu\text{s}$ ), light blue (309-357  $\mu\text{s}$ ), turquoise (357-405  $\mu\text{s}$ ), and the green and red (405-741  $\mu\text{s}$ ) regions as indicators of the damage.

As a result of the tap test performed on thick aluminum using the CATT system, the contact times obtained were used to calculate the stiffness values using Equation 1 for the locations where the impact was performed on the material surface. The 2D contour graphs, which are drawn using these stiffness values determined for both intact and damaged thick aluminum in both electric and magnetic fields, are provided in Figures 6a-d.

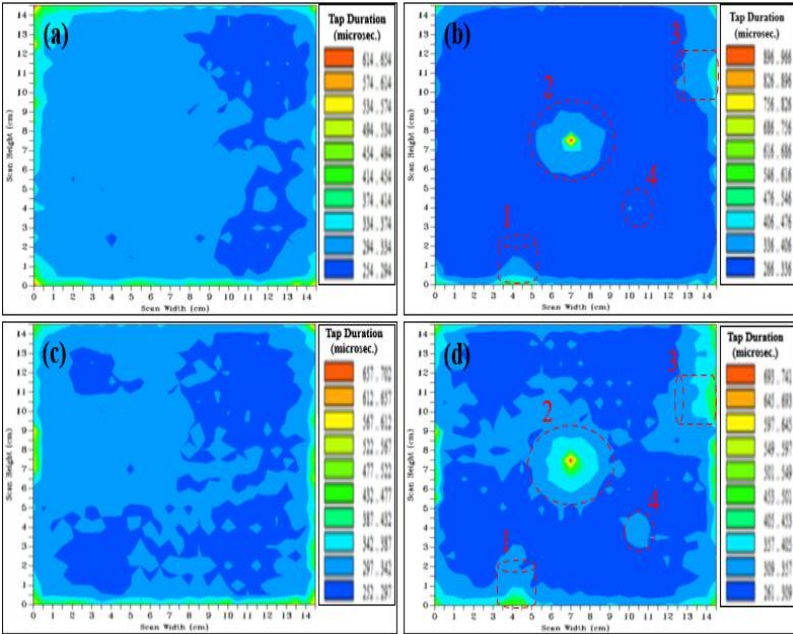


**Figure 5.** Images obtained based on the measured contact time ( $\tau$ ) values for the thick aluminum panel: a) In the electric field - Intact, b) In the electric field - Damaged, c) In the magnetic field - Intact, d) In the magnetic field - Damaged.

In the tap test conducted in the electric field on the intact thick aluminum honeycomb panel, the image obtained using stiffness values shows that the dominant colors are dark green (1.283-1.473 MN/m), light green (1.473-1.663 MN/m), and yellow (1.663-1.853 MN/m), while some regions also display orange (1.853-2.043 MN/m) and red (2.043-2.233 MN/m) colors (Figure 6a). The image obtained using stiffness values shows that, in the tap test conducted in the magnetic field on the intact thick aluminum honeycomb panel, the dominant colors are dark green (1.282-1.479 MN/m), light green (1.479-1.677 MN/m), and yellow (1.677-1.874 MN/m), while some regions also display orange (1.874-2.072 MN/m) and red (2.072-2.269 MN/m) colors (Figure 6c).

In the tap test conducted in the electric field on the damaged thick aluminum, the regions where dark green (1.095-1.283 MN/m), light green (1.283-1.472 MN/m), yellow (1.472-1.660 MN/m), orange (1.660-1.843 MN/m), and red (1.843-2.037 MN/m) colors appear, indicate the material structure. The newly emerged dark blue (0.154-0.342 MN/m), light blue (0.342-0.530 MN/m), and turquoise (0.530-0.719 MN/m) regions, along with evidence of the damage created, are shown in Figure 2b and referenced in Figure 6b. In the tap test conducted in the magnetic field on the damaged thick aluminum, the regions where dark green (1.188-1.374 MN/m), light green (1.374-1.559 MN/m), yellow

(1.559-1.744 MN/m), orange (1.744-1.930 MN/m), and red (1.930-2.115 MN/m) colors appear, along with the newly emerged dark blue (0.261-0.446 MN/m), light blue (0.446-0.632 MN/m), and turquoise (0.632-0.817 MN/m) regions, are indicators of the material structure and the damage created. These are given in Figure 2b (Figure 6d).

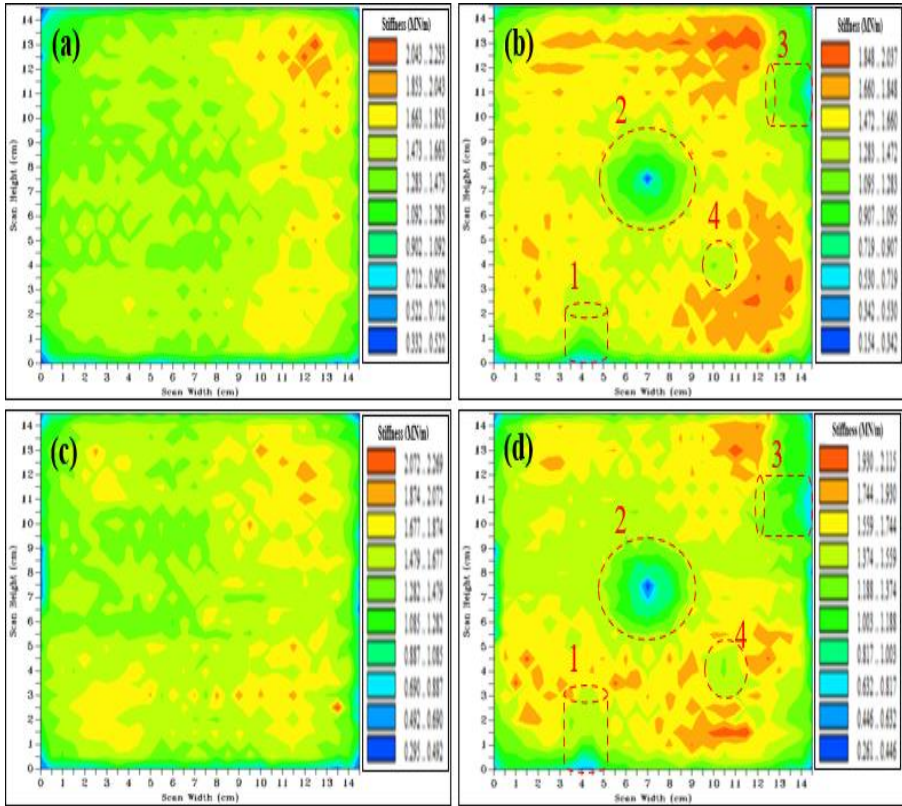


**Figure 6.** Images obtained according to stiffness (k) values for thick aluminum honeycomb panel: a) In electric field - Intact, b) In electric field - Damaged, c) In magnetic field - Intact, d) In magnetic field - Damaged.

One of the significant findings for both intact and damaged thick aluminum honeycomb panels in the electric (E) and magnetic (B) fields is that the stiffness values obtained for the damaged aluminum honeycomb were lower than those of the intact panels. This result indicates that the formation of damage in aluminum honeycomb materials generally reduces the strength of such materials. In addition to detecting all defects in the thick aluminum honeycomb panel in the E and B fields, a significant finding is that the damage in the material reduced stiffness values and, consequently, affected the strength of the undamaged regions of the

panel. This finding is of great importance for aerospace and aviation applications and makes a significant contribution to the relevant literature.

The 3D images, as shown in Figure 2b, drawn using the contact times obtained in the electric and magnetic fields for the thick aluminum material are also presented in Figure 7.

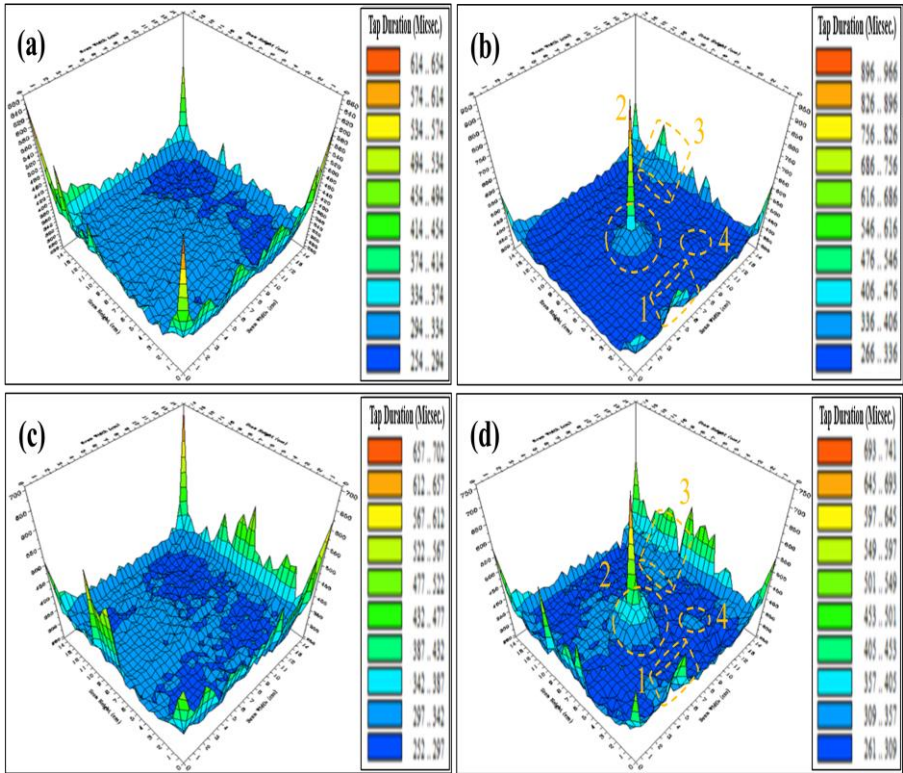


**Figure 7.** Three-dimensional (3D) images obtained based on the measured contact times for thick aluminum honeycomb: a) In electric field - Intact, b) In electric field - Damaged, c) In magnetic field - Intact, d) In magnetic field - Damaged.

In the 3D images shown in Figure 7, the height and width of the sharp peaks indicate the region and magnitude of the damage. When examining the 3D images drawn using the contact times obtained from the tap test conducted in the electric field on both intact and damaged thick aluminum honeycomb panels (Figure 7a and Figure 7b), it is observed that damages in regions 1, 2, and 3, as seen in Figure 2b, are detected. However, the damage in region 4 cannot be detected. In contrast, when examining, using the contact times obtained from the tap test conducted in the magnetic field, the 3D images drawn for both the intact and damaged thick aluminum honeycomb panels (Figure 7c and Figure 7d), it is observed that all the damaged regions shown in Figure 2b are detectable.

The contour images provided in Figure 8 were obtained from the tap test conducted on the iron material, using the contact time of the tapper with the iron material surface and the local stiffness values.

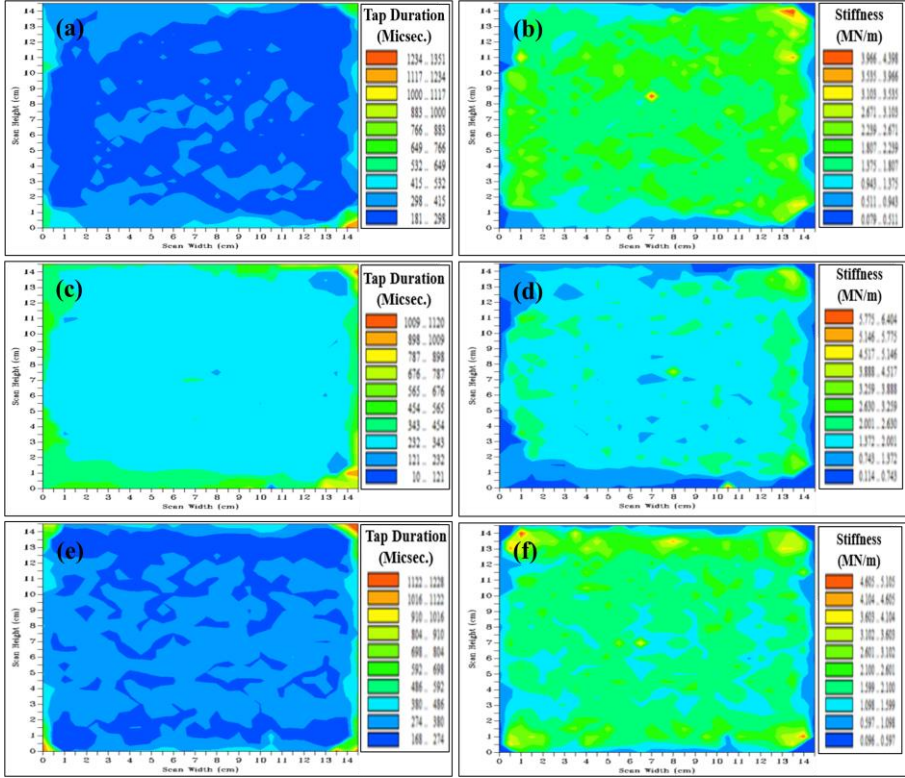


**Figure 8.** Images of contact time and stiffness values obtained for the damaged iron material: a) No field - Contact time, b) No field - Stiffness, c) In electric field - Contact time, d) In electric field - Stiffness, e) In magnetic field - Contact time, f) In magnetic field - Stiffness.

As seen in Figure 8a, the contact times the tap test conducted without any field show that most of the iron material surface appears dark blue (181-298  $\mu$ s), with some areas appearing light blue (298-415  $\mu$ s). As shown in Figure 8c, in the presence of an electric field, the contact times obtained from the tap test reveal that several spots on the iron material surface show light blue (121-232  $\mu$ s) while most of the surface is turquoise (232-343  $\mu$ s). Additionally, the light green spot (343-454  $\mu$ s) seen in the middle of the iron material in Figure 8c corresponds to error number 2 in Figure 2e. On the other hand, as seen in Figure 8e, in the presence of a magnetic field, the contact times obtained from the impact test indicate that most of the iron material surface is light blue (274-380  $\mu$ s), with some areas appearing dark blue (168-274  $\mu$ s). However, it can be observed that

none of the errors shown in Figure 2e are detected in the data from the tap test conducted in the magnetic field, as presented in Figure 8e.

An interesting result regarding the contact times is that in the absence of any field, the contact times for the material surface are generally in the range of 181-415  $\mu\text{s}$ , with light blue to dark blue colors. However, in the electric field, the contact times are in the range of 232-343  $\mu\text{s}$ , showing turquoise; in the magnetic field, the contact times range from 274-380  $\mu\text{s}$ , appearing light blue. This result clearly indicates that the upper limits of the contact times from the tap tests conducted in the electric and magnetic fields are lower than those from the tests conducted without any field.

As seen in Figure 8b, the local stiffness values for the iron material surface, obtained from the tap test, conducted without any field, are in the range of 1.375-1.807 MN/m (light green). Most of the values fall in the range of 1.807-2.239 MN/m (dark green). Additionally, the region representing the damage in area 1, as seen in Figure 2e, is depicted by a turquoise-colored area with a stiffness value of 0.943-1.375 MN/m.

As shown in Figure 8d, in the presence of an electric field, the local stiffness values for the iron material surface, obtained from the tap test, show that a small portion falls in the range of 2.001-2.630 MN/m (light green), while most of the surface has stiffness values in the range of 1.372-2.001 MN/m (turquoise). Moreover, the region representing the damage in area 2, as seen in Figure 2e, is depicted by a light-colored area with a hardness value of 0.743-1.372 MN/m.

In Figure 8f, showing the impact test results in the presence of a magnetic field, the local hardness values for the iron material surface are distributed as follows: a small portion in the range of 3.603-4.104 MN/m (yellow regions), a small portion in the range of 2.100-2.601 MN/m (dark green regions), some areas in the range of 1.098-1.599 MN/m (turquoise regions), and the majority in the range of 1.599-2.100 MN/m (light green regions). However, it is observed in Figure 8f that, based on the data from the impact test conducted in the magnetic field, none of the errors shown in Figure 2e are detected.

A striking result is that the local stiffness values for the material surface are generally in the range of 1.375-2.239 MN/m in the absence of any field. In the electric field, they are generally in the range of 2.100-2.630 MN/m, and in the magnetic field, they are generally in the range of 1.599-2.601 MN/m. This result clearly indicates that the local stiffness values obtained from the tap tests conducted in the electric and magnetic fields are higher than those obtained from the tests conducted without any field.

## DISCUSSION

With the development of technology, the increasing product diversity in the manufacturing sector introduces the concept of providing unconditional assurance of quality, technical safety, durability, and suitability for the intended use of the product. Since the goal is to ensure continuous and high-quality production, the importance of non-destructive testing (NDT) methods in quality control applications is also increasing. In this study, damage created in various materials was detected using computer-aided impact test (CATT) system, which measures contact times and local stiffness values of material surfaces, to obtain 2D contour images and 3D graphics, both with and without electric and magnetic fields. Thus, the effect of material thickness, material type, electric field and magnetic field on the detection of various damages in materials was investigated.

When comparing the contact times obtained from thin and thick aluminum honeycomb panels, the contact times for the thin sample are higher. However, when comparing the contact times from the damaged states of both thin and thick aluminum samples, the contact times obtained from the thick panel are higher than those obtained from the thin panel (Figure 3). This is because the thicker core reduces its impact resistance. In a rectangular prism-shaped panel, the material's strength generally decreases as the height (thickness) increases. Since the thicker aluminum panel has lower impact resistance, it has sustained more damage compared to the thinner panel. The clearer detection of damage in the thick panel is due to the larger extent of damage, which is caused by the thick panel's lower strength. In a material subjected to tap testing, regions with more damage exhibit longer contact times between the material surface and the tapper. Due to the longer contact times observed in the thick aluminum sandwich panel, damage has been detected more precisely.

The contact times obtained for both Poplar and Pine wood materials, with and without the presence of electric and magnetic fields as shown in Figure 4, were found to be different. Therefore, this result indicates that both the electric and magnetic fields influence the measured contact times. This finding supports the idea that Computer-Aided Tap Test (CATT), conducted in the presence of electric and magnetic fields, could be used for assessing damage in materials, especially in thick aluminum honeycomb panels and similar materials that are believed to be more affected by electric and magnetic fields.

When comparing the contact times obtained for a damaged thick aluminum honeycomb panel in Figure 5, it is observed that the contact times measured in the presence of electric and magnetic fields are higher than those obtained without any field. However, in the field-free environment, three out of the four damaged regions in the thick aluminum material were detectable. As seen in Figures 5b

and 5d, contact times obtained through tap testing in both electric and magnetic fields enabled clear detection of all four damaged regions. Similarly, the images obtained from the material's stiffness values, which are consistent with the contact results in electric and magnetic fields allowed for the detection of all four damaged regions (Figures 6b and 6d).

The difference observed in the images obtained in the presence of electric and magnetic fields was an expected result. This is because the thick aluminum sandwich honeycomb panel consists of a hexagonal honeycomb core and an outer aluminum surface layer. Aluminum's exhibition of both conductive and paramagnetic properties is the fundamental reason behind this difference. In a paramagnetic material, magnetic dipoles are randomly oriented; however, when a magnetic field is applied, these dipoles align parallel to the external magnetic field (Serway & Beichner, 2000). Therefore, for paramagnetic materials, the direction of magnetization is the same as the direction of the external magnetic field. As a result, paramagnetic materials are attracted by magnets (Päuser, Keller, Zschunke, & Mügge, 1993). Materials like aluminum, which possess electrical dipoles, can have their electrical dipoles realigned in the presence of an electric field and their magnetic dipoles realigned in a magnetic field. Consequently, in both intact and damaged aluminum materials, even small damage can be clearly detected when the tap test is conducted in the presence of electric and magnetic fields. When comparing the 3D images drawn using the contact times obtained from impact testing in both electric and magnetic fields for the intact and damaged states of the thick aluminum honeycomb panel in Figure 7, all the damages seen in Figure 2b, were detectable in the presence of a magnetic field, whereas in the electric field, damages in regions 1, 2, and 3 were detectable, but the damage in region 4 could not be detected. This result suggests that performing computer-aided tap testing in the presence of a magnetic field is more suitable for analyzing damage in structures like thick aluminum honeycomb panels.

An interesting result regarding the contact times is that in the absence of any field, they are generally in the range of 181-415  $\mu\text{s}$ , predominantly showing shades of light blue to dark blue. However, in the presence of an electric field, the contact times generally fall in the range of 232-343  $\mu\text{s}$ , indicated by turquoise, and in the presence of a magnetic field, 274-380  $\mu\text{s}$ , indicated by light blue. This result clearly shows that the upper limits of the contact times obtained from the impact tests performed in the electric and magnetic fields are lower than those obtained in the absence of any field (Figure 8). Similarly, an interesting result is that in the absence of any field, the local stiffness values for the material surface generally fall in the range of 1.375-2.239 MN/m, fall in the range of 2.100-2.630

MN/m in the electric field and 1.599-2.601 MN/m in the magnetic field. This result clearly indicates that the local stiffness values obtained from the tap tests performed in the electric and magnetic fields are higher than those obtained in the absence of any field.

As seen in Figure 8, damaged regions created on the iron surface were not completely detectable. However, the contact times and stiffness values obtained, like other materials, from the tap tests conducted in the presence of electric and magnetic fields were different from those obtained without any field. This is again an expected result, as iron is a conductive ferromagnetic material. Ferromagnetic materials, due to their permanent magnetization, can easily align their magnetic dipoles in the direction of an applied magnetic field. This factor can significantly alter the impact test values of a surface under examination. Based on the contact times, stiffness values, and contour images obtained for the iron material in Figure 8, it can be observed that of the three damaged regions on the iron material surface, only the damage at location 2 was detectable, albeit weakly, in the electric field. The reason for detecting the damage at location 2 only in the electric field, albeit weakly, is that iron is a conductive ferromagnetic material. However, since the stiffness values of the iron material surface and the steel striker tip are similar, the contact times for defects both on the surface and deeper inside the material do not differ significantly. Therefore, the damaged regions could not be clearly identified. On the other hand, the images obtained from the stiffness values for the iron material show the damage created on the surface better than the images obtained from contact times.

The iron material used in this study is only 2 mm thick. When materials like iron are thicker, larger defects occurring deeper than the surface might be more easily detected by CATT. In this study, the thin aluminum honeycomb panel, thick aluminum honeycomb panel, Poplar wood, and Pine wood, due to their structure, and Poplar wood and Pine wood materials, because their stiffness values are lower than the steel striker tip, allowed for more distinct detection of structural and damaged features. In contrast, where the stiffness values of the iron material are closer to those of the striker tip, the damaged regions could not be clearly detected. This result indicates that a sufficient stiffness difference is necessary between the striker tip used in the CATT device and the material being examined. In other words, using a steel striker tip in the CATT system will yield good results for materials such as honeycomb panels, which are softer than steel. Therefore, to use the CATT system for damage analysis of harder metals like iron, the striker tip in the impact testing device should be made from one of the hardest materials, such as diamond.

## **Conclusions and Recommendations**

In the study, the effects of material thickness, electric field, magnetic field, and material type on the detection of defects in materials such as intact and damaged aluminum honeycomb panels, Poplar wood, Pine wood, and iron were investigated using the Computer-aided Tap Test (CATT) system. The contact times between the material surfaces and the impact probe, along with the stiffness values determined from these contact times, were analyzed. The following conclusions were given based on the findings:

1. The tap tests showed that the material thickness and type affect the contact times and stiffness values.
2. It was figured out that thicker aluminum panels experienced greater damage, and this damage was detected more precisely compared to thinner panels.
3. It was found that electric and magnetic fields had a significant effect in detecting damage on material surfaces.
4. The damage in thick aluminum honeycomb panels was detected more clearly in the presence of a magnetic field.
5. Damaged regions on iron material were not detected in the presence of electric and magnetic fields.

The following suggestions were given based on obtained findings:

1. The effectiveness of the CATT system on materials with different structures and compositions should be investigated in the future.
2. The effects of electric and magnetic fields on CATT results can be investigated using different composites and harder materials.
3. Harder tapper should be used in CATT for damage detection in iron like materials.
4. The effects of electric and magnetic fields on paramagnetic materials like aluminum should be examined more thoroughly.
5. The CATT system should be developed to obtain faster and more reliable results.

Based on these suggestions, similar studies can be conducted using different intensities of electric and magnetic fields, different materials, and various tappers with different hardness.

## REFERENCES

- Alshits, V. I., Darinskaya, E. V., Koldaeva, M. V., Kotowski, R. K., Petrzhik, E. A., & Tronczyk, P. (2017). Dislocation kinetics in nonmagnetic crystals: a look through a magnetic window. *Physics-Uspekhi*, 60(3), 305. doi:10.3367/UFNe.2016.07.037869
- Barnard, D. J. (2015). *Nondestructive evaluation for damage in composites and their repair* (DOT/FAA/TC-14/27). Retrieved from USA: <http://www.tc.faa.gov/its/worldpac/techrpt/tc14-27.pdf>
- Barnard, D. J., Foreman, C., & Hsu, D. (2009). Generating tap test images with a free-hand motorized tapper. *AIP Conference Proceedings*, 1096(1), 1680-1686. doi:10.1063/1.3114160
- Bowkett, M., & Thanapalan, K. (2017). Comparative analysis of failure detection methods of composites materials' systems. *Systems Science and Control Engineering*, 5(1), 168-177. doi:10.1080/21642583.2017.1311240
- Campbell, J., Fahmy, Y., & Conrad, H. (1999). Influence of an electric field on the plastic deformation of fine-grained Al<sub>2</sub>O<sub>3</sub>. *Metallurgical and Materials Transactions A*, 30(11), 2817-2823. doi:10.1007/s11661-999-0119-4
- Carlson, J. D., & Jolly, M. R. (2000). MR fluid, foam and elastomer devices. *Mechatronics*, 10(4), 555-569. doi:https://doi.org/10.1016/S0957-4158(99)00064-1
- Cawley, P. (1991). High Frequency Coin-Tap Method Of Non-Destructive Testing. *Mechanical Systems and Signal Processing*, 5(1), 1-11.
- Cawley, P., & Adams, R. D. (1989). Sensitivity of the coin-tap method of nondestructive testing. *Materials Evaluation*, 47(5), 558-563.
- Chiba, D., Sawicki, M., Nishitani, Y., Nakatani, Y., Matsukura, F., & Ohno, H. (2008). Magnetization vector manipulation by electric fields. *Nature*, 455(7212), 515-518.
- Chiba, D., Yamanouchi, M., Matsukura, F., & Ohno, H. (2003). Electrical manipulation of magnetization reversal in a ferromagnetic semiconductor. *Science*, 301(5635), 943-945.
- Endo, M., Kanai, S., Ikeda, S., Matsukura, F., & Ohno, H. (2010). Electric-field effects on thickness dependent magnetic anisotropy of sputtered MgO/Co<sub>40</sub>Fe<sub>40</sub>B<sub>20</sub>/Ta structures. *Applied Physics Letters*, 96(21).

- Golovin, Y. I. (2004). Magnetoplastic effects in solids. *Physics of the Solid State*, 46(5), 789-824. doi:10.1134/1.1744954
- Gryzgoridis, J., & Findeis, D. (2013, 08.10.2013). *Tap testing of composites benchmarked with digital shearography*. Paper presented at the The British Institute of NDT's 52nd Annual Conference combined with the Materials Testing exhibition, Telford, UK.
- Gryzgoridis, J., & Findeis, D. (2015). *Tap testing vs. thermography*. Paper presented at the 54th Annual British Conference of Non-Destructive Testing, NDT 2015.
- Hsu, D. K. (2009). Nondestructive evaluation of sandwich structures: A review of some inspection techniques. *Journal of Sandwich Structures & Materials*, 11(4), 275-291. doi:10.1177/1099636209105377
- Hsu, D. K., Barnard, D. J., Peters, J. J., & Dayal, V. (1999, 25-30 July 1999). *Physical basis of tap test as a quantitative imaging tool for composite structures on aircraft*. Paper presented at the Review of Progress in Quantitative Nondestructive Evaluation, Montreal, Canada.
- Hsu, D. K., Barnard, D. J., Peters, J. J., & Dayal, V. (2000). *Physical basis of tap test as a quantitative imaging tool for composite structures on aircraft*. Paper presented at the AIP Conference Proceedings.
- Jagadish, H., & Ravikumar, L. (2013). Effect of temperature and electric field on the damping and stiffness characteristics of ER fluid short squeeze film dampers. *Advances in Tribology*, 2013(1), 526428.
- Kumar, S., & Singh, R. N. (1997). Influence of applied electric field and mechanical boundary condition on the stress distribution at the crack tip in piezoelectric materials. *Materials Science and Engineering: A*, 231(1), 1-9. doi:https://doi.org/10.1016/S0921-5093(97)00038-5
- Liu, B., Chen, Z., Wang, Y., & Wang, X. (2001). The effect of an electric field on the mechanical properties and microstructure of Al-Li alloy containing Ce. *Materials Science and Engineering: A*, 313(1), 69-74. doi:https://doi.org/10.1016/S0921-5093(01)00968-6
- Päuser, S., Keller, K., Zschunke, A., & Mügge, C. (1993). Study of the membrane permeability of a paramagnetic metal complex on single cells by NMR microscopy. *Magnetic resonance imaging*, 11(3), 419-424.
- Roman, B. M. (2004). Spin micromechanics in the physics of plasticity. *Physica-Uspeski*, 47(2), 125. doi:10.1070/PU2004v047n02ABEH001683

- Serway, R. A., & Beichner, R. J. (2000). Physics for Scientists and Engineers with Modern Physics, Volume II. *Brooks Cole*.
- Skvortsov, A. A., Pshonkin, D. E., Nikolaev, V. K., & Kulakov, P. A. (2023). Effect of magnetic fields on the formation of the neck of a flat aluminum sample with inclusions during stretching. *Mechanics Research Communications*, *129*, 104071. doi:<https://doi.org/10.1016/j.mechrescom.2023.104071>
- Weisheit, M., Fähler, S., Marty, A., Souche, Y., Poinsignon, C., & Givord, D. (2007). Electric field-induced modification of magnetism in thin-film ferromagnets. *Science*, *315*(5810), 349-351.

## **Chapter 10**

### **Magnesium Matrix Composites (MMCS): Materials, Processing, And Applications**

**Mikail Aslan<sup>1</sup>**

---

<sup>1</sup> Department of Metallurgical and Materials Science Engineering, Faculty of Engineering, Gaziantep University, 27310, Gaziantep, TURKEY  
[aslanm@gantep.edu.tr](mailto:aslanm@gantep.edu.tr), ORCID ID: <https://orcid.org/0000-0003-0578-5049>

# MAGNESIUM MATRIX COMPOSITES (MMCS): MATERIALS, PROCESSING, AND APPLICATIONS

## Abstract

Magnesium Matrix Composites (MMCs) represent a class of advanced materials that combine the light weight of magnesium with the enhanced mechanical and thermal properties of reinforcing phases such as ceramics, fibers, and particulates. These composites offer significant advantages over monolithic magnesium in terms of strength, wear resistance, and thermal stability. Magnesium, being the lightest structural metal, is ideal for applications where weight reduction is crucial, such as in automotive, aerospace, and electronic industries. This chapter explores the composition, processing methods, types of reinforcements, and properties of magnesium matrix composites, alongside their current applications and challenges. We also examine the future trends in MMCs, including emerging reinforcements and novel fabrication techniques aimed at overcoming the limitations of magnesium.

## 1. Introduction

Magnesium, due to its low density, has long been considered an attractive material for lightweight structural applications. As the lightest of all structural metals, it is widely used in automotive and aerospace industries where reducing weight is critical for improving fuel efficiency and performance. However, magnesium's mechanical properties, such as its strength, wear resistance, and thermal stability, are limited compared to heavier metals like aluminum and steel. To overcome these limitations, researchers have developed Magnesium Matrix Composites (MMCs), which integrate magnesium with a second phase reinforcement such as ceramics, fibers, or particulates. These reinforcements are selected to enhance the properties of the magnesium matrix while maintaining its low weight, making MMCs ideal for a range of engineering applications (Chawla, 2013; Kain, 2014).

The primary goal of magnesium matrix composites is to combine the lightweight nature of magnesium with improved mechanical properties, such as tensile strength, hardness, fatigue resistance, and thermal stability. Magnesium matrix composites are used in a variety of demanding applications, including automotive engine blocks, aerospace components, electronic casings, and other

areas where performance and weight are critical considerations (Ramesh & Kumar, 2016).

## **2. Composition of Magnesium Matrix Composites**

Magnesium matrix composites consist of two main components: the magnesium matrix and the reinforcing phase. The matrix phase is typically pure magnesium or magnesium alloys, which are selected for their lightweight and relatively good corrosion resistance. The reinforcement phase can take several forms, including particulate materials, continuous or short fibers, and whiskers. The choice of reinforcement and its volume fraction significantly influence the composite's final mechanical and thermal properties (Latha & Venkatesh, 2018).

### **2.1 Matrix Materials**

The matrix material in magnesium composites is almost always magnesium or magnesium-based alloys. The properties of these matrices can be modified by alloying magnesium with other metals, such as aluminum, zinc, manganese, and rare-earth elements, which help improve the material's strength, corrosion resistance, and thermal stability.

#### **Pure Magnesium:**

Pure magnesium is commonly used as the matrix in MMCs due to its light weight, good machinability, and ease of casting. However, it has limitations in terms of strength, particularly at elevated temperatures, which restrict its use in high-performance applications (Chawla, 2013).

#### **Magnesium Alloys:**

Magnesium alloys, such as AZ91D (alloy of magnesium with aluminum and zinc), WE43 (magnesium with yttrium and rare-earth elements), and Elektron 21 (magnesium with rare-earth elements), are used as matrix materials to improve the strength, creep resistance, and corrosion properties of the composite. These alloys are particularly important for high-temperature and high-performance applications, including aerospace and automotive industries (Kain, 2014).

### **2.2 Reinforcing Phases**

The reinforcing phase in magnesium matrix composites plays a critical role in determining the material's mechanical, thermal, and wear properties. Reinforcements can be classified into particulate, fiber, or whisker forms, each contributing to specific advantages in the final composite.

Particulate Reinforcements:

Particulate reinforcements, such as silicon carbide (SiC), alumina ( $\text{Al}_2\text{O}_3$ ), boron carbide ( $\text{B}_4\text{C}$ ), and graphite, are widely used in magnesium matrix composites. These materials enhance the hardness, wear resistance, and thermal conductivity of the composite. The properties of the composite depend significantly on the type, size, shape, and volume fraction of the reinforcing particles (Ramesh & Kumar, 2016).

Fiber Reinforcements:

Continuous and short fibers, such as carbon fibers, SiC fibers, and boron fibers, are commonly used to improve the tensile strength and stiffness of magnesium matrix composites. These fibers are particularly effective when aligned in the direction of the applied load, offering significant improvements in fatigue resistance and tensile properties (Latha & Venkatesh, 2018).

Whisker Reinforcements:

Whiskers, which are typically single crystals of ceramic materials, provide excellent reinforcement due to their high strength and aspect ratio. The addition of whiskers, such as SiC whiskers, into magnesium matrices improves the composite's hardness and wear resistance, although achieving uniform distribution and dispersion can be challenging (Chawla, 2013).

### **3. Processing Techniques for Magnesium Matrix Composites**

The fabrication of magnesium matrix composites involves several processing methods, which can be broadly classified into liquid-state, solid-state, and powder processing techniques. Each of these methods has its own advantages and challenges, depending on the type of reinforcement, matrix material, and desired composite properties (Ramesh & Kumar, 2016).

#### **3.1 Liquid-State Processing**

Stir Casting:

Stir casting is one of the most widely used techniques for manufacturing magnesium matrix composites. In this method, the reinforcing phase (usually particulate) is added to molten magnesium, and the mixture is stirred to ensure uniform dispersion of the particles. The slurry is then poured into molds and allowed to solidify. Stir casting is cost-effective and can be used for producing large components, but achieving uniform dispersion of the reinforcement can be challenging (Latha & Venkatesh, 2018).

Infiltration Casting:

Infiltration casting involves placing a preform of the reinforcement (typically a porous structure) into a mold and then infiltrating it with molten magnesium.

This technique allows for the creation of composites with a high volume fraction of reinforcement. However, the process can be more complex and expensive than stir casting (Kain, 2014).

### 3.2 Solid-State Processing

#### Powder Metallurgy (PM):

Powder metallurgy involves mixing metal powders (magnesium and reinforcement) and then compacting the mixture into a desired shape. The compacted powder is sintered at high temperatures to form a solid composite. This technique offers better control over the volume fraction of the reinforcement, leading to more uniform material properties. However, it is more expensive and requires more precise control of processing parameters (Ramesh & Kumar, 2016).

#### Hot Isostatic Pressing (HIP):

HIP is a solid-state process used to improve the density and mechanical properties of magnesium matrix composites by applying high pressure and temperature in an inert gas environment. HIP is particularly useful for eliminating porosity and improving the interfacial bonding between the matrix and reinforcement (Chawla, 2013).

### 3.3 Powder Processing

#### Metal Injection Molding (MIM):

MIM is a versatile technique for fabricating magnesium matrix composites with complex geometries. In this process, metal powder is mixed with a binder to form a feedstock, which is then injected into a mold. After injection, the binder is removed, and the part is sintered. MIM offers the potential for near-net-shape processing but is limited by the need for high-quality powders and molds (Ramesh & Kumar, 2016).

## **4. Properties of Magnesium Matrix Composites**

The addition of reinforcements to magnesium significantly enhances its mechanical, thermal, and wear properties. The properties of magnesium matrix composites depend on factors such as the type of reinforcement, volume fraction, and the processing method used.

### 4.1 Mechanical Properties

#### Tensile Strength and Modulus:

The tensile strength of magnesium matrix composites can be significantly improved by adding reinforcements such as SiC particles or carbon fibers. The

reinforcement phase helps to distribute the applied stress more effectively, enhancing the composite's strength and stiffness (Chawla, 2013). Fiber-reinforced composites, in particular, offer substantial improvements in tensile modulus and are widely used in structural applications.

**Fatigue and Creep Resistance:**

Magnesium matrix composites exhibit improved fatigue resistance compared to pure magnesium, as the reinforcing phase prevents crack propagation. Reinforcements like ceramic particles or fibers contribute to higher resistance to both high-cycle and low-cycle fatigue. Additionally, the addition of specific reinforcements improves the composite's creep resistance, which is particularly important in high-temperature applications (Kain, 2014).

**Wear Resistance:** The inclusion of hard ceramic particles such as SiC or B<sub>4</sub>C enhances the wear resistance of magnesium matrix composites, making them suitable for applications requiring high wear resistance, such as automotive brake components and aerospace engine parts (Ramesh & Kumar, 2016).

#### 4.2 Thermal Properties

Magnesium matrix composites typically exhibit improved thermal conductivity compared to pure magnesium. The addition of ceramic reinforcements, in particular, can lead to significantly enhanced thermal stability and heat dissipation capabilities. This makes MMCs suitable for applications in heat exchangers, automotive engines, and electronics, where efficient heat management is critical (Latha & Venkatesh, 2018).

### 5. Applications of Magnesium Matrix Composites

Magnesium matrix composites have found applications in industries where weight reduction, improved mechanical properties, and high thermal stability are essential. These include:

Automotive Industry: Magnesium's low density contributes to fuel efficiency in automotive applications. Its lightness enhances maneuverability in steering columns and bends, while its use in wheels improves performance and fuel efficiency.

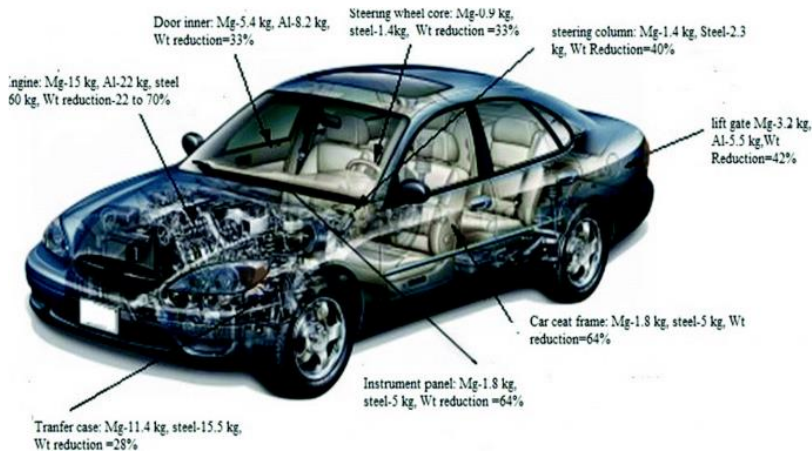


**Fig.1:** Areas of use of magnesium in the automotive industry and comparisons with other metals

Aerospace: Used in aircraft and helicopter parts for its lightweight and high strength, enhancing fuel efficiency in space vehicles due to its low density.



**Passenger Jet:** Rudder Pedal Assembly uses 3-piece Mg-die-cast alloy that is durable and 35% lighter than Al-parts used.  
© Photos courtesy of Ortal Diecasting Company



**AgustaWestland AW139 Helicopter:** Mg Seat Arm Supports, offers significant weight reduction and energy absorption.  
© Photo courtesy of Gulfstream



**Aircraft Door Parts and Back Panel** made of AZ31B Mg-alloy.  
© Photos courtesy of Palbam AMTS Israel



Convair B-36 Peacemaker:  
8600 kg of magnesium!



**Mg Seat Arm Support** withstands dynamic testing and is specifically designed to prevent injury during a crash.  
© Photo courtesy of AgustaWestland

20 % Weight Reduction → 10 % Fuel & Cost Savings

**Fig.2:** Areas of use of magnesium composites in the aerospace

Electronic Devices: Magnesium's lightweight and durability benefit portable devices, cameras, and optical equipment, enhancing portability, lifespan, and durability.



**Fig.3:** Areas of use of magnesium composites in the electronic devices

Medical Devices: Preferred in surgical instruments for its lightweight and durability. Its biocompatibility and slow dissolution in the body make it suitable for orthopedic implants without the need for removal.

## Representative Magnesium-based Implants

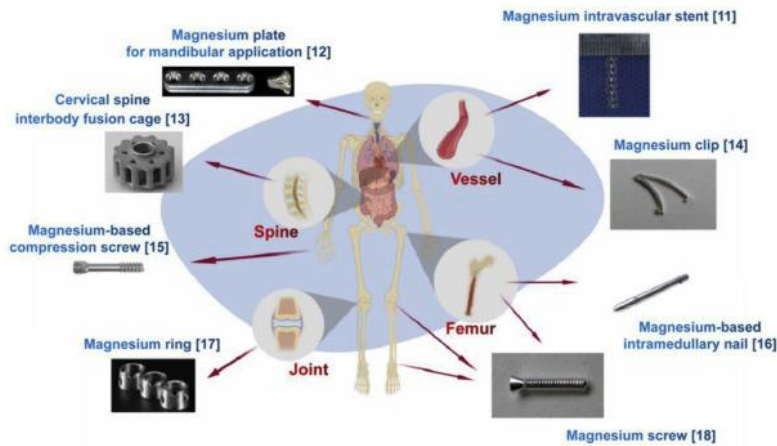


**Fig.4:** Areas of use of magnesium composites in the medical devices

Sports Equipment: Enhances performance in bicycle frames, golf clubs, and tennis rackets due to its lightweight and durability.

Defense Industry: Widely used in military vehicles, equipment, and ballistic armor due to its lightweight and durability, improving maneuverability and load capacity.

Construction and Architecture: Used in structural components to increase load-bearing capacity and accelerate the construction process.

Energy Storage and Battery Technologies: Investigated as an alternative to lithium in battery anodes due to its high energy and low cost.

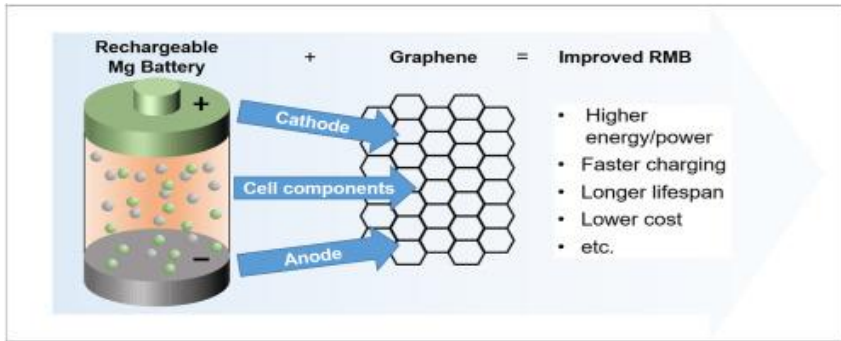


Fig.5: Areas of use of magnesium composites in the Energy Storage and Battery Technologies

## 6. Challenges and Future Directions

Despite the promising advantages of magnesium matrix composites, several challenges remain in their widespread adoption. Issues such as poor interfacial bonding, difficulty in achieving uniform reinforcement dispersion, and high production costs need to be addressed. Advances in processing technologies, such as improved stir casting techniques, new powder metallurgy methods, and the development of new reinforcements, are expected to improve the performance and cost-effectiveness of magnesium matrix composites. Research in this field is ongoing, with a focus on creating more efficient manufacturing methods and developing novel hybrid reinforcements (Chawla, 2013; Kain, 2014).

## 7. Conclusion

Magnesium matrix composites offer a promising solution to the growing demand for lightweight, high-performance materials. By combining magnesium with appropriate reinforcements, these composites exhibit enhanced mechanical, thermal, and wear properties, making them suitable for a wide range of advanced applications in the automotive, aerospace, and electronics industries. While challenges related to processing and cost remain, ongoing research is likely to result in more efficient production methods and the development of novel materials, paving the way for increased adoption of magnesium matrix composites in critical engineering applications.

## References

- Chawla, K. K. (2013). *\*Composite Materials: Science and Engineering\** (3rd ed.). Springer.
- Kain, V. (2014). *\*Metal Matrix Composites: Materials, Manufacturing, and Applications\**. CRC Press.
- Latha, K., & Venkatesh, K. (2018). "Fabrication and Properties of Magnesium Matrix Composites." *\*Journal of Materials Science & Technology\**, 34(7), 1219–1234.
- Ramesh, M., & Kumar, S. (2016). "Synthesis, Processing, and Applications of Magnesium Matrix Composites." *\*Materials Science and Engineering A\**, 657, 1–12.

## **Chapter 11**

### **Mechanical Alloying: Principles, Techniques, And Applications**

**Mikail ASLAN<sup>1</sup>**

---

<sup>1</sup>Department of Metallurgical and Materials Science Engineering, Faculty of Engineering, Gaziantep University, 27310, Gaziantep, TURKEY  
[aslanm@gantep.edu.tr](mailto:aslanm@gantep.edu.tr), ORCID ID: <https://orcid.org/0000-0003-0578-5049>

# MECHANICAL ALLOYING: PRINCIPLES, TECHNIQUES, AND APPLICATIONS

## Abstract

Mechanical Alloying (MA) is a solid-state powder processing technique that enables the creation of advanced materials with unique properties through the repeated deformation, fracturing, and cold welding of powder particles. Initially developed in the 1960s, MA has since become a vital method for producing high-performance materials that are difficult or impossible to achieve via conventional methods. This chapter provides a comprehensive overview of the principles, process mechanics, and applications of mechanical alloying. Key topics include the stages of MA, such as deformation, fracture, and cold welding, as well as the critical process variables that influence the outcome, including ball-to-powder ratio, milling speed, and temperature. The chapter explores the various types of materials produced through MA, such as metal matrix composites (MMCs), high-entropy alloys (HEAs), nanostructured materials, and amorphous alloys, along with their applications in industries like aerospace, automotive, and electronics. Furthermore, it discusses the advanced characterization techniques used to analyze mechanically alloyed materials, such as scanning electron microscopy (SEM), transmission electron microscopy (TEM), and X-ray diffraction (XRD). The chapter concludes by highlighting emerging trends in MA, such as the development of multi-functional materials and the integration of computational modeling and in-situ monitoring technologies, which will shape the future of mechanical alloying and its applications.

## 1. Introduction to Mechanical Alloying

Mechanical alloying is a solid-state process that involves the repeated deformation, fracture, and cold welding of powder particles to form homogeneous mixtures or new phases without the need for melting. The process was initially developed in the 1960s by Benjamin et al. at the International Nickel Company (INCO) and has since been widely adopted for creating advanced materials, including high-strength alloys, metal matrix composites (MMCs), nanostructured materials, and even amorphous materials (Benjamin, 1967; Suryanarayana, 2001). Unlike conventional alloying methods that rely on the liquid phase to mix metals, MA is performed at room temperature or slightly elevated temperatures, where powders undergo mechanical deformation in a ball mill.

The mechanical alloying process is characterized by the use of high-energy ball milling to mix powders in a controlled environment. As the ball mill rotates, steel or ceramic balls collide with the powder particles, causing them to deform, fracture, and cold-weld. This process produces materials with improved properties such as high strength, hardness, wear resistance, and, in some cases, high temperature stability. Because MA does not rely on high temperatures, it is particularly useful for producing materials that are sensitive to heat, such as high-entropy alloys (HEAs), nano-composites, and amorphous alloys.

## 2. Fundamentals of Mechanical Alloying

### 2.1 Basic Process Mechanics

The mechanical alloying process involves the repeated fracturing, cold welding, and plastic deformation of powder particles subjected to high-energy impacts. The basic sequence of events can be divided into three stages:

1. **Deformation:** The powder particles are plastically deformed as they are impacted by the milling balls. This deformation reduces the size of the powder particles, increases their surface area, and promotes the formation of new interfaces between particles.

2. **Fracture:** The deformed powder particles eventually fracture under the stress of repeated impacts, leading to the creation of smaller particles. These smaller fragments are highly reactive due to their high surface area.

3. **Cold Welding:** The fractured particles undergo cold welding, where they fuse back together. Cold welding occurs when the deformed particles, with their high surface energy, come into contact and bond. The welding and fracturing continue in cycles, refining the powder and creating new, homogeneous alloys or composites.

## 2.2 Process Variables

The efficiency and outcome of mechanical alloying depend on several critical process variables:

- **Ball-to-Powder Ratio (BPR):** The BPR refers to the mass ratio of milling balls to powder. Higher BPRs lead to more intensive milling, which accelerates the alloying process but can also cause more wear on the milling tools. Typically, BPRs range from 10:1 to 30:1 for effective alloying (Suryanarayana, 2001).
- **Milling Speed:** The rotational speed of the ball mill significantly affects the collision frequency and the energy imparted to the powder. Higher milling speeds increase the energy input, leading to faster refinement of the powder (Suryanarayana, 2001).
- **Milling Time:** The duration of milling plays a crucial role in controlling the microstructure and properties of the alloy. Longer milling times allow for more homogenous mixing but may lead to excessive particle refinement or the formation of undesirable phases (Sanderov, 1998).
- **Temperature:** While mechanical alloying is typically performed at room temperature, it can also be carried out at elevated temperatures to promote diffusion and phase formation. However, high temperatures can lead to unwanted phase transformations (Tjong, 1999).

Table 1: Effect of Process Parameters on Mechanical Alloying

Parameter	Effect on Process	Typical Values
Ball-to-Powder Ratio (BPR)	Higher BPR increases intensity of milling	10:1 to 30:1
Milling Speed	Higher speed increases collision frequency	100 to 300 RPM
Milling Time	Longer milling produces finer, more uniform powder	10 to 100 hours
Temperature	Elevated temperature aids phase formation	100°C to 300°C

## 3. Types of Materials Produced by Mechanical Alloying

Mechanical alloying is used to produce a variety of materials that exhibit superior properties compared to conventionally processed materials. These materials include:

### 3.1. Metal Matrix Composites (MMCs)

Metal matrix composites are materials made by reinforcing a metal matrix with a secondary phase, which can be either ceramic or another metal. MA is particularly effective for producing MMCs because it allows for the uniform dispersion of hard particles within the metal matrix, resulting in improved

mechanical properties such as strength, hardness, wear resistance, and thermal stability.

- **Reinforcement Materials:** The reinforcing phases typically include ceramic particles like silicon carbide (SiC), aluminum oxide (Al<sub>2</sub>O<sub>3</sub>), boron carbide (B<sub>4</sub>C), and graphite, but they can also involve other metals or alloys.

- **Applications:** MMCs produced by MA are used in applications where high strength, thermal conductivity, and wear resistance are critical. Common uses include automotive components (e.g., brake discs, pistons), aerospace (e.g., turbine blades, heat exchangers), and industrial tools (e.g., cutting tools, wear-resistant coatings).

- **Key Benefits:** The benefits of MMCs include enhanced mechanical properties such as:

- **High Strength-to-Weight Ratio:** Reinforced composites offer greater strength while maintaining low weight.

- **Improved Wear Resistance:** The ceramic particles help reduce wear, which is important for components that face high friction.

- **Thermal Conductivity:** Some composites exhibit better thermal conductivity than the matrix metal alone, making them useful in heat management applications.

### 3.2. High-Entropy Alloys (HEAs)

High-entropy alloys are a class of materials made from five or more principal elements in near-equal proportions (usually 5-10 elements), unlike conventional alloys which are based on a single principal element. The term "high-entropy" refers to the significant mixing of elements, which increases the configurational entropy of the system.

- **Composition and Properties:** HEAs often possess unique properties such as:

- **High Strength:** Due to the solid-solution strengthening effect from the multiple elements.

- **High Temperature Stability:** Many HEAs have high melting points and can maintain their strength at elevated temperatures, making them ideal for extreme environments.

- **Corrosion Resistance:** The multi-element nature of HEAs often improves their resistance to oxidation and corrosion.

- **Applications:** HEAs produced by MA are gaining attention in demanding industries such as aerospace, nuclear reactors, and defense, where materials need to withstand extreme conditions like high temperatures, radiation, and corrosion.

- **Challenges:** The challenges in producing HEAs through mechanical alloying include:

- **Phase Control:** The multi-element nature can lead to complex phase formation, and controlling the phase evolution during the milling process is critical.

- **Solid-Solution Phase Formation:** Achieving a stable solid-solution phase rather than phase segregation can be challenging.

### 3.3. Nanostructured Materials

Nanostructured materials are materials with structures on the nanometer scale (typically 1-100 nm). MA can produce these materials by controlling the particle size during milling, which results in fine microstructures with superior mechanical properties, including increased hardness, strength, and wear resistance.

- **Types of Nanostructured Materials:** These can include:

- **Nanocrystalline Alloys:** Alloys that have a grain size of less than 100 nm. The reduction in grain size leads to a significant improvement in strength (via the Hall-Petch effect), hardness, and corrosion resistance.

- **Nanocomposites:** Nanostructured composites created by incorporating nanoparticles (e.g., carbon nanotubes, graphene, or ceramic nanoparticles) into a metallic matrix, resulting in enhanced mechanical properties such as tensile strength, toughness, and fatigue resistance.

- **Applications:** Nanostructured materials are increasingly used in industries like aerospace, automotive, and electronics due to their superior mechanical and physical properties. These include advanced coatings, microelectronics, and components requiring high wear resistance, like cutting tools.

- **Key Benefits:**

- **Increased Strength:** Nanostructuring leads to significant increases in yield strength and hardness.

- **Improved Wear Resistance:** The fine grain structure provides enhanced resistance to wear and fatigue.

- **Enhanced Performance:** These materials often perform better under harsh conditions, such as high temperatures or exposure to corrosive environments.

### 3.4. Amorphous Alloys (Bulk Metallic Glasses)

Amorphous alloys, also known as bulk metallic glasses (BMGs), are metals that do not exhibit a regular atomic structure like conventional crystalline metals. Instead, they have a disordered, non-crystalline structure. Mechanical alloying is

an effective method for producing amorphous alloys by rapidly cooling the alloy mixture during the milling process, preventing crystallization.

- **Properties:** BMGs produced through MA can exhibit:
  - **High Strength:** Amorphous alloys often have a much higher tensile strength compared to crystalline metals due to the lack of grain boundaries.
  - **High Elasticity:** The absence of dislocations gives these materials high elastic limits, making them ideal for use in highly demanding applications.
  - **Corrosion Resistance:** Amorphous alloys tend to be more resistant to corrosion, especially in acidic or saltwater environments.
- **Applications:** Due to their unique properties, BMGs find applications in fields such as:
  - **Aerospace:** Components that require high strength and light weight.
  - **Medical Devices:** Implants and tools that benefit from the high hardness and biocompatibility of amorphous alloys.
  - **Sporting Goods:** Golf club heads and other equipment that require materials with excellent strength-to-weight ratios.
- **Challenges:** Producing bulk metallic glasses can be challenging due to the need for rapid cooling rates (to avoid crystallization) and the complex nature of alloy design. Additionally, processing techniques like MA require precise control to avoid structural degradation.

### 3.5. Intermetallics

Intermetallic compounds are phases formed between two or more metallic elements, often exhibiting unique properties that are superior to those of their individual constituent metals. Mechanical alloying has been used to create a wide range of intermetallics, such as titanium aluminides (TiAl), iron aluminides, and nickel-based superalloys.

- **Properties:**
  - **High Temperature Resistance:** Intermetallics like TiAl have excellent strength and stability at high temperatures, making them ideal for applications such as turbine blades and aerospace components.
  - **Lightweight:** Many intermetallics, particularly titanium aluminides, offer a good balance between strength and low density, making them attractive for weight-sensitive applications in aerospace.
  - **Corrosion Resistance:** Some intermetallic compounds offer excellent resistance to oxidation and corrosion, which is critical in harsh environments.
- **Applications:** These materials are used in demanding fields like aerospace, where high-temperature stability and strength are required, as well as in automotive and industrial applications.

## 4 Applications of Mechanical Alloying

Mechanical alloying has widespread applications across various industries due to the unique properties of the materials it produces. Some of the most important applications include:

### 4.1 Aerospace and Automotive Industries

In the aerospace and automotive industries, materials processed via mechanical alloying are used to manufacture components that require high strength, low weight, and excellent wear resistance. For example, aluminum and titanium matrix composites are used in engine components, structural materials, and high-performance brake systems (Jang et al., 2000).

Table 2: Applications of Mechanical Alloying in Aerospace and Automotive Industries

Material Type	Applications	Properties Enhanced
Aluminum Matrix Composites (Al-SiC)	Engine components, structural parts	High strength-to-weight ratio, wear resistance
Titanium Matrix Composites (Ti-B4C)	Aerospace structural materials, military components	High-temperature strength, hardness

### 4.2 Electronics and Energy Storage

In electronics, copper and aluminum-based composites processed by MA are used for electrical contacts, connectors, and switches, where both high conductivity and wear resistance are essential. Additionally, HEAs and amorphous alloys are increasingly being investigated for use in energy storage devices, such as lithium-ion batteries and fuel cells, due to their excellent stability, corrosion resistance, and high energy densities (Wang et al., 2012; Kim et al., 2005).

## 5. Characterization of Mechanically Alloyed Materials

The properties of mechanically alloyed materials are highly dependent on their microstructure, which can be characterized using several techniques:

### 5.1 Microscopic Techniques

- **Scanning Electron Microscopy (SEM):** SEM is widely used to observe the surface morphology of mechanically alloyed materials. It provides high-resolution images of the particle size, distribution, and welding behavior of powder particles (Tjong, 1999).

- **Transmission Electron Microscopy (TEM):** TEM offers high-resolution imaging at the nanoscale and is useful for observing the fine details of grain size, phase distribution, and the presence of any amorphous regions (Suryanarayana, 2001).

#### *5.2 X-ray Diffraction (XRD)*

XRD is used to study the crystalline phases in mechanically alloyed materials. By analyzing the X-ray diffraction patterns, the crystallite size, phase content, and any residual stresses can be determined (Ye et al., 2008).

### **6. Future Trends in Mechanical Alloying**

Mechanical alloying is a continually evolving field. Recent trends suggest a shift toward the production of high-entropy alloys (HEAs), nanocomposites, and multi-functional materials. Advances in in-situ characterization techniques, such as synchrotron X-ray diffraction, are providing deeper insights into the dynamics of the milling process, enabling better control over the material properties (Mala et al., 2008).

Furthermore, with the growing demand for lightweight materials, the development of advanced composites that combine metals with ceramics and polymers is becoming a major focus area. The integration of computational modeling and machine learning with mechanical alloying is expected to further enhance the efficiency of the process and accelerate the development of new materials.

### **7. Conclusion**

Mechanical alloying (MA) has proven to be an indispensable technique for the production of advanced materials that exhibit superior properties compared to those made by conventional processing methods. Through the use of solid-state processing, MA enables the creation of alloys, composites, nanostructured materials, and even amorphous phases without the need for melting. This ability to control microstructure and composition at the atomic level, coupled with the versatility of the process, has made MA a powerful tool in materials design for a wide range of high-performance applications across industries such as aerospace, automotive, electronics, and energy storage.

The process of mechanical alloying involves repeated deformation, fracture, and cold welding of powder particles, resulting in the formation of homogeneous materials or novel phases. The key to its success lies in the precise control of various process parameters such as ball-to-powder ratio (BPR), milling speed, milling time, and temperature. Each of these factors influences the degree of alloying, particle size, and final material properties. By adjusting these

parameters, it is possible to tailor the mechanical, thermal, and electrical properties of the resulting materials to meet specific application needs.

One of the most significant advantages of mechanical alloying is its ability to produce metal matrix composites (MMCs) that combine metals with reinforcing particles such as ceramics or carbon. These composites exhibit enhanced mechanical properties such as increased strength, wear resistance, and thermal stability, making them ideal for demanding applications in the automotive, aerospace, and manufacturing industries. For example, aluminum and titanium matrix composites, produced by MA, have found applications in high-performance engine components, structural parts, and lightweight materials.

High-entropy alloys (HEAs) represent another exciting area of growth in mechanical alloying. These alloys, composed of five or more elements in near-equal proportions, exhibit remarkable properties, including excellent high-temperature stability, corrosion resistance, and strength. The development of HEAs through mechanical alloying has led to the exploration of new materials that can withstand extreme operating conditions in industries such as aerospace, nuclear power, and defense. The inherent complexity of HEAs, combined with their potential for a wide range of desirable properties, underscores the importance of MA as a method for advancing material science.

In addition to the production of composites and HEAs, mechanical alloying has enabled the development of nanostructured materials and amorphous alloys. Nanostructured materials, known for their enhanced strength, hardness, and wear resistance, can be achieved through the fine control of particle size and distribution during the milling process. Amorphous alloys, which lack long-range atomic order, offer unique properties such as high corrosion resistance and mechanical strength. The production of these materials through MA has opened new avenues for their application in fields like electronics, energy storage, and even medical devices.

The characterization of mechanically alloyed materials is a critical aspect of understanding their structure, properties, and performance. Techniques such as scanning electron microscopy (SEM), transmission electron microscopy (TEM), and X-ray diffraction (XRD) provide valuable insights into the microstructure, phase distribution, and particle morphology of MA-produced materials. These techniques allow researchers to analyze the effects of milling parameters on the final properties of the materials, guiding further optimization of the process.

Looking to the future, mechanical alloying is poised to play an even greater role in materials development, driven by ongoing advancements in processing techniques, characterization methods, and computational modeling. As the demand for lighter, stronger, and more durable materials increases, especially in

the context of sustainable and energy-efficient technologies, MA will continue to offer solutions for producing high-performance materials with tailored properties. The integration of in-situ monitoring, synchrotron X-ray diffraction, and other advanced characterization methods will provide deeper insights into the dynamics of the milling process, enabling more precise control over material properties and accelerating the development of novel materials.

In addition, the incorporation of machine learning and artificial intelligence into the mechanical alloying process holds the potential to further enhance material design and process optimization. These technologies can be used to predict material behavior, optimize milling conditions, and accelerate the discovery of new alloys and composites with enhanced properties. As these technologies evolve, the combination of advanced simulation tools, real-time data analysis, and experimental processing will enable researchers to design and produce materials with unprecedented precision and performance.

Mechanical alloying's versatility and adaptability make it a cornerstone in the development of next-generation materials. The ability to fabricate materials with controlled microstructures and properties is critical in addressing the increasingly complex requirements of modern engineering applications. Whether it's producing advanced composites for high-performance vehicles, creating novel alloys for harsh environmental conditions, or developing materials for emerging technologies like renewable energy and quantum computing, mechanical alloying will continue to drive material innovation.

In conclusion, mechanical alloying is a powerful and versatile method that has significantly advanced the field of materials science. Its ability to produce materials with exceptional properties, such as high strength, corrosion resistance, wear resistance, and thermal stability, makes it indispensable for industries that rely on high-performance materials. As research progresses, MA will undoubtedly remain at the forefront of material design and processing, contributing to the development of innovative solutions to meet the ever-evolving demands of modern technology.

## References

1. Benjamin, J. S. (1967). "Dispersion strengthened superalloys." *Metallurgical Transactions*, 3(11), 2595–2602.
2. Suryanarayana, C. (2001). *Mechanical Alloying and Milling*. CRC Press.
3. Sanderov, S. A. (1998). "Effect of sintering temperature on the properties of mechanically alloyed copper-based composites." *Materials Science and Engineering A*, 241(2), 145-153.
4. Tjong, S. C. (1999). "Nanostructured materials: Processing, properties and applications." *Materials Science and Engineering: R: Reports*, 28(4), 157–190.
5. Miracle, D. B. (2004). "High-entropy alloys." *Nature Materials*, 3, 279–286.
6. Jang, H., Lee, Y., & Park, J. (2000). "Wear and mechanical properties of Al-SiC composites." *Journal of Materials Science*, 35(13), 3249–3256.
7. Ye, J., Zuo, T., & Cheng, Y. (2008). "High-entropy alloys: A new generation of materials." *Journal of Materials Science & Technology*, 24(6), 939–944.
8. Wang, X., Zhang, Y., & Liu, Z. (2012). "Electrochemical performance of copper-based nanocomposites for energy storage." *Journal of Power Sources*, 195(13), 4411–4416.
9. Kim, J., Lee, S., & Choi, W. (2005). "Amorphous alloys in energy storage systems." *Materials Science and Engineering B*, 120(2), 131–137.

## **Chapter 12**

### **Energy Consumption Analysis and Prediction of Household Appliances by Machine Learning Approach**

**Serhat Berat EFE<sup>1</sup>**

---

<sup>1</sup> Assoc. Prof. Dr., Bandırma Onyedi Eylül University, Dept. Of Electrical Engineering, 10200, Bandırma.  
[sefe@bandirma.edu.tr](mailto:sefe@bandirma.edu.tr), ORCID: 0000-0001-6076-4166

## **Energy Consumption Analysis and Prediction of Household Appliances by Machine Learning Approach**

### **Abstract**

Observing energy consumption in household appliances is a practical way to understand and manage electricity usage effectively. This approach can help design of energy efficient devices. This study focuses on observation and prediction of energy consumption for the household devices. In this context, the importance of energy efficiency was first explained, and then energy efficiency in household appliances was addressed. Then, a real-world dataset that consist of inside - outside temperatures of refrigerator and supply current variation according to these temperatures which obtained from an operating refrigerator was used for experimental prediction. Results were discussed in terms of energy efficiency by using graphs and numerical values.

**Keywords:** Energy efficiency, Consumption prediction, Machine learning

## **1. Introduction**

Energy is the most valuable commodity in the modern world. Therefore, it should be used in most efficient way. The concept of energy efficiency is an important definition that emerged due to this necessity. Energy efficiency, both in general and in household devices, refers to an appliance's capacity to execute its functions while using less energy, lowering utility costs, and limiting environmental effect [1–5]. Tracking usage of energy in household appliances is a useful approach to better understand and manage electricity consumption. Predicting the energy consumption of household devices entails assessing and modeling trends based on device type, usage behavior, environmental conditions, and device efficiency [6–8].

There are some methods and approaches to use household devices energy efficiently. For example, choosing the right size to avoid overuse, looking for “ENERGY STAR” certificate or selecting models with inverter compressors improve efficiency for refrigerators and freezers. Washing machines, dryers and dishwashers tend to use less water and energy. Replacing incandescent lamps with LEDs can help minimize the energy waste. To prevent phantom loads, unused devices should be turned-off. For cooking appliances, using induction stoves instead gas or electric coil stoves can help improve the energy efficiency.

On the other hand, usage habits can also make a positive contribution to energy efficiency. Regular maintenance such as cleaning filters in HVAC systems and dryers, smart usage like turning off appliances when not in use or run full loads in washing machines and dishwashers, use of smart plugs or energy monitoring devices to track usage and identify inefficiencies, upgrading to energy-efficient models like replacing older appliances with newer, more efficient ones and looking for government rebates or incentives for energy-efficient purchases can be given as examples to these habits [9,10].

Energy efficiency has benefits, such as cost savings through lower electricity bills over time, environmental impact through reduced carbon footprint, performance through using modern efficient devices that offer better functionality and incentives in tax credits and rebates may be available for energy-efficient upgrades.

## **2. Energy Efficiency and Consumption Monitoring**

Energy usage observation in household appliances is a practical technique to better understand and manage electricity consumption. There are various tools using for this aim. Use of smart plugs or energy monitors can help tracking real-time energy consumption of individual appliances. Home energy monitoring systems can be connected to electrical panel to monitor the usage of all

appliances. Also, there are many utilities offer detailed energy usage reports via smart meters. Observation workflow includes some key features. Standby power is one of the key observations because many appliances consume energy even when not in use, known as phantom or vampire loads. Another one is peak consumption as high-power appliances like water heaters, ovens, and HVAC systems have peak energy draws. One of the others is energy efficiency because newer and energy-efficient appliances often consume less power than older models. Behavioral impact observation is also important because usage habits, like leaving lights on or frequently opening the fridge, significantly affect consumption. Accordingly, analysis is figured out by observing which appliances consume the most energy at what times and convert energy consumption (kWh) into cost using recent electricity rate [11–14].

Observation steps can be summarized as the flowchart given in Figure 1.

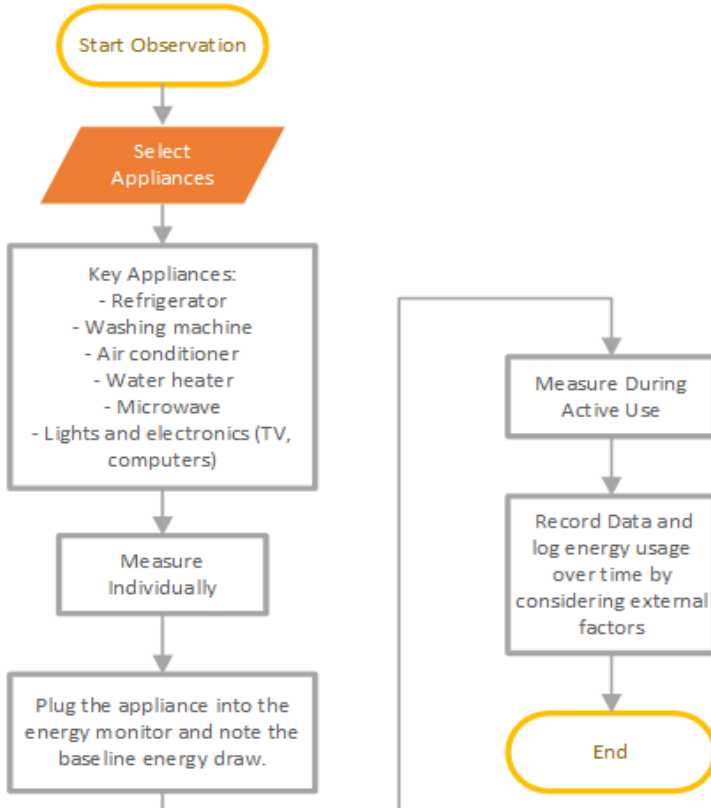


**Figure 1.** Observation workflow flowchart

For a better understanding, in this study one of the most common household device, refrigerator, is analyzed in terms of energy consumption and savings. Analyzing potential savings for refrigerators involves understanding their energy

consumption, comparing it with more energy-efficient models, and calculating the potential cost reductions. To determine a refrigerator's energy use, it starts by checking its energy label or specifications for the annual consumption listed in kilowatt-hours (kWh). Older refrigerators, especially those over 10 years old, typically consume between 1,000 and 2,000 kWh per year, whereas newer energy-efficient models use about 300 to 600 kWh annually. Alternatively, it can be measured actual usage by using an energy meter to track daily consumption and extrapolate this to annual usage. Once the energy consumption data obtained, the annual cost can be calculated by using the formula:

$$\text{Annual Cost} = \text{Energy Consumption (kWh)} \times \text{Electricity Rate (\$/kWh)} \quad (1)$$

For example, if the refrigerator uses 1,200 kWh per year and electricity rate is \$0.15 per kWh, the annual cost would be  $1,200 \times 0.15 = \$180$ . Next, this is compared with the energy consumption of modern, energy-efficient refrigerators. Energy Star-certified models typically use 30–50% less energy than older units. For instance, a new model consuming 400 kWh per year would cost  $400 \times 0.15 = \$60$  annually. To calculate potential savings, formula 2 is used:

$$\text{Savings} = \text{Current Annual Cost} - \text{New Annual Cost} \quad (2)$$

In this example, the savings would be  $\$180 - \$60 = \$120$  per year. When considering replacement, factor in the cost of a new refrigerator, which typically ranges from \$600 to \$2,000 depending on size and features. The payback period calculated by dividing the purchase price by the annual savings. For example, a \$1,200 refrigerator with \$120 annual savings would have a payback period of  $\$1,200 \div \$120 = 10$  years. Lastly, it is considered additional benefits such as recycling incentives offered by utilities for old appliances, the longer lifespan and reduced maintenance of newer models, and the environmental impact of lower energy consumption, which reduces the carbon footprint.

### **3. Methodology and Results**

Machine learning approaches have been widely using in all fields of engineering [15–17]. This study utilizes the Nonlinear Autoregressive Exogenous (NARX) Model, a time-series forecasting and modeling tool designed for systems where the future values of a variable depend on both its own historical values and the past values of an external input (exogenous variable). This approach is particularly effective in systems with nonlinear dynamics. The NARX model is mathematically represented as follows:

$$y(t) = f(y(t-1), y(t-2), \dots, y(t-n_y), u(t-1), u(t-2), \dots, u(t-n_u)) + h(t) \quad (3)$$

In equation (3),  $y(t)$  represents the output (dependent variable) at time  $t$ ,  $u(t)$  is the external input (exogenous variable) at time  $t$ ,  $n_y$  denotes the number of lagged output terms considered,  $n_u$  is the number of lagged input terms considered,  $h(t)$  accounts for model inaccuracies or random disturbances, and  $f(\cdot)$  is the nonlinear function linking inputs and outputs.

The NARX model has three key components:

1. **Autoregressive Component:** Captures the dependence of  $y(t)$  on its own previous values ( $y(t-1)$ ,  $y(t-2)$ , ...).
2. **Exogenous Input:** Represents the influence of an external variable  $u(t)$  on  $y(t)$ , distinguishing the NARX model from purely autoregressive models.
3. **Nonlinear Function ( $f(\cdot)$ ):** Accounts for complex relationships that linear models cannot capture. This function is typically unknown and must be estimated using techniques such as artificial neural networks (ANNs), polynomial models, kernel methods, or piecewise linear approximations.

The NARX model offers several advantages. Its nonlinear nature allows it to capture complex dynamics and incorporate external factors, making it more versatile than purely autoregressive models. As a result, it can be adapted to a wide range of applications [18–20].

According to the aim of study, a real-world dataset of a refrigerator was used. The dataset consists of a total 791397 row data with three columns that are inside temperature, outside temperature and current values of refrigerator. The dataset graph is shown in Figure 2.

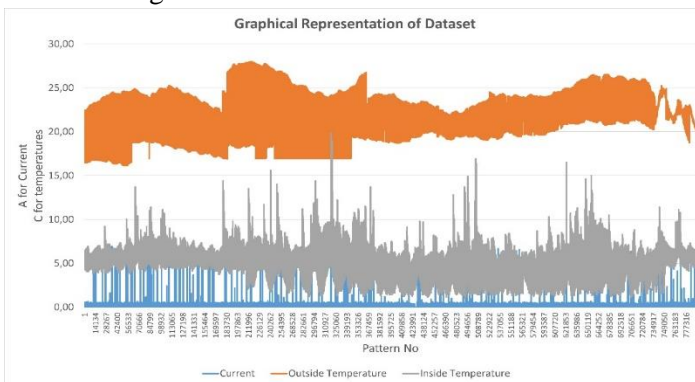


**Figure 2.** Graphic representation of dataset values

The model architecture consists of 20 layers, carefully designed to capture the complexity of the underlying system. A total of 553,977 data points, accounting for 70% of the entire dataset, were utilized for training. Another 118,710 data points, representing 15% of the dataset, were allocated for validation, while the remaining 118,710 data points (15%) were set aside for testing.

To optimize the model's performance, the Levenberg-Marquardt algorithm was selected as the training method due to its efficiency and suitability for nonlinear problems. The evaluation of the model's performance was conducted using the Mean Squared Error (MSE), a standard metric that measures the average squared difference between predicted and actual values. Lower MSE values indicate better model performance and closer predictions to the actual data.

The MSE values for training, validation and test were obtained as 0.0107, 0.0118 and 0.0098 respectively for the best result. Performance graph is given in Figure 3.

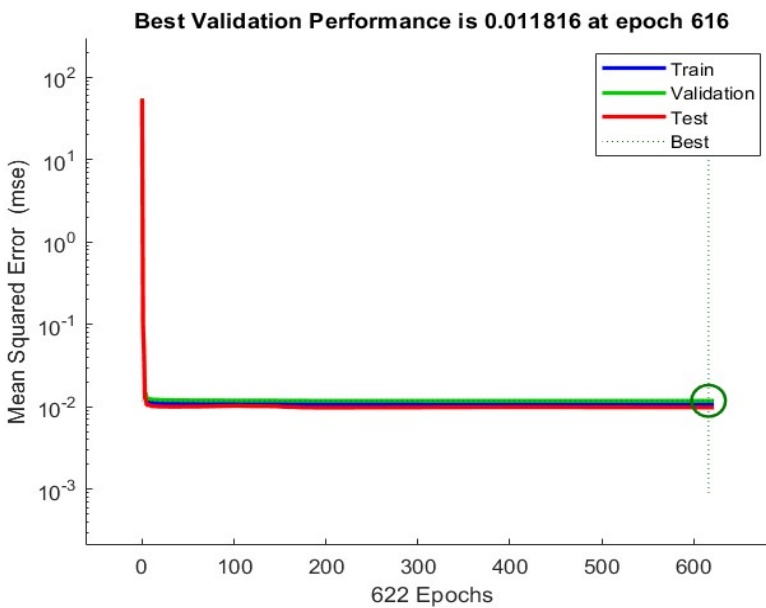


**Figure 3.** Performance graph

These results highlight the model's capability to generalize effectively across unseen data while maintaining robust performance during training. The small difference in MSE values across the three phases suggests that the model is well-trained and not overfitting, making it reliable for real-world applications.

Responses of the model is proposed in Figure 4.

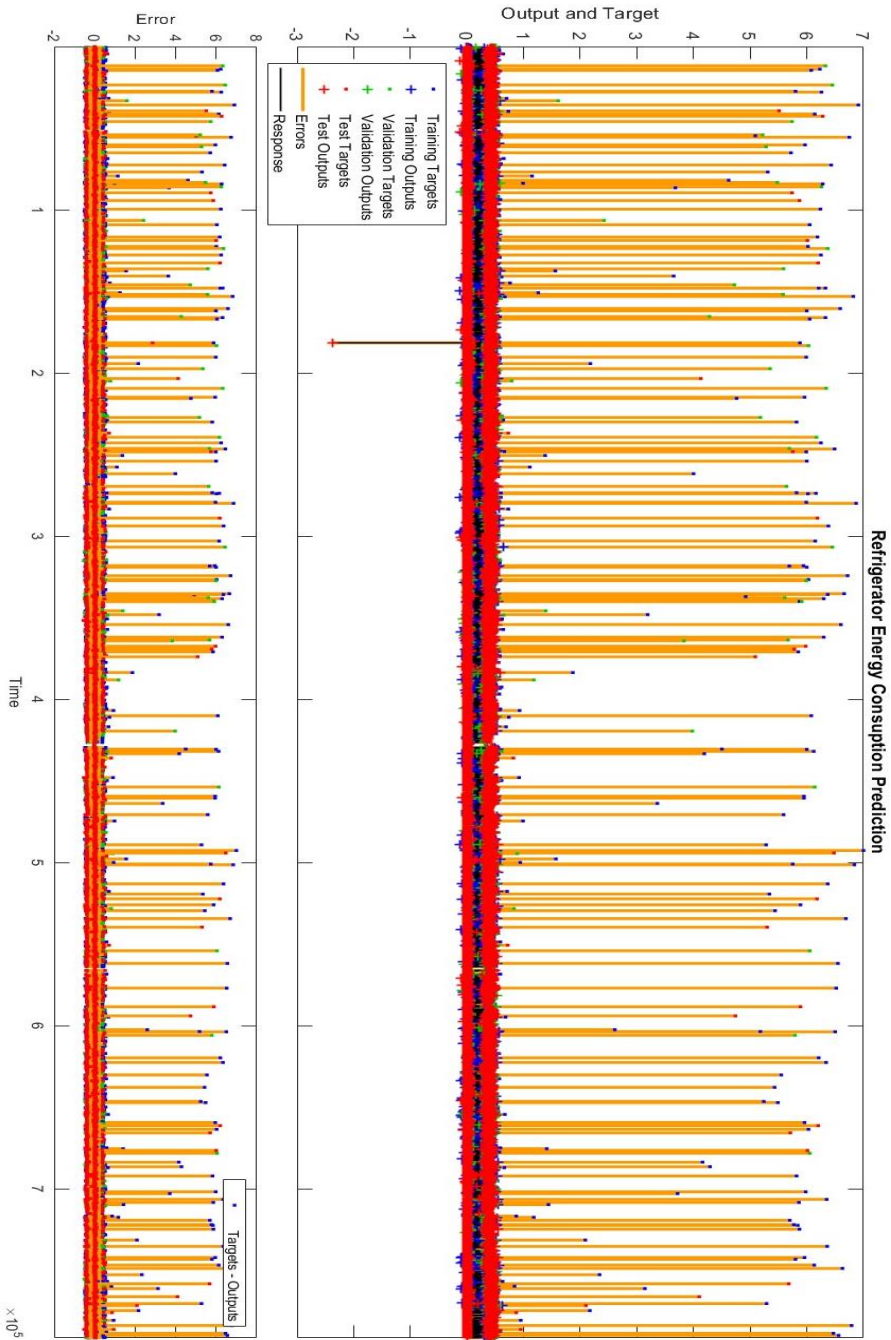


**Figure 4.** Model response graph

#### **4. Conclusion**

This research highlights the practical application of machine learning techniques, specifically the Nonlinear Autoregressive Exogenous (NARX) model, in predicting energy consumption of household appliances, with a focus on refrigerators. The study emphasizes the growing need for energy efficiency in a world where energy is a critical resource. By analyzing real-world data, including temperature variations and current usage, the model provided accurate and reliable predictions, as evidenced by the low Mean Squared Error (MSE) values across training, validation, and testing phases.

The findings underscore the significance of leveraging advanced computational models to monitor and predict energy consumption, offering valuable insights into energy-saving opportunities. For example, the comparison of older appliances with energy-efficient models demonstrated potential cost savings, reduced environmental impact, and shorter payback periods for investments in newer technologies.

This research not only reaffirms the value of monitoring energy use but also encourages the adoption of smarter, data-driven approaches to manage household energy consumption. Practical applications of this work include helping consumers make informed choices about appliance upgrades, optimizing daily usage patterns, and fostering the development of even more energy-efficient devices.

Future research can build on this foundation by expanding the dataset to include other types of household appliances, exploring the integration of renewable energy sources, and refining prediction models with additional variables like humidity, user behavior, and regional energy costs. These enhancements would further bolster efforts to reduce energy consumption, enhance sustainability, and contribute to a greener future.

## References

1. Akalp, O., Ozbay, H., and Efe, S. B., “Design and Analysis of High-Efficient Driver Model for LED Luminaires”, *Light & Engineering*, **29**(2), pp. 96–106 (2021).
2. Uddin, S., Shareef, H., and Mohamed, A., “Power quality performance of energy-efficient low-wattage LED lamps”, *Measurement (Lond)*, **46**(10), pp. 3783–3795 (2013).
3. Trianni, A., Cagno, E., and Accordini, D., “Energy efficiency measures in electric motors systems: A novel classification highlighting specific implications in their adoption”, *Appl Energy*, **252** (2019).
4. Wakabayashi, F. T. and Canesin, C. A., “A high efficiency HPF-ZCS-PWM Sepic for electronic ballast with multiple tubular fluorescent lamps”, *Conference Proceedings - IEEE Applied Power Electronics Conference and Exposition - APEC*, **2**(c), pp. 924–930 (2002).
5. Sun, X., Luh, P. B., Cheung, K. W., Guan, W., Michel, L. D., Venkata, S. S., and Miller, M. T., “An Efficient Approach to Short-Term Load Forecasting at the Distribution Level”, *IEEE Transactions on Power Systems*, **31**(4), pp. 2526–2537 (2016).
6. Cengiz, M. S., “Effects of luminaire angle and illumination topology on illumination parameters in road lighting”, *Light and Engineering*, **28**(4), pp. 47–56 (2020).
7. Rüstemli, S. and Cengiz, M. S., “Active filter solutions in energy systems”, *Turkish Journal of Electrical Engineering & Computer Sciences*, **23**, pp. 1587–1607 (2015).
8. Cengiz, M. S. and Yetkin, S., “Thermal Analysis in Fixed, Flowed and Airless Environment for Cooling in LED Luminaires”, *Light & Engineering*, **28**(6), pp. 28–35 (2020).
9. Djuretic, A. and Kostic, M., “Actual energy savings when replacing high-pressure sodium with LED luminaires in street lighting”, *Energy*, **157**, pp. 367–378 (2018).
10. Carli, R., Dotoli, M., and Pellegrino, R., “A decision-making tool for energy efficiency optimization of street lighting”, *Comput Oper Res*, **96**, pp. 223–235 (2018).
11. Kocaman, B. and Yiğit, Y., “Real-Time Monitoring, Analysis and Control of Power Parameters in Residential Houses Using LabVIEW”, *Balkan Journal of Electrical and Computer Engineering*, **10**(1), pp. 97–105 (2022).

12. Kocaman, B. and Tümen, V., “Detection of electricity theft using data processing and LSTM method in distribution systems”, *Sadhana*, **45**(286), pp. 1–10 (2020).
13. Cengiz, M. S., “THE RELATIONSHIP BETWEEN MAINTENANCE FACTOR AND LIGHTING LEVEL IN TUNEL LIGHTING”, *Light & Engineering*, **27**(3), pp. 75–84 (2019).
14. Kocaman, B. and Rüstemli, S., “COMPARISON OF LED AND HPS LUMINAIRES IN TERMS OF ENERGY SAVINGS AT TUNNEL ILLUMINATION”, *Light & Engineering*, **27**(3), pp. 67–74 (2019).
15. Özer, İ., Efe, S. B., and Özbay, H., “CNN / Bi-LSTM-based deep learning algorithm for classification of power quality disturbances by using spectrogram images”, *International Transactions on Electrical Energy Systems*, **31**(12), pp. 1–16 (2021).
16. Ozer, I., Efe, S. B., and Ozbay, H., “A combined deep learning application for short term load forecasting”, *Alexandria Engineering Journal*, **60**(4), pp. 3807–3818 (2021).
17. Efe, S. B. and Cebeci, M., “Power Flow Analysis by Artificial Neural Network”, *International Journal of Energy and Power Engineering*, **2**(6), p. 204 (2013).
18. Mazumdar, J., Harley, R. G., Lambert, F. C., and Venayagamoorthy, G. K., “Neural network based method for predicting nonlinear load harmonics”, *IEEE Trans Power Electron*, **22**(3), pp. 1036–1045 (2007).
19. Boussaada, Z., Curea, O., Remaci, A., Camblong, H., and Bellaaj, N. M., “A nonlinear autoregressive exogenous (NARX) neural network model for the prediction of the daily direct solar radiation”, *Energies (Basel)*, **11**(3) (2018).
20. Hatata, A. Y. and Eladawy, M., “Prediction of the true harmonic current contribution of nonlinear loads using NARX neural network”, *Alexandria Engineering Journal*, **57**(3), pp. 1509–1518 (2018).

## **Chapter 13**

### **A Review on Liquefaction Studies in Geotechnical Engineering**

**Narin AYENGİN<sup>1</sup>**

**Fatih YILMAZ<sup>2</sup>**

---

<sup>1</sup> Bayburt Üniversitesi

<sup>2</sup> Bayburt Üniversitesi

Liquefaction was first explained by Allen Hazen in 1918, as a result of a detailed analysis of the collapses that occurred in the California Caleveras dam, as the soil behavior caused by the sudden decrease due to the pore water pressure formed during the load applied to the soils. Karl Terzaghi made the first detailed definition of the concept of liquefaction in scientific sources in 1925. It occurs when the weight of the solid masses forming the soil is transferred to the surrounding water during the collapse of the saturated soil. As a result of this situation at any depth in the ground, the water pressure at rest increases and its size approaches the unit volume weight of the submerged ground.

In the studies carried out by Arthur Casagrande in 1936 [1], it was found that the critical equilibrium void ratio of the sand deposits was lower than the void ratio, and that it decreased in volume when under the influence of shear stresses. It has been determined that the soil strength will disappear over time and the soil will behave like a liquid. It is stated that the estimated effective stress will increase, on the other hand, it will become less porous at the critical equilibrium void level, and the pore water pressure will decrease with volumetric expansion under the stresses of the sands.

The concept of liquefaction was used by Mogami and Kuba (1953) [2] to explain the deformations that occur under non-regular, undrained and cyclic loads in cohesive soils. After the [Ms=7,5] Niigata and Great Alaska [USA Mw=9.2] earthquakes that occurred in Japan in 1964, the concept of liquefaction was focused on. These two severe earthquakes damaged all engineering structures and caused the concept of liquefaction to be examined in detail. In particular, the destructive effects of buildings such as tilting of buildings, landslides, overturning of retaining walls, cracks in roads, visible deformations in other transportation networks, deterioration of infrastructure elements have led researchers to examine the concept of liquefaction. Professor H.B.Seed and his students used balanced and unbalanced models to model earthquake loading conditions. They began to deal with this problem using consolidation undrained triaxial pressure tests.

Seed and Idriss explained the important variables affecting the liquefaction of sands affected by the earthquake in 1971 [3] and presented their potential liquefaction risk analysis. With the information they obtained as a result of the SPT experiment, studies that made liquefaction calculations possible were revealed.

Castro [4], as he explained the concept of liquefaction earlier in 1975, divided the classical liquefaction in saturated sands into two, and the mobility that occurs on the basis of dynamic experiments. He stated that the pore water pressure suddenly increased during dynamic loading in saturated loose sands, while

environmental mobility caused the development of positive pore water pressure in compacted sands under dynamic load, the displacement of grains and a decrease in volume. Castro divided the concept of liquefaction into two with dynamic experiment in saturated sands and cyclical motion during classical liquefaction, and examined the displacement of pore water and grains, volume changes in loose and compacted sands.

Seed (1976) [5], conducted experiments to examine the effect of the relative firmness factor in the liquefaction analysis. They interpreted the characteristics of the pore water head during and after the earthquake, and then analyzed the possible spillovers in sandy soils. As a result of the analysis, it has been determined that the hydrostatic pressure effect on the sand layers will continue for a long time after the earthquake. Improving and increasing the drainage conditions of the sandy layers is an effective method for stabilizing the ground.

Youd and Perkins (1978) [6], prepared liquefaction-induced susceptibility maps against soil failure. They stated that the history of the ground, including geological, geotechnical, seismicity, and topographic characteristics, is important in the creation of regional maps.

Castro, Enos, France, and Poulos (1982) [7], named the sudden decrease in shear resistance of soils under earthquake effect with the increase of pore water pressure as soil liquefaction. It has been proposed to classify the behavior types of soils during the earthquake due to the shear stresses that existed before the earthquake due to static loading. The researchers explained that the increase in pore water pressure was due to the soil's tendency to compact.

Tokimatsu and Yoshima [8], in their study in 1983, gave liquefaction relation depending on the SPT impact number and fine grain ratio. In the study, sands containing more than 10% fine grain with similar SPT impact numbers were more resistant to liquefaction than clean sands. It has been concluded that extensive damage will not occur in sands with more than 25 impact numbers according to the reference stress with high strength, silty sands with more than 10% fine grain content and sandy silts with 20% clay content, which are greater than 20. It was also stated that gravelly sands with the same SPT impact number were less resistant to liquefaction than clean sands.

Youd and Wiczorek (1984) [9], observed the effects of liquefaction in an area of 150 km<sup>2</sup> after the 1981 earthquake in Westmorland, a village in California, USA. The intensity of the ground motion and the effect of the liquefaction potential increase as the seismic focal point approaches.

Iwasaki (1984) [10], made evaluations on previous studies by making predictions about liquefied areas in terms of moment magnitude and focal length.

He stated that liquefaction zones affected by previous earthquakes may be exposed to liquefaction as a result of earthquakes that may occur again.

In their studies, Erken and Ansal (1985) [11], determined that after the 6.8 magnitude Erzincan earthquake, the water-saturated silty and clayey soils in the Ekşi water region became liquefied. . The results of the drilling revealed that the soil of the region consists of loose silty sand layers and soft silty, clayey and organic soils. Ishihara (1985) [12], studied the cyclic stresses and liquefaction analysis caused by seismic movements in coarse and fine grained soils. Researchers stated that liquefaction resistance will increase as the relative density increases.

Seed, Tokimatsu, Harder and Chang (1985) [13], observed that it plays an active role in determining the parameter of the SPT experiment, which is used as input data in liquefaction analyses. Kayen, et al. (1992) [14], determined shear wave velocities by seismic penetration test. They arranged the shear wave velocities according to the effective vertical stress. They analyzed and analyzed the data obtained from different regions in the Loma Prieta, also known as the 89 Tremor earthquake in 1989 with a magnitude of  $M_w=7.0$ .

Ishihara (1993) [15], explained the connection between the increase in the tip resistance and the amount of thin material and created a table. In this context, it has been shown that in silty sands with a fine grain ratio of more than 5%, the fine-grained material effect can be measured by adding the end resistance increments shown in the table to the previously measured end resistance to determine the end resistance of a similar amount of clean sand. Field and laboratory experiments of non-plastic silt liquefaction was observed. In addition, it has been observed that plasticity is more important than grain size in affecting liquefaction sensitivity. He stated in his study that cohesionless, non-plastic coarse silt particles are completely susceptible to liquefaction.

Robertson and Wride (1998) [16], reviewed the definitions of liquefaction potential, emphasizing that sandy and similar structures pose a risk for liquefaction. They evaluated these data by using the CPT experiment. They suggested the availability of corrections for properties such as fine grain ratio and plasticity for both SPT and CPT.

Ulusay and Tosun (1999) [17], stated that the ground and rock falls were caused by liquefaction in the 6.2 earthquake that occurred in Adana on 27 June 1998. Based on the results obtained from 6 drilling logs drilled in the earthquake zone, it was determined that the safety factor was lower than 1 in most of the sand layers in the ground and it was highly sensitive to liquefaction.

Chen and Juang (2000) [18], emphasized the importance of some variability in the earthquake and soil indices that make up the data in the studies conducted

for liquefaction potential in making a probability-based interpretation for liquefaction. The researchers proposed the concept of PL (liquefaction probability) associated with the factor of safety against liquefaction in their work. They classified the probabilistic liquefaction of soils by summarizing their deterministic methods of numerical evaluation of liquefaction.

Aydan, Ulusay and Kumsar (2000) [19], emphasized that liquefaction occurred in earthquakes that occurred until the 1992 Erzincan earthquake, but its importance was understood in the Erzincan earthquake. The geological and geotechnical properties of the soils, which were defined in areas prone to liquefaction during the earthquakes that occurred in Turkey until 1998, were examined, and samples taken from certain areas were tested in the laboratory. As a result of the investigations, the distances of the earthquakes to the focal point and the earthquake magnitudes were found in experimental approaches.

Çetin, Seed, Kiureghian, and Tokimatsu (2000) [20], conducted studies on the development of probability-based correlations in the use of SPT data for the interpretation of resistance to the effects of liquefaction or the onset of recurrent liquefaction. To present a Standard Penetration Test-based liquefaction trigger correlation, fines content correction based on the plastic limit value 20% for  $\sigma_v'=1$  atm at 7.5 earthquake magnitude was performed. The probabilistic and deterministic benefits of the proposed correlations that emerged in various studies were examined.

Broughton, Arsdale, and Broughton (2001) [21], are regions close to active seismic zones of Central and Eastern America, belonging to the Memphis and Shelby areas. Researchers have conducted studies to obtain liquefaction and deformation data in Memphis and Shelby regions using ground radar. They prepared liquefaction susceptibility maps of the region and classified them from high to low sensitivity. They determined that the filled areas in the region are of high sensitivity.

Hadush, Yashima, Uzuoka, Moriguchi, and Sawada (2001) [22], analyzed soil damage caused by liquefaction in the Taipei Rapid Transit System tunnels located in Taipei, the capital city of Taiwan. In particular, they observed that liquefaction analyzes about underground structures were limited and they focused on this area. It has been suggested to improve the ground by grouting method by evaluating the liquefaction in the study area.

In his research, Köleoğlu (2002) [23], evaluated the potential liquefaction analyzes in soils by using 43 drilling logs made in Adapazarı. Stating that the effective vertical stress has an effect on the liquefaction phenomenon, the researcher stated that the groundwater level is not deeper than 3 meters in the

places where the liquefaction event occurring in the study area is observed. It emphasizes that the relative firmness is an effective parameter in determining the risks of settlement and liquefaction in soils. In his study, the researcher emphasized that the settlement and effective vertical stress decrease due to seismic movements during the earthquake with the increase in the relative stiffness.

In his study, Polat (2002) [24], determined the properties of the ground after the earthquakes in Izmit and Düzce in the young alluvial fields in the Istanbul region, calculated the bearing forces and determined the liquefaction potential. After the analysis, he concluded that if the continuation of the KAF line in the Marmara Sea is broken, liquefaction due to the earthquake will occur.

Çetin, Işık, and Unutmaz (2002) [25], prepared maps showing the soil deformations in the form of lateral displacement caused by liquefaction in the 1999 Izmit earthquake.

Atak (2003) [26], interpreted the ground liquefaction and displacements in and around Sapanca Lake by comparing the aerial photographs obtained before and after the Kocaeli Izmit earthquake in 1999. Photograms at different scales were compared with photogrammetric procedures in terms of size and orientation.

Ündül and Gürpınar (2003) [27], investigated the liquefaction potential of alluvial deposits in the Çokal valley, which is still deposition. In the study, the particle size distributions were examined by using the drilling values made by DSI. According to the SPT data, it was stated that the liquefaction status of the alluvial soils in the study area is compatible when compared to the soils that liquefy before. Seed, et al. (2003) [28], talked about the importance of the issues that form the basis of potential liquefaction in soils, the conditions affecting liquefaction, and the liquefaction event according to soil types. An experimental correlation has been presented for the determination of the “rd” (strain reduction coefficient) value used in liquefaction analyzes depending on the depth, earthquake magnitude, seismic shaking intensity and field strength.

Youd (2003) [29], stated that the basic properties of the soil cause various deformations, especially in water-saturated cohesionless soils, due to the effect of repetitive stresses caused by earthquakes. He stated that in the areas damaged by liquefaction, the basement soil layers were mostly formed in thick, water-saturated sandy levels of similar structure. He stated that when liquefaction occurs in the soil, deformations occur in the soil due to dynamic and static loads. He stated that the measure of these deformations depends on the density, amplitude, thickness of the liquefied soil layer and the soil type of dynamic, seismic and static waves. In his study for the realization of the liquefaction event,

he revealed that the seismic energy point and this point are dependent on the material density, hardness and earthquake duration. Soil failures, which are analyzed as displacements due to liquefaction, are also; yield failure, lateral spreading and ground oscillation.

Kanıbir (2003) [30], observed with photogrammetric techniques to evaluate the ground deformations caused by liquefaction in the city center affected by the 1999 earthquake in Kocaeli and on the shoreline of Sapanca Lake. Data from 55 borehole logs obtained in the study area, SPT and laboratory experiments were used in liquefaction analysis. The methods suggested by Youd and Idriss were used. As a result of the study, it has been determined that liquefaction is observed along the coast and streams, especially in the alluvial soils in the range of 1-14 m.

Sivrikaya and Toğrol (2003) [31], the results of the SPT test on fine-grained soils in Turkey, and the detailed studies that focused on the equipment used during this test were mentioned. It has been stated that there are variations arising from the differences in the techniques and equipment used in the experiment. It was stated that corrections for the SPT-N value should be made carefully. By examining the previous experiments, evaluations were made for the most appropriate method about variables and SPT(N) corrections, and the relationship between SPT and  $q_u$  (free pressure value) was examined.

Lin and Chang (2004) [32], although it is thought that there is no liquefaction in gravelly soils, it is stated that there is also liquefaction in pebbly soils in the Chi Chi earthquake that occurred in Taiwan in 1999 and the earthquake in Armenia in 1988. Since it is difficult to perform SPT and CPT tests in gravelly soils, investigations were carried out on gravelly soil that liquefied during the Chi Chi earthquake using  $V_s$  (shear wave) and LPT (large penetration test) in gravelly soils. In order to confirm these studies, three-axis experiments were carried out in the laboratory environment. When the liquefaction analysis results were compared, it was seen that they overlapped with the LPT and  $V_s$  methods.

Özdemir and İnce (2005) [33], in their study, examined 45 boreholes in Ilgın district of Konya and used SPT data, groundwater level and laboratory tests in the liquefaction analysis calculation of the settlement area. In the calculations,  $PGA=0.1-0.2-0.3-0.4$  g acceleration values,  $M_w=6$  earthquake magnitude, depth 12 m are used as input data and the liquefaction sensitivity resulting from the calculations is expressed as high - very high, medium and low. has been done. Liquefaction analysis maps were created for 2,4,6,8,10 and 12 m depths.

Aydan, Hamada, Bardet, Ulusay, and Kanıbir (2004) [34], presented equations for various horizontal ground acceleration values of the lateral spreading rate in the region of Sapanca Lake. In the study, photogrammetric

methods were used by Masanori Hamada to determine permanent ground deterioration in different regions. The analyzes on the earthquake data and liquefaction potential in Adapazarı were carried out using the technique recommended by the Japanese Highway and Bridges Association (JRBS). The values obtained were compared with some values of the Nihonkai-Chubu, Niigata and Hyogo Ken-Nabu (Kobe) earthquakes that occurred in Japan.

Chu, Stewart, Lee, Tsai, Lin, Seed, Hsu, Yu, and Break (2004) [35], after the 7.6 magnitude Chi Chi earthquake that occurred in Taiwan in 1999, it was determined that there was a wide area of ground failure in that region. For the interpretation of the study area due to liquefaction, 25 drilling studies and 6 cone penetration test data were used. The NCEER method, the procedure of Youd and Idris, was used in their work.

In this study by Erken, Özay, Kaya, Ülker and Elibol (2004) [36], the stress, strain and pore water pressure of soft clays, water-saturated silty sands, low plasticity silts were mentioned. Afterwards, the modified liquefaction methods are mentioned, its use and how the strength losses and bearing capacity losses occur as a result of dynamic loading are explained.

Çetin and Unutmaz (2004) [37], in order to evaluate the soil properties in Bursa province, 354 drilling studies were examined and maps were created using ground acceleration and spectral acceleration values using information about active faults that will pose a threat in the study area. The effects of the change in acceleration values were compared according to the obtained drilling data and soil properties. Ground acceleration values in the study area were stated to be in the range of 0.34-0.48. Liquefaction risk distribution maps of the region were created using SPT data.

Çetin, Işık, and Unutmaz (2004a) [38], made seismic comparisons by using 0.35 g horizontal ground acceleration in Kocaeli earthquake in 1999 in Değirmendere and it was stated that there are liquefiable layers between 8-11 m. In their studies, it was stated that the landslide caused by the seismic tremors in Değirmendere was due to liquefaction.

Cetin et al. (2004b) [39], stated that the input values of the methods used in the determination of potential liquefaction analysis in their studies are historical data, and new methods were presented by the researchers to evaluate the possibility of liquefaction occurring. It is stated that numerical methods should be used when analyzing whether there is liquefaction in this method. The important factors for the stress relief factor are earthquake magnitude, depth and maximum ground acceleration. Considering these factors, liquefaction analysis of the land was carried out in 2153 different locations. In addition to the method proposed by Youd and Idriss, they added 300 different data to the database and

guided the probabilistic evaluation of potential liquefaction under the leadership of these data.

Yılmaz and Çetin (2004) [40], aimed to analyze the soil liquefaction based on GIS in order to evaluate the geotechnical data of earthquake-induced structural damage for the 1999 Kocaeli earthquake. For this reason, the data were transferred to the GIS program and it was stated that indexes such as potential liquefaction parameter liquefied layer thickness, layer depth and settlement after liquefaction are important engineering values.

In the study, a new probability-based concept, LSI (liquefaction intensity index), is proposed. In this newly presented recommendation, the risks are classified as very low, low, high and very high.

Ulusay and Kuru (2004) [41], investigated the potential liquefaction susceptibility in the Ceyhan earthquake that occurred in Adana with a magnitude of 6.2 in 1998. SPT-based data were used for different earthquake magnitudes. As a result of the studies, it has been revealed that the sand layers are more prone to liquefaction than the data obtained from the areas close to Osmaniye around Ceyhan. Microzonation maps were created with earthquake magnitudes of 6,2 and 7 showing the liquefaction index. With the help of the equations obtained in the study, Turkey's iso-acceleration map was created.

Ulusay, Tuncay, Sönmez and Gökçeoğlu (2004) [42], investigated the general geotechnical characteristics, ground condition, earthquake conditions and potential liquefaction risk of the Çay-Eber earthquake that occurred in 2002. It was observed that liquefaction occurred in a limited area during the Çay-Eber earthquake. It has been observed that liquefaction-induced lateral spreading, cracks and sand boils only occur at the depths of the silty sand layers that are susceptible to liquefaction, close to the surface. In order to examine the liquefaction data, the results of the triaxial pressure test were examined and they stated that the acceleration value should be 0.21 g for liquefaction to occur. In the study, the method introduced by Youd and Idriss (2001) was used while calculating the liquefaction analysis.

Yılmaz and Yavuzer (2005) [43], investigated the liquefaction potential of soils in Yalova, located on the NAF line, using the Standard Penetration Test. Liquefaction analysis maps were created by using the input values obtained for the 7.4 magnitude. Areas where liquefaction may occur for future earthquakes are specified.

Audemard, Gomez, Tavera, and Orihueala (2005) [44], investigated liquefaction based on the data obtained after the earthquake that occurred in Arequipa with a magnitude of  $M_w = 8.4$  in 2001. It was stated that the earthquake, which affected Chile and western Bolivia, occurred at a depth of 29 km and

triggered liquefaction between the soil layers. By examining the distribution of liquefaction properties and the distribution of sand boils regionally, graphs of sand boiling diameter versus focal length were created.

Juang, Yuan, Li, Yang, and Christopher (2005) [45], proposed an empirical method to predict the significance of soil damage due to liquefaction at or near the foundations of existing structures. The proposed procedures were obtained based on 30 case histories of the Kocaeli earthquake (1999) and the Chi Chi (Taiwan) earthquake. These data are It consists of observing the damage caused by the damage and the ground information obtained by CPT. Using these data, the PG (soil damage probability) value vs. potential liquefaction plot was evaluated according to damage class in the study. The value of the severity of the damage caused by liquefaction is called DSI and the classification criteria are; It is stated that it is valid for areas with a slope of  $< 10$ , an earthquake magnitude of  $M_w=7.4 - 7.6$ , and a liquefaction depth of  $< 20$  m. In this study by Ergüven (2005) [46], he gave information about the historical process of liquefaction by describing the research and studies carried out within the scope of liquefaction. In his work; Explaining the main factors affecting liquefaction, laboratory and field test results, how the obtained results are used and liquefaction estimation methods are explained in detail, Eurocode and Japan methods are examined in detail. Information was given about how the construction should be done in areas with liquefaction risk. Bray and Sancio (2006), a chart has been proposed considering the data obtained after the earthquake in Adapazarı, the results of the dynamic experiments on clay and silt mixtures, and the field conditions shown in the figure below.

Mollamahmutoğlu and Babuçcu (2006) [47], published a book based on liquefaction analysis and methods. In the book; Definition of liquefaction, liquefaction phenomenon, types of liquefaction, types of damage originating from liquefaction, variables affecting liquefaction, laboratory and field experiments used in liquefaction potential analysis, analysis methods, methods of reducing liquefaction-induced damages are mentioned. In the last part of the book, the liquefaction analysis program created by the researchers is explained and calculations and graphic drawings are presented.

Karanlık (2006) [48], in his study, obtained soil liquefaction analysis results by using the Standard Penetration Test results of Hatay, Samandağ, Altınköy and its surroundings. The correlation between ground acceleration, depth and SPT values was evaluated with the help of tables. The particle size distribution resulting from previous earthquakes was compared with the known particle size distribution.

Sönmez (2006) [49], investigated potential liquefaction status by using the drilling data in Kocaeli-Gulf region. In the study, liquefaction status was determined and maps were created. By examining the liquefaction effects that may occur on the surface in the cover layers of the soils, the data of both the Kocaeli-Gulf region and the Chi Chi earthquake were taken into account. In addition to this, a chart was created regarding the thickness of the cover layer.

Yılmaz and Bağcı (2006) [50], evaluated the liquefaction status of Kütahya province in their studies and mapped according to the liquefaction hazard. The liquefaction map shows liquefiable and marginally liquefiable areas in the alluvial soil layer and non-liquefiable areas in Neogene units for earthquake magnitude  $M_w=6.5$ . The liquefaction hazard map was prepared in very low and high categories, and it was stated that the maps created during the planning phase should guide the study in terms of engineering.

Taylan, Uysal, Lav and Erken (2007) [51], , after the Adapazarı earthquake in 1999, considering the structural damages such as settlement, collapse and rotation observed in Adapazarı and nearby regions, Adapazarı Erenler was chosen as the study area. The seismic live loads in the region were evaluated and the bearing capacity of the soil and potential liquefaction threats of the study area were examined.

Unutmaz and Çetin (2007) [52], examined the interaction between the structure and the ground in their studies, examined and analyzed the liquefaction potential of the soils on which the structure was located. In order to determine the liquefaction potential of the building foundations, the maximum value of the CSR variable, which is called the cyclic shear strength, and the calculation method are described numerically.

Özaydın (2007) [53], investigated soil liquefaction caused by earthquake movements. In the study; Obtaining the earthquake indirect cyclic shear strength ratio from SPT and CPT tests has been explained, and the safety factor against liquefaction has been determined and formulated. Shallow and pile foundations are described under the effect of liquefaction.

Lenz and Baise (2007) [54], selected the eastern strip of the San Francisco Bay as the study area in their research. Regionally, CPT and SPT-induced liquefaction potential indices were compared, and statistical and spatial variability of LPI was examined. Researchers, LPI It was concluded that regional mapping based on the cumulative distribution of the value showed different results depending on the data used.

Tosun and Orhan (2007) [55], in order to show the GIS-based soil properties in an area of 30 km<sup>2</sup> in Eskişehir province, maps of the study area were created. Evaluations were made on 170 drilling data, 383 undisturbed samples and 1394

disturbed samples belonging to the study area. SPT experimental profiles were created in the study area. Based on the profiles, the distribution was revealed by preparing SPT zone maps in the study area. By performing uniaxial pressure tests on the received data, maps were prepared in GIS environment depending on the unconfined compressive strength.

Koç (2007) [56], using the method suggested by Seed and Idriss (1971) in his study, evaluated the liquefaction potential of the surroundings of Gölcük district of Kocaeli province by means of LiquefyPro software.

Özaydın (2007) [57], evaluated the parameters, analyzes and definitions affecting liquefaction in soils in his study. In order to determine the potential liquefaction analyzes, it was stated that it should be correlated with the field test results based on the studies in Seed and Idriss (1971).

Hasançebi and Ulusay (2007) [58], stated that the lateral spreading effect after liquefaction caused serious deformation in the surface structures and buried structures and proposed a new method to minimize the error rates in the analysis of the displacement caused by the lateral spreading. Within the framework of the researches made by using 6907 drilling data, only the free surface, again only the topographic slope and the free surface were examined and predictions were made by examining the study area. Liquefaction analyzes in all boreholes were performed by both Youd and Idriss (2001) and Çetin et al. (2004) procedures.

Yılmaz, Yıldırım and Keskin (2008) [59], evaluated the Beydağı Dam in their studies by making improvements on the ground in areas with liquefaction potential, without removing the alluvial layer. In the analyzes performed, the CRR value was calculated separately depending on the CPT and SPT, using the Seed and Idriss (1971) method. For the calculation of the stress reduction coefficient affecting the analysis, the effect of the dam built on the soil with liquefaction potential was also taken into consideration. QUAD4M software was used for potential liquefaction analysis calculation.

Unutmaz (2008) [60], superstructure effect in terms of liquefaction potential was evaluated as a result of three-dimensional analysis with FLAC-3D software. A new method describing repetitive strain rates The method is proposed to investigate the pavement effect in terms of liquefaction potential. Static and dynamic situations on the ground were evaluated and approaches were made for different scenarios. As a result of the study, the average cyclic stress ratio for the structure under the influence of soil earthquake is presented. Sönmez and Ulusay (2008) [61], examined the liquefaction potential that occurred in the Gulf of İzmit during the Kocaeli earthquake and created micro-zonation maps based on LSI (liquefaction intensity index) using the data obtained as a result of the analysis. It has been stated that the obtained micro-zonation maps overlap with the predicted

and observed results after the 1999 earthquake. Liquefaction analyzes were calculated considering the method of Seed and Idriss (1971) and the updates suggested by Youd and Idriss (2001). In order to determine the LSI value, the liquefaction safety coefficient values calculated in different boreholes were evaluated according to the severity classes presented by Sönmez and Gökçeoğlu (2005).

Yalçın, Gökçeoğlu and Sönmez (2008) [62], prepared and analyzed liquefaction analysis maps of the city center based on the method proposed by Sönmez and Gökçeoğlu (2005) of Aksaray province located on the Tuz Gölü fault line. The soil geological features of Aksaray province, the parameters affecting liquefaction were examined at all levels within 20 m, and it was stated that the liquefaction potential is very high if the study area occurs with an earthquake of  $M_w=5.2$ . In his study,

Sağlam (2008) [63], made liquefaction analyzes with an earthquake magnitude of  $M_s=7.0$  and created potential liquefaction maps by using the CPT test as a result of geological studies in the areas subject to the zoning plan of Saruhanlı district of Manisa province.

Akın (2009) [64], the properties of the soil in Erbaa district of Tokat province were determined by dynamic analysis and micro-zonation studies of the region located on the NAF line were carried out. With these studies, the potential liquefaction analyzes of the region were examined, and the effects on the ground such as possible settlement and lateral spreading that may occur after liquefaction were evaluated. Pehlivan (2009) [65], made dynamic analyzes on CL, ML, CH, MH class soil properties and examined the behavior of fine-grained soils during the formation of pore water pressures. It has been stated that in the saturated state of sand soils, shear deformations versus pore water pressure ratio are dependent on LL, PI and  $w/LL$  values.

Bol, Önalp, Arel, Sert, and Özocak (2010) [66], analyzed and updated the studies conducted by Bray and Sancio in 2006 and evaluated the liquefaction status of silty soils during the earthquake by using the Marmara earthquake sounding data in 1999 in their CPT-based study. According to their studies, they put forward the Adapazarı criterion, which aims to improve the Chinese criteria. This criterion is similar to the current classification, with more emphasis on clay content. It has been stated that liquefaction occurs in seismic movements with  $M_w \geq 7$  if the following situations occur in the Adapazarı basin.

The liquefaction safety coefficient was calculated using the method suggested by Mhaske and Choudhury (2010) [67], Youd and Idriss (2006). Areas with possible liquefaction occurrence have been determined for earthquake scenarios between magnitudes.

Cao, Hou, Xu, Yuan, and Vibration (2010) [68], in their study, Mw occurring in China In the Wenchuan earthquake with a magnitude of =8.0, detailed field studies were examined and maps showing the liquefaction distribution were created. In order to determine the liquefaction effect in gravelly soils by examining the geological soil profiles, four different areas were selected and detailed field surveys were carried out to conduct drilling studies, dynamic analyzes Vs (shear wave velocity) experiments. It has been stated that SPT and CPT tests are not suitable for gravel soils, and the data obtained from DPT (dynamic penetration test) and Vs (shear wave velocity) methods and evaluated in this study will be a helpful resource in engineering applications.

Holzer, Jayko, Hauksson, Fletcher, Noce, Bennte, Dietel, and Hudnut (2010) [69], liquefaction-induced deformations that occurred as a result of the Mw = 5.2 magnitude Olanca earthquake that occurred in California in 2003 were examined and liquefaction analyzes were calculated using the Seed and Idriss (1971) method. . Assuming that the bladed cutter resistance data in sandy soil profiles in the study area approached the resistance value against shear, analyzes were made in terms of SPT impact numbers.

Aslan (2010) [70], The liquefaction status of the wastewater treatment plant area to be built in Gebze district of Kocaeli province was investigated. As input data, values of 8 drilling logs varying between 21-28 m were used in their studies. The geological characteristics of the alluvial ground in the study area were determined by field and laboratory experiments. As a result of the data obtained, possible liquefaction status was evaluated with the methods of different researchers and liquefaction-based maps were created. By making use of field and laboratory experiments, the geomechanical characteristics of the Wastewater Treatment Plant planned to be built in Gebze were determined and the liquefaction potential analysis was investigated. In the study, coarse grained soils, the 1999 Kocaeli earthquake value, Ms=7,4 earthquake magnitude and SPT test data were used. It is concluded that liquefaction will occur in the studied area, but liquefaction will not be observed on the surface due to the cover soil effect.

Orhan and Ateş (2011) [71], examined 28 drilling logs in their study and using CPT data, the liquefaction status of alluvial soils in Saruhan district of Manisa province was examined according to the Iwasaki (1982) method. The liquefaction analysis was carried out using the earthquake of magnitude Mw = 7.1 and ground acceleration values of 0.28 g. Areas with high liquefaction potential were determined in the study area.

Tosun, Seyrek, Orhan, Savaş and Türköz (2011) [72], conducted a study based on the SPT(N) values obtained from 232 borehole logs in Eskişehir. In addition, 106 research pits were opened to obtain geotechnical information. In the

earthquake scenario of  $M_w = 6.4$ , the possible liquefaction situation was examined by using SPT data. The analyzes were calculated for ground acceleration values of 0.19 g, 0.30 g and 0.47 g, and it was stated that the presence of groundwater level and alluvial soils together with the seismic characteristics of the region increased the possibility of liquefaction.

Akdeniz, et al. (2011) [73], The engineering properties of the soils of the Güllük, Yeni Bağlar and Bahçelievler neighborhoods of Eskişehir were evaluated on the basis of GIS. The data of the samples obtained from 136 drilling logs were evaluated. Three-dimensional modeling of the ground was created using the data of the ground in the study area. In their studies, it was stated that there is a linear relationship between the SPT(N) value and the unconfined compressive strength.

Papathanassiou, Seggis, and Pavlides (2011) [74], investigated possible liquefaction in the Thessaly Plain in Larissa, Greece, which has a high earthquake risk. The potential liquefaction index method was analyzed using the SPT data obtained from 53 borehole logs made in the study area. Mapping studies were carried out showing the properties and liquefaction status of the layers that may be liquefied. Factor of safety against liquefaction The method proposed by Youd and Idriss (2001) Calculated with. In this context, the safety coefficient value of the soil soil against liquefaction was calculated. The design acceleration for the liquefaction calculation in the Thessaly Plain of the town of Larissa was taken as 0.249, and it was examined with a probability of hanging over a 50-year period with a probability of 10%. Based on the data obtained as a result of the study, it was stated that liquefaction could occur in only two regions close to the Pinios River.

Chang, Kuo, Shau, and Hsu (2011) [75], analyzed the SPT(N) based analyzes used to evaluate the liquefaction status by using the values of liquefied and non-liquefied areas after the Chi-Chi earthquake in Taiwan.

Bhattacharya, Hyodo, Goda, Tazoh and Taylor (2011) [76], examined the fault line and seismic movements in the Tokyo Bay region in their research and evaluated the effects of liquefaction in the fill areas. The effect of liquefaction has been observed seriously in alluvial areas and reclaimed soil profiles in the filling areas. It has been stated that the degree of liquefaction-based damages in the filling areas depends on the age of the filling, the filling type and the soil improvement method used.

Kolat, Ulusay, and Suzen (2011) [77], conducted a geotechnical microzonation analysis regarding the suitability of settlement areas for their purpose in their research. The properties and dynamic behavior of quaternary alluvial soils in a seismically active area in Yenişehir district of Bursa province

were examined. Iwasaki et al. (1982) and the liquefaction intensity map was prepared by the method suggested by him.

Sönmezer, Çeliker and Kılınc (2012) [78], conducted geological ground surveys in Kırklareli Bahçelievler Fabrikalar neighborhood and obtained 21 drilling data. Liquefaction potential GIS-based YASS and probable liquefaction maps were created. It has been determined that the bearing capacity of the ground will decrease as a result of the earthquake that may occur in Bahçelievler and Fabrikalar district, which are areas where the YASS varies between 2m-4m. In their study,

Dixit, Deweikar and Jangid (2012) [79], examined the  $M_w = 6.5$  earthquake magnitude, the safety factor against liquefaction for two different PGA acceleration values for the recurrence periods of 475 and 2475 years. In order to evaluate the liquefaction analysis of Mumbai city, the calculation based on the SPT(N) impact number proposed by Seed and Idriss (1971) was made. For  $M_w = 6.5$  earthquake magnitude, maps showing the liquefaction status in the study area were prepared.

Habibullah, Pokhrel, Kuwano, and Tachibana (2012) [80], evaluated the Satte Region of Japan, which is an intense earthquake zone and also has a lot of damage as a result of the earthquake. In this region, liquefaction assessments were made and GIS-based liquefaction potential was examined. Data from different depths in the range of 10-50 m and laboratory results were used. 50 drilling data were evaluated; Using SPT(N), YASS and grain size distribution, maps showing the potential liquefaction status of the study area were produced.

Sharma and Hazarika (2013) [81], investigated 200 borehole logs for the city of Guwahati (India) in order to evaluate the liquefaction situation with an earthquake magnitude of  $M_w = 7.5$ . For the calculation of the liquefaction state of the study area, Seed and Idriss (1971), Seed et al. (1983) and Boulanger and Idriss (2004) procedures were taken into account and the calculation results were evaluated and compared for each method.

Akın, Özvan and Topal (2013) [82], carried out a study supporting the investigation of liquefaction and lateral spreading formations in the research area affected by the  $M_w = 7.2$  earthquake that occurred in 2011 on the eastern shore of Lake Van. In the levees of the Karasu River, one of the largest streams in the region, liquefaction-induced sand boiling and lateral spreading were observed, and ground data were evaluated. As a result of the experimental data examined, it was determined that the soil class was silty sand, and the potential liquefaction status was evaluated by considering the LPI and LSI methods. They stated that the cover soil thickness has an effect on the liquefaction phenomenon.

Aydan, Ulusay, and Kumsar (2013) [83], examined the liquefaction status of the Edremit and Erciş earthquakes that occurred in Van in 2011, and the deformations that occurred in the ground after the liquefaction event.

Huang and Yu (2013) [84], evaluated liquefaction and liquefaction-based damages by examining data from 12 different earthquakes that occurred in the beginning of the 21st century in their study.

Duman and İnkizler (2014) [85], conducted studies on the determination of the liquefaction risk situation of the province of Erzincan, which is close to the NAF line and where mountainous and seismic movements are quite active. The calculations of the analyzes were based on SPT and were carried out according to the method of Seed and Idriss (1971). Based on Sönmez and Gökçeoğlu (2005) procedure, liquefaction potential maps and liquefaction potential index maps were prepared for different earthquake magnitudes and different depths.

Akın, Akkaya, Özvan and Şengül (2015) [86], dynamic soil parameters related to the study area were determined by means of geophysical methods, soil survey studies in Van Yüzüncü Yıl University area located near Van Lake. The situation of the Pilya-Quaternary deposits in the project area related to the study area was examined, and various units with different geological characteristics were formed and lithological studies were carried out before working on the correct micro-regions. They stated that geotechnical studies (drilling and laboratory experiments) should be carried out in order to group the sub-units in this respect. Geotechnical studies were completed with 45 drilling logs and SPT tests. While calculating the liquefaction state,  $M_w=7.2$  and PGA value of  $0.4\text{ g}$  were taken into account and the Standard Penetration Test was taken into account. Liquefaction maps were created based on the data obtained using the methods suggested by different researchers. When the liquefaction maps are examined, it is stated that the risk of liquefaction in the study area can be described as very low or non-liquefiable.

Gücek and Zorluer (2021) [87], stated that it is not possible to prevent all loss of life, property, material and moral damage caused by earthquakes, but it is possible to minimize the damages against the destructions that may occur before the earthquake. It has been stated that due to the rapid increase in pore water in cyclic shear stresses under the influence of earthquake forces, soils with low saturated silt, clay and sand content are structurally damaged due to the fact that the strength of the soil decreases due to the effective stress and behaves like a liquid. Local ground values were obtained by using 11 different earthquake records and 124 sounding data for the liquefaction status of Afyonkarahisar province, which is in a tectonically serious position in Turkey, where active faults are located. Field and laboratory studies are dynamic The effect on dynamic

behavior was examined with the Deep Soil v6.1 software used in the analysis. According to TBDY, one dimensional non-linear analysis method was preferred in time history in soils with liquefaction status. As a result of this study, risk maps were created by evaluating the analyzes. It is aimed to calculate the dynamic behavior of the foundation soils of existing built structures and planned structures.

In this literature research, liquefaction studies in our country and around the world have been compiled. The fact that liquefaction studies have become more common means reducing/preventing possible losses of life and property. In geographies that are faced with the reality of earthquakes, the danger of liquefaction is a situation that must always be taken into consideration.

## References

- [1] Casagrande, A. (1938) "Notes on Soil Mechanics-First Semester," Harvard University (unpublished), 129 .
- [2] Mogami, T. ve Kubo, K. (1953). "The Behavior Of Soil During Vibration" Proceedings of the Third International Conference on Soil Mechanics and Foundation Engineering.
- [3] Seed, H. B. ve Idriss, I. M. (1971). Simplified Procedure for Evaluating Soil Liquefaction Potential, Journal of the Soil Mechanics and Foundation Div., ASCE, 97, 9.
- [4] Castro, G., "Liquefaction and Cyclic Mobility of Saturated Sands", Journal of the Geotechnical Engineering Division, ASCE, Vol.101, No. GT6, 1975, s.551-569.
- [5] Seed, H.B., Evaluation of soil liquefaction effects on level ground during earthquakes, ASCE National Convention on Liquefaction Problems in Engineering, P.A., pp. 27-52,(1976).
- [6] Youd, T. L. and Perkins, D. M. 1978. Mapping liquefaction-induced ground failure potential. Journal of the Geotechnical Engineering Division, ASCE, 104 (GT4), 433-446.
- [7] Castro, G., Poulos, S.J., France, J.W. and Enos, J.L., Liquefaction induced by cyclic loading, Report Submitted to the National Science Found, Washington D.C, (1982).
- [8] Tokimatsu, K.; Yoshimi, Y. "Empirical Correlationship on Soil Liquefaction Based on SPT N Value and Fires Content" Soil and Foundations, JSSMFE, Vol 23, No 4, 1983.
- [9] Youd, T.L., Wieczorek, G.F., Liquefaction during the 1981 and previous earthquakes near Westmorland, California. Geological Survey, Menlo Park, CA (USA), (1984).
- [10] Iwasaki, T., Arakawa, T. and Tokida, K.I., Simplified Procedures for Assessing Liquefaction During Earthquakes, Journal of Soil Dynamics and Earthquake Engineering, 3(1), 49-58, (1984).
- [11] Ansal A., Erken A. (1985): "Behavior of Clays Under Repetitive Stress", Earthquake Research Bulletin, V.48, p. 5-81.
- [12] Ishihara, K., Stability of natural deposits during earthquakes. Proceedings of the 11th International Conferance on Soil Mechanics and Foundation Engineering, Vol. 1.A, A. Balkema, Rotterdam, The Netherlands, 321-376, (1985).
- [13] Seed, H. B., Tokimatsu, K., Harder, L. F., and Chang, R. M., Influence of SPT procedures in soil liquefaction resistance evaluations, Journal of Geotechnical Engineering, ASCE, 111 (GT12), 1425-1445, (1985).

- [14] Kayen, R.E., Mitchell, J.K., Seed, R.B., Ladge, A., Nishio, S. and Countinho, R., Evaluation of SPT-CPT and shear wave-based methods for liquefaction potential assessments using Loma Prieta Data, Proceedings of the 4th Japan-US. Workshop on Earthquake Resistant Design of Lifeline Facilities and Countermeasures for Soil Liquefaction, NCEER-92-0019, 177-192, (1992).
- [15] Ishihara, K. , Liquefaction and flow failure during earthquakes. *Géotechnique*, 1993,43 (3),351–451. <https://doi.org/10.1680/geot.1993.43.3.351>.
- [16] Robertson, P., Wride, C., Evaluating cyclic liquefaction potential using the cone penetration test, *Canadian Geotechnical Journal* 35(3), 442-459, (1998).
- [17] Ulusay, R., Tosun, H., Assessment of geomechanical properties and liquefaction susceptibility of foundation soils at a dam site, Southwest Turkey. Turkish Earthquake Foundation, Report No. TDV/TR 020-34, 63 p, (1999).
- [18] Chen, C. J., and Juang, C. H., Mayne, P.W., Hryciw, R., Calibration of SPT and CPT based liquefaction evaluation methods. (eds) Innovations and applications in geotechnical site characterization, Geotechnical Special Publication, Vol.97, ASCE, Reston, 49–64, (2000).
- [19] Aydan, Ö., Ulusay, R., Kumsar, H., Liquefaction phenomenon in the earthquakes of Turkey, including recent Erzincan, Dinar and Adana-Ceyhan earthquakes, Proceedings of the 12th world conference on earthquake engineering, Auckland, 12WCEE-2000, (2000).
- [20] Cetin, K., Seed, R., Der Kiureghian, A., Tokimatsu, K., Harder, L., Kayen, R.J., Idriss, I.M., SPT-Based probabilistic and deterministic assessment of seismic soil liquefaction initiation hazard, Pacific Earthquake Engineering Research Center, PEER Report No. PEER-2000/05, (2000).
- [21] Broughton, A.T., Van Arsdale, R.B., Broughton, J.H., Liquefaction susceptibility mapping in the city of Memphis and Shelby County, Tennessee. *Engineering Geology* 62(1-3),207-222, (2001).
- [22] Hadush, S., Yashima, A., Uzuoka, R., Moriguchi, S., Sawada, K., Liquefaction induced lateral spread analysis using the CIP method., *Computers Geotechnics* 28(8), 549-574, (2001).
- [23] Köleoğlu, E., Evaluation of Liquefaction Potential and Comparison of Liquefaction Analysis Criteria, Istanbul, (2002)..
- [24] Polat, F., Liquefaction Potential of Quaternary Sediments in the Istanbul Settlement Area, Master Thesis, Istanbul Technical University, Institute of Science and Technology, Istanbul, 2002.

- [25] Cetin, K.O., Isik, N., Unutmaz, B., Engineering, E., Seismically induced landslide at Degirmendere Nose, Izmit Bay during Kocaeli (Izmit)-Turkey earthquake, *Soil Dynamics and Earthquake Engineering*, 24(3), 189-197, (2002).
- [26] Atak, V.O., Aksu, O., Önder, M., Aydan, Ö., Toz, G., Determination of Direction and Size of Displacements Due to Liquefaction and Faulting in Soils by Photogrammetric Methods Küçükçekmece and Its Surroundings Technical Congress, İstanbul, 8-9 November, (2003 ).
- [27] Undul, O. and Gürpınar, O., Liquefaction Potential of Alluvial Soils in Çokal Valley (Gallibolu), *Istanbul University Faculty of Engineering Journal of Geosciences*, 16 (1), 67-80, (2003).
- [28] Seed, R. B., Çetin, K. O., Moss, R. E. S., Kammerer, A. M., WU, J., Pestana, J. M., AndRiemer, M. F., “Recent Advances in Soil Liquefaction Engineering and Seismic SiteResponse Evaluation”, *Proc. 4th International Conference on Recent Advances in Geotechnical Earthquake Engineering and Soil Dynamics*, San Diego, March 28-31, USA, (2003).
- [29] Youd, T. L., Liquefaction Mechanisms and Induced Ground Failure. In: *International Handbook of Earthquake and Engineering Seismology*, 81B, pp. 1159e1173, (2003).
- [30] Kanibir, A., Investigation of lateral spreading in Sapanca and suggesting empirical relationships for the estimation of displacements due to lateral spreading, *High Engineering Thesis*, Hacettepe University Institute of Science and Technology, Ankara, 209 p, (2003).
- [31] Sivrikaya, O., Toğrol, E., 2003. A Study on the Correction of SPT Results in Fine Grained Soils. *ITU Journal of Engineering*, 2 (6), 59-67, Istanbul.
- [32] Lin, P.-S., Chang, C.-W., Chang, W.-J., Characterization of liquefaction resistance in gravelly soil: large hammer penetration test and shear wave velocity approach, *Soil Dynamics Earthquake Engineering Research Insititue* 24(9-10), 675-687, (2004).
- [33] Ozdemir, A & Ince, I. (2005). Geology seismotectonics and soil liquefaction susceptibility of Ilgin (west-central part of Turkey) residential area. *Engineering Geology - ENG GEOL.* 77. 169-188. 10.1016/j.enggeo.2004.10.002.
- [34] Aydan, Ö., Hamada, M., Bardet, J.P., Ulusay, R., Kanibir, A., Liquefaction induced lateralspreading in the 1999 Kocaeli earthquake, Turkey: case study around the Hotel Sapanca, *Proceedings of the 13th world conference on earthquake engineering*, Vancouver, BC, Canada, paper, (2004).
- [35] Chu, D. B., Stewart, J., Lee, S., Tsai, J., Lin, P., Chu, B., vd. (2004), “Documentation of soil conditions at liquefaction and non-liquefaction

- sites from 1999 Chi-Chi (Taiwan) earthquake”, *Soil Dynamics and Earthquake Engineering*, Vol 9-10 (24), 647-657.
- [36] Erken, A., Özay, R., Kaya, Z., Ülker, M., B., C., Elibol, B., Soil liquefaction and bearing capacity losses during earthquakes. *Turkey Engineering News*, 2004,3, 20–26.
- [37] Çetin Ö.K., Yunatici A.A., Çağlı S., Güllökar T., Aktaş R., Altıncık F., Çelik S., Arabacı M.H. and Çekmeceli M., GIS Aided Probabilistic Seismic Hazard Analysis and Liquefaction Risk Map Generation for the City of Bursa. *Soil Mechanics and Foundation Engineering Tenth National Congress*, Istanbul Technical University, Istanbul, 479-489, (2004).
- [38] Cetin, K.O., Isik, N., Unutmaz, B., Engineering, E., Seismically induced landslide at Degirmendere Nose, Izmit Bay during Kocaeli (Izmit)-Turkey earthquake, *SoilDynamics and Earthquake Engineering*, 24(3), 189-197, (2004a).
- [39] Cetin, K.O., Seed, R.B., Der Kiureghian, A., Tokimatsu, K., Harder Jr, L.F., Kayen, R.E., Moss, R.E., Standard penetration test-based probabilistic and deterministic assessment of seismic soil liquefaction potential. *Journal of geotechnical geoenvironmental engineering* 130(12), 1314-1340, (2004b).
- [40] Yılmaz, Z., Çetin, K. Ö., (2004), “GIS-Based Seismic Soil Liquefaction Assessment For Sakarya City After 1999 Kocaeli-Turkey Earthquake”, *Proc., The 11th Int. Conf. on Soil Dynamics and Earthquake Engineering and The 3rd Int. Conf. on Earthquake Geotechnical Engineering*, 7th-9th January 2004, University of California, Berkeley, USA, pp. 909-916.
- [41] Ulusay R, Kuru T., 1998 Adana-Ceyhan (Turkey) earthquake and a preliminary microzonation based on liquefaction potential for Ceyhan town. *Natural Hazards*(2004).
- [42] Ulusay, R., Tuncay, E., Sönmez, H., Gökçeoğlu, C., An attenuation relationship based on Turkish strong motion data and iso-acceleration map of Turkey, *Engineering Geology*, 74, 265-291, (2004).
- [43] Yılmaz, I., Yavuzer, D., Liquefaction potential and susceptibility mapping in the city of Yalova, Turkey. *Environmental Geology* 47(2), 175-184, (2005).
- [44] Audemard, F.A., Gómez, J.C., Tavera, H.J., Orihuela, N., Soil liquefaction during the Arequipa Mw 8.4, June 23, 2001 earthquake, southern coastal Peru. *Engineering Geology* 78(3-4), 237-255, (2005).
- [45] Juang, C.H., Yuan, H., Li, D.K., Yang, S.H., Christopher, R.A., Estimating severity of liquefaction-induced damage near foundation, *Soil Dynamics Earthquake Engineering Research Institute* 25(5), 403-411, (2005).

- [46] Ergüven, K. , Soil Liquefaction, Postgraduate Liquefaction, Mustafa Kemal University Institute of Science and Technology, Antakya, 2005.
- [47] Mollamahmutoglu, M. and Babuçu, F. (2006). "Soil liquefaction analysis and improvement methods" Gazi Publishing House, Ankara.
- [48] Karanlık, S., Determination of Soil Liquefaction Risk in Hatay Altinkoy Environment, M.Sc., Çukurova University Institute of Science and Technology, Adana, 2006.
- [49] Sönmez, B., 2006. Investigation of the Effect of Liquefaction Potential and Cover Floor Thickness on Surface Deformations on the Southern Coast of Kocaeli Bay, M.Sc., Hacettepe University, Institute of Science, Ankara.
- [50] Yilmaz, I., Bağci, A., Soil liquefaction susceptibility and hazard mapping in the residential area of Kütahya (Turkey), *Environmental Geology*, 49(5), 708-719, (2006).
- [51] Taylan, Z., Uysal, H., Lav, M., Erken, A., Istanbul, Case study covering settlements caused by liquefaction and loss of bearing capacity, *Earthquake Engineering Conference, Istanbul*, 471-482,( 2007).
- [52] Unutmaz, B., Cetin, K. O., Soil-structure-earthquake interaction in seismic soil liquefaction. In the *Sixth National Earthquake Engineering Conference; Istanbul, 2007*; pp. 495–506.
- [53] Ozaydin, K. (2007). Liquefaction in Soils, *Sixth National Earthquake Engineering Conference, October, Istanbul, Proceedings: 231-255*.
- [54] Lenz, J.A., Baise, L.G., Spatial variability of liquefaction potential in regional mapping using CPT and SPT data, *Soil Dynamics Earthquake Engineering Research Insititue* 27(7), 690-702,( 2007).
- [55] Tosun H., and Orhan A., The Use of Geographic Information System Programs in Determining the Geo-Engineering Properties of the Foundation Soil: The Example of Eskişehir. *ESOGUEng. Mim Fac. Journal, Eskişehir*, (2007).
- [56] Koç, G., Evaluation of the Liquefaction Potential of Gölcük and Its Surroundings. Master's Thesis, Kocaeli University, Institute of Science and Technology, Kocaeli, (2007).
- [57] Özaydın, K., Liquefaction in soils. *Sixth National Earthquake Engineering Conference in;2007*; pp. 231–255.
- [58] Hasançebi, N., Ulusay, R., 2007. Empirical Correlations Between Shear Wave Velocity and Penetration Resistance for Ground Shaking Assessments. *Bulletin of Engineering Geology and the Environment* 66, 203–213.

- [59] Yılmaz, D., Babuçcu, F., Batmaz, S. ve Kavruk, F., 2008. Liquefaction Analysis and Soil Improvement in Beydag Dam, Geotechnical and Geological Engineering, 26, 211-224.
- [60] Unutmaz, B., Assessment of soil–structure–earthquake interaction induced soil liquefaction triggering, Citeseer, (2008).
- [61] Sonmez, B., Ulusay, R. and Sonmez, H. (2008) A Study on the Identification of Liquefaction-Induced Failures on Ground Surface Based on the Data from the 1999 Kocaeli and Chi-Chi Earthquakes. Engineering Geology, 97, 112- 125.
- [62] Yalçın, A., Gokceoglu, C. and Sönmez, H, 2008. Liquefaction Severity Map for Aksaray City Center (Central Anatolia, Turkey), Nat. Hazards Earth Syst. Sci, 8, 641-649.
- [63] Sağlam, M., Examination of Liquefaction Potential of Areas Based on Saruhanlı (Manisa) Municipality Development Plan, Master Thesis, Gazi University Institute of Science and Technology, Ankara, 2008.
- [64] Akın, M., Seismic microzonation of Erbaa (Tokat-Turkey) located along eastern segment of the North Anatolian Fault Zone (NAFZ), (2009).
- [65] Pehlivan, M., Assessment of liquefaction susceptibility of fine grained soils, M.Sc.Thesis, Middle East Technical University. Ankara, Turkey, (2009).
- [66] Bol, E., Önalp, A., Arel, E., Sert, S., Özocak, A., Liquefaction of silts: the Adapazari
- [67] Mhaske, S.Y., Choudhury, D., GIS-based soil liquefaction susceptibility map of Mumbai city for earthquake events, Journal of Applied Geophysics 70(3), 216-225, (2010).
- [68] Cao, Z., Hou, L., Xu, H., Yuan, X.J.E.E., Vibration, E., Distribution and characteristics of gravelly soil liquefaction in the Wenchuan Ms 8.0 earthquake 9(2), 167-175,( 2010).
- [69] Holzer, T.L., Jayko, A.S., Hauksson, E., Fletcher, J.P., Noce, T.E., Bennett, M.J., Dietel, C.M., Hudnut, K.W., Liquefaction caused by the 2009 Olanca, California (USA), M5. 2 earthquake., Journal of Engineering Geology, 116(1-2), 184-188, (2010).
- [70] Aslan, R., Investigation of Liquefaction Potential of Soils in the Gebze Wastewater Treatment Plant (Kocaeli) Area, Master Thesis, Ankara University Institute of Science, Ankara, 2010.
- [71] Orhan M., Ateş A. Investigation of Liquefaction Potential of Soils with Cone Penetration Test (CPT) Data with Manisa-Saruhanlı Sample. Journal of Polytechnic. 2011; 14(1): 15-23.

- [72] Tosun, H., Seyrek E., Orhan A., Savaş, H. and Türköz, M., 2011. Soil Liquefaction Potential in Eskişehir, NW Turkey, *Nat. Hazards Earth Syst. Sci.*,11, 1071-1082.
- [73] Akdeniz E., Güney Y., Pekkan E., Avdan U, Tün M. and Ecevitoglu B., Evaluation of Geo-Engineering Properties of Foundation Soil Using Geographical Information System: Eskişehir Province, Güllük, Yenibağlar and Bahçelievler Neighborhoods Example, *International Advanced Technologies Symposium ( IATS'11), Elazig*, 202-206. (2011).
- [74] Papathanassiou, G., Seggis, K., Pavlides, S., Evaluating earthquake-induced liquefaction in the urban area of Larissa, Greece, *Bulletin of Engineering Geology the Environment* 70(1), 79-88, (2011).
- [75] Chang, M., Kuo, C.-p., Shau, S.-h., Hsu, R.-e.J.C., *Geotechnics, Comparison of SPT-Nbased analysis methods in evaluation of liquefaction potential during the 1999 Chi-chi earthquake in Taiwan* 38(3), 393-406, (2011).
- [76] Bhattacharya, S., Hyodo, M., Goda, K., Tazoh, T., Taylor, C., Liquefaction of soil in the Tokyo Bay area from the 2011 Tohoku (Japan) earthquake. *Soil Dynamics Earthquake Engineering Research Insititue* 31(11), 1618-1628, (2011).
- [77] Kolat, C., Ulusay, R., Suzen, M.L., Development of geotechnical microzonation model for Yenisehir (Bursa, Turkey) located at a seismically active region, *Journal of Engineering Geology*, 127, 36-53, (2012).
- [78] Sönmezer Y.B., Çeliker M., Kılınç M.Y., Analysis of liquefaction potential of Bahçelievler and Fabrikalar neighborhoods in Kırıkkale province in geographic information systems, *International Journal of Engineering Research and Development*, 4(1), 33-40, (2012).
- [79] Dixit, J., Dewaikar, D., Jangid, R.J.N.h., Soil liquefaction studies at Mumbai city 63(2), 375-390, (2012).
- [80] Habibullah, B.M., Pokhrel, R.M., Kuwano, J., Tachibana, S., GIS-based soil liquefaction hazard zonation due to earthquake using geotechnical data. *Internaitonal Journal of Geomate* 2(1), 154-160, (2012).
- [81] Sharma, B., Hazarika, P.J.G., Engineering, G., Assessment of liquefaction potential ofGuwahati city: a case study 31(5), 1437-1452, (2013).
- [82] Akın, M., Özvan, A., Akın, M., Topal, T., 2013. Evaluation of Liquefaction in Karasu River Floodplain after the October 23, 2011, Van (Turkey) Earthquake. *Natural Hazards*, 69, 1551–1575.
- [83] Aydan, Ö., Ulusay, R., Kumsar, H., 2013. Seismic, Ground Motion and Geotechnical Characteristics of the 2011 Van-Ercis, and Van-Edremit

Earthquakes of Turkey, and Assessment of Geotechnical Damages. Bulletin of Engineering Geology and Environment.

- [84] Huang Y., Yu M., (2013), Review of soil liquefaction characteristics during major earthquakes of the twenty-first century, *Natural Hazards*, 65, 2375-2384.
- [85] Duman, E.S., Ikizler, S.B., 2014. Assessment of Liquefaction Potential of Erzincan Province and its Vicinity, Turkey, *Nat Hazards*,73, 1863-1887.
- [86] Akın, M., Akın, M.K., Akkaya, İ., Özvan, A., Şengül, M.A., 2015b. Erciş (Van) Yerleşim Alanındaki Zeminlerin Sıvılaşma Potansiyelinin Değerlendirilmesi, *Ulusal Mühendislik Jeolojisi Sempozyumu*, 3-5 Eylül 2015, KTÜ, Trabzon. 208-215.
- [87] Gucek S., Zorluer I. Establishment of Site-Specific Liquefaction Risk Maps with One-Dimensional Analysis Method: The Example of Afyonkarahisar. *Afyon Kocatepe University Journal of Science and Engineering Sciences*. 2021; 21(4): 908-921.